Imperial College London
Department of Mechanical Engineering

Investigation of near and post stall behaviour of axial compression systems

Jose Pedro Nunes Teixeira Vaz Moreno

March 2021

Submitted in part fulfilment of the requirements for the degree of
Doctor of Philosophy in Mechanical Engineering of Imperial College London
and the Diploma of Imperial College London

Abstract

The design of modern gas-turbine engines is continuously being improved towards better performance, better efficiency and reduced cost. This trend of aero-engine design requires compression systems which produce higher pressure ratios and thus, have higher loaded blades and a closer spacing between blade rows. Such designs are more prone to aerodynamic instabilities and consequent stall and surge can be catastrophic. The majority of the research conducted on compressor stall and surge is limited to old designs with lower pressure ratios or single stage compression systems. In this thesis, the near and post stall behaviour of a modern multi-stage high-speed intermediate pressure compressor rig and an aero-engine three-shaft compression system are studied in detail. The main objective is to develop and validate reliable CFD models to predict surge and rotating stall and shed light on the underlying physical mechanism of the phenomena.

CFD computations were performed to gain understanding of the current capability to model the flow behaviour of a multi-stage compressor rig near stall condition. Two turbulence models were tested and an extensive grid discretization study was performed. In order to improve the prediction of the compressor's stability boundary, a modification in the widely known Spalart-Allmaras turbulence model is proposed. Subsequently, unsteady CFD computations were carried out to evaluate the impact of flow unsteadiness in the performance prediction of this compressor rig. It was found that for operating conditions characterized by non-axisymmetric flow features, an unsteady full annulus model is required to predict the compressor performance. For low speeds, these flow features develop over a wide range of operating conditions. When the compressor operates at high speeds, these flow features are limited to operating conditions near the stability boundary. The above findings were validated against experimental results.

Early stages of this research revealed that numerical calibration of a CFD surge computation in a three-shaft engine is a challenging task due to compressor matching. Hence, an iterative methodology for matching the compressors was introduced and validated against experimental data. This study considered a surge event where the engine was initially operating at mid power condition. When comparing the numerical result with measured data, it was found that the engine bleed system has a major impact on the aerodynamic loading predictions in the core system. Therefore, this system needs to be considered by component designers when accounting for robustness to surge loads.

The post stall response of a three-shaft engine compression system which is initially operating at design was investigated. It was found that the maximum surge over-pressures are caused by a combined effect between a surge induced shock wave and high pressure

gas travelling towards the core inlet during the surge blow-down period. Furthermore, it was demonstrated that the maximum surge loads are obtained for a surge event initiated by fuel-spike.

Finally, a cheaper computational approach to model surge in axial compression systems is proposed. This approach consisted of using an unsteady single passage model to predict the flow behaviour during the surge event. After comparison with full annulus results for three different scenarios, it was concluded that the single passage is capable of predicting the blow-down period of surge which is characterized by a long period of flow reversal. This model fails to predict the correct time and length scales during surge onset and flow transition between reverse to forward flow at the beginning of recovery. These time instants are characterized by non-axisymmetric flow features. However, the single passage model shows a good correlation with the results obtained using a full annulus model for estimation of average values of static pressure and mass flows during surge. This can drastically reduce simulations times from months to days during compressor surge analysis.

Declaration of Originality

I herewith certify that all material in this thesis which is not my own work has been properly acknowledged. No part of the work presented here has been submitted to any other University or Institution for any other qualification.

Jose Moreno

March 2021

Copyright Declaration

The copyright of this thesis rests with the author and is made available under a Creative Commons Attribution Non-Commercial No Derivatives licence. Researchers are free to copy, distribute or transmit the thesis on the condition that they attribute it, that they do not use it for commercial purposes and that they do not alter, transform or build upon it. For any reuse or redistribution, researchers must make clear to others the licence terms of this work.

Acknowledgements

I would like to express my sincere gratitude to my supervisor Professor Mehdi Vahdati. He has introduced me to this exciting PhD project and provided continuous technical and moral support throughout the past four years. I am very grateful for his guidance and advice since I joined Imperial College London. He has treated me as a true friend and helped me stay motivated during the most difficult times of this research. He was very kind and patient whilst he assisted the writing of research papers and this thesis. I would also like to thank him for teaching me such key aspects of research such as asking the correct questions in order to get the right answers. I have no doubt that my success as a researcher is shaped by all of his hard critics, experience and ability to suggest different solutions for very complicated problems.

I would also like to thank Dr. Fanzhou Zhao, Dr. Sina Stapelfeldt and Professor Nick Cumpsty for their insightful advice, encouragement and support. They provided invaluable guidance that contributed to this research. Dr. Fanzhou Zhao natural ability "to explain" is a skill that I admire and I wish to develop further. I am very grateful to Dr. Sina Stapelfeldt who assisted me in writing my first publication for a conference and reviewed in detail some chapters of this thesis. I would like to express my gratitude to Professor Nick Cumpsty, who has shared with me a lot of his experience and knowledge in compressor's surge.

Many thanks go to all my colleagues at the Vibration UTC at Imperial College, for providing such a friendly and pleasant environment for my PhD study. Among them, I would like to specially thank Dr. Prathiban Sureshkumar for many constructive discussions on aeroacoustic and software development, Dr. Wenqiang Zhang for sharing his knowledge on the topic of surge and Dr. Yaozhi Lu that, even thought his research was on a completely different topic than mine, gave me a lot of joy by being my desk neighbour and sharing with me pictures of funny cats.

I would like to gratefully acknowledge Rolls-Royce plc. for both sponsoring this PhD and allowing the publication of research papers. I would also like to specially acknowledge Dr. John Dodds and Christopher Sheaf at Rolls-Royce plc. for their continuous support.

Last but not the least, I would like to express my greatest gratitude to my partner, Catarina Paralta, who listened to a lot of my complaints about this research. She also made an effort to try to understand my problems so that she could suggest solutions. I also would like to thank my parents and my sister who have kindly encouraged me throughout my PhD.

Nomenclature

Coordinate System

x	Axial coordinate
y	Transverse coordinate
r	Radius
θ	Angular coordinate
t	Time

Geometry

A	Area
L	Length
V	Volume
d	Distance between cell center to the closest solid wall
y_2	Dimensional wall distance

Aerodynamics

$\bar{m}$	Corrected mass flow function
$\dot{m}$	Mass flow
T_0	Total temperature
P_0	Total pressure
p	static pressure
N	Mechanical speed
V_s	Velocity vector in the absolute frame of reference
V_r	Velocity vector in the relative frame of reference
α	Incidence angle in the absolute frame of reference
β	Incidence angle in the relative frame of reference
$\dot{W}$	Work input
H	Stagnation enthalpy
U	Rotor blade speed
ρ	Density
η	Efficiency
η	Speed of sound
γ	Heat capacity ratio
$\tilde{\nu}$	Eddy viscosity
$P_{\tilde{\nu}}$	Production term
ω	Vorticity magnitude
$D_{\tilde{\nu}}$	Destruction term

H^* Flow helicity

P^* Pressure gradient in the flow direction

Ma Mach number

m Mode number

y_2^+ Non-dimensional wall distance

c Speed of sound

Abbreviations

LPC Low pressure compressor

IPC Intermediate pressure compressor

HPC High pressure compressor

LPT Low pressure turbine

IPT Intermediate pressure turbine

HPT High pressure turbine

CFD Computational fluid dynamics

VSV Variable stator vane

IGV Inlet guide vane

$WBSL$ Wall bounded shear layer

WF Wall function

CFD Computational fluid dynamics

$2D$ Two-dimensional

$3D$ Three-dimensional

SM Surge margin

PR Pressure ratio

wl Working line

sl Surge line

BPF Blade passing frequency

BPP Blade passing period

$RANS$ Reynolds-Averaged Navier-Stokes

SA Spalart-Allmaras

MSA Modified Spalart-Allmaras

CW Compression wave

FA Full annulus

SP Single passage

Contents

1 Introduction **21**

1.1 Motivation . . . 21
1.2 Background . . . 23
1.3 Research objectives . . . 26
1.4 Thesis outline . . . 26

2 Literature review **28**

2.1 Overview . . . 28
2.2 Fundamentals of compressor aerodynamic stability . . . 28
2.3 Stability boundary . . . 31
2.4 Stall onset . . . 32
2.5 Post stall behaviour . . . 36
2.5.1 Rotating stall . . . 36
2.5.2 Surge . . . 37
2.6 High speed compressor matching . . . 41
2.7 Studies on high speed compressors stall and surge . . . 44

3 Limitations on steady aerodynamic stability predictions **46**

3.1 Problem description and overview . . . 46
3.2 Numerical code . . . 47
3.3 Turbulence modelling . . . 47
3.4 High speed baseline model . . . 48
3.4.1 Compressor aerodynamic performance . . . 49
3.4.2 Effect of the MSA model . . . 50
3.5 Mesh independence studies . . . 54
3.5.1 Mesh density . . . 55
3.5.2 Casing boundary layer modelling . . . 56
3.5.3 Inaccuracies of the SA formulation . . . 60
3.5.4 Discussion on casing flow turbulence modelling . . . 64
3.6 Tip clearance size effects . . . 67
3.7 Turbulence modelling effect in part speed calculations . . . 68
3.8 Concluding remarks . . . 69

4 Unsteady effects on a multi-stage compressor for performance prediction **71**

4.1 Problem description and overview . . . 71

4.2 Low speed . . . 72
4.2.1 Aerodynamic performance . . . 72
4.2.2 Unsteady effects on the pre stall condition . . . 75
4.2.3 Post stall development . . . 84
4.2.4 Comparison with experimental data . . . 87
4.3 High speed . . . 88
4.3.1 Aerodynamic performance . . . 88
4.3.2 Unsteady effects on the pre stall condition . . . 90
4.3.3 Comparison with experimental data . . . 92
4.4 Concluding remarks . . . 94

5 Methodology and validation of surge modelling in a three-shaft compression system 95
5.1 Problem description and overview . . . 95
5.2 Numerical model . . . 96
5.3 Methodology for a three-shaft compression system surge . . . 97
5.3.1 System matching . . . 97
5.3.2 LPC operating point . . . 98
5.3.3 IPC aerodynamic speed . . . 99
5.3.4 Core compressor matching . . . 99
5.3.5 System surge initiation . . . 102
5.4 Development of non-axisymmetric flow features . . . 104
5.5 Validation of the pre and post surge modelling - case P . . . 106
5.5.1 Overall transient behaviour . . . 106
5.5.2 Surge initiation . . . 108
5.5.3 Comparison with experimental data . . . 109
5.6 Concluding remarks . . . 115

6 Aerodynamic loading considerations in high power surge 116
6.1 Problem description and overview . . . 116
6.2 Cases A1 and A2 - HPC surge . . . 117
6.2.1 Overall transient behaviour . . . 117
6.2.2 Surge initiation . . . 121
6.2.3 Surge induced compression wave . . . 122
6.2.4 Effect of tip clearances on surge . . . 124
6.3 Case B - IPC surge . . . 127
6.3.1 Overall transient behaviour . . . 127
6.3.2 Surge initiation . . . 130
6.4 Comparison between cases A2 and B . . . 134
6.4.1 Surge induced compression wave . . . 134
6.4.2 Aerodynamic loading . . . 135

6.5 Maximum over-pressures and plenum size effects . . . 136
6.6 Concluding remarks . . . 139

7 Evaluation of a single passage model for surge behaviour predictions 140
7.1 Problem description and overview . . . 140
7.2 Case A2 . . . 141
7.2.1 Overall transient operation . . . 141
7.2.2 Surge initiation . . . 142
7.2.3 Blow-down . . . 145
7.2.4 System recovery . . . 148
7.3 Case B . . . 150
7.3.1 Overall transient operation . . . 150
7.3.2 Surge initiation . . . 152
7.4 Case S . . . 155
7.4.1 Numerical model . . . 155
7.4.2 Overall transient operation . . . 156
7.5 Aerodynamic loading considerations . . . 159
7.5.1 Comparison of aerodynamic loads between a rig and engine compression system . . . 161
7.6 Concluding remarks . . . 162

8 Conclusion and further work 163
8.1 Summary of the findings . . . 163
8.2 Suggestions for future research . . . 167

Bibliography 168

List of Tables

3.1 Grid density configurations. 56
3.2 Grid configurations in the proximity of the casing. 57
3.3 Tip clearance sizes normalized by blade span 68

5.1 Case studies for derivation of a methodology for surge modelling depending on the surge onset location. 96

6.1 Case studies for high power surge analysis. 117
6.2 Tip clearance sizes normalized by blade span 124

7.1 Case studies for evaluation of a SP model for surge predictions. 141

List of Figures

1.1 Rolls-Royce Trent XWB jet engine. . . . 23
1.2 Sketch of a compressor operating map flow regimes. . . . 24
1.3 Sketch of overall and stage-wise pre and post stall performance in multi-stage compressors. . . . 25

2.1 Velocity triangles for an axial compressor stage. . . . 29
2.2 Comparison between an ideal and real characteristic of an axial compressor. 30
2.3 Three dimensional viscous effects in a transonic axial rotor. . . . 31
2.4 Physical mechanism for inception of rotating stall. . . . 32
2.5 Example of a modal activity preceding stall. . . . 33
2.6 Example of a spike activity preceding stall. . . . 34
2.7 High incidence hypothesis for spike type stall inception. . . . 35
2.8 Tip leakage forward spillage criteria for spike stall onset. . . . 35
2.9 Different post stall phenomena. . . . 36
2.10 Flow streamlines across a stall cell. . . . 37
2.11 Sketch of surge cycle transient performance (a) and transient static pressure at different stations (b). . . . 38
2.12 Effect of the B-parameter on the compressor stall or surge. . . . 39
2.13 Schematic of Mazzawy's theory. . . . 40
2.14 Sketch of a forward (a) and reverse flow (b) mean line model. . . . 41
2.15 Comparison of a stage characteristic with flow function based on inlet (a) and outlet (b) conditions. . . . 42
2.16 Typical operating maps for front and rear stages of a two-stage high speed compressor. . . . 43

3.1 Meridian view of the four-stage IPC rig numerical domain. . . . 49
3.2 Steady aerodynamic performance of the compressor rig at 100% aerodynamic speed. . . . 50
3.3 Normalized axial velocity in the proximity of I4S suction surface (operating point "P2"). . . . 51
3.4 Comparison of span-wise variation in relative whirl angle upstream of I4R (a), absolute whirl angle upstream of I4S (b) and normalized eddy viscosity upstream of I4S (c) between turbulence models. . . . 52
3.5 Circumferentially averaged radial profiles of eddy viscosity at different compressor axial stations. . . . 53

3.6 Normalized source term contour at 90% and 20% span of the I4S passage. . 54
3.7 Comparison between grid cell density at casing surface for grid B (a) and Y (b). Comparison of grid radial levels between grid X (c) and Z (d). . . . 55
3.8 Comparison between grids at the same operating point (a) and span-wise variation of total pressure at inlet of I4S (b). 56
3.9 Differences between the grids used during the study on the casing boundary layer modelling. 58
3.10 Comparison between grids at the same operating point using an inviscid (a) and viscous (b) casing boundary condition using WF. 58
3.11 Grid influence on the normalized axial velocity near the casing surface of rotor 4 ("P3" operating condition). 59
3.12 Span-wise variation of normalized total pressure (a) and incidence angle (b) at the I4S inlet. 60
3.13 I4R performance (a) and I4S total pressure inlet profile (b) using grid E and Grid F. 61
3.14 I4R performance (a) and I4S total pressure inlet profile (b) using grid E and Grid G. 61
3.15 Overall (a) and B4 (b) measured and computed characteristics using grids B and D (MSA model) 62
3.16 Difference in incidence angles between grids D and B upstream of I4S at operating points "P3" and "P2", respectively (a). Grid D normalized axial velocity in the proximity of I4S suction surface at operating point "P3" (b). 63
3.17 Overall (a) and B4 (b) measured and computed characteristics using grids B and D considering the MSA model neglecting the eddy viscosity destruction near the casing surface. 64
3.18 Comparison between normalized eddy viscosity and source term at operating condition "P3" for grids B (MSA model) and grid D (MSA model with and without destruction term) - I4R axial cut near tip region at 50% chord. 65
3.19 Effect of tip leakage flow trajectory (a) and velocity profile interaction with the WBSL (b). Red and blue represent near stall and design condition, respectively. 66
3.20 Eddy viscosity budget for a flat plate boundary layer. 67
3.21 Effect of tip clearance size on the CFD model performance. 68
3.22 Comparison between the baseline and improved model at different aerodynamic speeds. 69
3.23 Expected CFD predictions relative to experimental results. 70

4.1 Normalized compressor performance. (a) Overall. (b) Front: IGV inlet to I2S inlet. (c) Back: I2S inlet to I4S inlet. 73
4.2 Comparison of radial profiles between experiment (top row) and steady-state model (bottom row). 74

4.3 Comparison of the flow field at points “P3” and “P4”: Mid passage entropy ((a) and (b)) and I1S and I2R blade surface axial Mach number ((c) and (d)). 75
4.4 Normalized compressor front stages performance. (a) B1: IGV inlet to I1S inlet. (b) B2: I1S inlet to I2S inlet. 75
4.5 Comparison of radial profiles between experiments and CFD models (steady and unsteady). Top row: Point E3 and P3. Bottom row: Point E4 and P4. 76
4.6 Contours of axial Mach number at I2R inlet (a-d). Time history of axial Mach number (e) and dynamic pressure modal content (f) at 60% span of I2R inlet. 78
4.7 Flow angle profiles at I1S inlet (a). Stall cell propagation mechanism for operating condition “P3” in I1S and I2R at 60% span (b-f). 79
4.8 Circumferential modal distribution of dynamic pressure at 60% span at I2R inlet and I2S inlet for the “Unst. A” operating conditions as the compressor exit mass flow is reduced (see Figure 4.4b): Point P3 ((a) and (b)) , Point P3a ((c) and (d)) and Point P3b ((e) and (f)). 80
4.9 Contours of axial Mach number at I2S inlet for the “Unst. A” operating conditions (see Figure 4.4b): $\bar{m} = 1.0$ (a), Point P3 (b) and Point P3b (c). 81
4.10 Normalized total pressure ratio across I1S (a) and I2R (b) and incidence at I2R inlet (c) for the “Unst. A” operating conditions (see points in Figure 4.4b). 81
4.11 Time history of axial Mach number (a) and dynamic pressure modal content (b) at 60% span of I2R inlet when throttling to point “P4” (see Figure 4.4b). 82
4.12 Time history of axial Mach number (a) and dynamic pressure modal content (b) at 95% span of I2R inlet when throttling to point “P4” (see Figure 4.4b). 82
4.13 Normalized pressure ratio across I1S (a) and I2R (b) in regimes “Unst. A” and “Unst. B” as the compressor exit mass flow is reduced (see Figure 4.4b). 83
4.14 Incidence angle upstream of I2R (a). Development of the flow field at inlet of I2S (see Figure 4.4b): P3b (b) and P4 (c). 84
4.15 Normalized overall compressor performance and post stall behaviour. 84
4.16 Circumferential modal distribution of dynamic pressure at 90% span of I1S and I2R inlets as the compressor exit mass flow is reduced (see Figure 4.15): Point P4 ((a) and (b)), Point P4a ((c) and (d)), Point P4b ((e) and (f)) and Point P5 ((g) and (h)). 85
4.17 Axial Mach number contours at 90% span for condition “P4b” (see Figure 4.15). 86
4.18 Axial Mach number contours at 90% span for condition “P5” (see Figure 4.15). 86
4.19 Experimental dynamic pressure signal envelope at several locations across the compressor casing as it is throttled towards a post stall condition. . . . 87

4.20 Normalized compressor performance. (a) Overall. (b) Front: IGV inlet to I2S inlet. (c) Back: I2S inlet to I4S inlet. 88
4.21 Normalized compressor back stages performance. (a) B3: I2S inlet to I3S inlet. (b) B4: I3S inlet to I4S inlet. 89
4.22 Comparison of normalized total pressure radial profiles between experiments (Point "E2") and steady single passage and unsteady full annulus models (Point "N1"). 89
4.23 Axial Mach number development in the proximity of I4R and I4S blade surfaces as the compressor is throttled from point "N1" towards "N3" for the steady single passage ((a),(b) and (c)) and unsteady full annulus ((d),(e),and,(f)) models. 90
4.24 Time history of axial Mach number (a) and dynamic pressure modal content (b) at 95% span of I4S inlet as the compressor is throttled from "N1" to "N2" (see Figure 4.21b). 91
4.25 Axial Mach number at 98% span at I3R, I3S, I4R and I4S for point "N2" (a). I4S inlet for point "N2" (b). 91
4.26 Time modal distribution of dynamic pressure at 95% span across the compressor using CFD data: point "N1" (a) and point "N2" (b) in Figure 4.21b. 92
4.27 Time modal distribution of dynamic pressure at the compressor casing using experimental data: point "E1" (a) and point "E3" (b) in Figure 4.20. The data at IGV exit is not available. 93

5.1 Meridian view of the engine compression system domain. 97
5.2 Block diagram of a three-shaft compression system. 98
5.3 LPC characteristics and selected operating points for cases A1 and P. . . . 99
5.4 Effect of the HPC mechanical speed on the core characteristics (from IGV inlet to HPC exit) - case A1. 100
5.5 Effect of the HPC mechanical speed on the IPC (a) and HPC (b) characteristics - case A1. 101
5.6 Effect of the HPC mechanical speed on the HPC inlet aerodynamic speed (a) and HPC inlet total temperature (b) - case A1. 101
5.7 Experimental (a) and numerical (b) manoeuvres to initiate surge in the front stages of the IPC. 103
5.8 Effect of the HPC mechanical speed on the IPC (a) and HPC (b) performance - case P 103
5.9 Mid passage axial velocity - case A1 (a) and case P (b). 104
5.10 Axial velocity at I2R, I2S and I3R inlet planes for case P at revolutions 0.1 and 9. 105
5.11 Circumferential modal content of axial velocity for case P - revolution 0.1 (a) and revolution 9 (b). 105

5.12 HPC characteristic and transient performance between revolution 0 and 39 - case P. . . . 107
5.13 IPC characteristic and transient performance between revolution 0 and 39 - case P. . . . 107
5.14 Axial velocity at I1S, I2R and I2S inlets for case P during the surge onset (revolutions 11.5 to 16.5). . . . 108
5.15 Axial velocity at H1S and H6S inlets for case P during the surge onset (revolutions 16 to 16.75). . . . 109
5.16 CFD time history of cross-sectional averaged mass flow (a). Static pressure of numerical probes for several stations of the IPC (b). . . . 110
5.17 Experimental measurements of static pressure at the casing for several stations of the IPC. . . . 110
5.18 Axial variation of static pressure throughout the surge cycle. . . . 112
5.19 H3S bleed patch geometry (a). Time history of corrected mass flow ($\dot{m}\sqrt{T_0}/P_0$) at H3S and H4R with and without bleed patch (b). . . . 113
5.20 CFD time history of cross-sectional averaged static pressure with (dashed lines) and without (solid lines) bleed flow. . . . 113
5.21 Over-pressure (a) and static pressure (b) axial variation across the compression system with and without the bleed patch. . . . 114

6.1 HPC characteristic and transient performance between revolution 0 and 25 - case A2. . . . 117
6.2 IPC characteristic and transient performance between revolution 0 and 25 - case A2. . . . 118
6.3 Time history of cross-sectional averaged mass flow (a) and static pressure (b) at several HPC stations and I7S between revolution 0 and 9 - case A2. . . . 119
6.4 Time history of cross-sectional averaged mass flow (a) and static pressure (b) at several IPC stations and H1S between revolution 0 and 9 - case A2. . . . 120
6.5 Axial velocity contours at the inlet of several HPC stations - case A2. . . . 121
6.6 Circumferential averaged axial Mach number at revolutions 3.34, 3.76 and 4.09 - case A2. . . . 122
6.7 Shock wave strength (a) and axial Mach number (b) at the IPC stations and HPC front stage - case A2. . . . 123
6.8 Normal shock wave modelling. . . . 124
6.9 HPC characteristic and transient performance - cases A1 and A2. . . . 125
6.10 IPC characteristic and transient performance - cases A1 and A2. . . . 125
6.11 HPC (a) and IPC (b) performance. Front (c) and rear (d) IPC block performance. - cases A1 and A2. . . . 126
6.12 Effect of the IPC tip clearances configuration on the HPC aerodynamic speed - cases A1 and A2. . . . 126

6.13 HPC characteristic and transient performance between revolution 0 and 37 - case B. . . . 128
6.14 IPC characteristic and transient performance between revolution 0 and 37 - case B. . . . 128
6.15 Time history of cross-sectional averaged mass flow (a) and static pressure (b) at several IPC stations and H1S between revolution 15 and 36 - case B. 129
6.16 IPC overall and block performance between revolution 0 and 20.5 - case B. 131
6.17 Annulus area with negative mass flow at the inlet of several IPC stations and H1S - case B. . . . 131
6.18 Axial velocity contours during the pre surge development at I1S, I5S and I7S inlets - case B. . . . 132
6.19 Axial Mach number at 50% span of I1S, I7S, H1S and H6S inlets during the surge onset - case B. . . . 133
6.20 Circumferential averaged axial Mach number at revolutions 9.71, 22.80 and 23.58 - case B. . . . 134
6.21 Time history of cross-sectional averaged static pressure at the fan outlet - cases A2 and B. . . . 135
6.22 Static pressure in the core stations at initial condition, arrival of the CW ("Pre shock") and time instant of maximum pressure ("Max. pressure") - cases A2 and B. . . . 135
6.23 Time history of cross-sectional averaged static pressure at H1S inlet - cases A2 and B. . . . 136
6.24 Time history of cross-sectional averaged static pressure at H6S inlet with different plenum volumes - case A2. . . . 137
6.25 Time history of cross-sectional averaged static pressure (log-scale) at H1S inlet with different plenum volumes - case A2. . . . 137
6.26 Time history of cross-sectional averaged mass flow (a) and static pressure (log-scale) (b) at H1S and H6S inlets with different plenum volumes - case A2. . . . 138

7.1 HPC characteristic and transient performance between revolution 0 and 35. FA model in solid lines and SP model in dashed lines - case A2. . . . 142
7.2 IPC characteristic and transient performance between revolution 0 and 35. FA model in solid lines and SP model in dashed lines - case A2. . . . 142
7.3 Time history of cross-sectional averaged mass flow (a) and static pressure (b) at H1S, H4S and H6S inlets - case A2. . . . 143
7.4 Time history of axial velocity (a) and corresponding modal content (b) at 95% span of H6S inlet - case A2. . . . 144
7.5 Time history of the H6R harmonics of axial velocity for the FA and SP solutions prior to surge - case A2. . . . 145

7.6 Time history of cross-sectional averaged mass flow (a) and static pressure (log-scale) (b) at the inlet of several IPC and HPC stations - case A2. . . . 145
7.7 Time history of annulus area with negative mass flow at I1S and H1S inlets between revolutions 0 and 14 - case A2. 146
7.8 Time history of axial velocity (a) and corresponding modal content (b) at 50% span of I1S inlet between revolutions 0 and 14 - case A2. 147
7.9 Time history of axial velocity (a) and corresponding modal content (b) at 50% span of H2S inlet between revolutions 0 and 14 - case A2. 148
7.10 Axial velocity contours at H2S inlet during revolutions 6, 6.7 and 7.5. . . . 148
7.11 Time history of mass flow (a) and annulus area with negative mass flow at I1S (b) and H1S (b) inlets between revolutions 16 and 32 - case A2. 149
7.12 Time history of axial velocity (a) and corresponding modal content (b) at 50% span of I1S inlet between revolutions 16 and 35 - case A2. 150
7.13 HPC characteristic and transient performance between revolution 0 and 43. FA model in solid lines and SP model in dashed lines - case B. 151
7.14 IPC characteristic and transient performance between revolution 0 and 43. FA model in solid lines and SP model in dashed lines - case B. 151
7.15 Time history of cross-sectional averaged mass flow (a) and static pressure (b) at the inlet of several IPC stations and H1S - case B. 152
7.16 Time history of axial Mach number at 50% span of I1S, I7S, H1S and H6S inlets between revolutions 16 and 27 - case B. 153
7.17 Annulus area with negative mass flow along the core for HPC revolutions 20, 21, 22, 23 and 24 when using the FA (a) and SP models (b) - case B. . . 155
7.18 Meridian view of the numerical domain considered in case S. 156
7.19 Time history of cross-sectional averaged mass flow ((a) and (b)) and static pressure ((c) and (d)) at the inlet of several IPC stations when using the FA and SP models, respectively - case S. 157
7.20 Time history of axial velocity (a) and corresponding modal content (b) at 90% span of I6S inlet between revolutions 0 and 28 - case S. 157
7.21 Axial velocity contours at I1S and I6S inlets during surge 2 - case S. 158
7.22 Static pressure in the core stations at initial condition, arrival of the CW ("Pre shock") and time instant of maximum pressure ("Max. pressure") for the SP and FA results - case A2. 160
7.23 Static pressure in the core stations at initial condition, arrival of the CW ("Pre shock") and time instant of maximum pressure ("Max. pressure") for the SP and FA results - case B. 160
7.24 Static pressure in the IPC stations at initial condition, arrival of the CW ("Pre shock") and time instant of maximum pressure ("Max. pressure") in surge 2 for the SP and FA results - case S. 160
7.25 Over-pressure at the inlet of IPC axial stations for cases A2, B and S. . . . 161

1 Introduction

1.1 Motivation

A fierce competition exists amongst aero-engine manufacturers to supply tomorrow's aircraft with engines which are lighter, quieter, more efficient and with lower emissions than the ones used today. This has led to recent developments towards lightweight structures, shorter intakes, higher by-pass ratios and higher pressure ratios. To cope with new design requirements, the next generation of engine architectures is being developed.

Modern compression systems are required to produce higher pressure ratios and thus, have higher loaded blades and closer spacing between blade rows. These are more prone to aerodynamic instabilities and consequent stall and surge can be catastrophic. A recurrent rotating stall event can lead to structural fatigue which results in costly maintenance or even engine grounding and thus, loss in revenue. Stall followed by surge in a high speed compressor can lead to violent disruption of the flow, damage to the structure and eventually engine shutdown. To prevent these events, the compressor aerodynamic stability must be ensured which severely constrains the aerodynamic and mechanical design of modern gas turbine compression systems.

In response to the challenges mentioned above, physical understanding of the stall and surge phenomena is needed. Research on this topic is always more qualitative than quantitative due to the inherent difficulty of the problem. Many of the stall flow features are common between compressors. However, there are always unexpected variations when comparing two compressor designs and particularly, when a new design is conceived. Due to the large variance of core compressor designs, operating ranges and engine architectures, a generalized theory of these phenomena is hard to establish and a significant number of problems remain poorly understood. From a research perspective, it is sensible to learn a compressor's response to an aerodynamic perturbation and associate the phenomena with previous known technologies. For example, a surge event may originate from aerodynamic instabilities caused by distinct engine malfunctions such as a variable stator vane (VSV) malschedule or a fuel spike in the combustion chamber. Also, wear and tear can have an impact on the system performance and reduce its stability margin of operation. Depending on the scenario, the axial compression system behaviour is different. Hence, an investigation of potential post stall scenarios is required to identify critical conditions that must be taken in consideration for future designs and develop appropriate numerical tools for this purpose.

This research aims to develop new methods for estimating surge loads not only for

safety but also for efficient design. To construct such models, a better understanding of the flow during surge in modern compression systems is required. Surge loads may cause deflections of jet engine components. This can lead to mechanical rubbing between parts causing titanium fires and damage to the aircraft airframe. The current models for estimating surge loads like the one presented in [1] are based on empirical observations from old designs (lower pressure ratio and different compression system architectures). These models tend to be over-conservative which lead to larger size and heavier components which penalize aerodynamic performance.

Past research on stall and surge is more common on low speed compressors [2] which is not fully representative of modern aircraft engines that are formed by high speed machines. Experimental campaigns on high speed machines are associated with higher costs and experimental data is not always collected successfully due to limitations in the instrumentation and complex experimental environment which is hard to control. Additionally, rotating stall and surge may damage the compressor rig components which can potentially delay and increase the cost of test campaigns.

Experimental studies on engines are even more rare than high speed compressor rigs. This is because of their higher cost and the fact that compressors and turbines when assembled are limited to operate on a fixed working line. It is unrealistic to build a brand new engine and perform tests on the compressor‘s post stall behaviour which will likely damage the engine components. Moreover, adding the instrumentation for proper measurements is difficult. Naturally, a full engine compression system test case is highly relevant from an engineering perspective because it provides an opportunity to study the interaction between compressors and overall system responses to different flow perturbations which lead to surge/rotating stall in an assembled flight device.

Computational fluid dynamics (CFD) simulations provide an alternative and economical way for further understanding of the compressor behaviour of high speed machines. Although three-dimensional (3D) CFD methods have been used for some time, only recently the computational resources have allowed the modelling of unsteady phenomena such as rotating stall and surge in full-scale multi-stage compressors. However, the CFD modelling of such flow conditions requires a robust and validated CFD code. The objective of this work is to develop such CFD models and shed some light on the underlying physical mechanism behind surge and rotating stall in axial compression systems, namely, a four-stage modern high speed intermediate pressure compressor (IPC) rig and a jet engine compression system.

1.2 Background

Gas turbine engines are formed by three essential parts: compressor, combustor and turbine. The compressor delivers pressurised air to the combustor. When fuel is injected in the combustor, it burns and hot high pressure exhaust gas enters the turbine. The turbine and compressor are connected through the same shaft and as a result, the energy generated on the turbine is used to drive the compressor. Gas turbine engines can have multiple compressors and turbines with several stages. Modern high bypass jet engine architectures have two or three concentric shafts depending on the manufacturer and operate over a wide range of speeds. In this thesis, emphasis is given to three-shaft architectures and in particular, to the compression system.

Figure 1.1 shows an example of a modern three-shaft engine designed by Rolls-Royce and constituent systems. In three-shaft architectures, the compression system is formed by three essential parts: low pressure compressor (LPC) which is typically named as fan, intermediate pressure compressor (IPC) and high pressure compressor (HPC). These compressors are driven by the operation of three distinct turbines on three separate shafts: low pressure turbine (LPT), intermediate pressure turbine (IPT) and high pressure turbine (HPT), respectively. The direction of rotation and speed varies depending on the shaft.

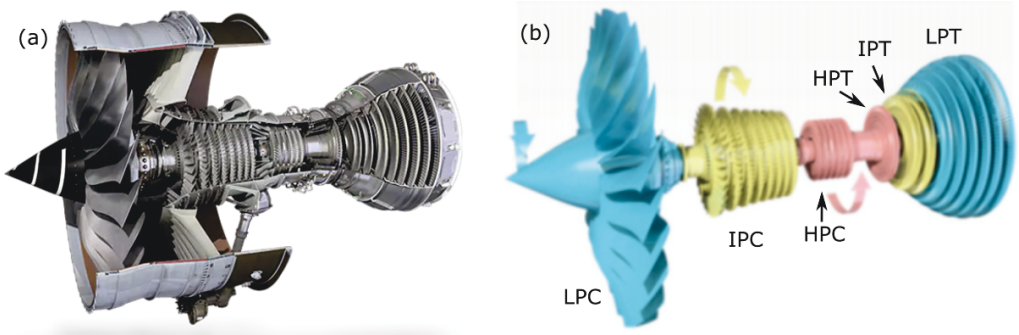


Figure 1.1: Rolls-Royce Trent XWB jet engine [3].

Despite the presence of two or three-spools[1] in modern jet engines, each compressor is still studied as an individual part using an operating map such as the one displayed in Figure 1.2. This map shows the compressor pressure ratio as a function of corrected inlet mass flow ($\dot{m}\sqrt{T_0}/P_0$) for different compressor aerodynamic speed lines ($N_i/\sqrt{T_0}$). A compressor map is typically obtained by rig testing where an electric motor drives a compressor shaft to accurately control the speed and an exit variable area nozzle controls the operating condition across each of the speed lines. To determine the aerodynamic speed characteristics and corresponding stability boundary (often named as surge/stall line), a gradual closure of the nozzle exit is performed at each of the aerodynamic speeds (constant shaft speed and inlet total temperature).

Although the compressor speed varies depending on flight cycle stage (take-off, cruise

[1] 'Spool' refers to a connected compressor, shaft and turbine.

or landing), an aircraft engine core compressor is designed to operate on a working line. However, in scenarios where a rapid transient is needed such as acceleration or deceleration, it is likely for the compressor to drift away from this line. Additionally, due to system malfunctions, wear, thermal effects and external environmental conditions, the compressors stability line may move towards the working line. When the compressor operating condition and aerodynamic stability line intersect each other, the system performance drops significantly.

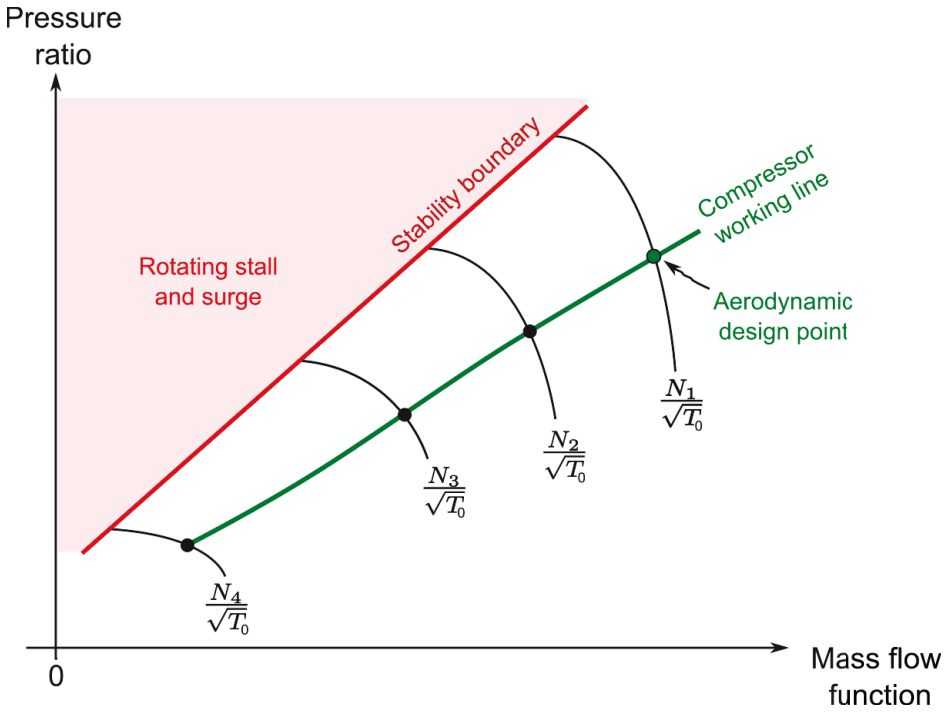


Figure 1.2: Sketch of a compressor operating map flow regimes.

In literature, the compressor stability boundary at each speed characteristic is defined as the point where the compressor performance characteristic has zero slope [2, 4–6] as seen in Figure 1.2. However, when the compressor operates past its stability limit, the compressor does not necessarily become unstable. Alternatively, **the stability limit defines the point where a further mass flow decrease causes a drop in the system overall pressure ratio**. This is typically a consequence of an aerodynamic instability (thus often called "unstable" operation) defined by the presence of stall in one or more blade rows.

The aerodynamic instability can develop into two forms: 1) rotating stall and 2) surge. The transient behaviour of rotating stall and surge is shown in Figure 1.3a. Rotating stall is characterized by the growth of one or more stalled flow sections which rotate around the annulus (named stall cells). At this condition, the time-averaged operating point stabilizes around a single point on the compressor map. Surge occurs when an aerodynamic instability causes the flow to reverse across the entire compressor. After a depressurization period, the compressor repressurizes and repeats the cycle unless corrective action is taken.

For single-stage compressors, the stability line is crossed when the compressor stalls, i.e., the operation transitions towards a post stall condition. Consequently, the stability limit is often associated with a post stall condition. For multi-stage compressors, this is not necessarily true. Figure 1.3 shows a sketch of overall and stage-wise performance in a two-stage mismatched multi-stage compressor. Consider that the compressor is operating at condition A (Cond. A). It is seen in Figure 1.3b that stage 1 operates on a positive sloped characteristic (on a post stall condition) whilst the overall operation remains on the negative sloped characteristic. Further mass flow reduction does not cause the overall pressure ratio to drop and hence, the stability limit has not been reached. The overall stability line is only reached when stage 2 operation crosses its stage stability point. As it will be demonstrated in this work, multi-stage compressors can potentially maintain their stable operation whilst one or more stages operate on a post stall condition.

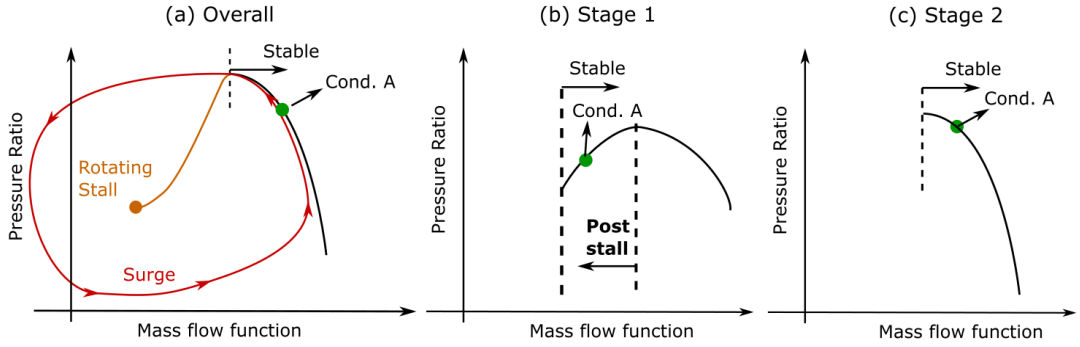


Figure 1.3: Sketch of overall and stage-wise pre and post stall performance in multi-stage compressors.

This thesis will study near and post stall compressor operation and establish modelling strategies for such conditions. Additionally, numerical results will be compared with experimental data and a detailed investigation of the flow behaviour of a future engine IPC and a modern three-shaft compression system will be presented.

1.3 Research objectives

This thesis aims to give further insight into the flow behaviour in modern high speed compression systems both at near stall and post stall operation. This investigation concentrates on both the physical phenomena as well as the numerical strategies and requirements for modelling of such flows. To the best of the authors knowledge, this is the first time worldwide that a three-shaft engine compression system simulation (using a URANS full annulus approach) is performed. The main goals of this work can be summarized as follows:

1. Develop and validate a numerical strategy for accurate prediction of near and post stall flows in modern high speed compression systems. Study the effect of turbulence modelling and grid refinements.

2. Study the near stall behaviour of a modern high speed compression system at high and low speed conditions and determine the main flow features.

3. Development and validation of an efficient numerical methodology for surge modelling in a three-shaft engine compression system.

4. Determination of the three-shaft compression system post stall response to two types of aerodynamic disturbances: compression system fuel-spike and IPC variable stator vanes (VSV) malschedule.

5. Propose, test and demonstrate the advantages and disadvantages of a computationally cheaper model for the prediction of surge behaviour in modern compression systems.

1.4 Thesis outline

Chapter 2 presents an overview on the fundamental concepts of compressor stability and it is accompanied by a brief literature survey of relevant past research on compressor pre and post stall behaviour.

A single-shaft 4-stage modern high speed rig is studied in chapters 3 and 4. This compressor rig is a part of a new architecture for a future engine and therefore, it is fundamental to understand its near stall behaviour. This case is used to analyse the limitations and advantages of different numerical models for compressor aerodynamic predictions on near stall operation. In particular, it focuses on turbulence modelling limitations and unsteady effects at both high and low speed conditions. The flow field within the compressor at these conditions is studied. The outcome provides a baseline model for studies in multi-stage compressors.

The investigation on the post stall behaviour is performed on a three-shaft engine compression system rather than a single-shaft compressor rig. In high pressure ratio aircraft

engines, the post stall behaviour is characterized by surge. This phenomena is system dependent and therefore, it is naturally important to consider the entire compression system as test case. Chapter 5 presents an efficient methodology for compression system matching using CFD calculations and a surge event at part speed which is used for comparison against experimental data. Chapter 6 focuses on the physical phenomena which drive the aerodynamic overloading during high power surges (when the engine is operating at design) and its dependence on two different surge initiation methodologies: fuel-spike and VSV malschedule. This study permits determining the worst case scenario which should be considered for certification/design. This understanding can also be used for improving existing low fidelity models such as [1, 7, 8]. Chapter 7 proceeds with the introduction of a computationally cheaper methodology for modelling of surge events for which the advantages and potential limitations are demonstrated. A comparison between the aerodynamic loading obtained for a surge event on a rig and on an engine is also presented in this chapter.

Finally, the conclusions and a series of recommendations for future work are presented in Chapter 8.

2 Literature review

2.1 Overview

The key background concepts related to compressor stability, stall and surge are presented in this chapter. Emphasis is given to high speed compressors and in particular, to past experimental and numerical investigations on stall and surge which facilitate the understanding of this work. Recently, Day [2] has published a very comprehensive literature survey on this topic (rotating stall and surge).

2.2 Fundamentals of compressor aerodynamic stability

Axial compressors are designed with the intent of maximising pressure ratio and efficiency whilst minimising cost and weight. During the flight cycle, these machines are exposed to a wide range of operating conditions. Aerodynamic stability must be ensured at all times and thus, it is an important constraint in the compressor design phase.

Compressors comprise one or several blade rows which are responsible for pressurising air by imposing a force and momentum on the flow. The mean line theory applied to a two-dimensional compressor cascade [9, 10] is widely used as a starting point to describe the fundamentals of compressor operation and stability. Though undoubtedly useful, this model relies on the assumption that the fluid is inviscid, the span-wise velocities are negligible.

Consider the compressor stage velocity triangles with key parameters identified both in the stationary and relative frames of reference as the one presented in Figure 2.1. One can define the compressor work input ($\dot{W}$) into the fluid using the Euler energy equation as:

$$\dot{W} = \Delta H = C_p \Delta T_0 = U \Delta V_\theta \tag{2.1}$$

where ΔH is the stagnation enthalpy, C_p is the heat capacity at constant pressure, ΔT_0 is the variation of total temperature, U is the rotor blade velocity and ΔV_θ is the variation in swirl velocity through the rotating rows.

The flow is guided through a stator vane into a given velocity V_{s1} with inflow angle α_1 towards the rotors blades. The rotor transfers energy to the fluid in the form of work and consequently, the flow turns into outflow angle α_2 and velocity vector V_{s2}. Under the assumption that the process is steady and adiabatic, a rise in fluid stagnation enthalpy

(ΔH) will be observed due to a variation of swirl velocity through the rotating row. Naturally, in multi-stage compressors, this process is repeated in each of the stages.

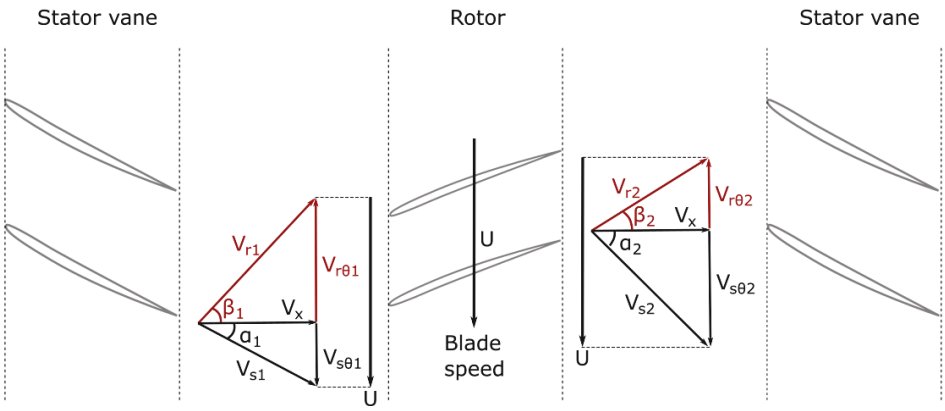


Figure 2.1: Velocity triangles for an axial compressor stage. The black and red vectors represent the stationary and relative frames, respectively.

The scenario described above is ideal where the inflow and outflow conditions are fixed and the blade airfoils are designed to maximize efficiency and pressure ratio. Unfortunately, gas turbine engines need to operate over a range of conditions and thus, flow angles and mass flow adjust in order to deliver the amount of air imposed at the core outlet, i.e., combustion chamber. Furthermore, the problem complexity increases because air compression is not a reversible process, i.e, entropy will be generated and loss in total pressure is unavoidable.

Figure 2.2 shows a comparison between an ideal and real characteristic of an axial compressor. The ratio between these curves is the compressor efficiency which is essentially the ratio between the work transferred to the fluid and actual work input into the compressor. It is evident that the difference between these curves increases as the compressor operation moves away from design condition. This is because the levels of diffusion across a compressor blade row increase causing the blades to turn the flow less effectively, which contribute to an increase in total pressure loss and fall in efficiency. Further details on compressor loss generation mechanisms can be found in published research [5, 11, 12].

This thesis focuses on the compressor flow behaviour when it approaches the stall boundary at which point either rotating stall or surge occurs. Stall is characterized by a flow detachment or separation from a blade surface and results in a prompt change in flow pattern around an airfoil where lift decreases and drag increases. Lieblein [13] has published one of the most famous works in aerodynamic stability in 2D blade cascades. Under the assumption that the flow turning and pressure rise are limited by the suction surface boundary layer diffusion, he derived the diffusion factor. This coefficient indicates how likely is the boundary layer to separate in the presence of an adverse pressure gradient.

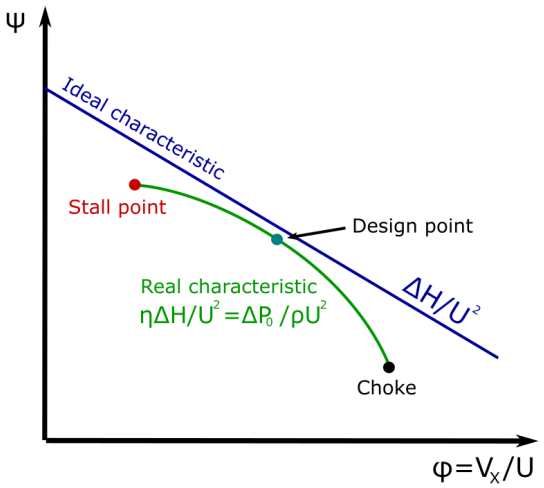


Figure 2.2: Comparison between an ideal and real characteristic of an axial compressor.

Each airfoil geometry is characterized by a diffusion factor limit that when exceeded is recognized as the beginning of blade stall. The compressor flow angles and level of diffusion on the suction surface boundary layer of each blade increase as the flow coefficient is reduced towards the stall point. When the flow coefficient is reduced below the stall point, the flow separates from the blade suction surface and the compressor (or compressor stage) transitions into a stalled condition.

Although the fundamentals of aerodynamic stability discussed until this point have considered a 2D inviscid compressor cascade, these conditions are far from real. Compressor flows are much more complex due to viscous and 3D effects. These lead to a variation of effective flow area which has an enormous impact in the flow capacity and pressure rise.

Viscous effects are ultimately responsible for all loss generation mechanisms in compressors with exception of losses introduced by shock waves in transonic machines. Even though shock waves can interact with boundary layers resulting in flow separation which is a viscous effect. End wall boundary layers, tip leakage flows, hub corner separations and blade wakes contribute to a reduction in effective flow area. Consequently, these flow features cause total pressure loss and they need to be considered when studying core compressors at off-design condition. Figure 2.3 shows a sketch of the flow field in a transonic compressor rotor which incorporates these viscous effects. A detailed review on viscous effects can be found in [9].

It is worth noting the importance of a multi-stage arrangement in core compressors. In these machines, the flow field is defined by the flow dynamics across all blade rows stacked together and can hardly be studied in isolation. Furthermore, because of the relative movement between stationary and rotating components, blade-row interactions occur and unsteadiness is generated.

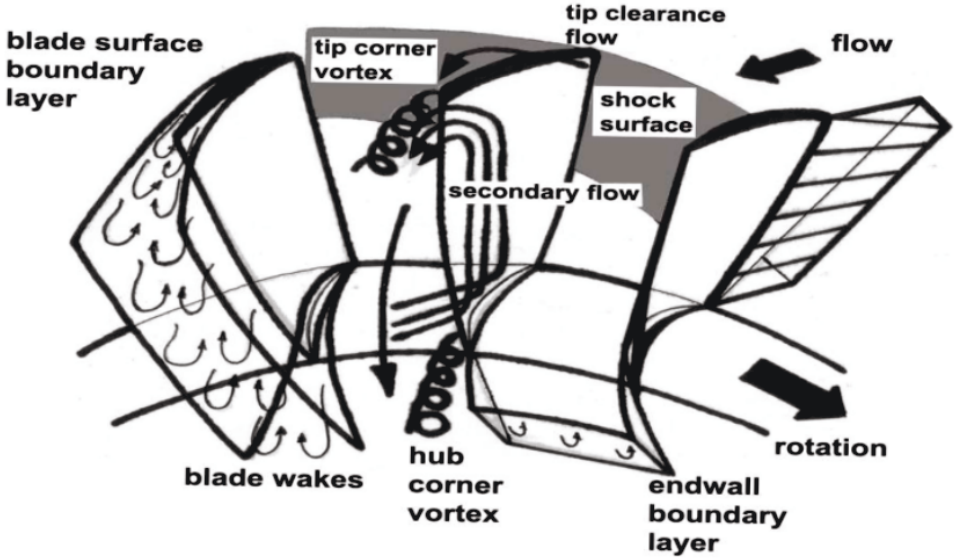


Figure 2.3: Three dimensional viscous effects in a transonic axial rotor [14].

2.3 Stability boundary

Determining the compressor stability range is a very challenging task because of uncertainties of operation. These may be caused by unexpected changes in external conditions or imposed by changes in the system dynamics such as a transient throttle change during an acceleration, a tip clearance variation due to speed change and blade erosion and wear. In order to deal with these uncertainties and ensure that the compressor stability is maintained across the whole compressor operating range, aerodynamic designers use a widely known parameter named "surge margin".

In literature, surge margin can be defined in different ways [9]. The most simple definition is given by the pressure ratio (PR) at working line (wl) and surge line (sl) (see Figure 1.2) for a constant aerodynamic speed as:

$$SM = (PR_{wl} - PR_{sl})/PR_{wl} \tag{2.2}$$

While the aerospace industry is driven towards higher pressure ratio machines, aerodynamic design improvements are required to maintain the surge margins. These can include blade geometries improvement, stage matching or casing treatment. Unfortunately, low fidelity models are not accurate enough to predict the stability boundary, study transient performance and drive major changes in design. Furthermore, Consequently, high speed rig testing is still required to map the surge line accurately.

CFD studies can be used as an alternative to estimate the compressor stability margin. Although they are not accurate enough to replace rig testing, they can be used to select which conditions to test and help understanding the 3D flow field near the stability boundary. This permits a more efficient iterative aerodynamic design and better planning on

testing campaigns. Two essential moments need to be considered when studying compressor aerodynamic stability: stall/surge onset and post stall behaviour. Stall/surge onset is dependent on the compressor design and operating condition whilst post stall behaviour is also constrained by the system design such as the downstream volume, throttle and duct. Below, previous work on stall and surge onset and post stall transient behaviour is discussed.

2.4 Stall onset

Stall and surge can be encountered as a result of different flow perturbations but in general, the onset occurs at a point where a mass flow reduction causes an abrupt change in the flow pattern of the compressor. Emmons [15] was the first to study the conditions at which a small amplitude perturbation grows in a compressor cascade. Due to geometric irregularities or non-uniformity in overloaded blade rows, low momentum regions may form in one or more blade-to-blade passages across the compressor annulus and consequently, incoming streamlines deviate into adjacent passages as seen in Figure 2.4.

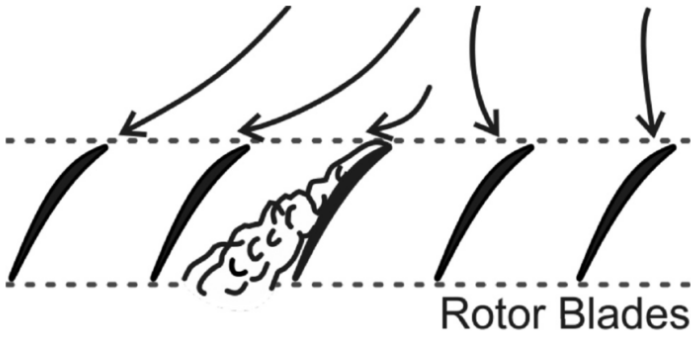


Figure 2.4: Physical mechanism for onset of rotating stall [15].

The behaviour described above is regarded as the onset of rotating stall and is associated with a localized perturbation which grows due to flow separation on the suction surface in one or more of the compressor blade passages. Two theories are widely accepted regarding the origins of rotating stall: either the onset is caused by modal or spike activity. A detailed study on these phenomena for a low speed machine is presented by Camp and Day [6].

Modal type

Experimental evidence of modal activity prior to rotating stall was first observed by McDougall et. al. [16] in a low speed compressor and later by Garnier et. al. [17] in a high speed multi-stage compressor. Modal disturbances are characterized by 2D long wavelength and small amplitude oscillations usually between 20% and 50% of the rotor frequency. They can only be excited over a limited range of operating points and typically near peak total-to-static pressure ratio [18]. They can be sustained over hundreds of shaft

revolutions and can be easily controlled by changing the downstream throttle area. It is clearly stated in [19] that modal waves are a stall precursor rather than a stall trigger, i.e., they are reversible and do not indicate that stall is occurring or about to occur. Nonetheless, modal velocity perturbations at either the tip or hub will impact the flow throughout the compressor and in most cases will gradually breakdown into rotating stall if corrective actions are not applied. Figure 2.5 presents an example of hot-wire measurements obtained prior to stall due to a modal perturbation.

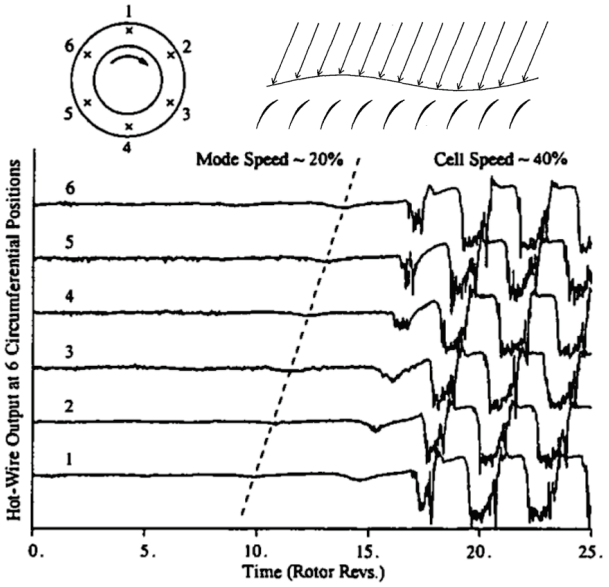


Figure 2.5: Example of a modal activity preceding stall [6, 19].

Spike type

Stall onset can be encountered without a modal perturbation. Alternatively, disturbances prior to stall can have a form of "spikes" which are characterized by 3D narrow structures which rapidly emerge into stall cells with greater sizes. Day [19] identified this type of pre stall disturbances to have higher rotational frequencies and smaller length scales than what was found in modal waves. It is worth noting that spike type inception can occur solely or in combination with modal waves if those are well established prior to the formation of spikes. Figure 2.6 shows an analogous plot to Figure 2.5 for a "spike" type perturbation prior to rotating stall.

Spike stall inception is more common and dangerous due to its rapid breakdown into rotating stall or surge. According to Hoying et. Al. [20], modal activity can be analysed based on the knowledge gathered on blade row pressure rise and turning characteristics. Therefore, modal activity can be controlled using active control. In contrast, spikes are highly unsteady and the root cause of this type of pre stall activity is still debated nowadays.

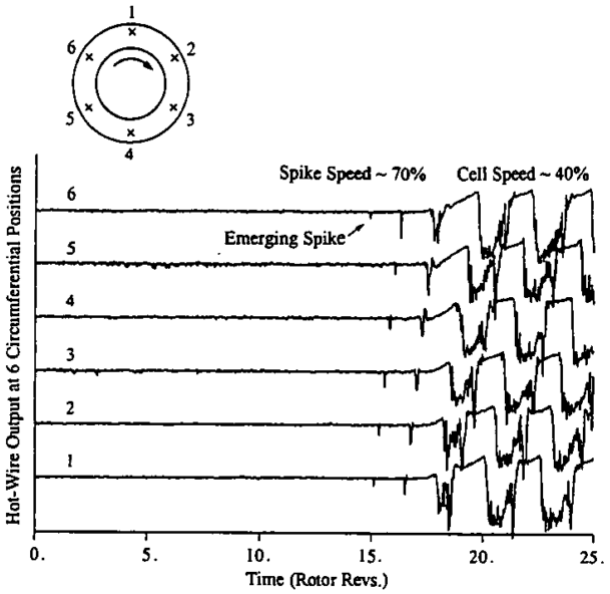


Figure 2.6: Example of a spike activity preceding stall [6].

Two well known criteria for spike stall inception are established in the literature: high incidence and tip leakage flow spillage. These criteria do not contradict each other regarding the origins of spike stall onset. Since a lot of uncertainties arise both from experimental and numerical results, it may be even possible that spike disturbances can arise from different conditions depending on the test case.

The high incidence hypothesis was introduced by Inoue et. al. [21] who observed experimentally short wavelength transient disturbances that suggested spike formation. He linked these disturbances to radial vortices which form on the blade suction surface when the rotor incidence limit is reached. These vortices travel ahead of the rotor leading edge plane in the circumferential direction. They are stretched and break down resulting in reverse flow regions near the casing downstream of the rotor. More recently, this phenomena was investigated in detail experimentally on a high speed compressor rig by Brandstetter et. al. [22]. Pullan et. al. [23] showed numerical evidence and proposed an explanation for this phenomena as seen in Figure 2.7. As an initial vortex propagates across the passage, the incidence onto the adjacent rotor increases. Consequently, that blade also stalls and the disturbance travels circumferentially and grows in amplitude when a newly shed vortex is augmented by the vorticity of the previous. In these numerical experiments, they demonstrated that this behaviour is also present in the absence of a tip clearance.

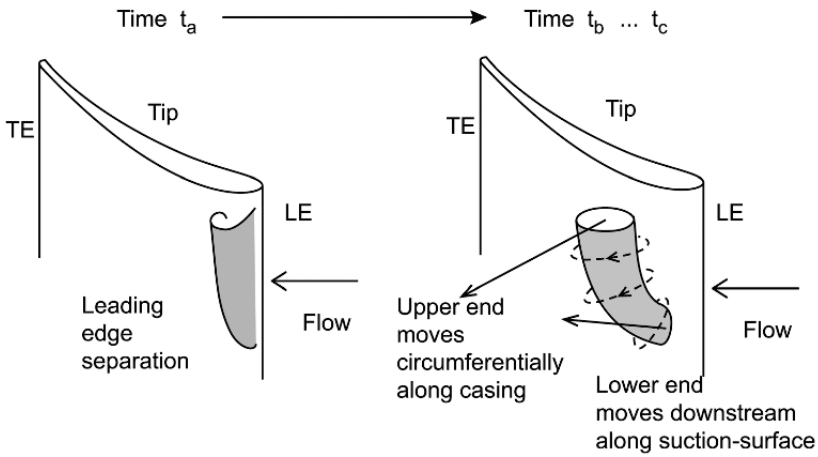


Figure 2.7: High incidence hypothesis for spike type stall inception [23].

Vo et. al. [24] presented a criteria for spike inception based on the role of the tip leakage flow. According to this theory, two conditions are required for spike type disturbances onset. The first is a tip leakage forward spillage which was firstly observed in an unsteady CFD computation by Hoying et. al. [20] where short-length scale disturbances were found when the tip leakage flow was aligned with the adjacent blade row leading edge plane. When the compressor is loaded to the extent that the tip leakage flow moves upstream of the blade leading edge, the flow is pushed around the adjacent blade leading edge causing the stall onset (forward spillage as shown in 2.8a and 2.8b). The second is the tip clearance backflow that interacts with the trailing edge of the adjacent passage as shown in Figure 2.8c. Experimental investigations on a low speed compressor by Deppe et. al. [25] revealed that the tip leakage flow was continuously reversing the flow in the vicinity of the rotor leading edge. However, spikes were only observed when the flow reversed at the trailing edge of the adjacent blade passage.

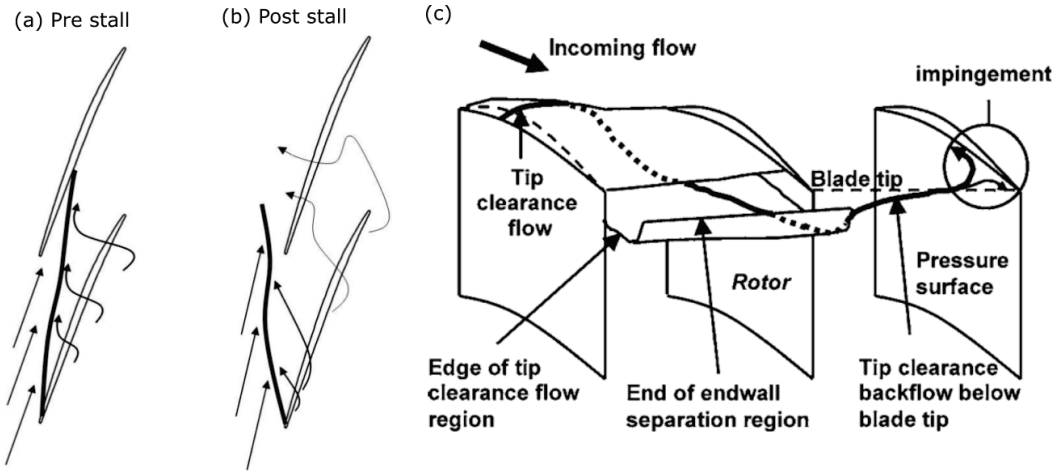


Figure 2.8: Tip leakage forward spillage criteria for spike stall onset. (a) and (b) Tip leakage spillage [26]. (c) Backflow at rotor trailing edge [24].

Previous published research on this topic shows that the compressor flow pattern is increasingly dependent on the tip clearance geometry as the mass flow is reduced [27–29]. During operation, tip clearances increase and decrease as the compressor is decelerated and accelerated, respectively, due to centrifugal forces and thermal effects. Moreover, due to engine use, the trend is for tip gaps to increase, defecting engine performance and reducing stability margin compared to design.

Although, the transition into a post stall condition is typically driven by a flow separation in the tip of a rotor blade, rotating stall can also form at lower spans. Dodds [30] has observed the formation of rotating stall cells at lower spans in a multi-stage compressor which were limited in size and did not compromise the compressor overall stability, i.e., the overall pressure ratio still increases as the mass flow is reduced.

2.5 Post stall behaviour

When the compressor operates past the stability line, it can transition into either rotating stall or surge depending on the system and operating condition. Figure 2.9 shows three distinct compressor flow behaviours that can take place after the stall onset in terms of pressure ratio as function of flow coefficient. These are discussed in the following two subsections.

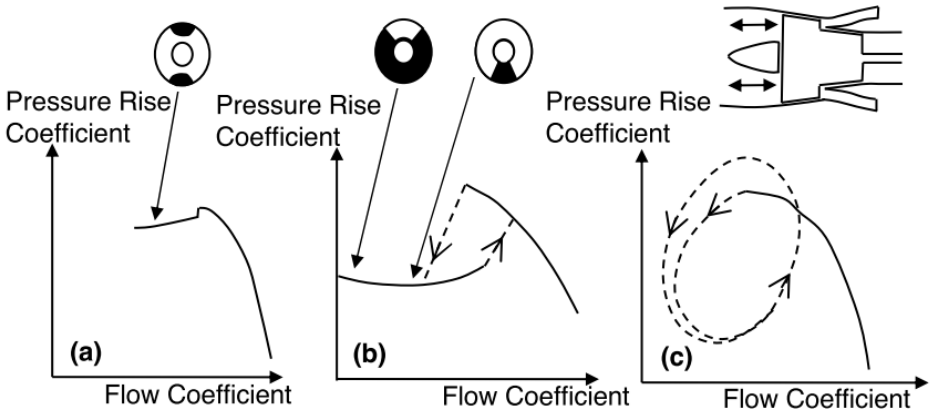


Figure 2.9: Different post stall phenomena [18]. (a) Part-span rotating stall. (b) Full-span rotating stall. (c) Surge.

2.5.1 Rotating stall

Rotating stall can be split into two distinct types: part-span and full-span rotating stall. The first is characterized by the presence of an asymmetrical flow pattern with multiple cells localized either around the hub or tip region. These cells are usually characterized by low pressure amplitudes and lead to a small drop in overall performance as shown in Figure 2.9a. In contrast, full-span rotating stall is typically characterized by the presence

of one large size stall cell which results in a large decrease in pressure ratio and mass flow (significant drop in performance) as seen in Figure 2.9b. Part-span rotating stall is axially limited to a part of the compressor. Full-span rotating stall typically extends axially throughout the machine. By further throttling a compressor from a condition with a part-span rotating stall, it can progress into a full-span rotating stall.

The flow in stall cells is characterized by either low positive velocities or reverse flow. These stall cells propagate circumferentially at a lower speed than the shaft. Day and Cumpsty [4] noted that stall cells should not be treated as a bluff body wake because the unstalled flow region in the compressor does not follow the streamlines around the stall cell. Instead, they have observed that the flow decelerates and accelerates axially as it enters and exits a stall cell, respectively, as shown in Figure 2.10.

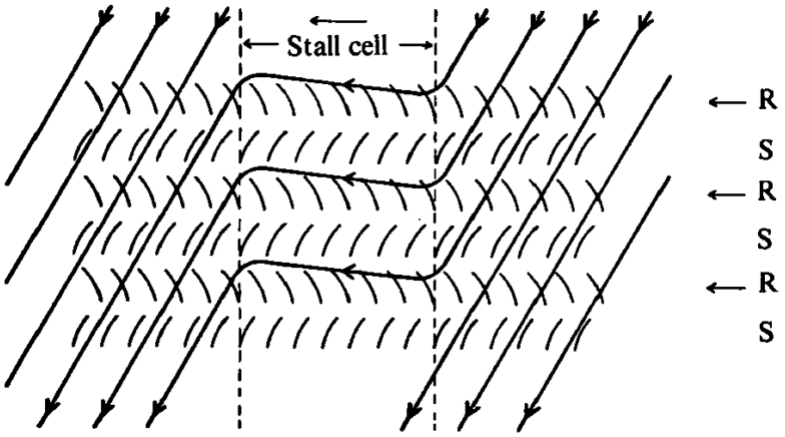


Figure 2.10: Flow streamlines across a stall cell [4].

2.5.2 Surge

Surge is characterized by large mass flow and pressure ratio oscillations as observed in Figure 2.9c. While rotating stall is solely dependent on the compressor aerodynamics, surge is also conditional on the compression system characteristics. The surge cases studied in this thesis consider a high pressure modern three-shaft engine compression system. However, because literature on this type of systems is non-existent, the literature survey on the topic will focus on single-shaft compression systems.

A surge event follows a limit cycle which can be divided in four different moments as shown in Figure 2.11a: flow reversal, blow-down, flow resumption or recovery and repressurisation. At surge onset, flow separation causes the blockage of one or several passages and rapidly grows circumferentially around the annulus. In high pressure systems (such as a modern aircraft compression system), this results in the formation of a shock wave which propagates upstream until the system inlet. The flow reverses as this wave travels along the core. Conversely, for lower pressure systems, the shock wave may not form and a transient state of rotating stall can occur before full flow reversal. After a

complete flow reversal, the machine goes through a period of depressurisation where the compressor "blows" air through its inlet. When the plenum pressure decreases to near atmospheric, the compressor initiates recovery, unstalls and moves its operating condition towards the original characteristic. If the system configuration (geometries, speeds and external conditions) is maintained, the system repressurizes and falls into a second surge event.

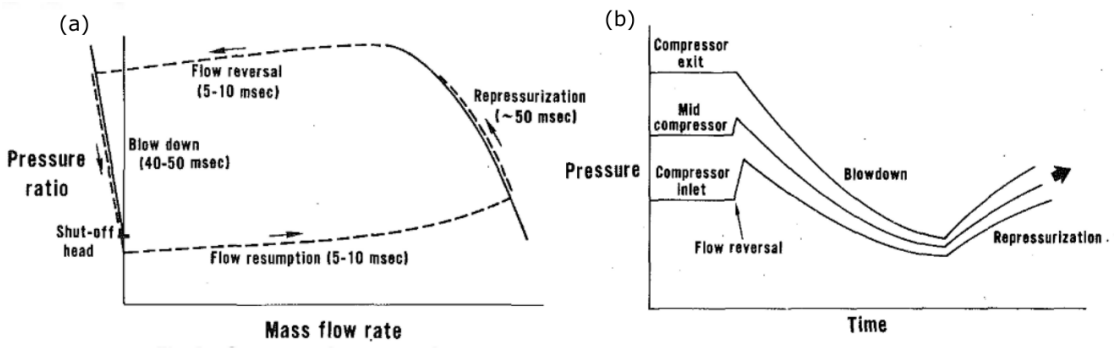


Figure 2.11: Sketch of surge cycle transient performance (a) and transient static pressure at different stations (b) [1].

Figure 2.11b shows a sketch of the static pressure time history for several compressor stations during a surge event initiated in the rear stages. It is thought that after the surge onset, the pressure increases at each of the core stations as a result of the shock wave passing[1]. This is followed by the blow-down period until the pressure decreases to a near atmospheric value at which point the compressor initiates the recovery/repressurization.

Moore and Greitzer [31, 32] derived a widely accepted surge model based on the Helmholtz resonator concept. This led to the formulation of the non-dimensional B-parameter:

$$B = \frac{U}{2c} \cdot \sqrt{\frac{V}{AL}} \tag{2.3}$$

where U refers to the blade speed, c refers to the speed of sound, V refers to the exit plenum volume and L and A are the effective compressor duct length and area, respectively. This parameter reflects the ratio between the pressure and inertial forces and it indicates whether the compressor transitions into rotating stall or surge. When the B-parameter is large, the energy in the plenum is sufficient for surge to occur. In contrast, when the B-parameter is small, rotating stall is more likely to occur. As an example, surge breakdown is typically observed in high pressure systems such as an aircraft compression system whilst rotating stall is more likely in low speed machines where the downstream pressure is not large enough. Unfortunately, the critical value at which surge occurs is highly dependent on the compression system and cannot be generalized.

[1] It will be demonstrated in this work that this sketch is incomplete and the phenomena is significantly different after the shock wave passing.

Figure 2.12 shows the effect of varying the B-parameter on a low speed test rig [33]. The downstream plenum volume was used in order to change the B-parameter. The surge event becomes "deeper" as the B-parameter is increased, i.e., more mass is expelled through the compressor inlet and the blow-down period is larger as seen in Figure 2.12a. In contrast, for a small B-parameter, the flow may stabilize on a stalled flow characteristic in a rotating stall regime as seen in Figure 2.12b.

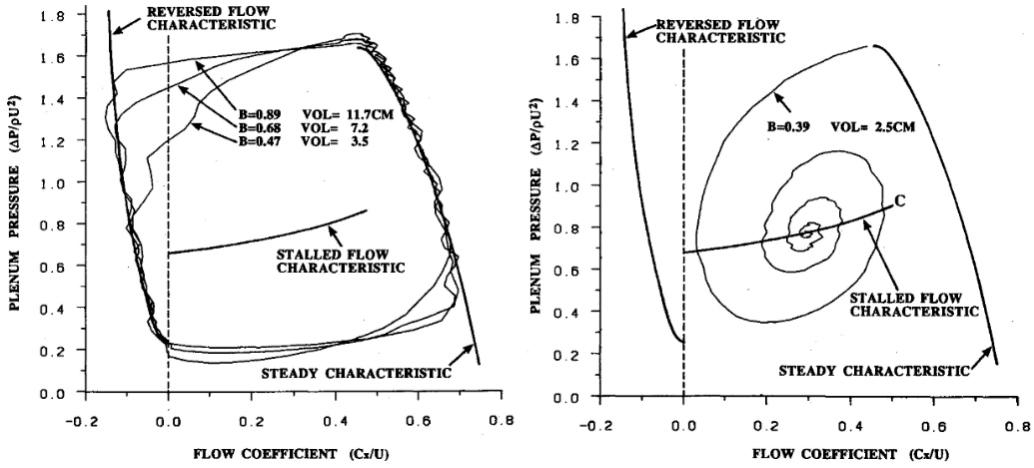


Figure 2.12: Effect of the B-parameter on the compressor stall or surge [33].

The majority of publications related to surge distinguishes two critical moments of structural solicitation during a surge cycle: firstly, the initial few instants where a shock wave propagates upstream through the compression system [1, 34]; secondly, the reverse flow phase where previous studies [35–37] have found that aeroelastic phenomena can occur and lead to blade failure. Below, a brief revision on the existing literature for these two moments is presented.

Surge hammershock

When an engine surges, a pressure pulse (often referred as hammershock/shock wave due to its typical characteristics) introduced by the abrupt change in the flow field propagates upstream. For high power systems, the force associated with this pulse can be sufficient to deflect blades or shafts and damage compressor cases and blades. This pressure pulse strength is highly dependent on the pre stall flow condition and the stall onset [38].

Mazzawy [1] derived a widely used empirical correlation for prediction of aerodynamic loads during surge in core compression systems. In this model, he assumes that the peak post-surge static pressure variation across all the core stations is linear from the inlet to the outlet. This is based on the assumption that the surge inception occurs in the rear stage of the compression system. Furthermore, this model also assumes that the flow behaviour is axisymmetric. Figure 2.13 shows a sketch of a post surge loading prediction according to Mazzawy's theory.

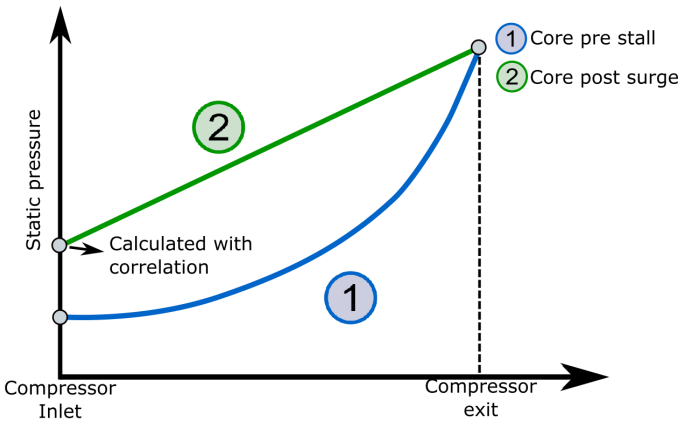


Figure 2.13: Schematic of Mazzawy's theory.

More recently, Huang [34] introduced a dynamic progressive shock tube model for prediction of loads in core compression systems. In his approach, he considered the propagation of shock and expansion waves on several shock tubes stacked together. This model has two main disadvantages: firstly, it requires a priori knowledge on which station the surge onset will occur; secondly, the behaviour of the shock and expansion waves inside the core system remains unknown. Nonetheless, Huang results have shown a good agreement with the experimental results provided by Mazzawy.

These methods are undoubtedly useful however, they rely on empirical correlations or over-simplistic assumptions that may result in over-conservative designs. Until today, there is no clear evidence that these assumptions are true and thus further investigations on the surge behaviour in core compression systems are needed. Furthermore, the models are derived based on old engine designs which may not be representative of new engine architectures.

Reverse flow behaviour

After the surge onset, the flow transitions into a reverse flow period (see Figure 2.11). This phase is associated with the longest period of the surge cycle where the compressor follows a reverse flow characteristic in a quasi-steady fashion [31].

Gamache and Greitzer [39] studied experimentally the reverse flow behaviour in axial compressors using a three-stage test rig. They observed a tangential velocity component increase in front of the rotors and stators rows. For the rotors, this component had the direction of rotation whilst for the stators it had the opposite direction. A study on a transonic compressor by Waniczek [40] demonstrated a similar phenomena. The measured inflow and outflow angles of the rotor rose to nearly 90 degrees during the reverse flow period. The differences observed in these studies between the forward and reverse flow angles is demonstrated in Figure 2.14. This is due to a combined effect of the rotor rotation and flow separation at the trailing edges of both rotors and stators which significantly contribute to an annulus blockage.

The phenomena described above has two direct consequences. Firstly, potential aeroelastic response that leads to vibration and potential blade failure. Aeroelasticity is not in the scope of this work and further information on aeroelastic studies during reverse flow can be found in [36, 37, 41]. Secondly, a temperature rise from outlet to inlet which can result in deterioration of the compressor components. This has been observed and explained both experimentally [39, 40] and numerically [42, 43].

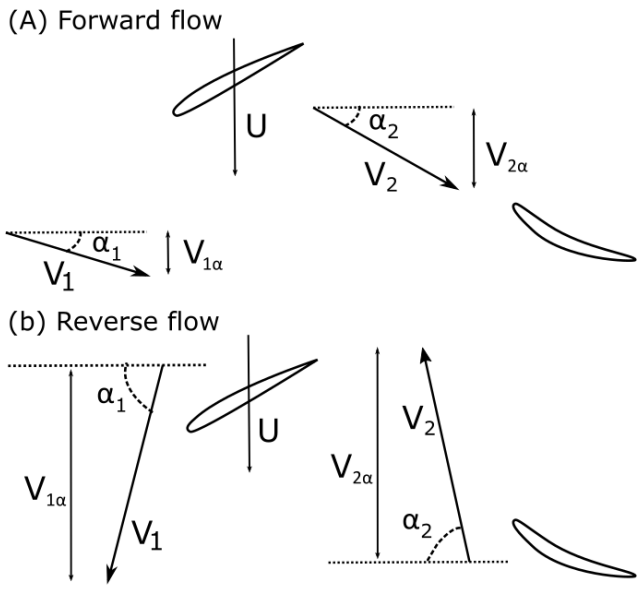


Figure 2.14: Sketch of a forward (a) and reverse flow (b) mean line model (stationary frame of reference).

2.6 High speed compressor matching

The literature survey presented until this point has not highlighted the importance of multi-stage arrangements on pre and post stall flow behaviour. For multi-stage high speed machines, compressible effects are present and thus, stage matching must be taken into consideration. As a result, it is important to understand how matching impacts the compressor performance and changes the system surge margin.

The aerodynamic design point of a multi-stage compressor is selected based on the condition at which it will operate for most of the time. Typically, the compressor is "matched" at this condition where the efficiency is maximized and a safe surge margin is ensured. In jet engines, there is a need for a wide range of operations and thus, compressors often work away from design. The problem of mismatching occurs when one or more stages operate at a stalled condition dropping the machine pressure ratio and efficiency.

Longley and Hynes [44] studied the effect of compressor matching experimentally on a three-stage low speed compressor. In their work, they found that the compressor front stage could operate at points well beyond the stall point whilst the overall compressor stability was maintained. This phenomena was explained by an attenuation of stall cells

forming in the front stage as a result of a very stable downstream stage (operating near the choke side). Dodds [30] studied the effect of VSVs and stage matching in a high speed compressor both experimentally and numerically. In his work, he found that at part speed the compressor is able to develop distinct rotating stall patterns depending on the VSVs settings whilst maintaining overall stability.

The studies above show that compressor matching has a big impact on the compressor pressure ratio and flow capacity and particularly, on the near and post stall flow. This work focuses on multi-stage compressor aerodynamics and thus, the basic knowledge of compressor matching is very important to be understood. Despite the fact that the fundamental behaviour of stage matching is explained in [9, 30], for completeness, it will be summarized here.

Compressor mismatching is a consequence of one stage inlet flow condition being given by the outflow of another stage located upstream and vice-versa. In practice, the compressor operating condition is controlled by imposing a fixed non-dimensional exit flow function ($\bar{m} = \dot{m}\sqrt{T_0}/P_0$), typically via a choked nozzle. Compressible flow theory combined with the assumption of continuity and isentropic flow allows the change in corrected mass flow function between a compressor stage inlet and exit to be written as:

$$\bar{m}_{inlet} = \bar{m}_{exit} \times \left(\frac{P_{0,exit}}{P_{0,inlet}}\right)^{\frac{\gamma+1}{2\gamma}} \tag{2.4}$$

For unstalled blades, a reduction in stage exit flow function ($\bar{m}_{exit}$) is associated with a much smaller reduction in inlet flow function ($\bar{m}_{inlet}$). This is because the pressure ratio increases when the stage exit flow function is reduced. This phenomena is demonstrated in Figure 2.15 which shows a comparison between pressure ratio as function of inlet and exit flow functions in a stage characteristic.

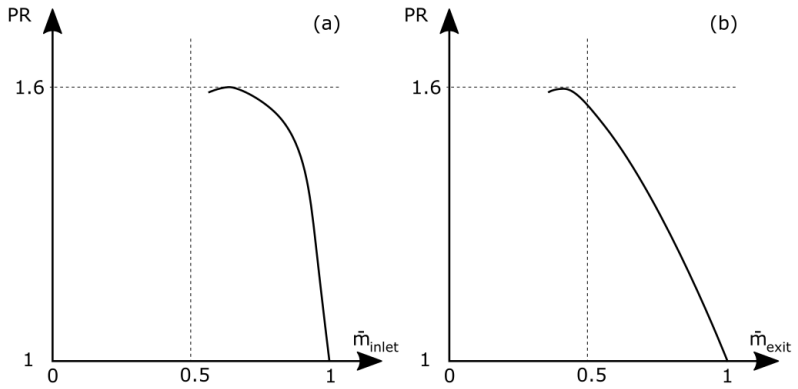


Figure 2.15: Comparison of a stage characteristic with flow function based on inlet (a) and outlet (b) conditions.

Consider now a stage-wise operation of a two-stage high speed compressor as illustrated on Figure 2.16. The rear stage of the compressor delivers an exit flow function which is imposed by the choked exit nozzle. The front stage is forced to deliver an exit flow function equal to the rear stage inlet flow function.

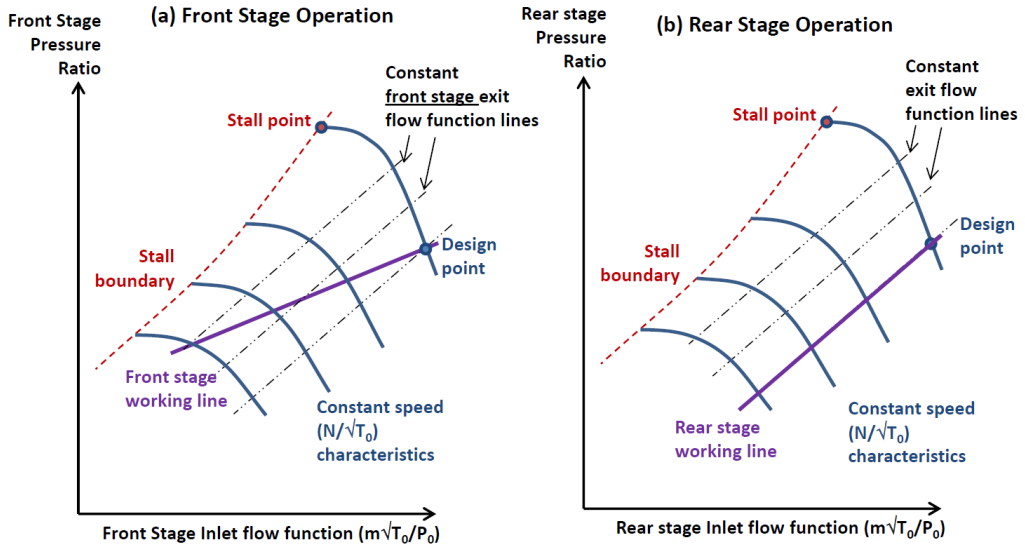


Figure 2.16: Typical operating maps for front and rear stages of a 2 stage high speed compressor [30].

For high speed operation, multi-stage compressors are more likely to reach the stability boundary on the rear stages as a result of the design configuration. The compressor design point is characterized by a condition where both the front and rear stages operate far below the surge line. In some designs, front stages may even operate in a choked condition. Because the flow rear stage exit flow function is reduced to a greater extent when the compressor is throttled (see Figure 2.15), these stages progress towards the stall boundary more rapidly.

For low speed operation, the front stage is more susceptible to stall. As the speed falls, the rear stage inlet flow function is forced to follow the rear stage working line imposed by the choked nozzle whilst delivering a lower pressure ratio (see rear stage working line in Figure 2.16b). In contrast, the front stage does not follow a constant exit flow function line. As the speed is reduced, the excursion between inlet and exit flow functions is also reduced because of the lower pressure ratio. Consequently, the front stage is effectively throttled and forced to deliver a higher pressure ratio and lower inlet flow function. This can be observed in Figure 2.16a which shows that the front stage working line progresses towards the stall boundary as the speed is reduced.

The concepts introduced above are also applicable for a three-shaft engine arrangement. In this scenario, an intermediate pressure compressor (IPC) operates upstream of a high pressure compressor (HPC) and compressor matching plays a crucial role to prevent surge and ensure operability.

2.7 Studies on high speed compressors stall and surge

Most of the studies carried out on stall and surge are based on low speed compressor testing. These studies are not fully representative of modern compression systems. Firstly, in low pressure systems the flow remains incompressible thus, the matching problem is not present; secondly, modern compression systems are capable of producing much higher pressure ratios than what was observed when most of the literature on surge was published.

Day and Freeman [45] were the first to make comparisons between low speed experiments and an aircraft engine high speed compressor on the topic of stall and surge. They studied an eight-stage compressor and they were able to differentiate pre and post stall behaviour at different operating conditions (high, mid and low speeds). In agreement with Greitzer's [32] previously suggested analytical model, they found that lower speeds are more prone to the development of rotating stall whilst surge occurred at higher speeds. This experiment also revealed further insights regarding the stall inception mechanism. They found that stall inceptions always occurred through spikes without the presence of any modal waves across the whole operating range. This suggests that modal type inception is a characteristic of low speed machines.

Depending on the operating speed, the post stall operation of the machine was different. At low speed, several part-span stall cells formed in the front of the machine whilst at a mid speed a full span rotating stall cell developed occupying the whole length of the compressor. At high speed, surge was encountered and they found evidence of a "blast wave" which almost instantaneously resulted in flow stoppage and reversal. Due to the almost instantaneous nature of the surge event, apart from having evidence that the surge was initiated in the mid stages, they were not able to unravel further details.

In high pressure machines, measurements of transient surge and induced loads are very challenging to obtain and the experimental data for this type of flow is very limited. Adding gas-path instrumentation is very difficult and thus, experimental techniques are usually constrained to inflow/outflow measurements and casing mounted sensors such as static pressure probes [6, 18]. Furthermore, close to the surge line, the flow field is characterized by high frequency unsteady phenomena which is difficult to obtain experimentally [46]. For these reasons, 3D CFD methods have captured the interest of the research community and with the significant reduction of computational cost, some progress has been made on stall and surge studies in full scale multi-stage high speed compressors.

Throughout this chapter, important numerical studies on stall and surge have been discussed. However, the majority of these studies are focused on single-stage and low speed compressors. Vahdati et. al. [35] pioneered the CFD studies on stall and surge on multi-stage high speed compressors. They simulated a two-shaft core compression system during rotating stall and surge. Due to the lack of computational resources at the time, they used a single passage model to study surge and were able to resolve a fully axisymmetric flow reversal. To study rotating stall, they used a full-annulus model on the blade rows which they knew apriori would form a rotating stall pattern. This work has

effectively demonstrated the capability of using 3D CFD methods for studying high speed compressors during stall and surge. Recently, 3D URANS simulations using either multi-passage[2] models [42, 47] or a full-annulus (360 degrees) approach [30, 43, 48] have been explored to study stall and surge in multi-stage high speed compressors. The research objectives enumerated in chapter 1 aim to answer some of the research questions opened by these studies. In particular, this thesis presents a numerical methodology and model to study a three-shaft compression system which has never been attempted before.

[2]URANS model which only simulates a slice of the annulus.

3 Limitations on steady aerodynamic stability predictions

3.1 Problem description and overview

Prediction of compressor's near and post stall behaviour is very important. This allows early identification of aerodynamic problems during engine development. The objective of this chapter is to investigate the current CFD ability to predict the compressor stability boundary. Ultimately, the goal is to identify the best available model to study pre and post stall behaviour in axial compression systems.

The compressor stability limit prediction using RANS is mainly dependent on the combined effect between two key flow features: turbulence modelling and flow unsteadiness. Both of these effects are taken into consideration in this thesis. The first stage of this research consists in evaluating the CFD solver turbulence modelling capability and underlying sources of errors.

Two different categories of modelling inaccuracies are addressed: physical modelling and numerical uncertainty. The physical modelling errors will arise directly from the models, i.e., the source of uncertainty is related to how well the mathematical set of equations describes the physical features that one is aiming to capture in the flow solution. The numerical uncertainty error is independent of the models used and it measures how accurately the set of equations is solved.

In RANS calculations, turbulence modelling plays an important role in the physical modelling uncertainty. For this reason, the suitability of the Spalart-Allmaras (SA) model [49] and modified SA model (MSA) [50] for multi-stage compressors predictions is studied. The shortcomings of the SA formulation are identified and a modification is introduced in order to improve the current ability to predict compressors' performance characteristics. Furthermore, to evaluate the impact of numerical uncertainty, an extensive grid independence study is performed.

In this chapter, a four-stage high speed compressor rig is used as test case. The study is carried out at design speed (high speed condition) due to its natural relevance in compressor design. All CFD calculations consider a steady single passage mixing plane model, which is computationally inexpensive and can be performed routinely during the design of core compressors. Nonetheless, the knowledge gathered from this study can be extended to full annulus unsteady calculations.

A shorter version of the work presented in this chapter was previously published in [51].

3.2 Numerical code

The numerical solutions were obtained using AU3D [52]. This CFD code is a three-dimensional time-accurate viscous and compressible Reynolds-Averaged Navier-Stokes solver that has been developed at Imperial College London for nearly 30 years. This code has been developed to predict both aerodynamic and aeroelastic phenomena however, the calculations presented throughout this work are purely aerodynamic.

The solver employs a finite volume method where the flow variables are represented on the cells center of an unstructured grid and the numerical fluxes are computed along the edges. The numerical solutions were obtained with a central scheme with artificial dissipation in space [53, 54]. An implicit second order time integration scheme is used to advance the system of equations in time. Numerical techniques such as local time stepping and residual smoothing were used to accelerate the solution. Further information regarding the solver is given by Sayma [52].

3.3 Turbulence modelling

In RANS, mathematical modelling of turbulence is crucial for closure of the Navier-Stokes equations. Due to its robustness, simplicity and efficiency, the default turbulence model in AU3D is the widely used one-equation Spalart-Allmaras (SA) turbulence model [49]. This model is selected as baseline since it has been tuned to give reliable predictions for turbomachinery operating at off-design conditions [18, 48, 55]. Due to shortcoming of the SA model such as premature stall, over-prediction of total pressure loss and of separation regions other turbulence models such as [56, 57] could have been considered. However, to further improve the existing model and give continuity to previous work, only a modified version of the SA model (MSA) is investigated. Instead of simply comparing different turbulence modelling formulations, the objective is to evaluate the SA formulation ability to study off-design operation of compression systems. These models are introduced in this section.

The SA model [49] defines the eddy viscosity equation as:

$$\frac{\partial \tilde{\nu}}{\partial t} + u_j \frac{\partial \tilde{\nu}}{\partial x_j} = Diffusion + Source\ term \tag{3.1}$$

where $\tilde{\nu}$ is the eddy viscosity, u_j is the velocity component in the j^{th} direction, x_j is the coordinate vector and t is the time.

The convective and diffusive terms in this model are derived directly from their classical definitions. On the other hand, the source term is derived from flows in simplified conditions using empirical observations. The source term in the SA model can be broken down in two terms: production ($P_{\tilde{\nu}}$) and destruction ($D_{\tilde{\nu}}$). For fully turbulent flows, the production term can be written as a function of vorticity magnitude (ω) and eddy viscosity

present in the flow:

$$P_{\tilde{\nu}} = f(\omega, \tilde{\nu}) \tag{3.2}$$

The extra terms in the production term of the original SA model are numerical and empirical corrections in laminar and transition regions. These are not considered for fully turbulent flow computations such as the ones in this work.

The destruction term can be defined as a function of the ratio between eddy viscosity and distance of each cell to the closest solid wall (d):

$$D_{\tilde{\nu}} = f((\frac{\tilde{\nu}}{d})^2) \tag{3.3}$$

This term represents the turbulent dissipation of the small eddies in the vicinity of a solid surface and it should be passive in free shear flows.

The works of Liu et. al. [58] and Li et. al. [59] introduced a modification in the SA model source term to improve turbomachinery flow predictions. The former considered a helicity function in order to increase the eddy viscosity production and suppress the region of hub corner separation in compressors. The latter considered the effect of pressure gradient in shock-wave and boundary layer interactions to locally correct the levels of eddy viscosity.

Lee et. al. [50, 60] combined these ideas and suggested the use of a β function which would be multiplied by the production term in the original SA model. The β function is dependent on the flow helicity (H^*) and pressure gradient in the flow direction (P^*). This modification leads to a local increase of eddy viscosity in the presence of rotational flows and adverse pressure gradients. The rest of the SA model remains unchanged. The modified production term can be written as:

$$P_{\tilde{\nu}} = \beta(H^*, P^*) f(\omega, \tilde{\nu}) \tag{3.4}$$

The results obtained for low speed fan modelling using the modified SA model (MSA) showed promising results in [50, 60, 61] however, it has never been tested for high speed core compressor predictions. In this chapter, a comparison between the original SA and MSA models is made with the objective of selecting the most appropriate model to be used in the following chapters.

3.4 High speed baseline model

Firstly, an accuracy evaluation of the baseline model is performed. Secondly, grid quality and turbulence modelling modifications are introduced to find the best available model for near stall compressor predictions. The four-stage high speed compressor rig shown in Figure 3.1 is used as case study. A choked nozzle is used to control the compressor operation and an intake duct is added to improve the numerical stability of the solver.

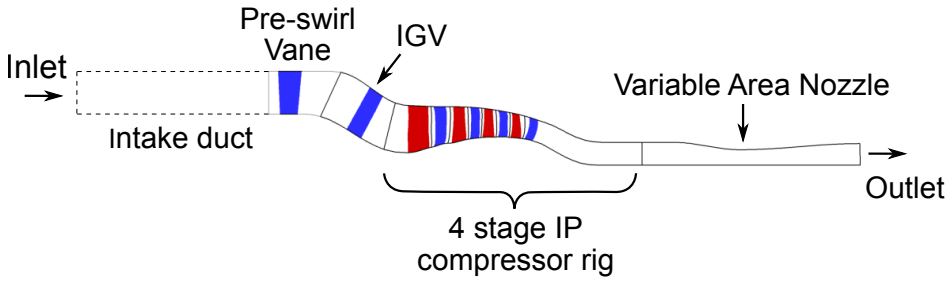


Figure 3.1: Meridian view of the four-stage IPC rig numerical domain.

This rig is designed to demonstrate the aerodynamics of a modern intermediate pressure compressor (IPC) of a future generation engine and aims to deliver a pressure ratio of 3:1 at design operation. Significant design changes have been introduced in this compressor relative to older IPC architectures and therefore, there is a need to verify and validate the current computational capability for off-design modelling. The knowledge gained from this study will be used for future design iterations.

The baseline model uses a grid which contains approximately 0.3 M points per passage and it is unstructured within the passage with a body-fitted two-dimensional O-grid around the blade geometries. The rotor passages have 47 radial grid levels across the blade span with refinements towards the hub and tip. The tip gap/casing boundary layer region is modelled using 6 equally spaced radial layers. The number of radial layers in the stator vanes is 53. The average non-dimensional distance (y_2^+) between the first cell and the solid surfaces of blades, hub and casing is approximately 50, 40 and 130, respectively. The SA turbulence model is selected and wall function (WF) is used to calculate the wall shear stresses on all the solid boundaries. The numerical model does not include any secondary geometric features such as penny gaps in the VSVs, shroud flows and geometrical fillets.

The boundary condition at the inlet is prescribed using total pressure, total temperature and flow angles. The inlet profile is kept the same as the one measured in the experiment. The outflow boundary condition is set via a variable area choked nozzle which is throttled to push the compressor towards the stall boundary. As previously explained in chapter 1, the stability limit defines the point where a further mass flow decrease causes a drop in the system overall (not stage) pressure ratio. This relates to the operating point where the compressor performance characteristic has zero slope [2, 4–6]. Stable operation refers to operating conditions with higher mass flows than this point.

3.4.1 Compressor aerodynamic performance

A comparison between the experimental results and numerical results obtained using the SA and MSA turbulence models is shown in this section. The nomenclature used in this chapter for addressing each station considers 3 characters: "INT". The "I", "N" and "T" stand for IPC, station number and rotational/stationary station type, respectively. For example, the compressor rig rotor 2 and stator 2 are addressed as I2R and I2S, respectively.

Figure 3.2 shows the overall and block normalized pressure ratio and mass flow measured from IGV inlet to I4S outlet, from IGV inlet to I2S inlet and from I2S inlet to I4S inlet. The results obtained using the MSA model show a slight increase in surge/stall margin compared to the original SA. Both in terms of overall and block performance, it is clear that the MSA model is capable of obtaining a stable numerical solution at lower mass flow and higher pressure ratio. Despite the correct trend of the CFD results relative to measured data, it is observed that the overall stability margin is under-predicted, which was not the case for the fan test cases used by Lee et. al. [50] to derive the model.

For similar values of pressure ratio, a slight overflow is observed for all of the CFD results relative to experiments. This phenomena has been justified by the absence of secondary geometry features (penny gaps and shroud flows) in the model [35, 48, 62]. Particularly, the work of Wang et. al. [63] has shown an increase of blockage across the compressor when these secondary geometric features are included. Since the overall trend is satisfactory and a constant overflow (around 1-2%) is observed for all of the cases studied throughout this work, an assessment on the effect of modelling secondary geometric features is not addressed here.

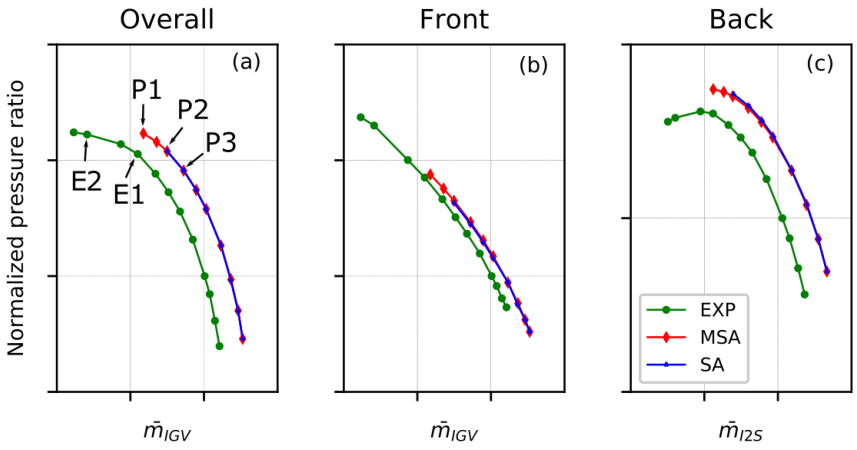


Figure 3.2: Steady aerodynamic performance of the compressor rig at 100% aerodynamic speed.

The measured data shows that the stability boundary is reached first in the rear stages of the machine. The CFD results obtained with both models are in agreement with experiments. However, closer to the stall boundary, they show a different trend of the characteristic relative to the measured data. Neither of the models is capable of capturing the compressor characteristic over its entire range.

3.4.2 Effect of the MSA model

In the following analysis, the rear stages of this compressor are analysed and it is found that I4S is the first blade row to stall. Figure 3.3a and 3.3b show the normalized axial velocity contours on the I4S suction surface at operating condition "P2" seen in Figure 3.2. The

flow streamlines in the proximity of the blade surface are also illustrated. The numerical solutions show inward radial flow migration above 20% span. The highlighted circles in Figures 3.3a and 3.3b show a region with flow reversal between 20%-40% span. This region is more evident when the SA model is used. This explains why the compressor rig can be pushed further towards the stall boundary with the MSA model. The delayed separation at the I4S suction surface using the MSA model can have three different explanations:

1. The flow angles changed at the I4S inlet due to the flow differences in the upstream stages of the compressor.

2. Eddy viscosity at I4S inlet increased due to the higher production of turbulence accumulated across the compressor.

3. Eddy viscosity in the I4S boundary layer increased due to the higher production term in the MSA model.

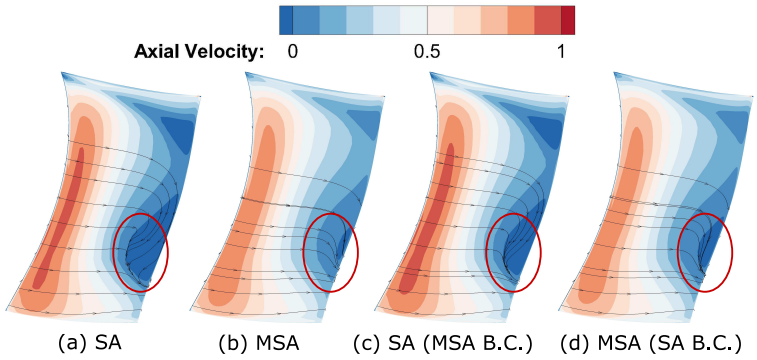


Figure 3.3: Normalized axial velocity in the proximity of I4S suction surface (operating point "P2").

Flow angles

To determine the cause of the delayed separation, radial profiles of relative whirl angle upstream of I4R and absolute whirl angle upstream I4S are shown in Figures 3.4a and 3.4b, respectively. The results show that the difference in incidence angle between the two models is very small across the majority of the span. Close to the casing, the MSA model presents higher incidences upstream of I4S which should promote an earlier separation in the I4S suction surface. This is not consistent with what is shown in Figures 3.3a and 3.3b where the MSA model shows a smaller low momentum region above 90% span relative to the SA model. Also, the characteristics shown in Figure 3.2 indicate that the MSA model stability limit is reached at a lower mass flow. Therefore, it is evident that the I4S incidence angles is not the main drive for the premature stall onset.

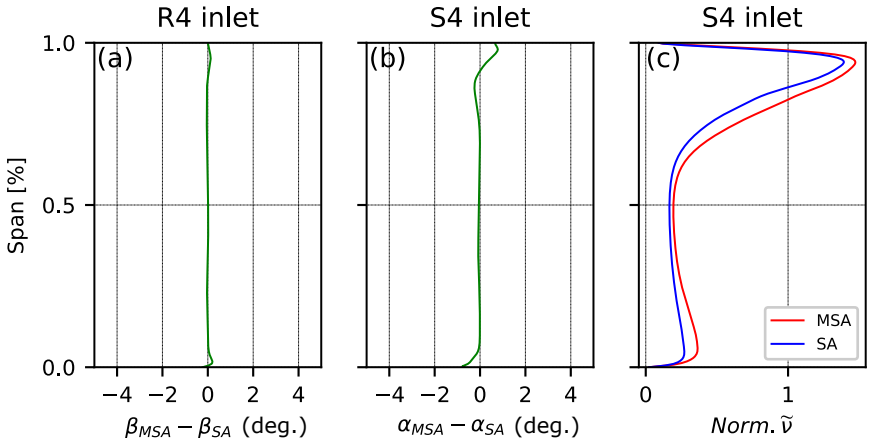


Figure 3.4: Comparison of span-wise variation in relative whirl angle upstream of I4R (a), absolute whirl angle upstream of I4S (b) and normalized eddy viscosity upstream of I4S (c) between turbulence models.

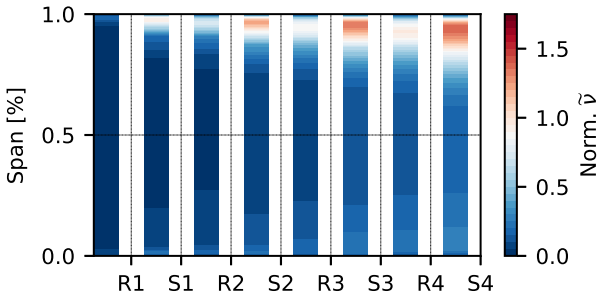
Inlet turbulence

Figure 3.4c shows the span-wise variation in normalized eddy viscosity at the inlet of I4S for the two turbulence models. Higher levels of turbulence are observed upstream of I4S when the MSA model is used. In order to isolate the effect of inlet turbulence on the I4S separation, two extra computations using a smaller domain formed by the I4S and nozzle are performed. The imposed inlet boundary condition and selected turbulence model are different between the calculations: in the first, the SA turbulence model is used and the inlet boundary condition at I4S is prescribed using the mixing plane obtained from the single-passage computation using the MSA model; in the second setup, the opposite combination is used.

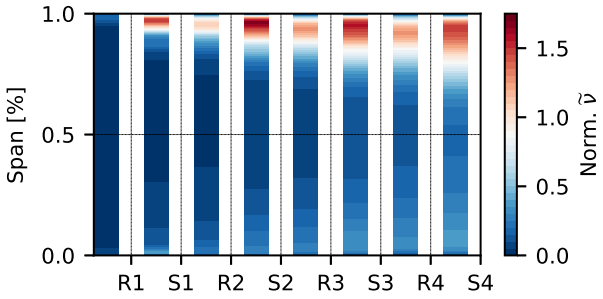
Figure 3.3c and 3.3d present the normalized axial velocity at the I4S suction surface for the cases stated above. By comparison of the numerical solutions in Figure 3.3, it is evident that the separation region identified by the circles around 20%-40% span is mainly dependent on the turbulence model used. Nonetheless, small differences can be found in the solutions which considered the same turbulence model. This indicates that the inlet eddy viscosity influences the flow behaviour on the I4S but it is not the primary reason behind the premature stall when the SA model is used.

Eddy viscosity

Figure 3.5 shows a comparison of eddy viscosity between the models across the different axial stations of the compressor. The change in the SA source term increases the eddy viscosity predominantly above 80% span. It is possible to observe a decay of eddy viscosity as the flow passes across the stators while it increases across the rotors.



(a) SA model.



(b) MSA model.

Figure 3.5: Circumferentially averaged radial profiles of eddy viscosity at different compressor axial stations.

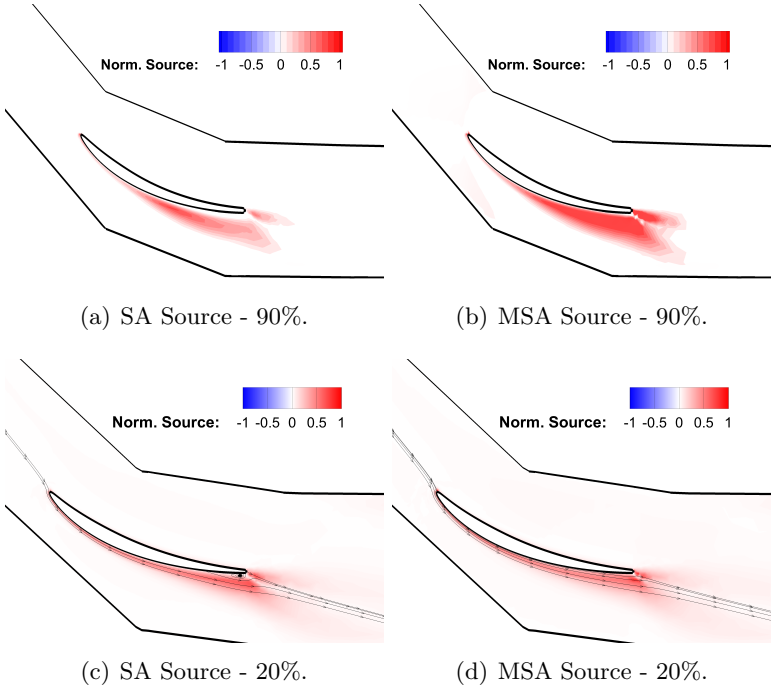
Further insight regarding the causes of premature separation can be gained by analysing the flow field at 90% and 20% span of I4S. Figures 3.6a and 3.6b illustrate the source term intensity in the stator passage at 90% span. An analogous plot is presented in Figures 3.6c and 3.6d for 20% span . The results show that the source term becomes more dominant in the proximity of solid surfaces which is an expected behaviour in boundary layers. For 90% span, the solution source term registers larger values for the MSA model relative to the SA model which is an effect of the introduced modification in the production term. The eddy viscosity increases in the proximity of the blade surface and the flow remains attached for longer which reduces the inward flow migration on I4S suction surface. As a consequence, the flow separation region between 20%-40% span is reduced as shown in Figures 3.3a and 3.3b.

At around 20% span, the flow is less separated in the solution obtained with the MSA model relative to the SA model (see Figures 3.3a and Figure 3.3b). However, similar levels of source term are observed for both models near the suction surface trailing edge at 20% span in Figures 3.6c and 3.6d. This indicates that the MSA model is capable of producing more eddy viscosity in smaller separated regions.

The delayed separation of the MSA model can hence be attributed to two causes: primarily, to an increase of eddy viscosity in the suction surface of the stator vane; secondly, to the growth of inflow turbulence due to the cumulative effect across the multi-stage compressor. This study indicates that the MSA model presents an improvement towards the prediction of the aerodynamic stability limit in high speed multi-stage compressors as

it predicts the stability point closer to the measured data.

The results presented above showed that the MSA formulation is not capable of predicting the entire range of compressor operation. It is even more difficult to determine whether it represents the flow physics correctly. For this reason, the numerical and modelling inaccuracies of the baseline grid and MSA formulation are investigated in more detail in the following sections.



(a) SA Source - 90%.

(b) MSA Source - 90%.

(c) SA Source - 20%.

(d) MSA Source - 20%.

Figure 3.6: Normalized source term contour at 90% and 20% span of the I4S passage.

3.5 Mesh independence studies

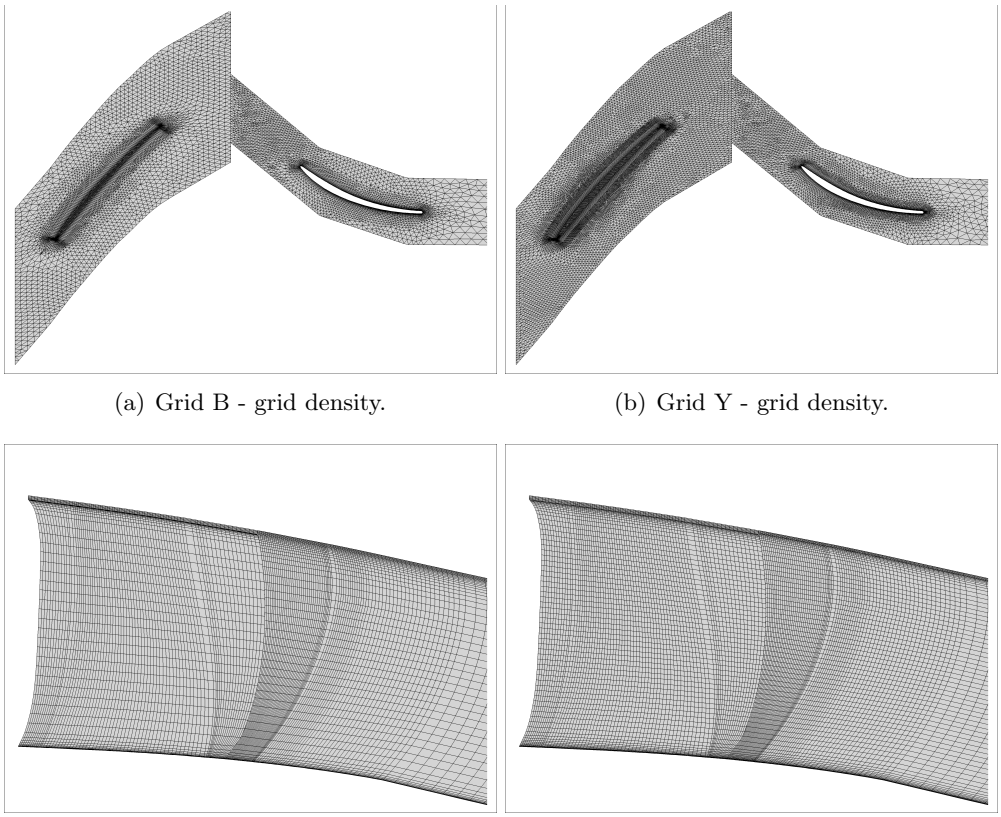
The first step to improve the baseline model is to reduce the amount of numerical uncertainty due to numerical diffusion or poorly resolved boundary layers. For this purpose, two grid sensitivity studies are performed: firstly, the effect of mesh density whilst the first cell distance to solid surfaces are kept constant; secondly, the effect of first cell distance to the casing surface whilst mesh density is kept constant. For the baseline grid, while the average non-dimensional distance (y_2^+) of the blades and hub is close to the log-law lower limit ($y_2^+ \sim 30 - 50$), the casing average y_2^+ is greater than 100. Spalart [64] showed that in high fidelity calculations of a plate in zero pressure gradient the log-law upper limit can vary between 10^2 and 10^3 depending on the Reynolds number. For pipe flows, this upper limit can vary between 10^2 and 10^5 [65]. These conditions are far from representative of the flow in the casing region of a compressor and thus, further investigation is needed.

The last stage of the compressor rig (I4R and I4S) and nozzle shown in Figure 3.1 is used as test case in these studies to reduce the computational cost. The MSA model

is selected for this investigation. The nozzle throat area is the one used in condition "P3" in Figure 3.2. The inlet boundary condition is the one obtained with the multi-stage computation at I4R inlet, i.e., the inlet boundary profile is the mixing plane total pressure, total temperature, flow angles and eddy viscosity.

3.5.1 Mesh density

Three additional grids are generated to study the solution grid independence in terms of radial layers and base cell size. The baseline grid is refined in the azimuthal and circumferential direction in order to create grid X, which is then further refined to create grid Y. Grid X is also refined radially to create grid Z. The differences between these grids are shown in Figure 3.7 and summarized in Table 3.1. The number of tip gap radial levels is kept constant in this study.



(a) Grid B - grid density.

(b) Grid Y - grid density.

(c) Grid X - radial levels.

(d) Grid Z - radial levels.

Figure 3.7: Comparison between grid cell density at casing surface for grid B (a) and Y (b). Comparison of grid radial levels between grid X (c) and Z (d).

Table 3.1: Grid density configurations.

Grid	B (Baseline)	X	Y	Z
Number of radial layers	53	53	53	72
Number of tip gap layers	6	6	6	6
Number of mesh points [Million]	0.6	0.85	1.2	1.2

Figure 3.8a shows the operating conditions obtained for the different grids and the I4R characteristic obtained from the baseline model with the entire domain. It is shown that the solution obtained with the baseline grid (B) is independent of the number of radial levels and grid density. Moreover, the radial profile of total pressure obtained downstream of I4R is approximately the same for all grids as shown in Figure 3.8b.

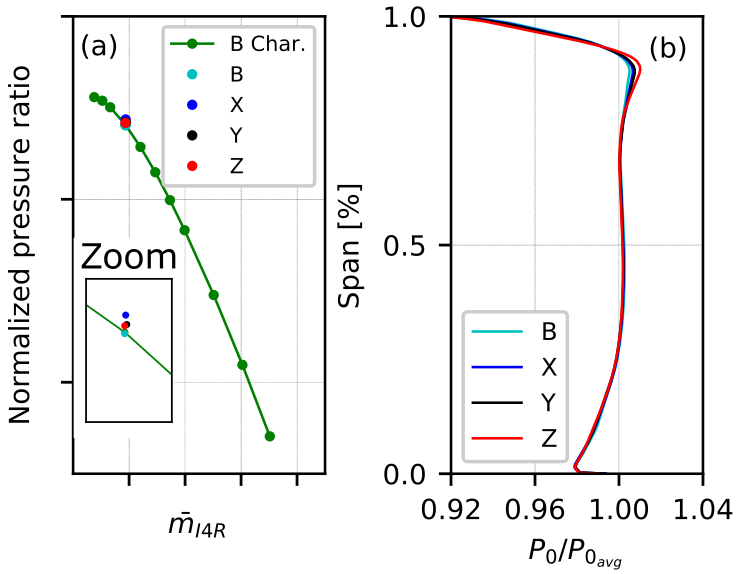


Figure 3.8: Comparison between grids at the same operating point (a) and span-wise variation of total pressure at inlet of I4S (b).

3.5.2 Casing boundary layer modelling

The first cell distance to the casing and number of grid layers which is used for modelling the end-wall boundary layer and tip gap flow varies in the literature. It is common amongst papers which study rotating stall and tip clearance flows to use 5-12 tip gap layers [23, 24, 30, 66]. Moreover, attempts have been made for compressor prediction using more than 17 layers on the end-wall boundary layer region [67, 68]. Common guidelines specify the non-dimensional distance for the no slip condition as $y_2^+ < 1 - 5$.

The work of Zante et al. [69] showed that an increased grid density near the casing wall is required to predict the leakage vortex flow accurately. This permits an improvement on

the stability boundary prediction of the compressor. Depending on the relative velocity difference between the tip leakage flow jet and the casing, different shear strength is observed and the stability limit will differ. Obviously, depending on the turbulence model, operating condition and geometry, the modelling requirements will differ. A generic model which gives a correct trend and accurate prediction of compressor performances is still sought. Here, the objective is to examine the importance of near wall refinement and grid density in the tip region on a modern compressor operating at high speed.

In order to evaluate the grid requirements to obtain a mesh independent solution two different sources of error are considered:

1. "*Discretization error*" is the numerical uncertainty that arises from change in the grid density in the end-wall boundary layer region. This is caused by the transformation of a continuous set of partial differential equations into a discrete algebraic system. It depends on the scheme and methods used (finite-volume, finite-differences, etc.) and should decrease as the grid is refined.

2. "*Boundary layer modelling error*" near the end-wall region. This source of uncertainty is an error in the physical modelling of turbulence and/or WF.

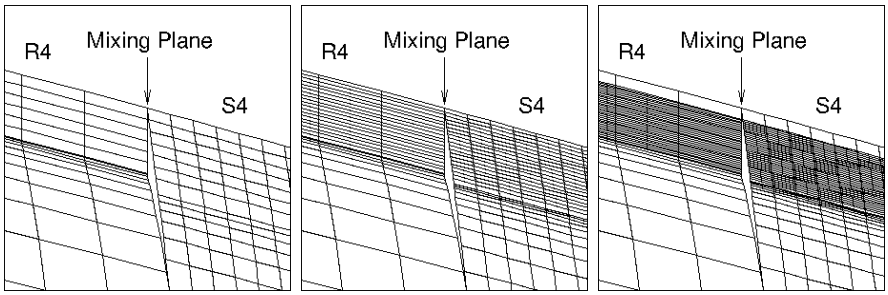
It is clear that both error sources are related to the grid resolution: the first one is directly related to the mesh base size while the latter is simultaneously dependent on mesh resolution and models applied. This is because increasing the resolution near the wall decreases the first cell wall distance which has an impact on WF and turbulence model source term. In order to clearly differentiate between the two, the terminology "*discretization error*" and "*modelling error*" is used.

Discretization error

To evaluate the impact of the discretization error, 5 grids with different numbers of layers in the casing region were tested. The number of layers in the tip gap/casing region for each grid is listed in Table 3.2 (Grids A-E). Figures 3.9a and 3.9b illustrate the differences between grid B and D.

Table 3.2: Grid configurations in the proximity of the casing.

Grid	**A**	**B (Baseline)**	**C**	**D**	**E**	**F**
Number of layers	2	6	12	19	39	156
Casing average y_2^+	500	130	89	55	28	0.65



(a) Grid B (b) Grid D (c) Grid G

Figure 3.9: Differences between the grids used during the study on the casing boundary layer modelling.

In order to isolate *discretization error* from the *modelling error*, a preliminary set of computations was performed where the casing was modelled as a slip wall. The blade tip was still modelled as a viscous wall. This treatment only neglects the casing shear stress on the fluid but resolves the tip leakage flow and its interaction with the main passage flow.

Figure 3.10a compares the I4R operating point predictions considering an inviscid casing for grids A-E. This plot also shows the I4R characteristic from the calculations with the entire domain. The results in terms of overall pressure ratio and mass flow are the same for all grids, which shows that only two layers are sufficient if the losses due to the casing wall are not considered.

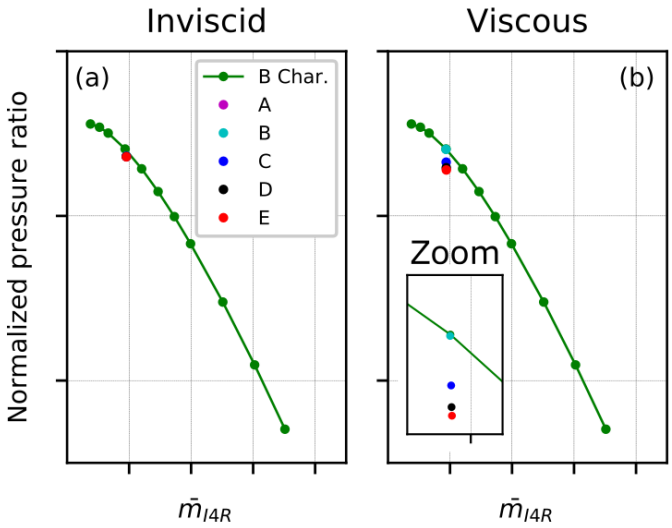


Figure 3.10: Comparison between grids at the same operating point using an inviscid (a) and viscous (b) casing boundary condition using WF.

Boundary layer modelling error

To evaluate the boundary layer modelling error, the effect of the above grid refinements on a non-slip wall with WF is investigated. As before, grids A-E were tested. Figure 3.10b shows the predicted normalized mass flow against the normalized pressure ratio obtained for the same exit nozzle area as before. The results show that the total pressure ratio decreases if the number of grid layers in the end-wall region is increased. Also, the predictions of grid D and E are very close to each other which indicates that the solution is grid independent if more than 19 layers are used. Note that for grids D and E, y_2^+ values are close to the log-law lower limit ($y_2^+ > 30 \sim 50$).

Figure 3.11 illustrates the flow for the different grids in terms of axial velocity in a radial plane at 98.5% span. The tip leakage flow reversal area changes depending on the grid. As the grid is refined, the tip leakage flow is pushed forward in the passage and the amount of reversed flow increases. As a consequence, the flow blockage is higher and the total pressure ratio drops for the same operating point. Furthermore, the flow separation in the casing region changes the flow pattern downstream of the rotor.

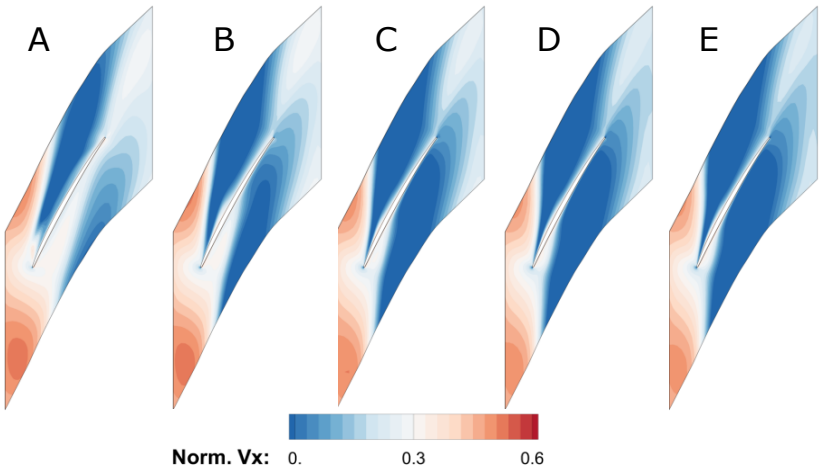


Figure 3.11: Grid influence on the normalized axial velocity near the casing surface of rotor 4 ("P3" operating condition).

Figure 3.12 shows the difference for grids A-E in terms of radial profiles of total pressure across the entire span and outflow angles above 80% span downstream of I4R. The tip clearance refinement has a major effect on the total pressure profiles above 50% span, with higher total pressure predicted for the coarser grids. The results obtained using 2 and 6 layers are very similar which indicates that using a grid with 6 layers does not capture the interaction of the flow with the casing wall. As the grid is refined, higher incidence angles at I4S inlet above 95% span are observed. This is caused by the change in tip leakage flow trajectory in I4R.

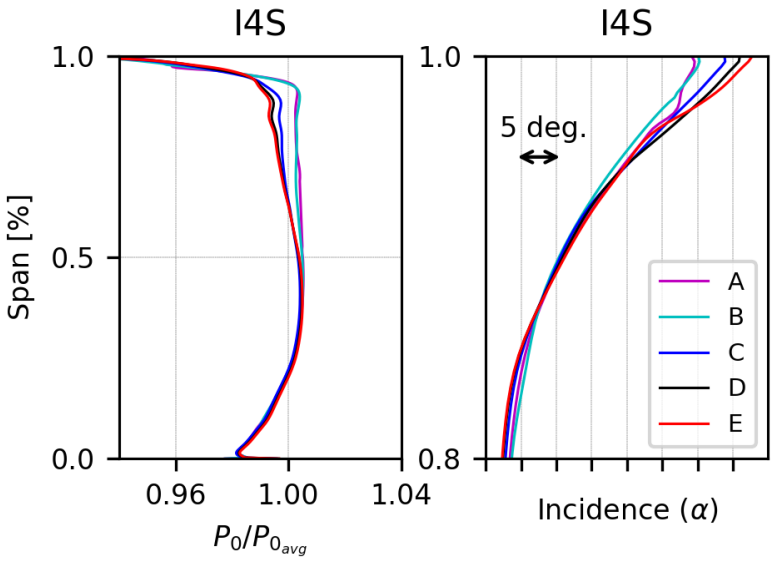


Figure 3.12: Span-wise variation of normalized total pressure (a) and incidence angle (b) at the I4S inlet.

3.5.3 Inaccuracies of the SA formulation

Wall distance limitation

The previous section showed that a grid independent solution is achieved with 19 layers in the tip gap region as long as WF is used. However, the use of WF in this context is questionable as it assumes a zero pressure gradient velocity profile. In order to test this assumption, the casing boundary layer is resolved using grid F (see Table 3.2) which considers a no slip boundary condition. Figure 3.13 shows the results from grid F compared with grid E (finest grid with WF) and the I4R characteristic. The results obtained with the two modelling approaches are very similar. It can be concluded that for the current test case, WF presents a good approximation to the no slip boundary condition even in the presence of strong favourable pressure gradient within the gap between the rotor tip and the casing.

Since the use of WF was excluded as a cause for the differences in performance predictions seen in Figures 3.10-3.13, a new hypothesis was investigated. The SA and MSA models contain a destruction term which is directly dependent on the cell distance to the closest solid surface (d). By reducing d to resolve the boundary layer, the amount of eddy viscosity in the boundary layer is reduced, which promotes flow separation in the casing region leading to high levels of total pressure loss. To examine this hypothesis, Grid G was generated with the same minimum near wall distance (dimensional y_2) as grid B. The level of refinement in the end wall region was kept similar to grid E. Figure 3.9c shows the configuration of grid G. Figure 3.14 shows the results obtained in terms of I4R aerodynamic performance and radial profiles of total pressure. Results obtained using grid G shift the operating point back towards the result obtained with grid B. It can be

concluded that when y_2 value is decreased below a certain threshold, the destruction term is over-predicted.

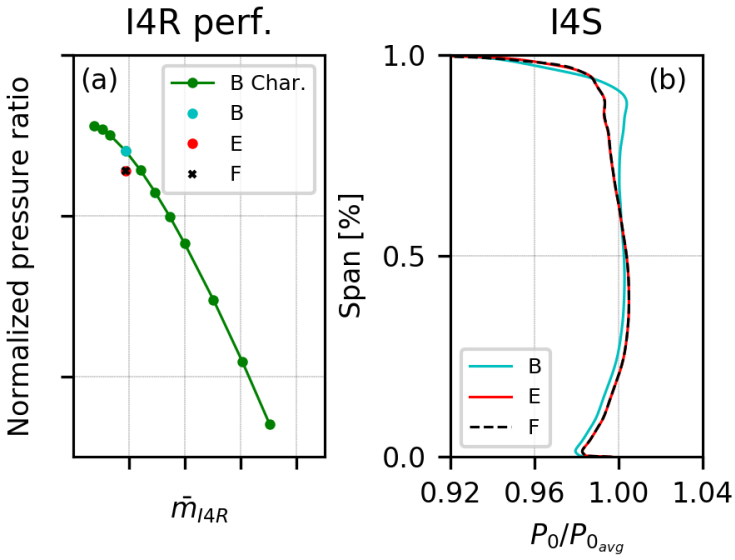


Figure 3.13: I4R performance (a) and I4S total pressure inlet profile (b) using grid E and Grid F.

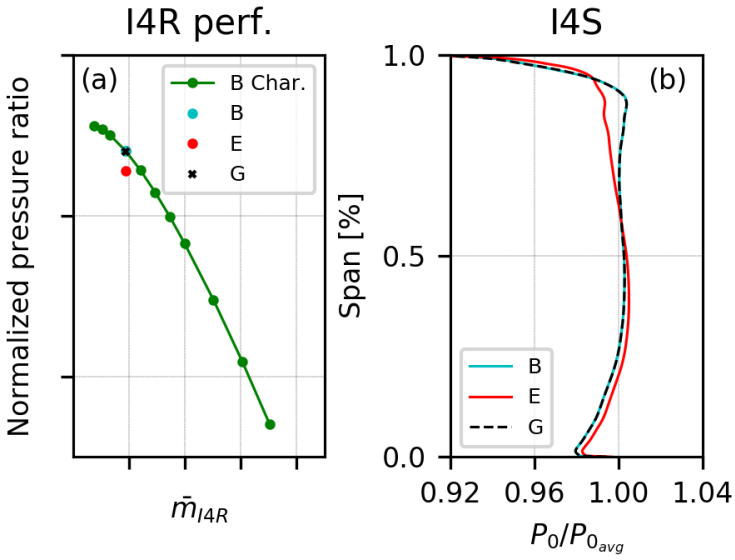


Figure 3.14: I4R performance (a) and I4S total pressure inlet profile (b) using grid E and Grid G.

A common assumption amongst industry and scientific community is that grid refinements for well resolved boundary layers result in an accuracy improvement when using the SA model in high speed compressor flows. It is demonstrated here that refined casing end walls leads to poorer performance predictions. This is particularly important for the current test case which is a high speed rotor where the relative velocity difference between

the casing and blade tip is very large. The effect of the under-prediction of eddy viscosity in the casing region is less relevant for low speed machines and smaller tip gaps as suggested in [69].

Multi-stage effects

This section will test the effect of the destruction term in a multi-stage compressor and present a comparison against measured data. To obtain a multi-stage grid independent solution, the grid D (see Figure 3.9b) configuration was used through the entire rig. The rig performance obtained at 100% aerospeed is presented in Figure 3.15 which compares the measured characteristics with numerical solutions obtained using grids B and D. The block 4 characteristic is measured from I3S inlet to I4S inlet. As before, a loss in stall margin is evident when the casing boundary layer is resolved with a finer grid (grid D) as seen in Figure 3.15b.

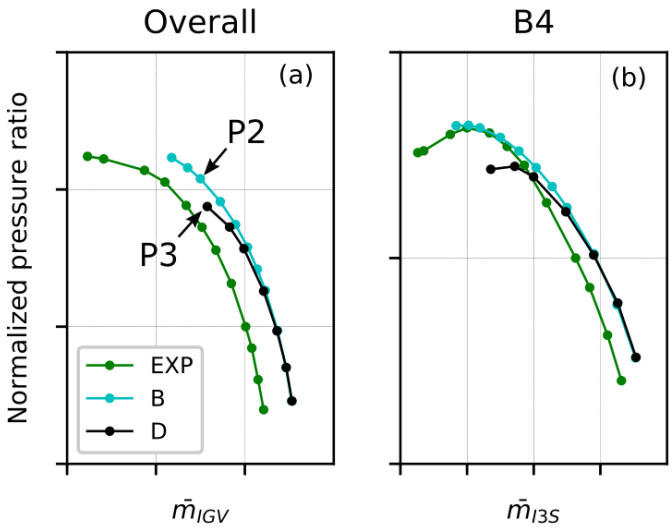


Figure 3.15: Overall (a) and B4 (b) measured and computed characteristics using grids B and D (MSA model)

Figure 3.16 presents the differences in incidence angles between grid D and grid B plotted against span. The flow pattern on the I4S suction surface when using grid D at operation point "P3" (see Figure 3.15) is also shown in this plot. Figure 3.16a shows that for the same nozzle area, grid D registers an increase in the incidence angle above 70% span relative to grid B.

By comparing the results obtained with grid D at condition "P3" illustrated in Figure 3.16b and grid B at condition "P2" illustrated in Figure 3.3b, it is seen that above 80% span grid D shows a larger separation zone relative to grid B. This occurs despite the fact that operating point "P2" has a lower nozzle area than "P3" (see Figure 3.15). Figure 3.16b also shows that the radial flow migration between 20%-40% span is no longer present. The larger separation region above 80% span increases the casing end-wall blockage and

the incidence at lower spans decreases (due to higher mass flow at these spans) as shown in Figure 3.16a.

The aforementioned observations suggest that the effect of grid refinement on the rotors is cumulative across the stages leading to further performance deterioration as the number of stages in the compressor increases.

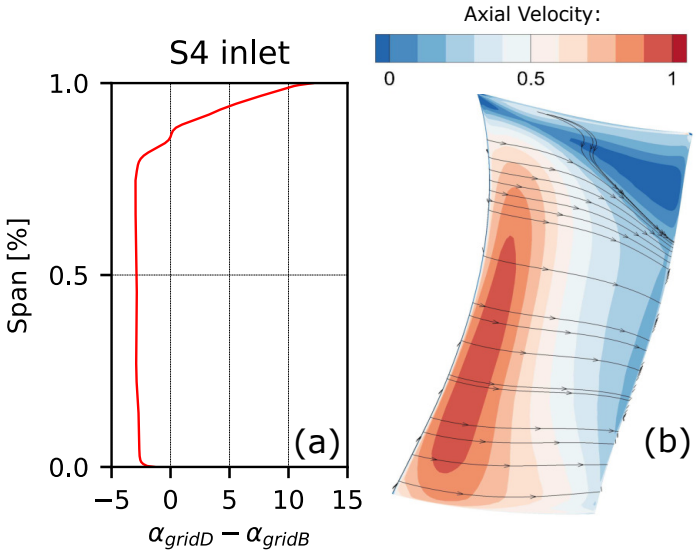


Figure 3.16: Difference in incidence angles between grids D and B upstream of I4S at operating points "P3" and "P2", respectively (a). Grid D normalized axial velocity in the proximity of I4S suction surface at operating point "P3" (b).

In order to isolate the wall distance effect on multi-stage arrangements, two extra computations were performed. Grids B and D were used and the MSA model destruction term was set to zero in the cells which considered the rotor casing as the closest surface. The original formulation of the MSA model was kept in stator blade rows. Figure 3.17 shows the results obtained. The differences between the characteristics for the coarse (Grid B) and the fine grid (Grid D) are minor with this formulation of the MSA. This shows that by deactivating the destruction term locally on the rotors casing, the solution becomes grid independent. It is also possible to obtain a stable steady solution at a lower mass flow operating condition (smaller throat area) relative to what was observed before with the baseline model (Figure 3.2).

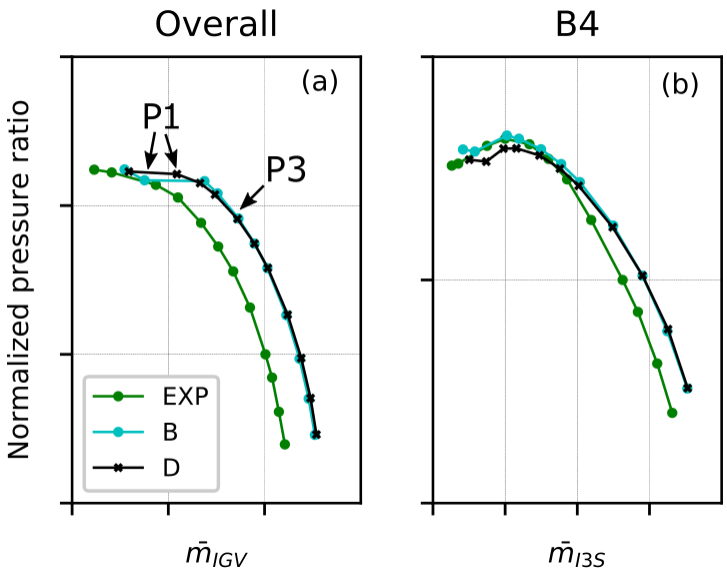


Figure 3.17: Overall (a) and B4 (b) measured and computed characteristics using grids B and D considering the MSA model neglecting the eddy viscosity destruction near the casing surface.

3.5.4 Discussion on casing flow turbulence modelling

From the results presented throughout this chapter, it is clear that the SA formulation is not capable of capturing the entire compressor's characteristic accurately. Furthermore, it is also observed that the stall boundary is closer to the experiment when using a coarser grid or neglecting the SA destruction term in the vicinity of the casing. This section aims to give a qualitative analysis of the tip gap flow physics in high speed compressor flows and relate it to the SA formulation. It also aims to establish a "best practice" when using this model which will be applied in the next chapters of this work.

Destruction term dependence

Figure 3.18a and 3.18c show the normalized eddy viscosity at an axial cut at 50% chord of I4R with grids B and D, respectively. A similar plot is presented in 3.18e where grid D is used and the destruction term is neglected for the cells which consider the casing as the closest surface.

In the end wall region, there is a clear difference between results. When the destruction term is considered, grid D shows lower values of eddy viscosity than grid B (Figures 3.18a and 3.18c). The reduction in eddy viscosity promotes the flow separation in the casing region which leads to the high levels of total pressure loss described in the previous sections. When the destruction term is neglected in the casing vicinity, that low eddy viscosity region vanishes (Figure 3.18e) and the numerical solutions with grids B and D become similar.

Figures 3.18b, 3.18d and 3.18f present the MSA model source term corresponding to the cases outlined before. High positive values of source term indicate that the production term is dominant whilst high negative levels indicate that the destruction term is larger. The tip leakage flow can be described in terms of two shear layers: 1) the free shear between the tip leakage flow and the main flow within the passage; 2) the wall bounded shear layer (WBSL) due to the interaction between the jet and the casing. All of the solutions in Figure 3.18 show that the production term is more pronounced in the region where the tip leakage jet interacts with the main flow in the passage. Furthermore, as the flow approaches the gap, a turbulence decay is observed. This is a result of the tip clearance flow being predominantly inviscid, driven by the pressure gradient between the pressure and suction surfaces of the blade as previously suggested in [6, 70].

When analysing the results obtained with the original MSA model (Figure 3.18b and 3.18d), the destruction term is the dominant term in the region where the tip leakage jet interacts with the casing shear layer. The destruction term dominance is more pronounced for grid D. Therefore, the levels of eddy viscosity drop when grid D is used. When the destruction term is not considered in the proximity of the casing, the eddy viscosity destruction does not have an impact on the WBSL modelling (Figure 3.18f). These observations indicate that the modelling of the shear layer between the tip leakage jet and the casing in the SA formulation has a significant destruction term dependence.

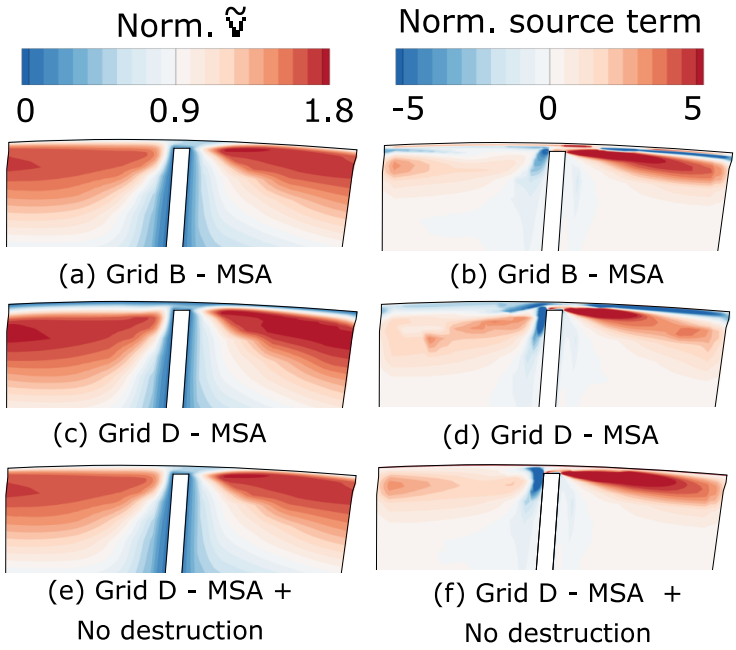


Figure 3.18: Comparison between normalized eddy viscosity and source term at operating condition "P3" for grids B (MSA model) and grid D (MSA model with and without destruction term) - I4R axial cut near tip region at 50% chord.

Flow physics

To understand why the differences between grids B and D in Figure 3.15 become larger as the compressor is pushed towards the stability limit, the flow physics of the tip leakage jet are discussed in this section. In compressor flows, when viewed from the rotor's frame of reference, the compressor casing is rotating at constant speed in direction of the tip leakage jet. Figure 3.19a presents a 2D sketch which illustrates the effect of the casing rotation on the tip leakage jet and its interaction with the casing shear layer for near stall (red) and design (blue) conditions. Figure 3.19b presents a 2D illustration of an axial cut in a blade passage which shows the jet velocity profiles near the casing wall. The strength of the shear layer between the tip leakage jet and the casing is highly dependent on the velocity difference between the tip leakage jet and the casing velocity [69]. As the compressor loading increases, the pressure difference between pressure and suction surfaces of the blade increases. Consequently, the jet velocity increases, the tip leakage flow is pushed upstream and the shear layer becomes stronger.

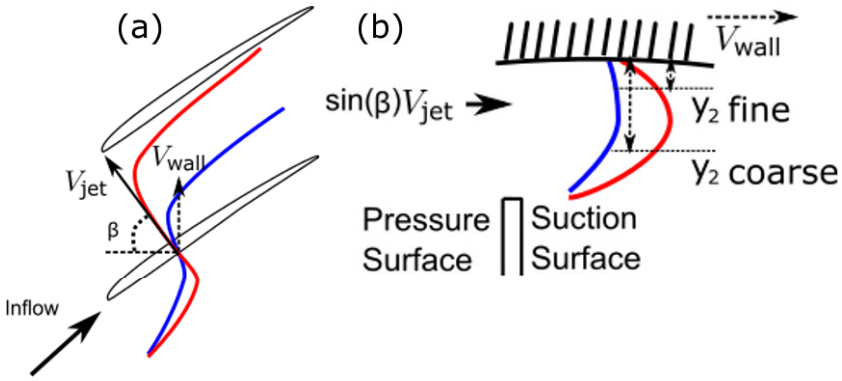


Figure 3.19: Effect of tip leakage flow trajectory (a) and velocity profile interaction with the WBSL (b). Red and blue represent near stall and design condition, respectively.

Figure 3.20 shows a decomposition of the different terms of the eddy viscosity equation for a turbulent boundary layer in zero pressure gradient. The δ_* is the boundary layer displacement thickness. It is evident that when finer grids are used (small d), the eddy viscosity transport in the SA model formulation is dominated by destruction. Additionally, grid refinements towards the casing wall will approximate the velocity of the cells near the casing to the rotational speed of the surface. Because of a reduction in velocity difference between the jet and the wall velocity, the turbulence production in this region is inevitably reduced. These effects point towards a reduction in eddy viscosity in the casing boundary layer and a promotion of separation when finer grids are used. Due to flow separation, the δ_* of the boundary layer in the casing region increase further. As a consequence, instead of generating turbulence due to the interaction between the jet and the casing, the model decreases the eddy viscosity, which appears to be over-dissipative for this type of flows. For high values of y_2^+, the destruction term does not play a significant role which results

in higher levels of turbulence near the casing and the flow separation is delayed.

The results presented here indicate that eddy viscosity levels near the casing end wall should be higher than what is predicted by the model. It has also been demonstrated that neglecting the destruction term near the casing when using the MSA model improves the compressor's performance predictions. This change is introduced in the baseline model for all the following calculations in this work. This modification assumes that the turbulent dissipation on the casing wall is negligible when compared with the eddy viscosity production due to the tip leakage flow interaction with the WBSL.

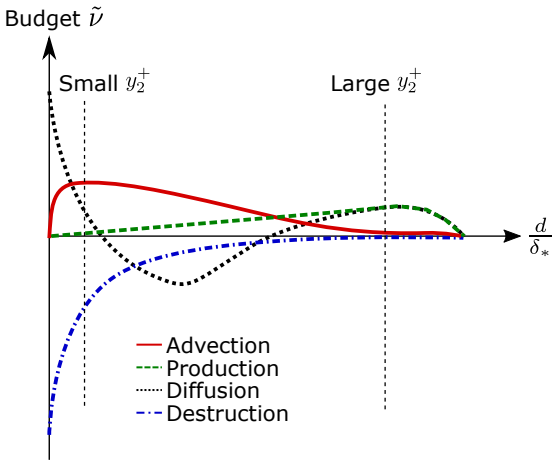


Figure 3.20: Eddy viscosity budget for a flat plate boundary layer.

3.6 Tip clearance size effects

The previous sections focused on the CFD uncertainty for prediction of compressors' performance however, experimental measurement of tip clearance gaps also have an associated uncertainty which can influence the results. This section aims to show the impact of tip clearance size on the CFD results when considering the MSA model without the destruction term near the rotor's casing.

The compressor rig studied offers two configurations of tip clearance sizes which were measured by the industrial sponsor: tight clearance and open clearance. A third configuration is also tested where the size of the tight clearance configuration is halved. Note that the CFD model presented in the previous sections had the tight clearance configuration. Table 3.3 shows a summary of the tip clearances configurations used.

Figure 3.21 shows the measured and CFD results for the overall, front and back stages characteristics of the compressor with different tip clearance configurations. The experimental results (curves "EXP B" and "EXP O") show that opening the tip clearances reduces the stability margin and that the stability limit is reached first in the back stages. The CFD results show a similar behaviour however, it is observed that, as the tip clearances are increased, the CFD prediction capability is worse. Furthermore, by halving the

tip clearance size, the CFD characteristics are closer to the measured data which suggest that CFD tends to over-predict the losses due to the tip leakage flow. These results also indicate that an accurate measurement of tip clearance sizes during experimental campaigns is crucial in order to improve the modelling capability of the available RANS models.

Table 3.3: Tip clearance sizes normalized by blade span [%].

Configuration	**I1R**	**I2R**	**I3R**	**I4R**
B (Tight)	0.71	1.01	1.14	1.54
O (Open)	1.23	1.65	2.08	1.93
H (Half tight)	0.35	0.55	0.57	0.77

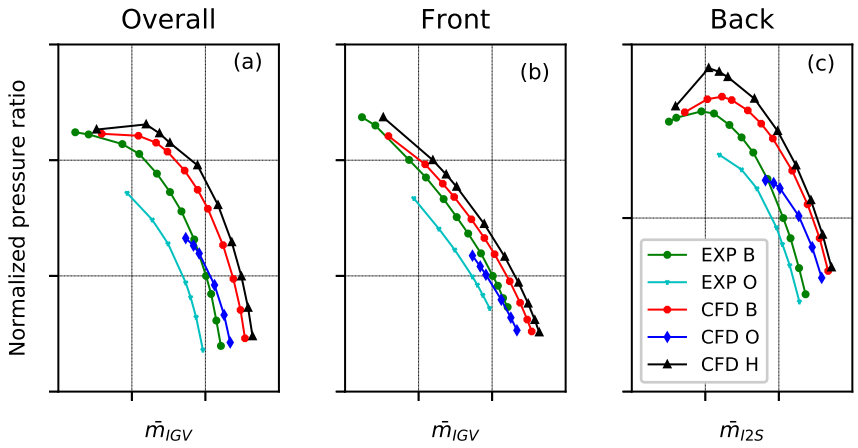


Figure 3.21: Effect of tip clearance size on the CFD model performance.

3.7 Turbulence modelling effect in part speed calculations

To finalize this chapter, the baseline model is compared with the new model which will be used in the following chapters. This model uses a mesh independent solution and the MSA turbulence model without destruction term on cells where the closest surface is the casing. Figure 3.22 shows the measured and CFD compressors' steady-state characteristics at different aerodynamic speeds. The improved model ("CFD-New") shows an improvement in the prediction of the compressor's stability boundary across the entire operating range however, it still under-predicts the compressor stall margin. Recent results published by He et al. [71] imply that recalibration of the SA model coefficients does not lead to prediction improvements in compressor flows and rather a modification in the SA formulation is needed.

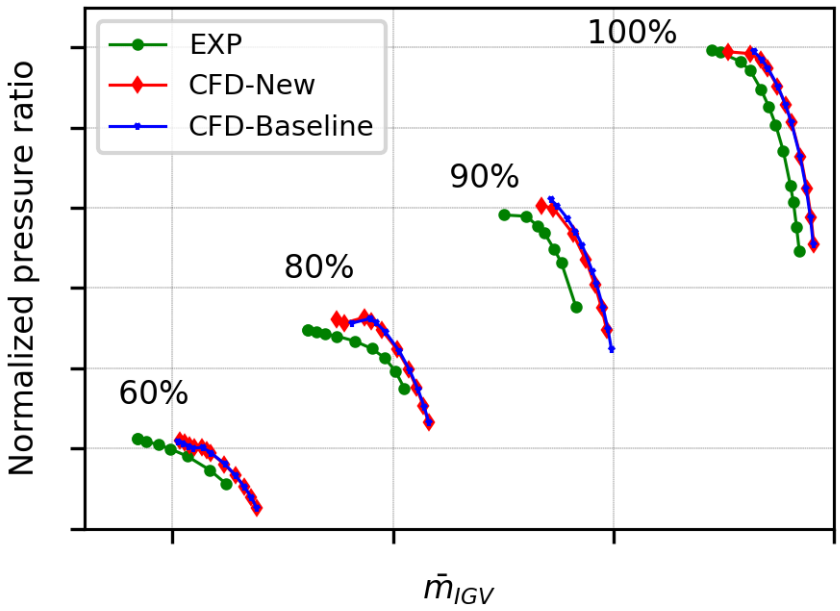


Figure 3.22: Comparison between the baseline and improved model at different aerodynamic speeds.

3.8 Concluding remarks

In this chapter, a comparison between the prediction capability of two turbulence models in a high speed multi-stage compressor was shown. Numerical and physical modelling uncertainties of the SA formulation were investigated. It was found that the MSA model gives a better prediction of the compressor stability line relative to the original SA model. The solutions obtained with the MSA model have higher levels of turbulence in localized separation regions and, as a consequence, numerical solutions are obtained closer to the stability limit.

Tip leakage flow modelling using the SA formulation results in an under-prediction of eddy viscosity in the near casing region. Ultimately, these results in premature flow separation and early compressor stall. This issue is more relevant for multi-stage arrangements. In single-stage compressors, the premature flow separation does not affect the flow behaviour of the blade rows located downstream and therefore, it might not compromise the stall margin prediction to the same extent. In order to improve the prediction of the stability boundary, an alternative formulation is proposed where the destruction term in the SA formulation is neglected in cells which consider the casing as the closest surface.

The effect of the tip gap size on the compressor performance was demonstrated. It was shown that both experiments and CFD are very sensitive to small changes in tip clearance sizes. This result shows the importance of accurate measurement of tip clearance during experimental campaigns which should be shared with CFD engineers for improvement of RANS models. Furthermore, it was also shown that CFD predictions are worse for larger

tip clearances.

Finally, the "best" available CFD model was defined in order to be used in the following chapters for near and post stall modelling applications. A comparison is made for different aerodynamic speeds of the compressor to demonstrate the limitations of this RANS model in capturing the stability boundary. The CFD results showed a higher correct mass flow condition for the same levels of pressure ratio and an under-prediction of the stall margin when compared to measured data. Figure 3.23 illustrates a comparison of an expected compressor map predictions against experiments based on the current CFD capability.

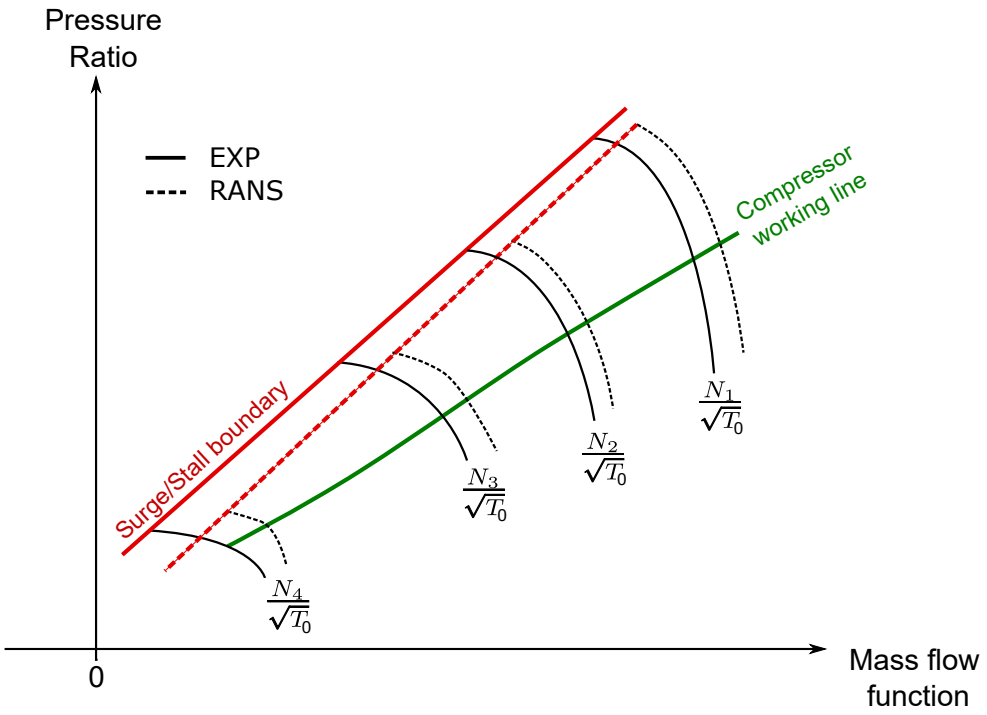


Figure 3.23: Expected CFD predictions relative to experimental results.

4 Unsteady effects on a multi-stage compressor for performance prediction

4.1 Problem description and overview

The flow field in multi-stage compressors is characterized by circumferential non-uniformities due to wakes convected from upstream blade-rows and the potential field arising from blade-rows located downstream. The relative motion between adjacent blade-rows causes interactions, which inevitably generate an unsteady flow field. This unsteadiness is defined by high frequency content such as blade passing frequencies (BPF) harmonics and respective row-to-row interactions. Additionally, the levels of flow unsteadiness also depend on the blade aerodynamic loading which influence the boundary layer characteristics. As the compressor progresses towards stall, the blade wakes grow and flow separations may occur which also generates flow unsteadiness. This may lead towards the formation of aerodynamic disturbances with lower frequency content, which potentially break the flow axisymmetry.

Flow unsteadiness which originates from blade-row interactions is characterized by well defined frequencies (integral engine orders[1]). This unsteadiness can be modelled using single or multi-passage domains with phase-lagged boundary conditions [72, 73]. In contrast, unsteady aerodynamic disturbances, such as vortex shedding or rotating stall occur at non-integral frequencies. If these aerodynamic disturbances travel circumferentially, as in the case of rotating stall, full annulus sliding plane models must be used. The complexity and associated computational cost increases significantly when adopting this approach. As a result, a question arises about the real benefit of modelling non-axisymmetric flow unsteadiness in axial compressors. Previous research [60, 61, 74, 75] has been conducted to assess the benefits of using an unsteady full annulus sliding plane to predict compressor performance. However, it is still not clear on which conditions such approach should be used.

For all of the studies mentioned above, the investigations were performed on a single compressor speed. For modern high speed compressors, the levels of unsteadiness vary depending on operating speed due to stage matching effects. For example, when a high speed compressor operates at low speed, it is common for the front stages to become mismatched and develop non-axisymmetric flow features. Hence, a full annulus sliding plane may be required to model the flow accurately. For a low speed compressor, where

[1] Engine order refers to frequency normalized by shaft speed.

the stage matching is not as important, this may not be the case. Consequently, it is necessary to test and evaluate the modelling requirements to study high speed multi-stage compressors at different speeds and relate it to different levels of flow unsteadiness.

The objective of this chapter is to gain further confidence in the URANS model and study the relevance of unsteady effects on the aerodynamic performance prediction in modern multi-stage compressors at two different conditions: low and high speed operation. The results obtained using a steady single passage and unsteady full annulus models are presented and compared with experimental data.

The numerical model of the four-stage IPC (introduced in chapter 3 for the steady analysis) is expanded to a full annulus domain. Sliding planes are introduced at the blade-row interfaces and unsteady calculations are performed. The steady characteristics for each speed studied are identified in Figure 3.22 as 100 % and 60%, respectively. The VSVs settings are adjusted to their nominal condition depending on the aerodynamic speed. The tip clearance sizes are also increased to the levels of the experiment as the rotational speed decreases. The time resolution considered 2150 time steps per revolution which is in agreement with previous aerodynamic studies on multi-stage compressor performance predictions using AU3D [18, 48, 76]. This results in approximately 1 day of computation time per revolution using 192 Intel Xeon 2.2GHz CPUs.

As previously explained in chapter 1, the stability limit defines the point where a further mass flow function decrease causes a drop in the system overall (not stage) pressure ratio. Stable operation refers to operating conditions with higher mass flow function than this point.

4.2 Low speed

4.2.1 Aerodynamic performance

The low speed condition is the first studied in this chapter. Figure 4.1 shows the predicted performance of the compressor obtained using the steady ("Steady") and unsteady ("Unst. A" and "Unst. B") models in terms of normalized pressure ratio as a function of inlet corrected mass flow ($\dot{m}\sqrt{T_0}/P_0$), referenced as "$\bar{m}$". The corresponding experimental measured characteristics ("EXP") are also shown. The distinction between "Unst. A" and "Unst. B" aims to differentiate two compressor flow behaviours which are studied later. Similarly as before, the nomenclature used in this chapter for addressing each station considers 3 characters: "INT". The "I", "N" and "T" stand for IPC, station number and rotational/stationary station type, respectively. For example, the compressor rig rotor 2 and stator 2 are addressed as I2R and I2S, respectively. The inlet guide vane is addressed as "IGV". Figure 4.1 shows the overall, front and back stages performance calculated from IGV inlet to I4S outlet, IGV inlet to I2S inlet and I2S inlet to I4S inlet, respectively.

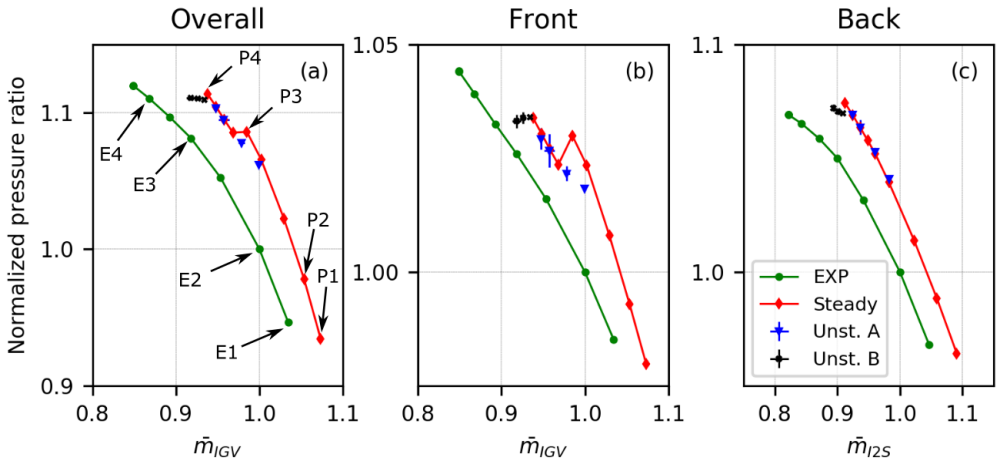


Figure 4.1: Normalized compressor performance. (a) Overall. (b) Front: IGV inlet to I2S inlet. (c) Back: I2S inlet to I4S inlet.

The overall trend of the predicted characteristics is in good agreement with the experimental results for both the steady and unsteady models. An over-prediction in mass flow is observed for all stations. This phenomena has been justified by the absence of secondary geometry features in the model as explained in the previous chapter.

The results show that a discontinuity is present in the overall steady-state characteristic in Figure 4.1a around $\bar{m} = 0.98$. In contrast, the predicted characteristic using the unsteady model is continuous. This can also be observed in Figure 4.1b which suggests that flow unsteadiness and non-axisymmetric flow features are present in the front stages of the compressor. Later in this chapter, the compressor flow field is studied to understand this phenomena.

Figure 4.1a shows that the unsteady full annulus model is capable of sustaining a stable operating condition at a lower mass flow relative to the steady model. For the unsteady model, the compressor back stages operation "rolls-over" towards the stall line in a similar fashion to the experiment as seen in Figure 4.1c. The front stages are expected to become more loaded as the mass flow in the rear stages is reduced. However, as seen in Figure 4.1a for "Unst. B" points, the front stages remain at an approximately constant pressure ratio as the flow is decreased. This indicates a total pressure loss over-prediction.

To gain confidence in the model's ability to predict the compressor pre stall operation at this speed, a comparison between the steady-state CFD solution and measured radial profiles at the inlets of I1S, I2S, I3S and I4S is presented in Figure 4.2. The operating points shown on this figure are highlighted in Figure 4.1a. The results show a very good agreement with the experiments across the whole operating range of the compressor at the inlets of I1S, I3S and I4S. The trend is for the total pressure to rise in the upper spans and decrease in the lower spans as the compressor operation moves closer to the stall boundary.

Figure 4.2 also shows that the radial profiles at I2S inlet obtained with CFD are similar to the experimental results for points "P1", "P2" and "P3". When the mass flow is

reduced further to condition "P4", the CFD radial profile shows a "dip" in total pressure around 50% span. This is not seen in the experimental results which indicates that the steady-state model over-estimates the levels of total pressure loss in this region.

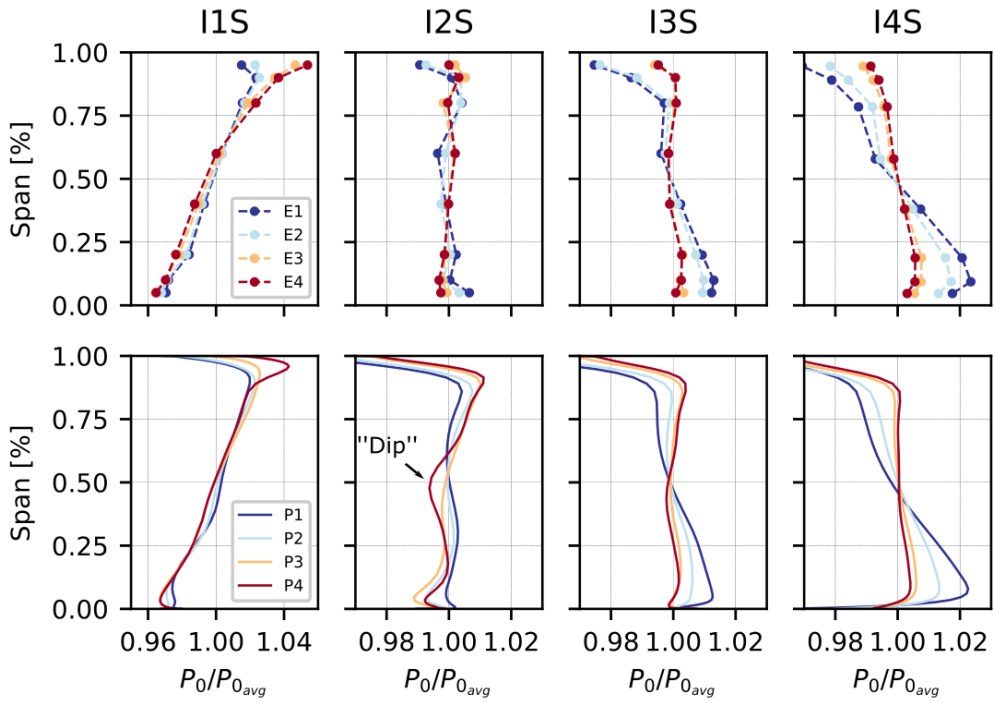


Figure 4.2: Comparison of radial profiles between experiment (top row) and steady-state model (bottom row).

Further insight into the flow field can be gained by analysing Figures 4.3a and 4.3c, which show the mid-passage entropy obtained with the steady-state model for points "P3" and "P4" (see Figure 4.1). Figures 4.3b and 4.3d show the corresponding contours of axial Mach number in the proximity of I1S and I2R blade surfaces. Figure 4.3 shows that the flow separates heavily at mid-span of I1S. The "blockage" on the mid-span region also causes I2R to stall. These flow separations may develop non-axisymmetric flow features and thus, they require a full annulus unsteady model. The difference between the steady and unsteady operating points at around $\bar{m} = 0.98$ (which corresponds to the discontinuous characteristic with the steady model) in Figure 4.1a is proved by this analysis.

Despite the discrepancies between CFD and experiments found in the steady model at the inlet of I2S, it is important to note that the radial profiles of I1S, I3S and I4S are modelled accurately. This indicates that the effect of the stalled region mentioned before is limited axially between the inlets of stations I1S and I3S. The following sections investigate how these flow features develop when considering an unsteady full annulus model.

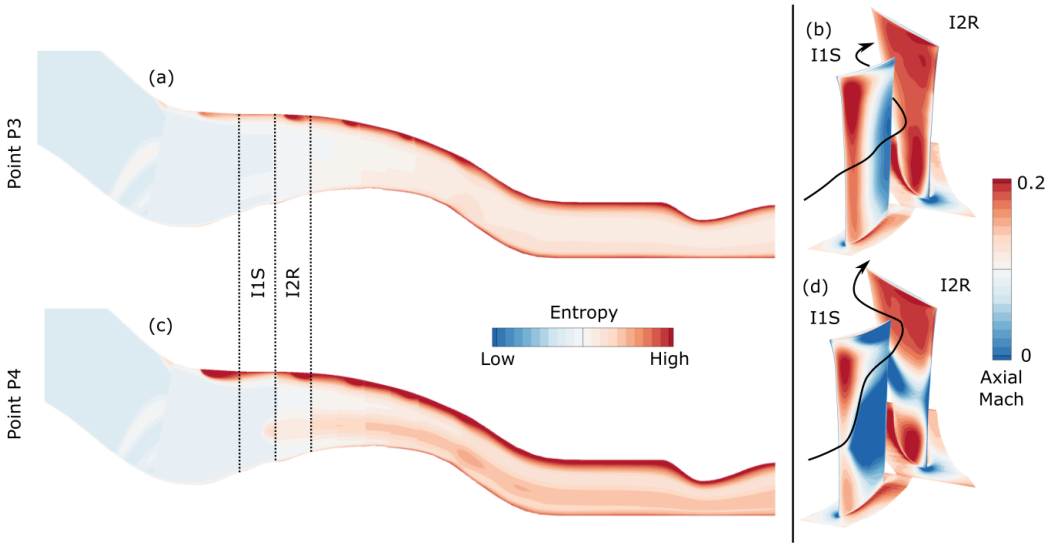


Figure 4.3: Comparison of the flow field at points "P3" and "P4": Mid passage entropy ((a) and (b)) and I1S and I2R blade surface axial Mach number ((c) and (d)).

4.2.2 Unsteady effects on the pre stall condition

Further insight about the unsteady effects in the front stage of this machine can be gained by analysing Figure 4.4 which shows the performance split between the first and second stages of the machine. Both the experimental and simulation (steady and unsteady) results are presented in this figure.

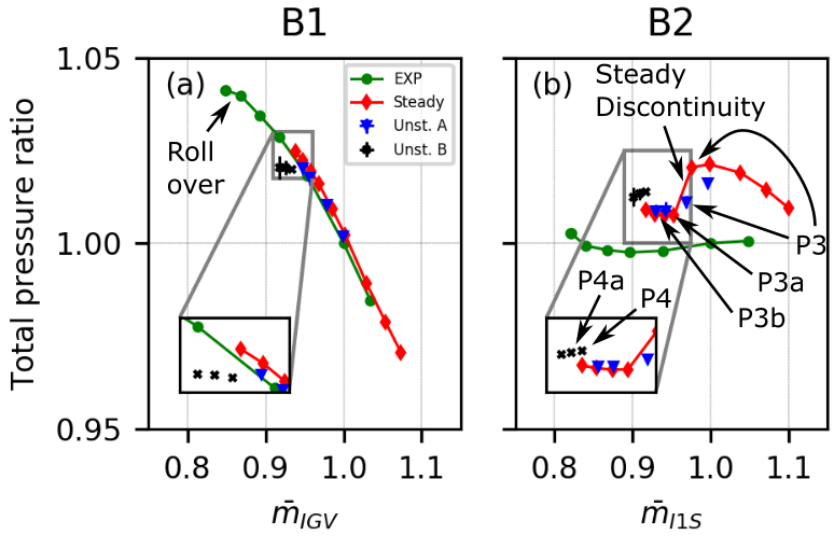


Figure 4.4: Normalized compressor front stages performance. (a) B1: IGV inlet to I1S inlet. (b) B2: I1S inlet to I2S inlet.

The measured data shows that the first stage of the compressor ("B1") follows a regular negative slope characteristic. The second stage ("B2") operates on a positive slope characteristic between $\bar{m} = 1.0$ and $\bar{m} = 0.9$. Despite this, the compressor's stability is maintained. Further mass flow reduction causes "B2" to recover the negative slope characteristic whilst "B1" characteristic starts to "roll-over" (see Figure 4.4a). This result suggests that "B1" constrains the stability margin of the compressor.

The trends reported above are captured in both the steady and unsteady simulations however, the pressure ratio is under-predicted for "B1" and over-predicted for "B2". For the steady results, it is seen that the discontinuity seen previously in Figure 4.1a is also present in Figure 4.4b. The unsteady model is able to capture a more gradual positive slope characteristic for "B2". This is evident by comparing point "P3" in Figure 4.4b.

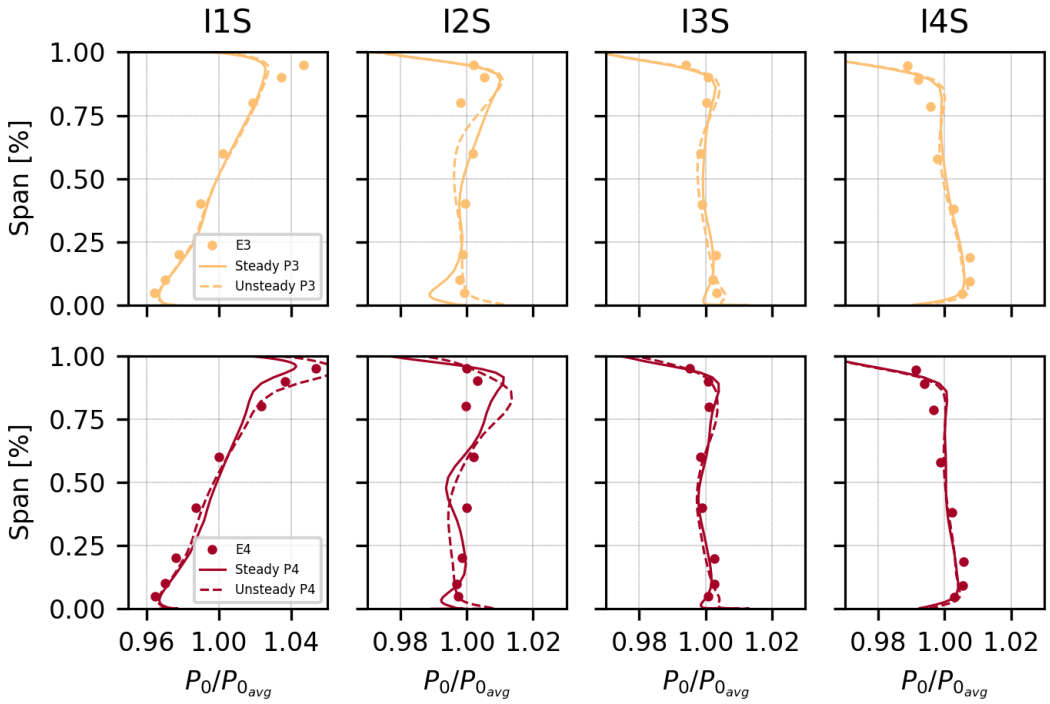


Figure 4.5: Comparison of radial profiles between experiments and CFD models (steady and unsteady). Top row: Point E3 and P3. Bottom row: Point E4 and P4.

Figure 4.5 shows a comparison between the measured radial profiles at conditions "E3" and "E4" and CFD results (both steady and unsteady) at conditions "P3" and "P4" (see Figure 4.1a). The back stages of the compressor (I3S and I4S) show similar radial profiles for both the steady single passage and unsteady full annulus models for these conditions which are also in agreement with the experimental data. For condition "P3", it is visible that the disparities between the steady and unsteady models are limited to the radial profile at I2S inlet. When the compressor is throttled to point "P4", the differences expand axially upstream and a higher total pressure is found at the tip region of I1S for the unsteady model. These observations indicate that the levels of unsteadiness and flow field non-axisymmetry increase in the front stages of the machine as the compressor is

throttled towards the stall line.

The unsteady model matches the experiments better than the steady model. This can be seen by the profiles at inlet of "I1S" above 75% at condition "P4" and below 50% span at inlet of I2S in both conditions "P3" and "P4". To further understand the driving mechanisms of this unsteady phenomena, the unsteady points plotted in Figure 4.4 are studied. Two distinct unsteady flow regimes are found: 1) "Unst. A" characterized by a positive slope characteristic in "B2"; 2) "Unst. B" characterized by a "roll-over" in "B1". These are addressed below.

Stator 1 and rotor 2 mid-span stall - "Unst. A"

The flow non-axisymmetric behaviour obtained with the unsteady model only developed after throttling the compressor to condition "P3" (see Figure 4.4b). Figures 4.6a-4.6d show the contours of axial Mach number at I2R inlet. Figures 4.6e and 4.6f show the time history of axial Mach number and modal content of dynamic pressure at 60% span of the I2R inlet (I1S exit), respectively. These plots were constructed based on interpolation of numerical probes around the annulus. In this figure, the dynamic pressure modal content is normalized by the average value at each time step[2], i.e., mode 0 of the dynamic pressure spectrum (m=0).

The results show that the flow is axisymmetric until approximately revolution 1.2 as seen by the sole presence of the modes which characterize the I2R and I1S blade counts in Figure 4.6f. As time progresses, the flow separates at I1S mid-span region and a rotating stall pattern develops from revolution 2.5. This pattern is characterized by 16-18 stall cells which travel circumferentially at approximately 11% shaft speed as seen by the increase in amplitude of mode 16-18 (number of cells) and 40-42 (I1S blade count minus the number of cells).

To understand the physics behind these rotating perturbations, Figure 4.7 displays the circumferential propagation of a rotating cell at 60% span of I1S and I2R. The flow angle profiles at the inlet of the stator vanes for the different equidistant time intervals are presented in Figure 4.7a. Note that the position from where the flow angle profiles are extracted is displayed in Figures 4.7b to 4.7f (lines A-C).

Consider the passages 1, 2 and 3 identified in 4.7a. Figure 4.7b shows that passage 3 is partially "blocked" due to boundary layer separation of vane 4. As described by Emmons et. al. [15], the low momentum region close to the vane 4 suction surface redirects the flow into the adjacent passages and vane 3 pressure surface. This results in an increase of incidence at the leading edge (LE) of vane 3, as seen on profile "A" in Figure 4.7a. This causes the flow to separate at the time instant $\tau + \Delta t$. As the passage 2 is blocked, the separation region within passage 3 shrinks and vane 4 recovers its unstalled condition as seen in Figures 4.7d-4.7f. The process described here is repeated as each cell propagates

[2]This gives the amplitude of each circumferential mode as a percentage of the mean value of dynamic pressure in each time step.

around the annulus at 11% of the shaft speed. Each stall cell is limited to one stator passage. The phenomena is non-synchronous which is a characteristic of rotating stall.

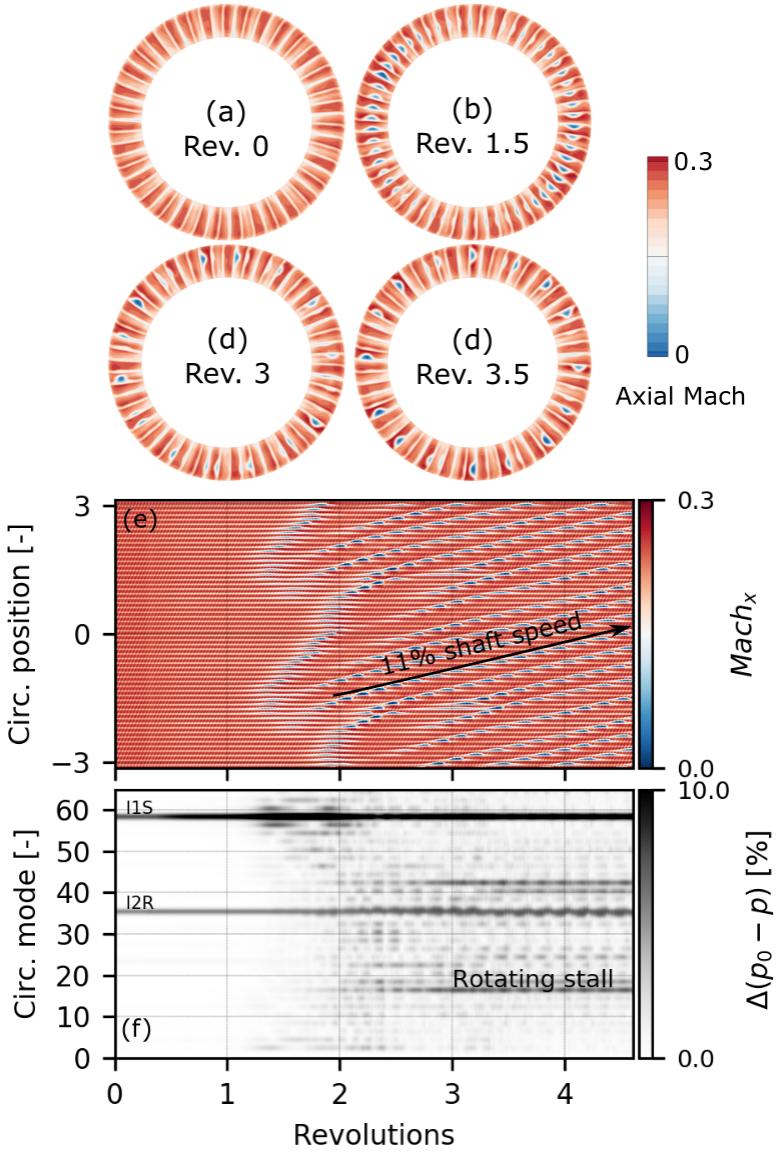


Figure 4.6: Contours of axial Mach number at I2R inlet (a-d). Time history of axial Mach number (e) and dynamic pressure modal content (f) at 60% span of I2R inlet.

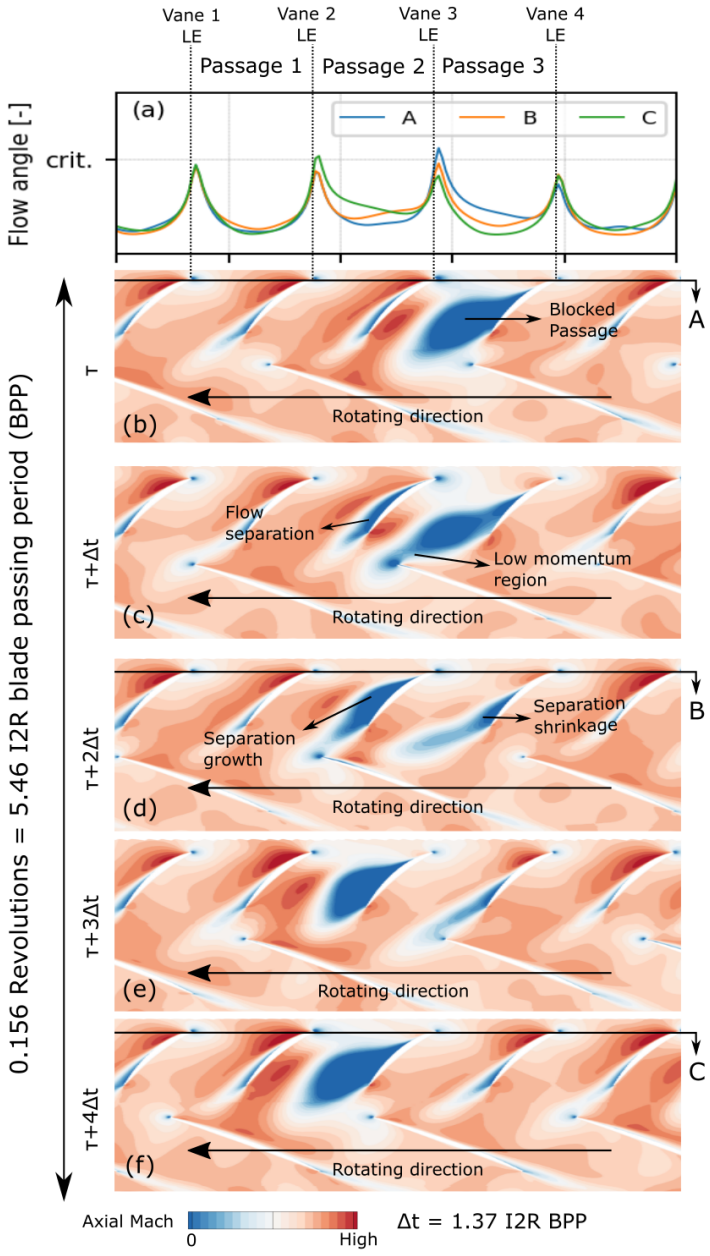


Figure 4.7: Flow angle profiles at I1S inlet (a). Stall cell propagation mechanism for operating condition "P3" in I1S and I2R at 60% span (b-f).

Figure 4.4b shows that as the compressor is throttled, "B2" mass flow is reduced and follows a positive slope characteristic. This behaviour can be understood by analysing Figure 4.8, which shows the circumferential modal content of dynamic pressure for I2R and I2S inlets at 60% span for the points identified as "P3", "P3a" and "P3b" in Figure 4.4b.

As previously explained, when the compressor is throttled towards point "P3", modes 16 and 18 emerge (see Figure 4.8a) as a result of flow separation at I1S suction surface. When the compressor operation moves towards the stability boundary, a broadband signal spreads across the entire spectrum. Moreover, the perturbations introduced by modes 16 and 18 remain dominant and mode 18 rises above the I2R blade signal as displayed in Figures 4.8c and 4.8e. Mode 40 amplitude also increases by this manoeuvre since it is one of the interaction modes between the dominant stall mode number (m=18) and the I1S blade count (m=58). The amplitude growth of the stall modes suggests higher levels of unsteadiness and flow separation within "B2".

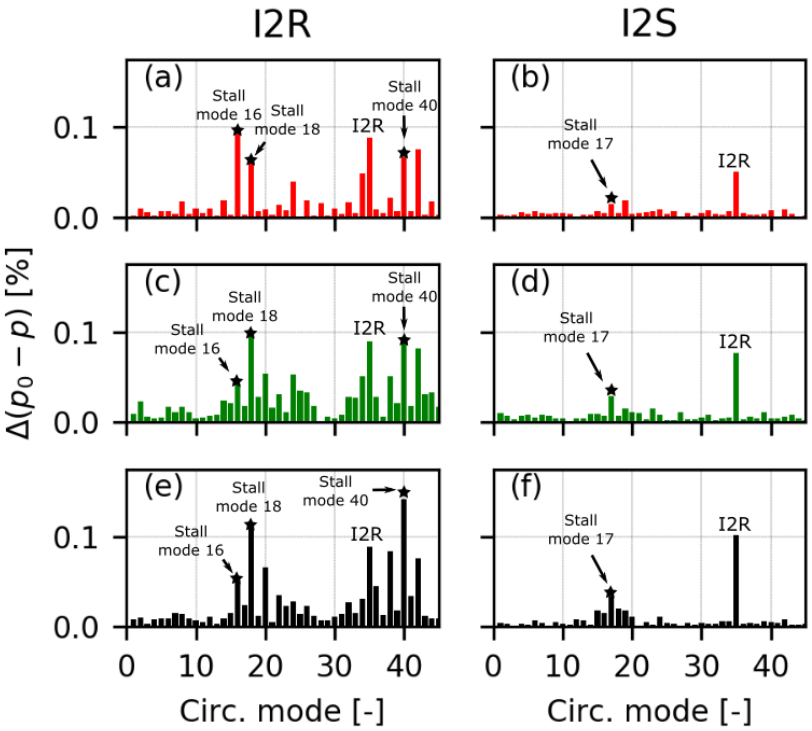


Figure 4.8: Circumferential modal distribution of dynamic pressure at 60% span at I2R inlet and I2S inlet for the "Unst. A" operating conditions as the compressor exit mass flow is reduced (see Figure 4.4b): Point P3 ((a) and (b)) , Point P3a ((c) and (d)) and Point P3b ((e) and (f)).

Although the "B2" pressure ratio decreases as the compressor is throttled during flow regime "Unst. A" (see Figure 4.4b), the compressor overall pressure ratio increases (see Figure 4.1a). To gain further insight about this phenomena, the I2R behaviour is analysed in Figures 4.8b, 4.8d and 4.8f . The modal content at inlet of I2S (I2R exit) shows that mode 35 (I2R blade count) and mode 17 (interaction between I2R blade count and 18 stall

cells present at the inlet of I2R) amplitudes increased as the compressor is throttled. This suggests that the stall cells previously embedded within the I1S blade-row are changing the I2R operation. Figure 4.9 shows the flow field development at I2S inlet (I2R exit) for the operating points identified in Figure 4.4b as "Unst. A" from the highest to lowest mass flows. The results show that as the compressor is throttled, the mid-span rotor wake grows significantly.

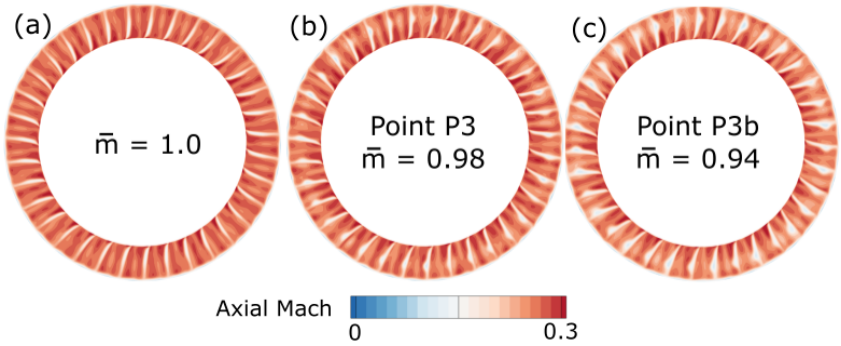


Figure 4.9: Contours of axial Mach number at I2S inlet for the "Unst. A" operating conditions (see Figure 4.4b): $\bar{m} = 1.0$ (a), Point P3 (b) and Point P3b (c).

Figure 4.10a and 4.10b show the radial profiles of total pressure ratio across I1S and I2R for the unsteady points "Unst. A". It is seen that as the compressor is throttled, the total pressure losses increase through I1S. In contrast, the total pressure ratio across I2R increases. This is caused by a rise in incidence upstream of I2R due to I1S stall as seen in Figure 4.10c. I2R does not reach the stability limit as the operating condition changes and thus, it is able to partially compensate for I1S losses. This effect combined with the pressure ratio increase on the other stages as the compressor is throttled leads to an increase in overall pressure ratio.

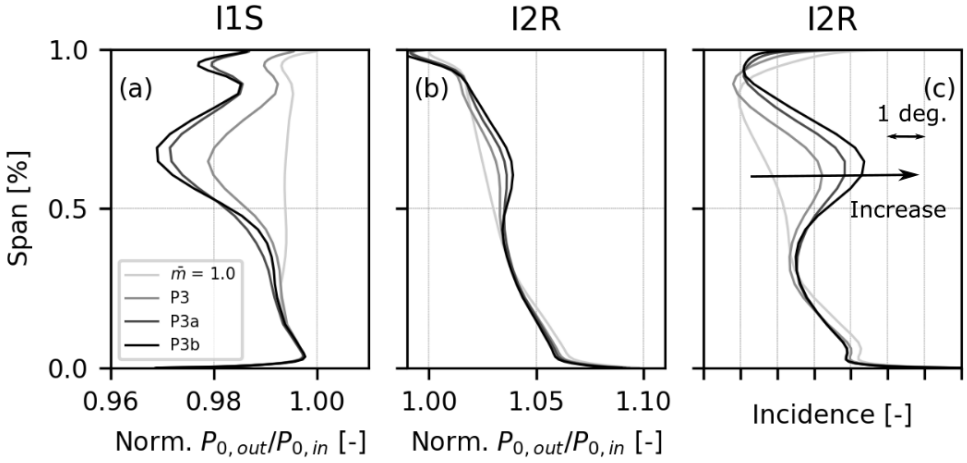


Figure 4.10: Normalized total pressure ratio across I1S (a) and I2R (b) and incidence at I2R inlet (c) for the "Unst. A" operating conditions (see points in Figure 4.4b).

Stator 1 tip stall - "Unst. B"

Figure 4.4b shows that when the compressor is throttled from point "P3b" in regime "Unst. A" to point "P4" in regime "Unst. B", the total pressure ratio across "B2" characteristic recovers a negative slope operation. Figures 4.11 and 4.12 display the time history of axial Mach number and dynamic pressure modal content (as percentage of m=0) at 60% and 95% spans, respectively, at the inlet of I2R during this throttling manoeuvre.

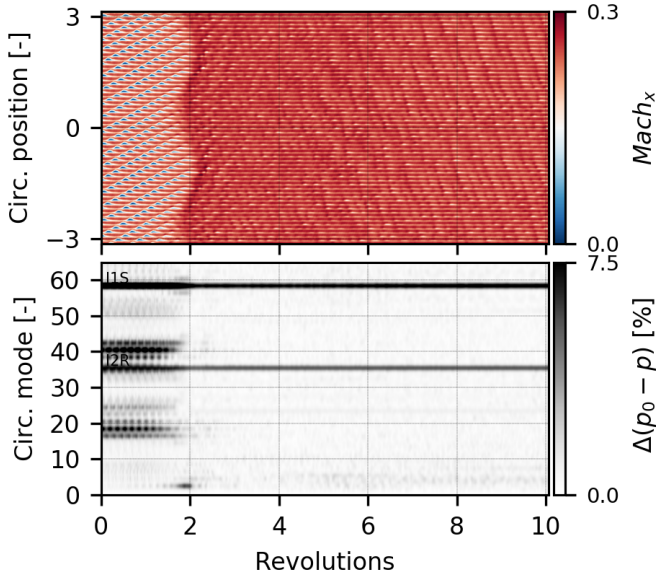


Figure 4.11: Time history of axial Mach number (a) and dynamic pressure modal content (b) at 60% span of I2R inlet when throttling to point "P4" (see Figure 4.4b).

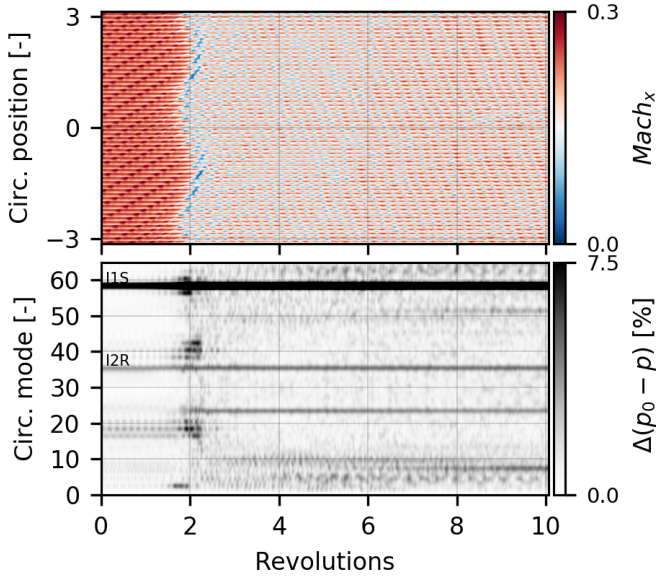


Figure 4.12: Time history of axial Mach number (a) and dynamic pressure modal content (b) at 95% span of I2R inlet when throttling to point "P4" (see Figure 4.4b).

Figure 4.11 shows that the rotating stall pattern located at 60% span of I1S vanishes as the compressor mass flow reduces. The modal content in this Figure clearly indicates that, after revolution 2, the dominant modes are m=35 and m=58 which are the blade counts of I2R and I1S, respectively. Simultaneously, Figure 4.12 shows that I1S stalls after revolution 2 at 95% span. This behaviour indicates that the stalled region within I1S has moved radially outwards to the casing region.

The rotating stall pattern is different from the 16-18 cells seen before. At this condition, a broadband type signal spreads over the low order modes (below m=10) as seen after revolution 2 in Figure 4.12b. Between revolution 8 and 10, this broadband signal develops into a better defined pattern being mode 7 dominant. Despite the presence of these low order modes, the level of unsteadiness introduced by the stalled region is lower in comparison to what was seen before. As a result, the BPF of I2R (m=35) and I1S (m=58) as well as their interaction (m=23) are still clearly visible in the spectrum after revolution 2.

Figure 4.13 shows an analogous plot to Figures 4.10a and 4.10b for comparison between "Unst. A" and "Unst. B" flow conditions seen in Figure 4.4b. The results show that as the mass flow is reduced, the total pressure ratio decreases above 75% span of I1S whilst it increases for spans below 75%. This is justified by the outward movement of the stalled region within the I1S blade-row which significantly increases the total pressure losses near the casing region. Furthermore, due to the presence of a low momentum region on the upper span, the flow is pushed inwards through I1S and accelerates which results in the total pressure increase at the lower spans.

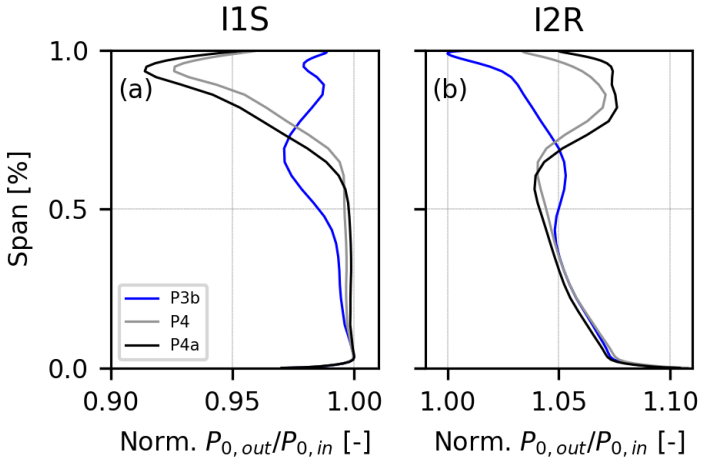


Figure 4.13: Normalized pressure ratio across I1S (a) and I2R (b) in regimes "Unst. A" and "Unst. B" as the compressor exit mass flow is reduced (see Figure 4.4b).

The profile across I2R in Figure 4.13b displays a significant increase in total pressure ratio at higher spans as the compressor mass flow is reduced. This can be further explained by analysing Figure 4.14 which shows the incidence angle upstream of I2R and the axial Mach number downstream of I2R as the mass flow is reduced from "P3b" to "P4". First, Figure 4.14a shows that the incidence increases at I2R inlet between 70% and 100% span.

Secondly, as the stalled region in I1S moves towards the casing, the incidence at I2R mid-span decreases and causes the I2R wake to decrease in size as seen in Figures 4.14b and 4.14c.

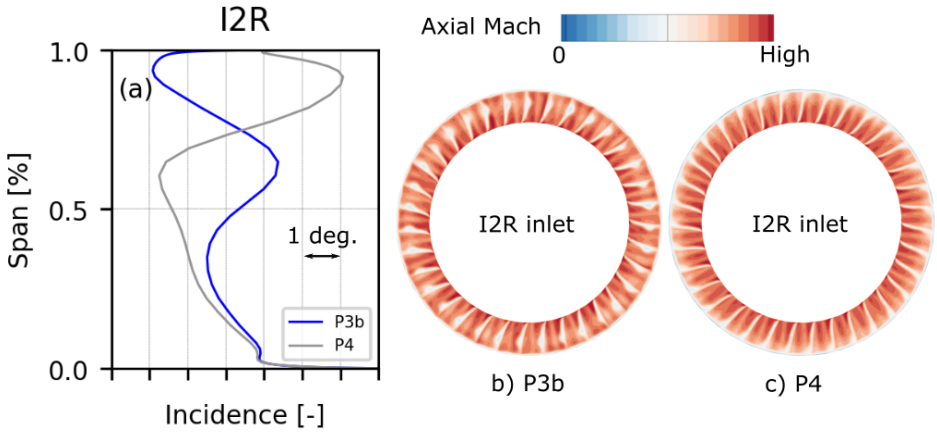


Figure 4.14: Incidence angle upstream of I2R (a). Development of the flow field at inlet of I2S (see Figure 4.4b): P3b (b) and P4 (c).

The balance between the total pressure loss and work load increase across I1S and I2R, respectively, leads to the "B2" horizontal S-shaped characteristic obtained in Figure 4.4b whilst the overall compressor stability is maintained.

4.2.3 Post stall development

Figure 4.15 shows the overall compressor performance in terms of normalized pressure ratio as function of inlet corrected mass flow ($\bar{m}$). The transient behaviour of the compressor when it crosses the stall line is also included (labelled as "Post stall"). The results show that, when the nozzle throat area is reduced further than "P4b", the compressor pressure ratio decreases abruptly. After, the compressor operating point stabilizes on a stalled characteristic at point "P5".

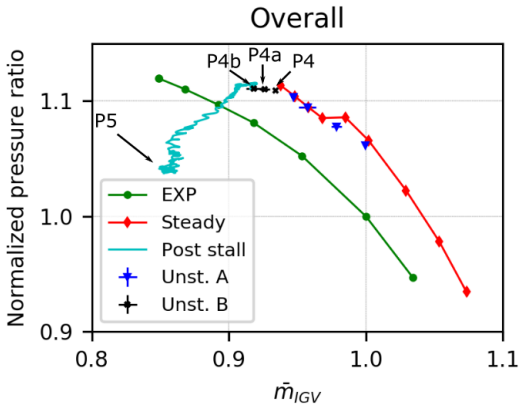


Figure 4.15: Normalized overall compressor performance and post stall behaviour.

To gain further insight on the post stall development of the compressor, the dynamic pressure modal content (as percentage of the mean dynamic pressure at each time instant) at 90% span of I1S inlet and exit (inlet I2R) for the points indicated in Figure 4.15 are displayed in Figure 4.16. The modes which relate to the blade count of I1R, I2R and interaction between I2R and I1S are also identified in this plot. Figure 4.17 and 4.18 display the axial Mach number contours at 90% span across all of the compressors stations at points "P4b" and "P5", respectively.

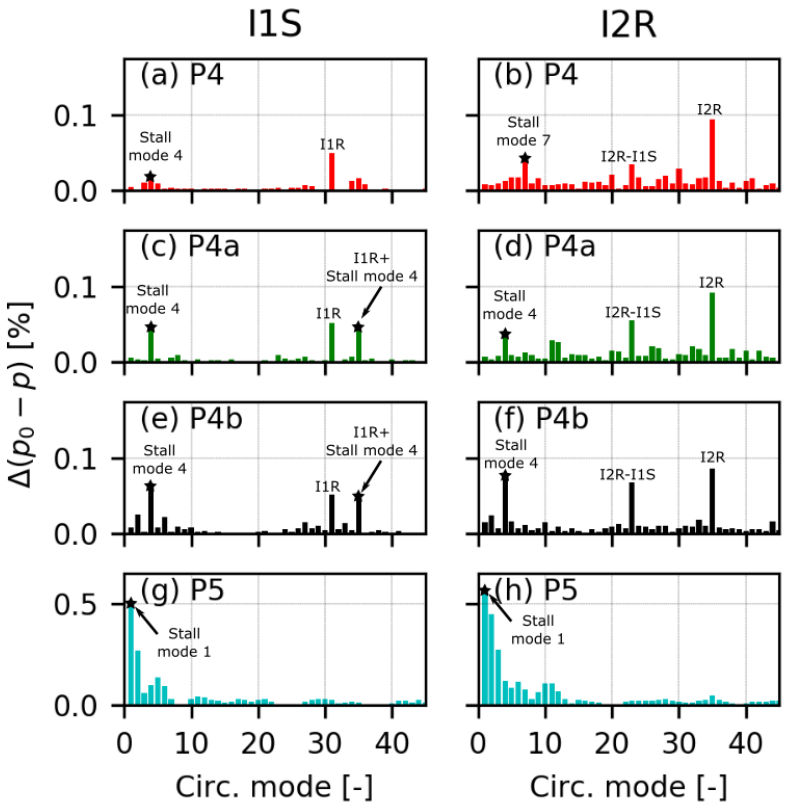


Figure 4.16: Circumferential modal distribution of dynamic pressure at 90% span of I1S and I2R inlets as the compressor exit mass flow is reduced (see Figure 4.15): Point P4 ((a) and (b)), Point P4a ((c) and (d)), Point P4b ((e) and (f)) and Point P5 ((g) and (h)).

At point "P4", the low order modes which characterize the flow field are mode 4 and 7 at inlets of I1S and I2R, respectively, as seen in Figures 4.16a and 4.16b. Mode 7 is linked to the flow separation at the higher spans of I1S showed before. Mode 4 appears first at the inlet of I1S as seen in Figures 4.16a. As the compressor operation moves towards the stall line, the amplitude of mode 4 grows and also appears at I2R as seen in Figures 4.16c-4.16f. This aerodynamic disturbance is caused by unsteadiness in the tip leakage flow of I1R as seen in Figure 4.17.

As the compressor is throttled from point P4b to P5, the stall mode 4 amplitude grows further and ultimately, coalesces into 1 rotating stall cell as seen by the sharp rise in amplitude of mode 1 in Figures 4.16g and 4.16h. This result suggests that I1R reaches the

stall line first in regime "Unst. B" and thus, it is responsible for driving the compressor across the stability limit. The flow field is characterized by one clear rotating stall cell which extends throughout all of the compressor axial stations and occupies approximately 30% of the circumference as seen in Figure 4.18. This is in agreement with the experimental data in Figure 4.4 which shows that "B1" "rolls-over" whilst "B2" recovers its negative slope characteristic at the point with lowest mass flow.

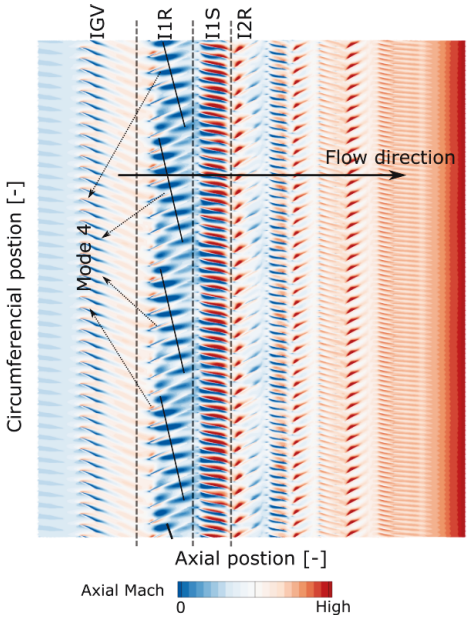


Figure 4.17: Axial Mach number contours at 90% span for condition "P4b" (see Figure 4.15).

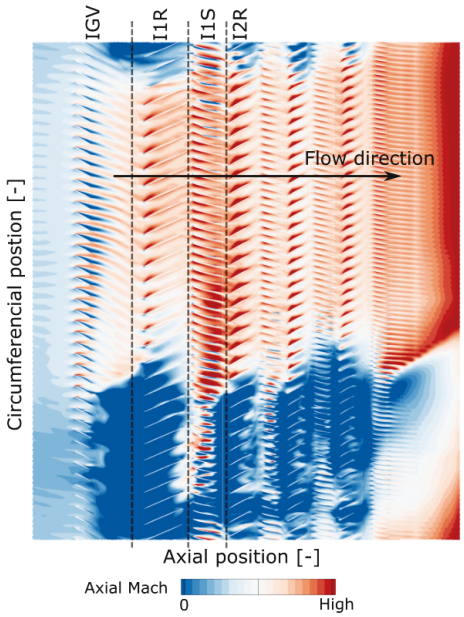


Figure 4.18: Axial Mach number contours at 90% span for condition "P5" (see Figure 4.15).

4.2.4 Comparison with experimental data

Figure 4.19 shows the recorded dynamic pressure signal envelope[3] at the mid chord of I1R and trailing edges (TE) of I1S, I2R and I4R obtained during the experimental campaign. The manoeuvre consisted in throttling the compressor rig from the point with the lowest mass flow on the experimental characteristic in Figure 4.15 towards a post stall condition. Afterwards, the throttle is re-opened towards a higher mass flow condition to avoid damage on the compressor rig. The envelope is indicative of the level of unsteadiness in the flow field, i.e., the difference between the higher and lower envelope is higher as the level of unsteadiness in the flow field increases and vice-versa.

The measurements demonstrate that prior to stall, the levels of unsteadiness are greater at the mid chord of I1R and trailing edge of I1S. This is in agreement with the CFD results presented in Figure 4.16 which showed the development of lower order circumferential modes at inlet of I1S and I2R prior to a transition to rotating stall (RS). The levels of unsteadiness present at I4R trailing edge are approximately the same before rotating stall and after the throttle being opened. This indicates that the flow is stable and approximately axisymmetric in the rear stages of the machine. This behaviour is also in agreement with the CFD results as previously demonstrated using the radial profiles in Figures 4.5.

The results clearly show a sharp increase in the difference between the upper and lower envelopes of the dynamic pressure signal, which occurs almost simultaneously across the entire compressor. This signal suggests the presence of a large scale rotating stall cell occupying the whole length of the compressor as predicted by the CFD simulations and shown in Figure 4.18.

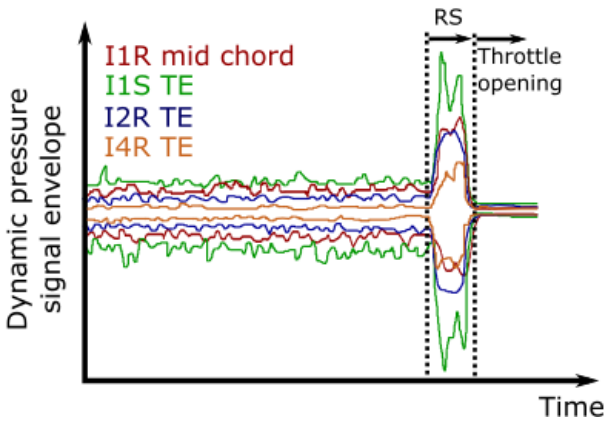


Figure 4.19: Experimental dynamic pressure signal envelope at several locations across the compressor casing as it is throttled towards a post stall condition.

[3]The envelope of a signal is a curve outlining its extremes.

4.3 High speed

4.3.1 Aerodynamic performance

In order to differentiate the pre stall phenomena between low and high speed, the following sections focus on the URANS model capability applied to the high speed case (NRT=100%) which was studied extensively using a single passage steady model in chapter 3.

Figure 4.20 presents a comparison between the predicted performance of the compressor obtained using the steady single passage ("Steady") and unsteady full annulus ("Unsteady") models with experimental data in terms of normalized pressure ratio as a function of inlet corrected mass flow ($\dot{m}\sqrt{T_0}/P_0$), referenced as "$\bar{m}$". As a starting condition for the unsteady model, the single passage solution is expanded to 360 degrees at point "SU" and it is throttled gradually from point "SU" to "N4". The compressor becomes unstable when the nozzle throttle area is reduced below point "N4". The time step was adjusted based on the mechanical speed to keep a similar setting as before (2150 time steps per revolution).

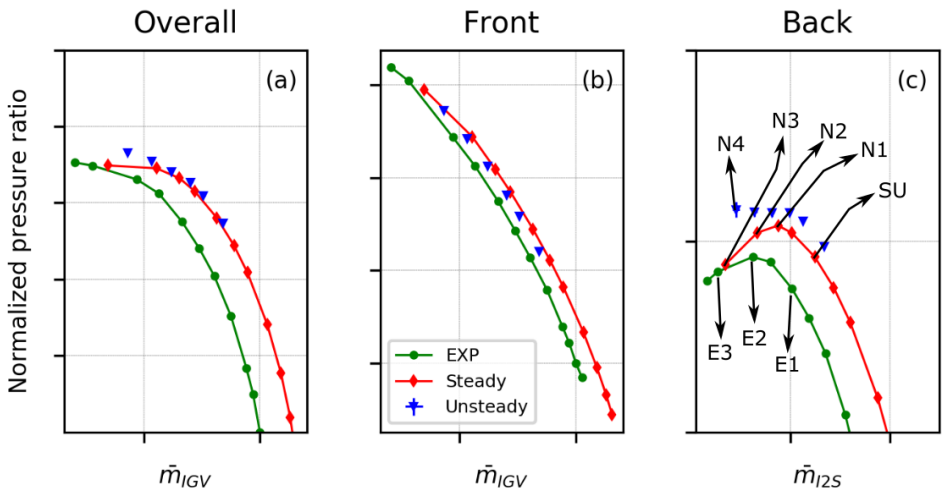


Figure 4.20: Normalized compressor performance. (a) Overall. (b) Front: IGV inlet to I2S inlet. (c) Back: I2S inlet to I4S inlet.

Figure 4.20 shows a good agreement between experimental data and both the steady and unsteady results. Similarly to the low speed case, an over-prediction in mass flow is observed for all stations which has been previously attributed to the absence of secondary geometry features in the model. The differences between the steady and unsteady model are limited to the points in the proximity of the compressor's stability limit. The solution obtained with the unsteady model stabilizes on a flat characteristic when the compressor is throttled towards point "N4" whilst it becomes unstable when the steady model is used.

Figure 4.21 shows the aerodynamic performance split between back stages of this compressor rig. The stability boundary is reached at the rear stage first for both models which is in agreement with experimental data. This result indicates that the compressor is well matched at this speed. In contrast to the low speed case, where the compressor's "B2"

operates on a nearly flat characteristic over most of the operating range (see Figure 4.4), all stages can produce further pressure rise after throttling until "B4" "rolls-over" towards the positive slope of the characteristic.

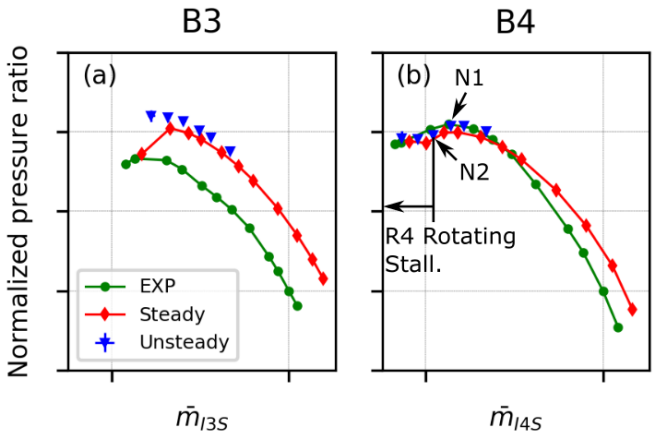


Figure 4.21: Normalized compressor back stages performance. (a) B3: I2S inlet to I3S inlet. (b) B4: I3S inlet to I4S inlet.

A comparison between the measured and predicted total pressure radial profiles at points "E2" and "N1" (see Figure 4.20c) is presented in Figure 4.22. A good overall agreement is found across the compressor however, an under-prediction in total pressure near the hub surface at I2S and I3S inlets is observed. The results presented by Wang et. al. [63] showed that the inclusion of shroud leakage flows may correct this effect by reshaping the rotors hub corner separations. For the present study, these secondary flow features do not have a significant impact in the stability boundary prediction since the compressor stalls from I4R as it will be shown later.

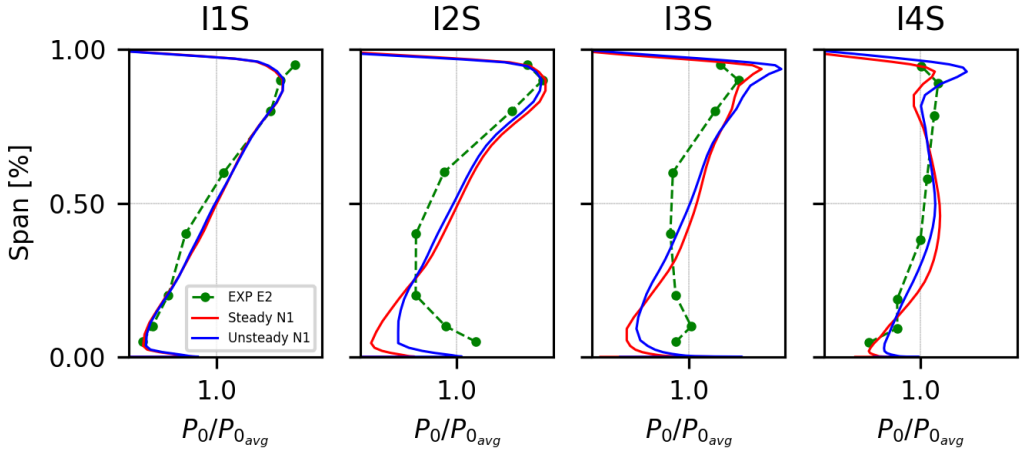


Figure 4.22: Comparison of normalized total pressure radial profiles between experiments (Point "E2") and steady single passage and unsteady full annulus models (Point "N1").

4.3.2 Unsteady effects on the pre stall condition

To gain further insight into the flow phenomena, the flow field development in the blade proximity of I4R and I4S as the compressor is throttled from point "N1" to "N3" is presented in Figure 4.23 for the steady single passage and unsteady full annulus models. The I4S blade-row becomes heavily stalled at this operating speed when the nozzle throttle is reduced from point "N1" for the two models.

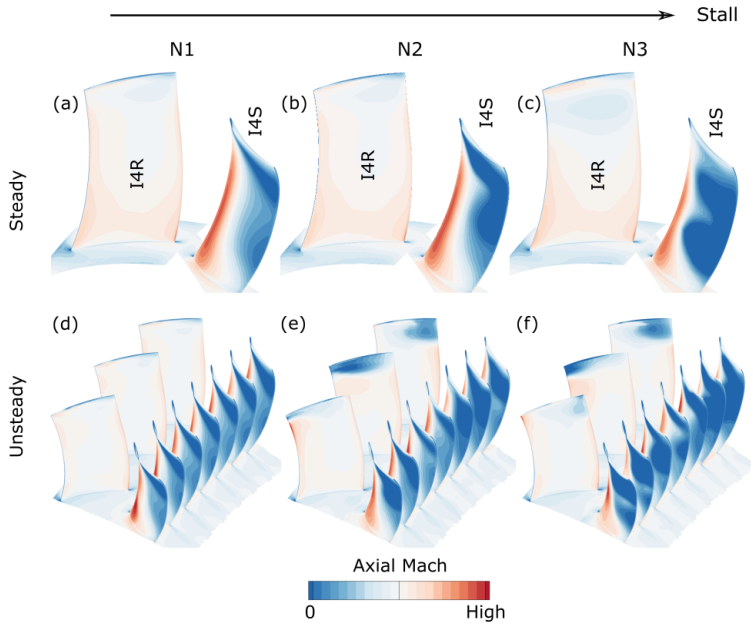


Figure 4.23: Axial Mach number development in the proximity of I4R and I4S blade surfaces as the compressor is throttled from point "N1" towards "N3" for the steady single passage ((a),(b) and (c)) and unsteady full annulus ((d),(e),and,(f)) models.

Figure 4.24 shows the time history of axial Mach number and dynamic pressure modal content at 95% span of I4S inlet as the compressor is throttled from "N1" towards "N2" when considering the full annulus model. At point "N1", mode 47 (I4R blade count) is the dominant mode which indicates that the flow field is axisymmetric. When the compressor is throttled from point "N1" towards "N2", I4R stalls and a rotating stall pattern is formed in the proximity of the casing as seen in Figure 4.24b. This pattern is characterized by 33-35 short-scale stall cells. The flow behaviour at 98% span across the compressor's stage 3 and 4 at condition "N2" can be observed in Figure 4.25. The inlet of I4S is also illustrated. It is seen that this rotating stall pattern is limited axially to I4R and radially to the tip region of the machine.

Non-axisymmetric flow features develop for point "N2", which corresponds to the condition where "B4" starts operating on the positive slope of the characteristic as seen in Figure 4.21b. A similar flow behaviour was found for the low speed case when "B2" operation was on the positive slope of its characteristic. This shows that an unsteady full annulus model is required when one of the compressor stages operates in such condition.

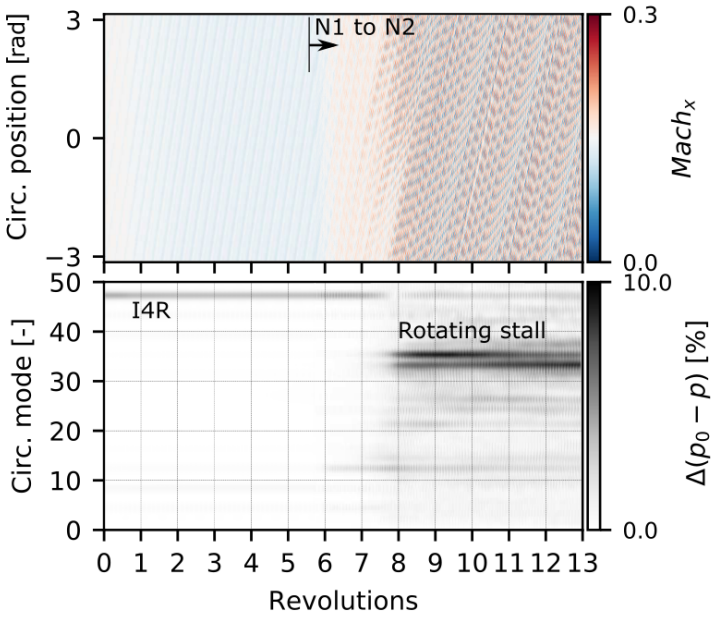


Figure 4.24: Time history of axial Mach number (a) and dynamic pressure modal content (b) at 95% span of I4S inlet as the compressor is throttled from "N1" to "N2" (see Figure 4.21b).

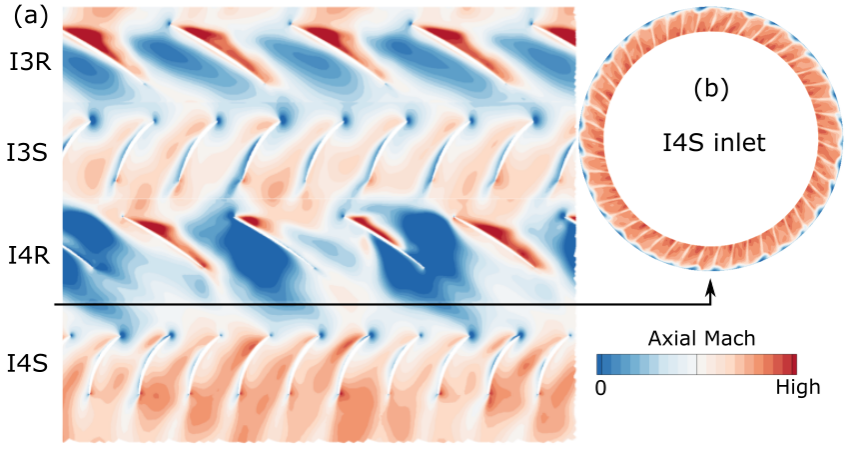


Figure 4.25: Axial Mach number at 98% span at I3R, I3S, I4R and I4S for point "N2" (a). I4S inlet for point "N2" (b).

4.3.3 Comparison with experimental data

Figure 4.26 shows the CFD time modal distribution of dynamic pressure at 95% span for each of the sliding planes of the compressor rig at points "N1" and "N2" (see Figure 4.21b). At point "N1", several engine orders are observed across the machine which correspond to the rotor blade counts (modes 31, 35, 43 and 47). When the compressor is throttled to a condition where "B4" operates on the positive slope of the characteristic (point "N2"), a broadband spectrum forms at the inlet of I4S. The modes with higher amplitude are located between 23-27 engine orders which indicates the presence of a stall cell pattern rotating around the annulus at 70%-80% shaft speed[4] (stationary frame of reference) in the direction of the rotors.

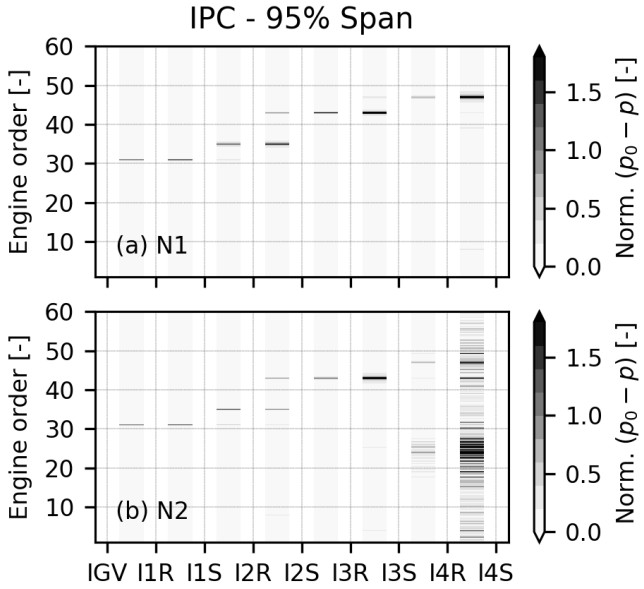


Figure 4.26: Time modal distribution of dynamic pressure at 95% span across the compressor using CFD data: point "N1" (a) and point "N2" (b) in Figure 4.21b.

In order to gain further confidence in these results, the modal distribution of dynamic pressure collected during the experiment at the intersection between the trailing edge of each blade-row and casing is presented in Figure 4.27. The experimental results show that at point "E1", the modal spectrum across the compressor is dominated by modes corresponding to rotor blade counts and its interactions. After the throttling towards point "E3", a broadband spectrum forms around modes 38-60 in "B4". This is in agreement with the CFD results regarding the prediction of the stall inception location. It should be noted that the CFD was not capable of capturing the same frequencies as the experiment. However, since more experimental data was not available, further studies to determine the rotating stall cells count or speed were not performed.

[4]Note that 33 cells were identified in the previous section.

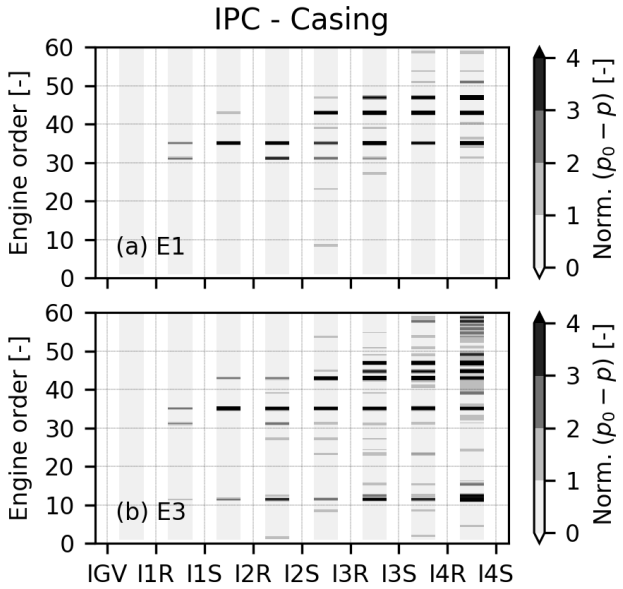


Figure 4.27: Time modal distribution of dynamic pressure at the compressor casing using experimental data: point "E1" (a) and point "E3" (b) in Figure 4.20. The data at IGV exit is not available.

4.4 Concluding remarks

This chapter presents a study on unsteady effects in a modern multi-stage compressor at two operating conditions: low and high speed. The results obtained using a steady single passage and unsteady full annulus models were presented and compared with experimental data. The results provide evidence that URANS CFD methods are capable of capturing the relevant flow features which characterize the flow behaviour in multi-stage compressors at both low and high speed conditions of operation.

It was demonstrated that in multi-stage compressors, unsteady full annulus models are required when one of the compressor stages is locally stalled and operates on the positive slope of the characteristic. The flow field is characterized by a rotating stall pattern with a high number of short-scale stall cells embedded in one of the compressor stages. For the low speed case, 16-18 stall cells rotate in the I2S blade-row at around 11% shaft speed. For the high speed case, 33-35 stall cells rotate in the I4R blade-row at approximately 70%-80% shaft speed.

Unsteady effects and the development of non-axisymmetric flow features in multi-stage compressors are strongly correlated with the formation of rotating stall in one of the compressor's stages. For low speeds, rotating stall is seen on the front stages over a wider operating range. For high speeds, the presence of non-axisymmetric flow features is limited to the rear stage and operating conditions near the stability boundary. Consequently, the differences between the steady single passage and unsteady full annulus models are more evident at lower speeds than higher speeds.

5 Methodology and validation of surge modelling in a three-shaft compression system

5.1 Problem description and overview

The objective of this chapter is to develop and validate an efficient technique for initiating surge in a three-shaft engine compression system. During this research, it became evident that preparing a calculation in a three-shaft compression system is a very challenging task. Therefore, a detailed description of the steps required for such modelling is given in this chapter which will be helpful to other researchers in the field.

Two key steps are required to successfully perform these type of simulations. In the first step, it is necessary to obtain a steady-state solution at a specified operating condition. In the second step, the surge calculation is initiated by introducing a disturbance in the flow field which causes the compression system operating condition to cross the surge line.

The process to obtain a steady-state solution requires an extensive investigation of compressor matching which is not straightforward to perform. Additionally, when multi-stage compressors operate at off-design condition, non-axisymmetric flow features tend to form and unsteady full annulus calculations may be needed to allow these flow disturbances to develop. For this reason, the validity of using steady single passage solutions as pre surge condition becomes questionable. Both of these problems are addressed here.

To initiate a compression system surge, the flow disturbance introduction needs to be clinical in the sense that the resulting surge event is realistic to the problem in study. For example, if the interest is to study a surge event initiated on the IPC front stages, the aerodynamic flow disturbance must cause the surge onset at that location. In contrast, the introduction of a weak perturbation in the flow field may not initiate the surge event but instead, rematch the IPC and HPC to a new operating condition. As an example, turning the IPC VSVs to a schedule that does not promote an instability can potentially lead to several days or weeks of simulation with a very expensive model waiting for a surge event to start that will never do. This work presents a methodology that will avoid such scenarios.

This chapter considers two distinct test cases to obtain a three-shaft engine compression system surge model for two operating conditions and surge initiation strategies:

- Case A1 - The compression system is tuned to a high power condition close to design

and the surge event is initiated via abrupt throttling of the core nozzle. This is a close approximation to the "fuel-spike" situation where a short duration of over-fuelling causes the HPC working line to transiently rise and provoke a surge originating in the HPC.

- Case P - This case is a mid power engine surge where the VSVs of the IPC are malscheduled and surge is initiated via a slight decrease in the HPC mechanical speed. The HPC speed reduction causes the mass flow into the HPC to decrease, effectively throttling the IPC.

The cases described above are summarized in Table 5.1. First, the numerical model is introduced and methodologies to obtain the steady-state solutions for both cases are presented. Secondly, the impact of unsteady non-axisymmetric flow features for these conditions is evaluated. Finally, case P is validated against measured data.

Table 5.1: Case studies for derivation of a methodology for surge modelling depending on the surge onset location.

Case	**Initial Cond.**	**Pre surge VSVs**	**Trigger**	**Surge onset location**
A1	High power	Nominal	HPC throttle	HPC
P	Mid power	Malscheduled	HPC decel.	IPC

5.2 Numerical model

The research is performed on a modern compression system which is a part of an engine with a three-spool[1] architecture designed by Rolls-Royce showed in Figure 5.1. The numerical low pressure (LP) domain of this machine is formed by a farfield chamber, intake, fan (LPC), outlet guide vane (OGV), engine section stator (ESS), and a choked bypass nozzle to control the fan operation. The intermediate pressure (IP) domain has an eight-stage IPC which has 3 VSVs: IGV, stator 1 and stator 2. A swan neck duct (SND) connects the IPC to a six-stage HPC with an engine representative volume plenum[2] and a core nozzle to control the core operation. For brevity, the core stations will be identified using two letters and one number: the first letter identifies the compressor where "I" stands for IPC and "H" for HPC; the second distinguishes between rotor ("R") or stator ("S"); finally, the number corresponds to the stage of the compressor. For example, station "H2S" refers to stator 2 of the HPC.

The numerical grid used was generated using the techniques described by Sbardella [77]. The spatial resolution and wall distance (y^+) were selected based on the findings presented

[1] Spool refers to a connected compressor, shaft and turbine.
[2] The geometry is different from the engine combustor.

in chapter 3. The grid has 47 radial grid layers across the span with refinements towards the tip and hub on each of the rotor passages. The tip gap region is modelled using 12 equally spaced radial layers. The number of radial layers in the stator vanes is 59. This results in a total number of cells in the domain of approximately 12 million for the single passage model and 1 billion for the full annulus model. Secondary flows such as penny gaps, bleed flows and shroud flows were not included in the model.

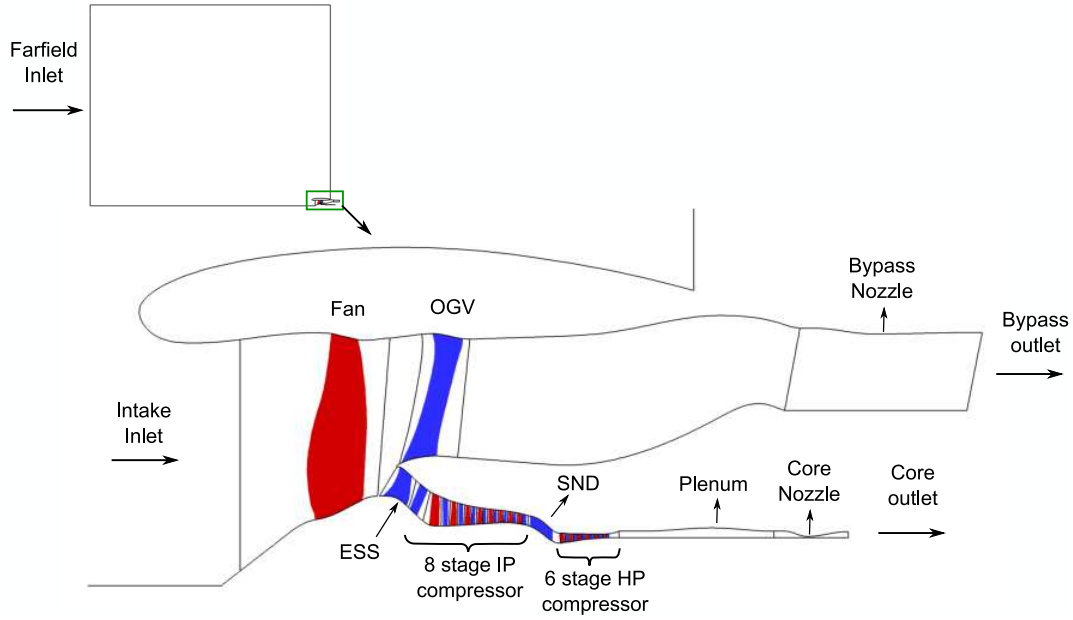


Figure 5.1: Meridian view of the engine compression system domain.

The inlet far field boundary condition (BC) was set to the sea-level static ambient condition whilst two choked nozzles were used as outlet boundaries for the bypass and core. Pressure at the outlet boundaries is set to values sufficiently low to ensure that the nozzles remain choked [78] during both the steady and unsteady simulations. Wall function is used to model the solid walls. The turbulence model selected is the modified Spalart-Allmaras (MSA) model without destruction term in the proximity of the casing as suggested in chapter 3. For the unsteady calculations, the time resolution considered 2150 time steps per IPC shaft revolution which corresponds to approximately 1500 time steps per HPC shaft revolution. This resulted in a run-time of approximately 1.1 days per HPC shaft revolution using 576 Intel Xeon 2.2GHz CPUs.

5.3 Methodology for a three-shaft compression system surge

5.3.1 System matching

To study a compression system numerically at a target operating condition, each compressor setting needs to be calibrated via boundary conditions. This section provides a strategy on how to model and control numerically the operation of a three-shaft engine

compression system.

The first step for such strategy consists of selecting an initial target condition for each of the compressors based on an engine deck[3]. This data contains detailed information of the LPC, IPC and HPC aerodynamic speeds ($\Omega/\sqrt{T_0}$), bypass ratio and overall system pressure ratio along the working line.

Figure 5.2 shows a simplified block diagram of the compression system used in this research. The system inlet condition is prescribed using total temperature ($T_{0,LPC}$) and total pressure ($P_{0,LPC}$) upstream of the LPC. The actual operating points of the LPC, IPC and HPC are controlled using the following parameters:

- LPC - Bypass nozzle area (A_{bypass}) and fan mechanical speed (Ω_{LPC});
- Core compressors (IPC and HPC) - VSVs schedule, IPC mechanical speed (Ω_{IPC}), HPC mechanical speed (Ω_{HPC}) and core nozzle area (A_{core}).

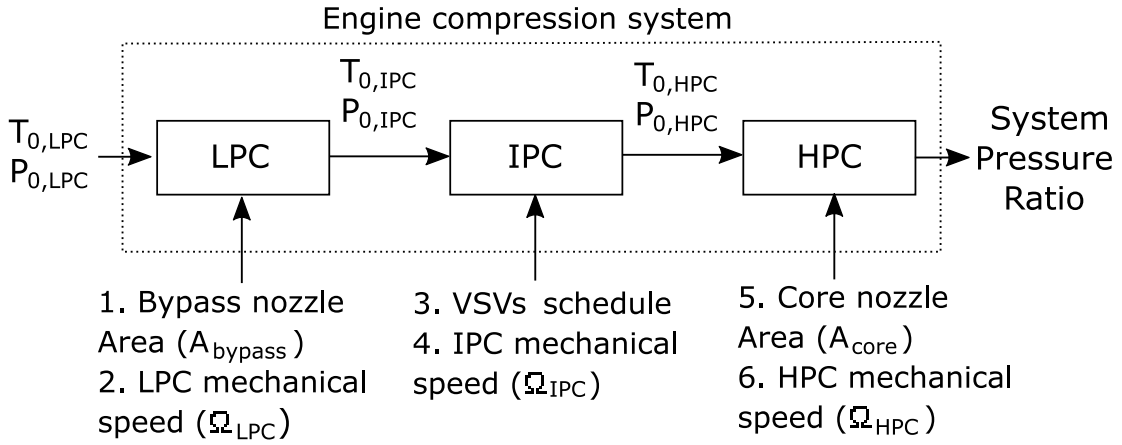


Figure 5.2: Block diagram of a three-shaft compression system.

Each compressor (LPC, IPC and HPC) operation is dependent on the other ones. For example, by opening the IPC VSVs, the mass flow in the core increases and, as a consequence, higher temperature gas is delivered to the HPC inlet changing its aerodynamic speed for a fixed mechanical speed. The complexity of these interactions demands a systematic approach to achieve an acceptable compressor matching using the minimum number of iterations. To reduce computational cost, the compressor matching is obtained by using a single passage mixing plane model. The approach undertaken here consists of a step-by-step process where initially, each of the compressors is computed independently.

5.3.2 LPC operating point

The first step consists of obtaining a steady solution of the fan (LPC) at the target operating point. For this purpose, the numerical domain of the LP system shown in Figure 5.1 is used. The fan mechanical speed is chosen to ensure a target LPC aerodynamic speed

[3]Engine performance data provided by the manufacturer of the engine.

($\Omega_{LPC}/\sqrt{T_{0,LPC}}$). A constant core mass flow based on engine data at the target condition is imposed at the ESS exit. Finally, the fan is throttled by changing the bypass nozzle area (A_{bypass}) until the target operating point is reached. Figure 5.3 shows the fan normalized inlet corrected mass flow ($\bar{m}$) against normalized total pressure ratio characteristics. The selected LPC operating conditions for cases P and A1 were selected as shown in Figure 5.3. The bypass nozzle area (A_{bypass}) and LPC mechanical speed (Ω_{LPC}) determined from these computations are fixed in subsequent studies.

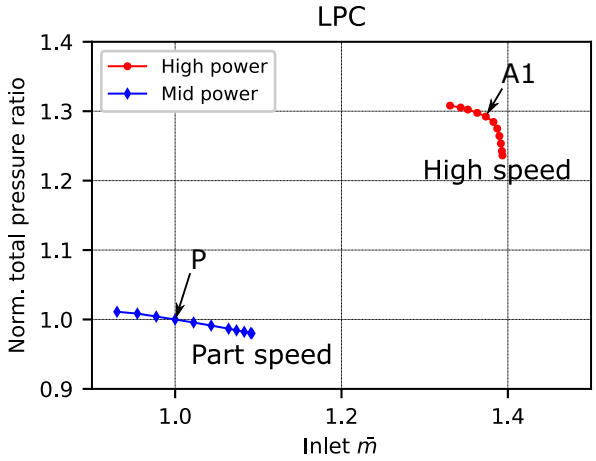


Figure 5.3: LPC characteristics and selected operating points for cases A1 and P.

5.3.3 IPC aerodynamic speed

In the following step, the IPC aerodynamic speed is determined. First, the steady-state solution of the isolated IP system (IGV to I8S) and SND is obtained by attaching a nozzle downstream of the SND to control the IPC operation. The ESS outlet condition obtained from the LPC computation is imposed as the IPC inlet condition. The IPC mechanical speed (Ω_{IPC}) is defined based on the IPC inlet total temperature ($T_{0,IPC}$) to achieve the target aerodynamic speed. The VSVs angles are set according to the schedule.

After, the LPC and IPC steady solutions are combined. The IGV inlet plane is no longer a boundary condition and thus, the total temperature ($T_{0,IPC}$) changes slightly. To match the engine deck, a final adjustment in the IPC aerodynamic speed is made by changing the IPC mechanical speed. Even though the aerodynamic speed of the IPC is fixed, its operating point still remains undetermined, as it is controlled by the exit flow into the HPC.

5.3.4 Core compressor matching

Before obtaining a solution for the IPC target operating point, a solution of an isolated HPC (H1R inlet to the exit of the compression system) is obtained. The HPC mechanical speed (Ω_{HPC}) is selected based on a guess of the HPC inlet total temperature ($T_{0,HPC}$) and aerodynamic speed design intent. This guess can be made based on the total temperature

at the IPC exit from the LPC and IPC systems computation. In the next step, the LPC and IPC coupled system is connected to the HPC system and an initial solution of the full coupled system is obtained. This calculation results in an arbitrary operating condition of both the IPC and HPC. After, a compressor matching procedure is employed to define the IPC and HPC operating points. This consists of an iterative process based on tuning of the HPC mechanical speed (Ω_{HPC}) and core nozzle throat area (A_{core}).

The compressor matching process is explained here for case A1. Figure 5.4 shows a plot of normalized total pressure ratio of the core (IPC and HPC) as a function of core exit corrected mass flow ($\bar{m}$). The three performance curves in this plot were obtained by increasing the HPC mechanical speed in an orderly fashion with $\Omega_{HPC,1} < \Omega_{HPC,2} < \Omega_{HPC,3}$ [4]. The results show that as the nozzle throat area is reduced, the system overall pressure ratio increases in a similar fashion for all the three HPC mechanical speeds which indicates that the core overall pressure ratio is solely a function of nozzle throat area.

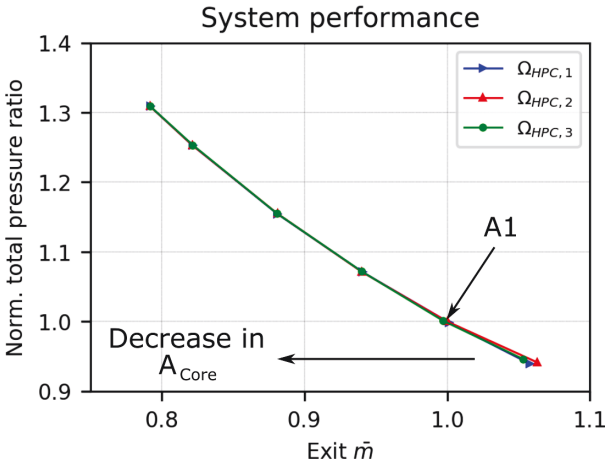


Figure 5.4: Effect of the HPC mechanical speed on the core characteristics (from IGV inlet to HPC exit) - case A1.

In order to gain further insight into the IPC and HPC operation, Figure 5.5 shows the obtained performance curves for the IPC and HPC for the three HPC mechanical speeds and different core nozzle throat areas (A_i). Figure 5.5a shows that the IPC pressure ratio increases as the HPC mechanical speed is decreased for the same nozzle throat area. An inverse relation is observed for the HPC in Figure 5.5b where, for the same nozzle throat area, lower pressure ratios are obtained as the HPC mechanical speed is decreased. These dependencies indicate that the IPC and HPC load split can be adjusted by using the HPC mechanical speed and core nozzle throat area.

Figure 5.6 presents the effect of the HPC mechanical speed and nozzle throat area (in terms of exit corrected mass flow) on the HPC aerodynamic speed ($\Omega_{HPC}/\sqrt{T_{0,HPC}}$) and inlet total temperature of the HPC ($T_{0,HPC}$). Figure 5.6a shows that for a constant mechanical speed, the HPC aerodynamic speed decreases as the core nozzle throat area is decreased. This effect is caused by an increase in the IPC load which ultimately results

[4]The difference between each mechanical speed is 1.5% of the nominal HPC mechanical speed.

in a total temperature rise at the inlet of the HPC (exit of the IPC) as shown in Figure 5.6b. Simultaneously, by decreasing the HPC mechanical speed, the HPC aerodynamic speed also decreases.

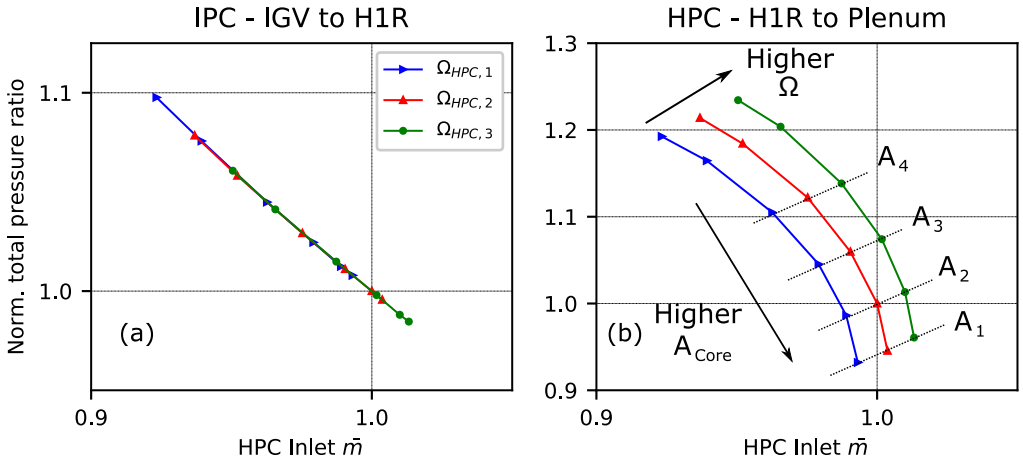


Figure 5.5: Effect of the HPC mechanical speed on the IPC (a) and HPC (b) characteristics - case A1.

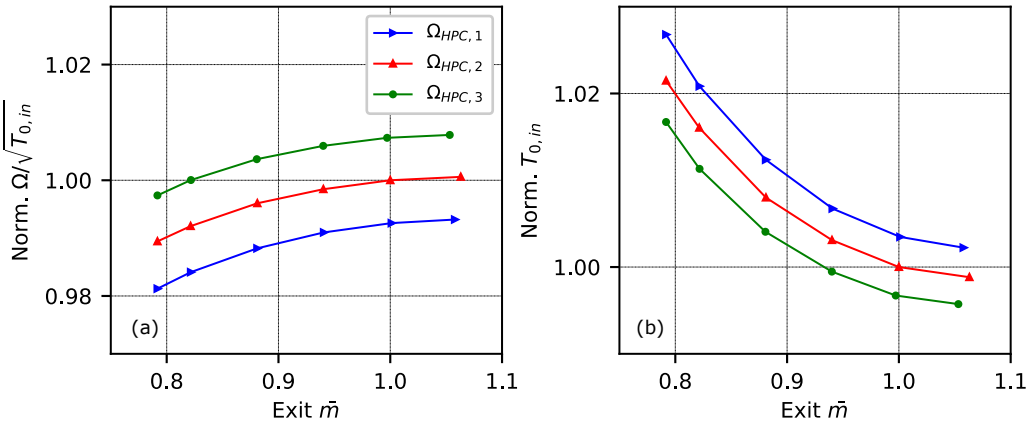


Figure 5.6: Effect of the HPC mechanical speed on the HPC inlet aerodynamic speed (a) and HPC inlet total temperature (b) - case A1.

These results show that the constant mechanical speed curves shown in Figure 5.5b are not at constant aerodynamic speed since the temperature at HPC inlet ($T_{0,HPC}$) varies as a function of nozzle throat area for a constant HPC mechanical speed (Ω_{HPC}). It also shows that the IPC and HPC operating conditions are functions of two variables: Ω_{HPC} and A_{core}. As a result, an iterative method is required to match the IPC and HPC to their respective target operating points.

For case A1, the steady solution identified in Figure 5.4 is selected because it approximately matches the target condition aerodynamic speeds and pressure ratio from the engine deck provided by the engine manufacturer. This condition corresponds to core nozzle area A_2 and HPC mechanical speed $\Omega_{HPC,2}$ in Figure 5.5.

5.3.5 System surge initiation

Surge occurs when the compression system operating condition intersects the engine surge line. This can be achieved either by raising the compression system operating condition towards the surge line or dropping the surge line towards the compression system operating condition. For example, deterioration may cause the tip clearances to increase sufficiently in some stages so that the surge line drops towards the working line. Similarly, a change in IPC VSVs angles away from their design may cause the fronts stages of the IPC to become unstable, resulting in a drop in the surge line. Rapid engine transients (acceleration or decelerations) may also cause the compressor working line to rise sufficiently to intersect the surge line.

CFD calculations of full annulus engine models are expensive and therefore, one needs to ensure that the introduced disturbances are capable of disrupting the engine operation to provoke surge. This section aims to demonstrate two preliminary studies that will build confidence in the models and ensure that for each of the disturbances introduced, the compression system will surge from the desired onset location. For cases A1 and P, the surge events are initiated from the HPC and IPC, respectively.

Case A1

For case A1, surge is initiated via abrupt throttling of the HPC. In order to achieve this, it is necessary to ensure that the HPC reaches the stability limit earlier than the IPC. Figure 5.4 shows that the engine stability limit is reached at the same exit mass flow for the three HPC speeds tested during the IPC/HPC matching process. As previously demonstrated, the loading on the IPC rises as the HPC mechanical speed is decreased. Therefore, the fact that the engine stability limit remains unchanged as the HPC mechanical speed is varied indicates that the HPC is the first compressor to surge. In this case, to initiate surge, the throat area of the core nozzle (A_{core}) must be decreased further from the lowest mass flow point in curve $\Omega_{HPC,2}$ in Figure 5.5b.

Case P

For case P, the objective is to reproduce an experimental condition where the surge is initiated at the IPC front stages. Figure 5.7 shows the sketch of the experimental and numerical manoeuvres used to initiate surge in terms of IPC total pressure ratio as a function of IPC inlet corrected mass flow. In the experimental campaign, the surge is initiated in two steps: first, the IPC VSVs are opened towards a malscheduled position driving the IPC operation from point "E1" towards point "E2". After, the bleed valves are closed[5] which effectively throttles the IPC from point "E2" towards point "E3". Due to the VSVs malschedule, the compressor surge line has dropped and consequently, the whole system surges before reaching point "E3".

[5]The bleed valves are designed to be opened at this speed during engine operation.

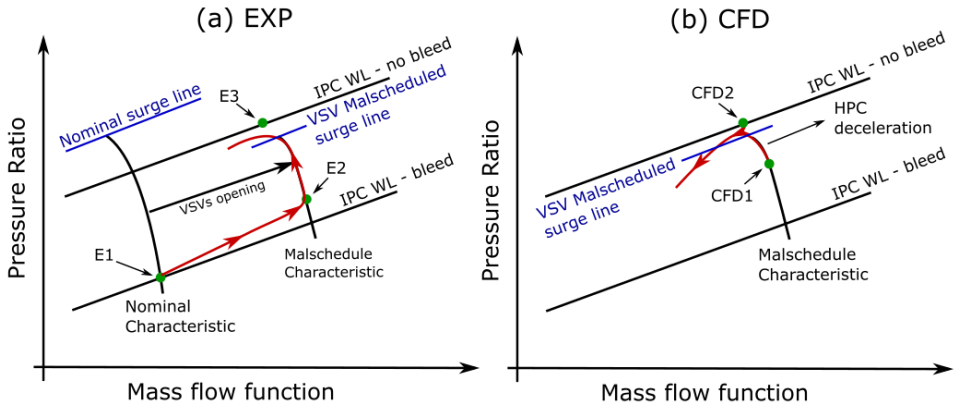


Figure 5.7: Experimental (a) and numerical (b) manoeuvres to initiate surge in the front stages of the IPC.

The process described above was simplified to initiate surge using CFD. Instead of starting the simulation at point "E1", the steady solution was obtained using the point "CFD1" as target condition in the compressor matching process. After, the surge is initiated by decelerating the HPC, which effectively throttles the IPC and moves its operation from point "CFD1" towards "CFD2" as shown in Figure 5.7b. Similarly as before, the IPC operation crosses the surge line and the whole compression system surges.

Figure 5.8 shows the IPC and HPC performance curves at different HPC mechanical speeds in terms of normalized total pressure ratio as a function of HPC inlet corrected mass flow for case P. Figure 5.8b demonstrates that the HPC stability margin increases as the HPC mechanical speed is increased ($\Omega_{HPC,1} < \Omega_{HPC,2} < \Omega_{HPC,3}$). Figure 5.8a shows that the IPC surge line is reached before the HPC becomes unstable for all three HPC mechanical speeds. This indicates that the IPC surge line defines the system stability margin.

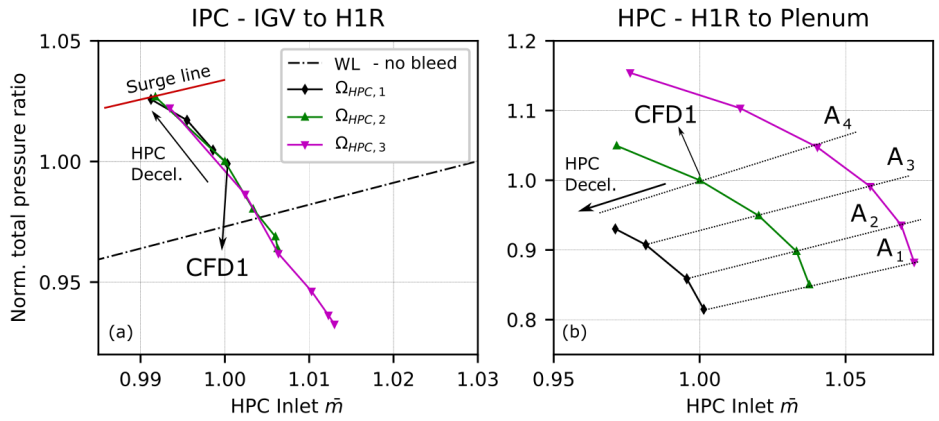


Figure 5.8: Effect of the HPC mechanical speed on the IPC (a) and HPC (b) performance - case P

To trigger surge in case P, the HPC mechanical speed is decreased from $\Omega_{HPC,2}$ to $\Omega_{HPC,1}$ whilst keeping the core nozzle constant with throat area A_4. This process mimics

the closure of the bleed valve system in the rear of the IPC as done in the experimental campaign which effectively pushes the IPC operating condition towards its surge line (as illustrated in Figure 5.7b).

5.4 Development of non-axisymmetric flow features

As previously demonstrated in the chapter 4, the development of non-axisymmetric flow features in multi-stage compressors is present when one of the stages operates on the positive slope of its characteristic. Therefore, unsteady simulation using full annulus model is needed to allow the development of flow unsteadiness before introducing a disturbance to initiate surge. This requirement is examined in this section by analysing cases A1 and P pre surge behaviour.

The mid passage axial velocity at the IPC front stages obtained using the steady single passage model is shown in Figure 5.9 for cases A1 and P. For case A1, the compressors are operating near design and thus, they are matched. Consequently, the solution does not show signs of compressor stall. On the contrary, for case P, it is clearly visible in Figure 5.9b that the I1S and I2S are stalled in the hub region. This is caused by an operation below design speed and the VSVs malschedule which deteriorates the performance of the IPC front stages.

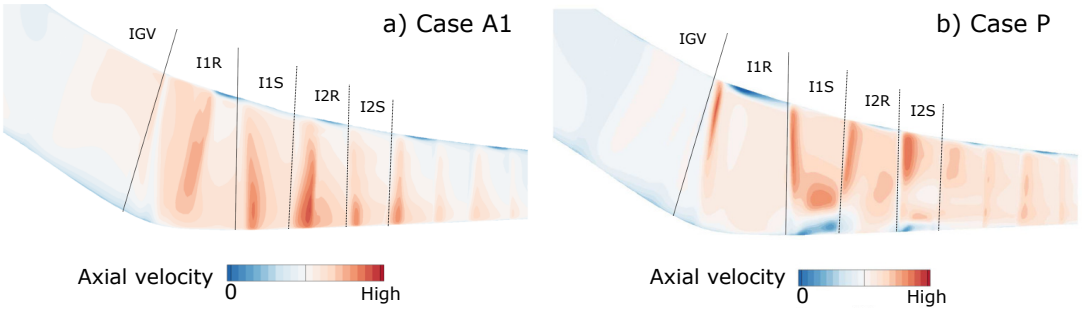


Figure 5.9: Mid passage axial velocity - case A1 (a) and case P (b).

Both of these solutions were expanded to 360 degrees and unsteady calculations were performed for 9 IPC revolutions. For case A1, the IPC and HPC solutions did not show significant changes and the axisymmetric behaviour was maintained. For case P, the stalled flow region developed. This is shown in Figure 5.10 which presents the contours of axial velocity at the planes located upstream of I2R, I2S and I3R at the end of revolutions 0.1 and 9 for case P. It is seen that the flow field in the hub region of I2S and I3R inlets is non-axisymmetric at revolution 9. The distribution of axial velocity modal content at 10% span in the front stages of the IPC is displayed in Figure 5.11 at IPC revolutions 0.1 and 9. These plots were constructed based on the modal content of axial velocity collected by numerical probes around the annulus. The axial velocity modal content amplitude is normalized by the average velocity at each time step, $\bar{U}_x$, i.e., mode 0 of the velocity spectra (m=0). Figure 5.11a shows that at the beginning of the unsteady full annulus

calculation, the modal content present in the IPC front stages is limited to the blade passing frequencies (BPF). By revolution 9, low order modes are observed at the inlets of I2R, I2S and I3R as shown in Figure 5.11b. These results show the importance of using an unsteady full annulus model to obtain a realistic pre surge solution for cases where some of the stages are locally stalled.

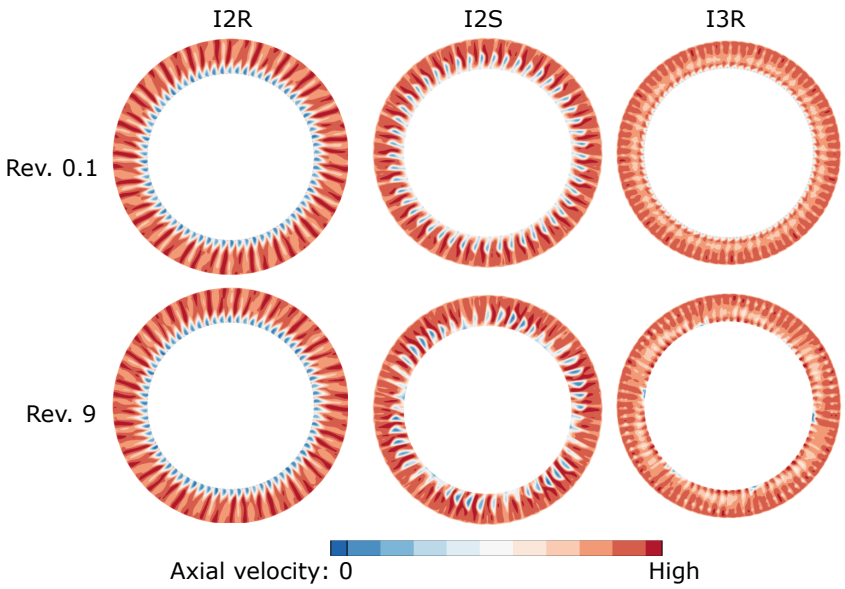


Figure 5.10: Axial velocity at I2R, I2S and I3R inlet planes for case P at revolutions 0.1 and 9.

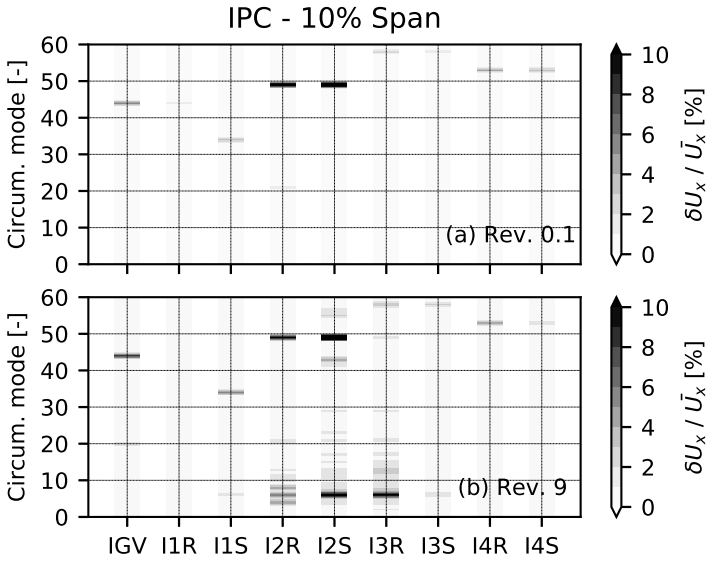


Figure 5.11: Circumferential modal content of axial velocity for case P - revolution 0.1 (a) and revolution 9 (b).

5.5 Validation of the pre and post surge modelling - case P

This section studies case P which consists of a mid power surge initiated via a HPC deceleration. For certification and safety reasons, high power surge events are more relevant. However, case P is studied for validation because experimental data is available. This test case mimics a bleed valve closure in IPC rear stages. It is also representative of a high pressure turbine failure or a faulty valve which is not open when the engine system operates at mid power condition. A combined effect of an IPC VSVs malschedule with a HPC shaft speed reduction causes the IPC to cross its stability limit resulting in surge.

5.5.1 Overall transient behaviour

Figures 5.12 and 5.13 show the surge transient performance of the HPC and IPC, respectively, in terms of static pressure ratio as a function of corrected mass flow ($\dot{m}\sqrt{T_0}/P_0$) at the inlet of each compressor, referenced as "$\bar{m}$". HPC shaft revolutions are used to indicate elapsed time from revolution zero (steady solution), which are added to several points on these figures to indicate how the operating condition of each compressor varies with time. The HPC shaft speed was decreased by 1.5% at revolution 9.

The HPC deceleration causes its aerodynamic speed to decrease between revolution 9 and 15 as shown by the corrected mass flow and pressure ratio decrease in Figure 5.12. When the HPC operating condition is changed to a lower speed, the IPC operating condition moves towards the surge line (see Figure 5.8) and consequently the IPC becomes unstable and surges as indicated by the rapid mass flow decrease shown in Figure 5.13 from revolution 15 onwards. Figure 5.12 shows that, between revolution 15 and 16.5, the HPC pressure ratio increases along a lower aerodynamic speed characteristic. At revolution 16.5, the slope of the transient operating condition becomes positive which indicates that HPC surge line has been crossed. This is a consequence of the IPC losing its ability to pressurise which causes a rapid pressure drop at the inlet of the HPC and subsequent HPC pressure ratio increase.

Figure 5.12 shows that the HPC transient characteristic crosses the zero flow boundary at around revolution 16.8 at which point the HPC starts discharging air into the IPC. During the reverse flow period, the HPC settles on its reverse flow characteristic and goes through a blow-down period between revolution 16.8 and 18. After, the HPC recovery is initiated. Figure 5.13 shows that the IPC goes through the reverse flow period between revolution 17 and 25.2. During this period, the HPC tries to recover and falls back into reverse flow since the IPC is still in blow-down, resulting in multiple "HPC secondary surges" as shown in Figure 5.12.

Figure 5.13 shows that the blow-down period of the IPC is initiated around revolution 18 where the minimum mass flow being discharged through the IPC inlet is found. This instant corresponds approximately to the time instant where the IPC exit mass flow (HPC inlet mass flow) becomes positive after the first surge as seen in Figure 5.12. This is in agreement with observations in a single-shaft compressor rig [48].

The system recovery is initiated when both the compressors reach an approximate zero flow condition (around revolution 25.2). However, a full recovery to the pre surge condition was not obtained and the system goes through a second surge between 33.1 and 39.2. This is caused by the mismatching of the compressors throughout the recovery process where the system ends up falling back into an unstable condition before reaching the overall recovery.

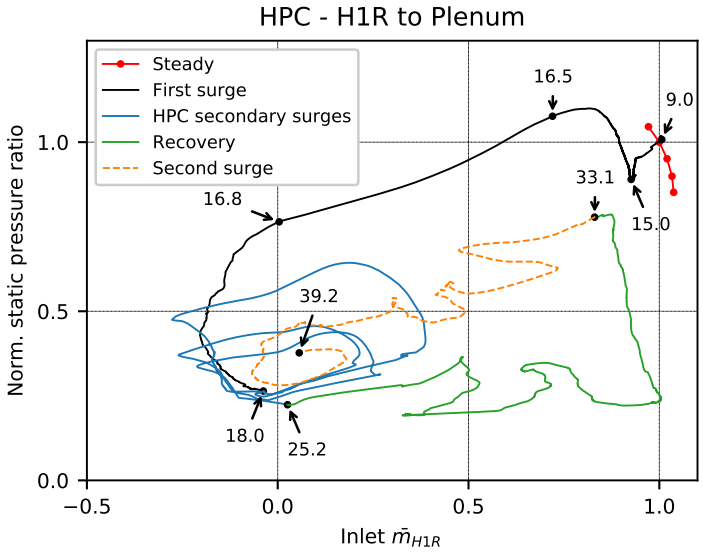


Figure 5.12: HPC characteristic and transient performance between revolution 0 and 39 - case P.

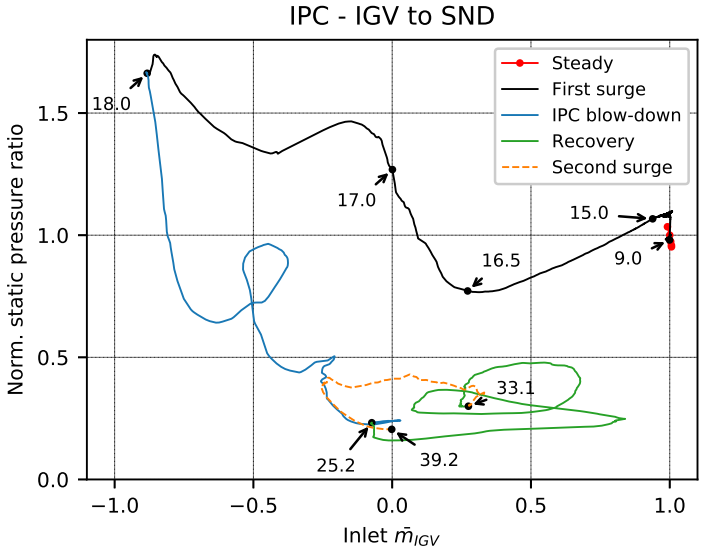


Figure 5.13: IPC characteristic and transient performance between revolution 0 and 39 - case P.

5.5.2 Surge initiation

Figure 5.14 shows axial velocity contours at I1S, I2R and I2S inlets for several revolutions during the surge onset. After the HPC deceleration at revolution 9, the stalled flow pattern remains unchanged until revolution 12.5, at which point I1S inlet shows signs of tip separation in some of its passages which indicates I1R tip stall. By revolution 15, the tip blockage region observed at I1S inlet grows and coalesces into a stall cell which extends axially along the first and second stages of the IPC. At revolution 15.5, the hub separation initially present at I2R inlet grows in the radial and axial direction and merges with the existing tip rotating stall cell. Consequently, a large scale rotating stall cell forms occupying more than half of the annulus at revolution 16.5.

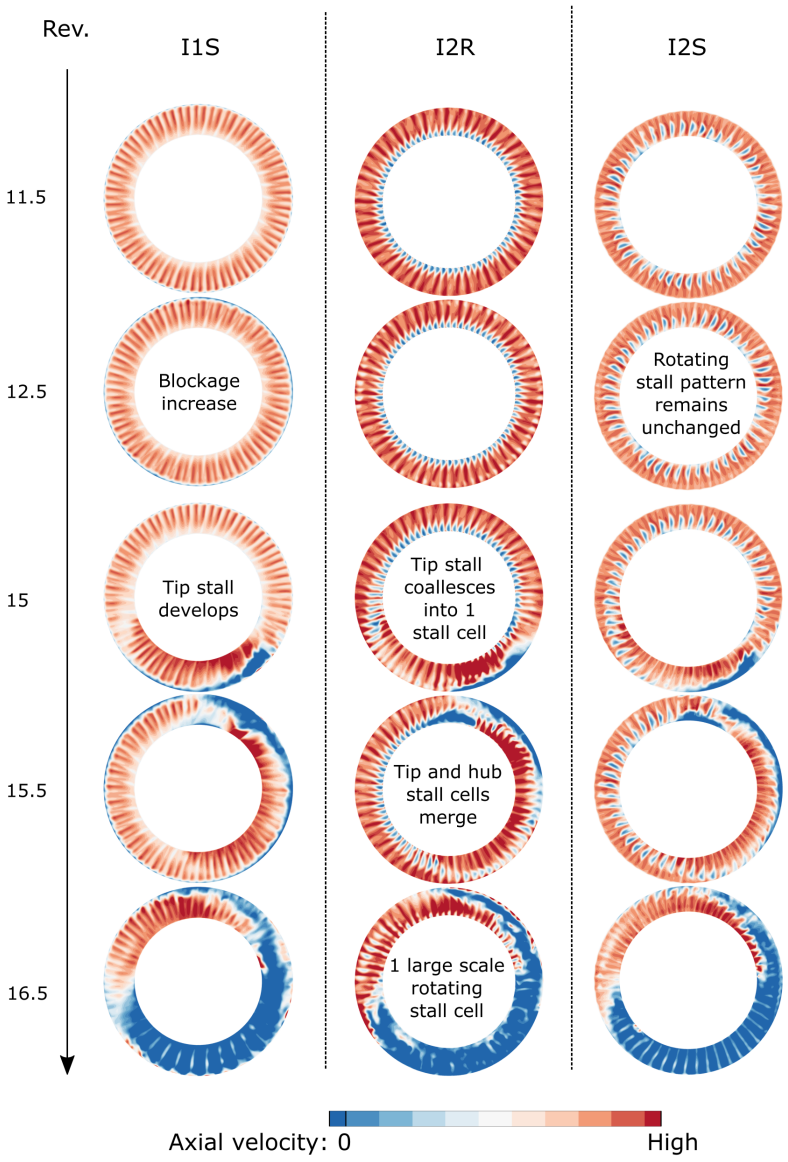


Figure 5.14: Axial velocity at I1S, I2R and I2S inlets for case P during the surge onset (revolutions 11.5 to 16.5).

Figure 5.15 presents axial velocity contours at H1S and H6S inlets for several time instants between revolution 16 and 16.75. This period relates to the surge onset in the HPC as seen in Figure 5.12. On the contrary to what is observed in the IPC, a rotating stall pattern does not develop in the HPC prior to surge. The flow reverses initially in a few passages of H1R as seen by the low velocity region present in the inlet plane of H1S at revolution 16.25. This non-rotating reverse flow region expands in axially, radially and azimuthally. By revolution 16.5, half of the annulus has a negative velocity flow field in the HPC and finally, by revolution 16.75 the HPC surges.

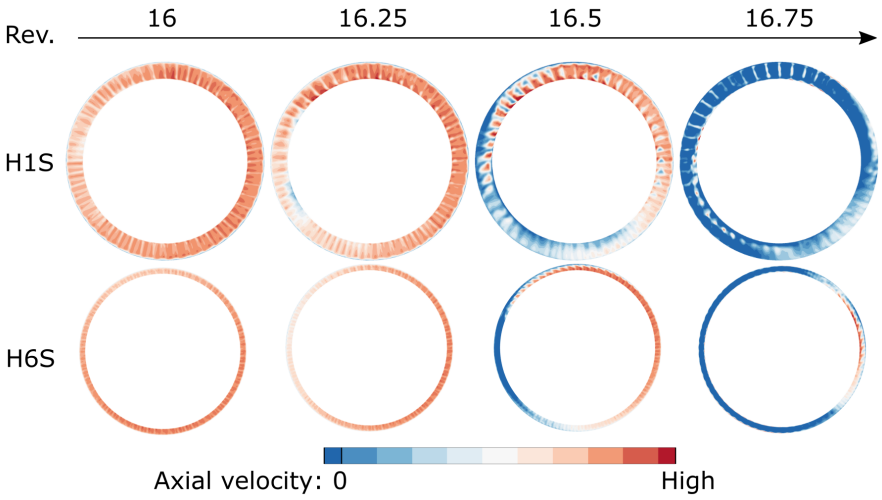


Figure 5.15: Axial velocity at H1S and H6S inlets for case P during the surge onset (revolutions 16 to 16.75).

5.5.3 Comparison with experimental data

In order to gain confidence in the CFD surge model, a comparison with experimental data is shown in Figures 5.16 and 5.17. Figure 5.16a shows the time history of cross-sectional averaged mass flow at different inlet stations in the IPC. The static pressure variation over time shown in Figures 5.16b is obtained using numerical probes at different locations[6] across the IPC (radial height of 95% span). The corresponding experimental results are shown in Figure 5.17. The experimental data was collected using casing mounted static pressure transducers (DC Kulites) located at several stations across the IPC during an engine surge test. The origin of Figure 5.17 is adjusted to match the "Surge" (marked in both Figures) initiation of the CFD results.

Pre surge behaviour

In the CFD computation for case P, the surge is initiated by decelerating the HPC to mimic the bleed valve closure at the rear stage of the IPC. The effect of the HPC speed change is evident in Figure 5.16 (identified as "HPC decel."). Around revolution 9, the

[6]The CFD data at I3S inlet was not collected.

mass flow at all of the IPC stations decreases whilst a static pressure rise is recorded at the numerical probes located in the rear stages of the IPC. From Figure 5.16b, it is observed that the numerical probe positioned at the inlet of I1S is the first to show signs of rotating stall (RS) in the form of spikes just before IPC revolution 12.66. This corresponds to the blockage increase observed previously in Figure 5.14 between revolution 12.5 and 15. These spikes grow in amplitude as the rotating stall (RS) expands axially throughout the IPC and ultimately reaches the IPC rear stages as noted by the static pressure drop defined by "RS on IPC rear" in 5.16b.

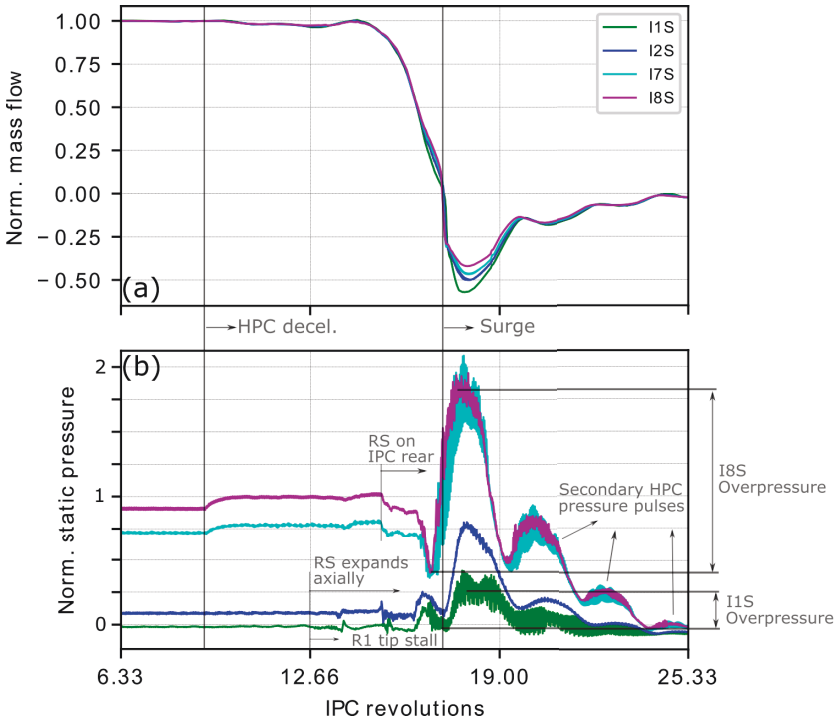


Figure 5.16: CFD time history of cross-sectional averaged mass flow (a). Static pressure of numerical probes for several stations of the IPC (b).

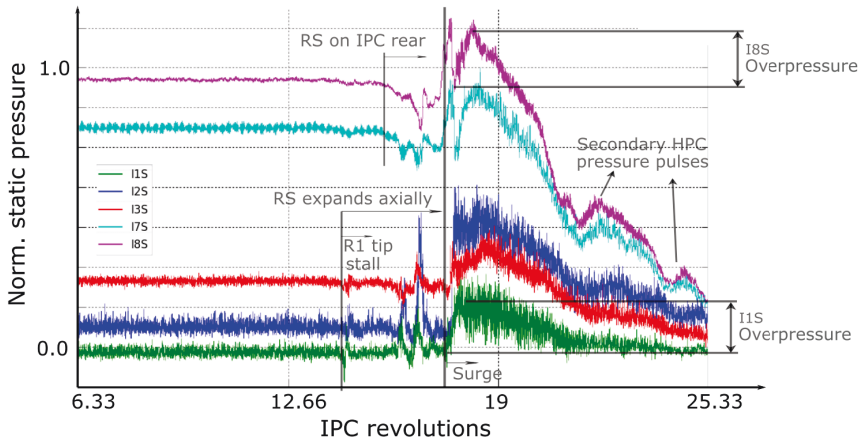


Figure 5.17: Experimental measurements of static pressure at the casing for several stations of the IPC.

For the IPC rear stages, Figure 5.17 shows that static pressure recorded after the bleed valve closure in the experimental test (which occurred before IPC revolution 6.33) is lower than the value predicted after the HPC speed reduction in the CFD. However, the IPC stalls in the same order as CFD, from stage 1 to stage 8. This shows that the pre stall behaviour of the IPC is predicted reasonably well when compared with measured data.

Maximum pressures

Figure 5.16 shows a steep rise in static pressure at all of the IPC stations when the flow reverses. Though the trend is captured correctly by the CFD, the maximum over-pressures (identified in Figure 5.16b and Figure 5.17 for I1S and I8S) are over-predicted. This raised concern regarding the quality of both the experimental and CFD results and an investigation was conducted. It should be noted that, to the best of the author's knowledge, this is the first time that both instantaneous static pressure measurements and a full-annulus CFD predictions are compared for a three-shaft compression system during surge. The following study and discussion aims to provide information to improve both the numerical and experimental methodology.

a. Uncertainty in the experimental data

The first inconsistency is found in the experimental data in Figure 5.17 when comparing the static pressure signals at I2S and I3S inlets. It is observed that after surge is initiated at around revolution 17 (flow reverses), the static pressure at I2S rises above what is recorded at I3S. This is not physically possible because I3R (located between I2S and I3S) is unable to pressurise during the reverse flow period. It was not possible to determine the reason for this phenomena.

Secondly, the experimental results show that over-pressure values recorded at the different axial stations are approximately the same (with exception of I2S). This is not in agreement to what has been previously reported by Mazzawy [1] during an experimental campaign on a ten-stage compressor with a pressure ratio of 24. Zhao et. al. [43] conducted a numerical study on an eight-stage high speed compressor with pressure ratio of 9 and found a similar trend to Mazzawy's results. In summary, the axial variation of surge over-pressure has an approximately linear variation from the location at which the surge onset occurs towards the core inlet as shown in Figure 5.18. The compressor inlet pressure is mainly influenced by the surge hammer shock and a correlation to determine it in a constant annulus area core duct can be found in [7].

The points mentioned above raise a question about the accuracy of the measured data during the reverse flow period. Surge measurements rely on pressure traducers which are initially calibrated at a specific temperature range. A "temperature compensation" correction is applied to reduce the measurement errors introduced by changes in the surrounding environment temperature. During the reverse flow period, hot gas travels backwards throughout the core and the temperature at the core stations increases significantly

[39, 47]. Consequently, the exact pressure level measured by the transducer may not be accurate and only a qualitative assessment can be performed.

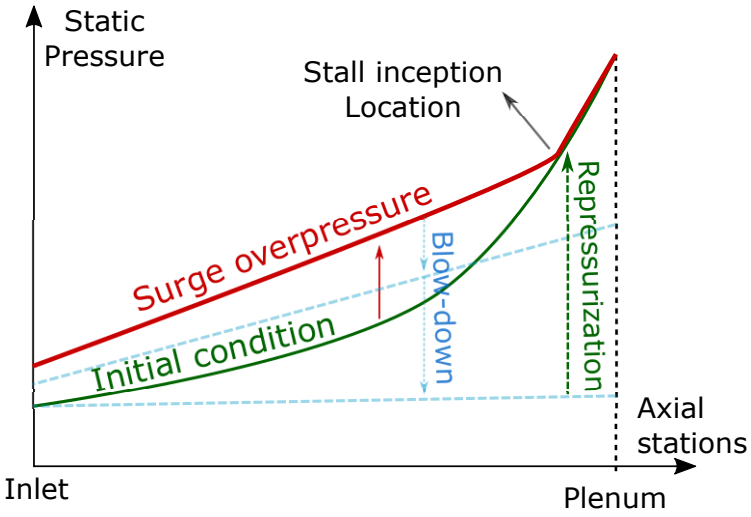


Figure 5.18: Axial variation of static pressure throughout the surge cycle.

b. Uncertainty in the CFD model - Bleed valve effect

The possible sources of inaccuracies in the CFD are examined next. Since the CFD code has been validated previously for pre and post stall behaviour in chapter 4 and in [18, 35, 48, 55], the hypothesis to find the root cause for these differences consists of revisiting the initial assumptions of the model, namely, the engine bleeding system.

The engine compression system has an emergency system which upon detecting a surge onset, opens the bleed valves in IPC stage 8 and HPC stage 3, releasing high pressure gas into the bypass duct. This emergency system is designed to reduce aerodynamic loading on the engine and consequently, the damage caused to the engine components during surge. The measurement system cannot determine the exact moment at which the bleed valves were opened during the experimental campaign and therefore, a CFD study is performed to assess qualitatively the effect of opening the bleed valves during the surge onset.

A numerical bleed port was introduced on the H3S casing wall as shown in Figure 5.19a (in a similar manner to what is shown in [62]). The static pressure at this boundary is set to a low enough value in order to ensure a choked boundary condition (similar to a choke nozzle) where an approximately constant corrected mass flow ($\dot{m}\sqrt{T_0}/P_0$) is extracted from the main gas path.

Figure 5.19b shows the time evolution of the corrected mass flow at the bleed patch and main path in the simulation without and with bleed. The subscript "B." in the legend of this figure aims to identify the simulation results when considering bleed. The bleed patch is activated at revolution 16.5 and reaches an approximately constant corrected mass flow, mimicking a choked valve. The computed corrected mass flow at inlet of H3S is similar for both calculations immediately after the bleed patch is activated. In contrast, the mass

flow at inlet of "H4R B." increases when compared with H4R. This shows that more mass is being blown out of the stages downstream of the H3S when the bleed is activated. The difference in mass flow at H4R between the two simulations is approximately the same as the mass flow extracted through the bleed slot.

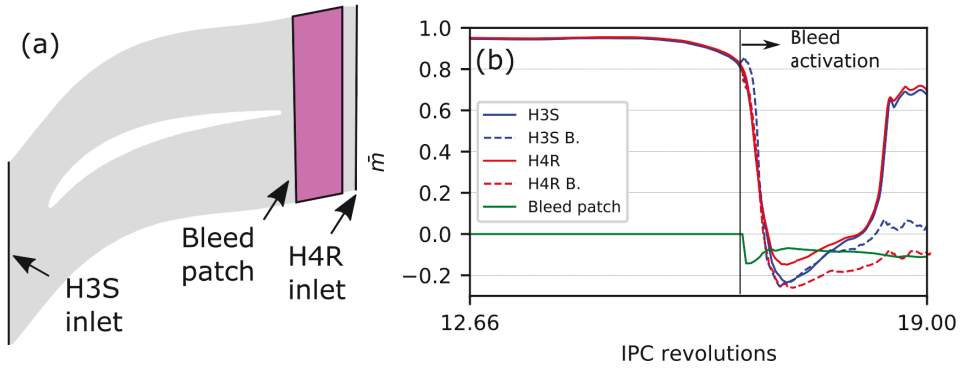


Figure 5.19: H3S bleed patch geometry (a). Time history of corrected mass flow ($\dot{m}\sqrt{T_0}/P_0$) at H3S and H4R with and without bleed patch (b).

Figure 5.20 presents a comparison of cross-sectional averaged variation of static pressures at several IPC stations during the surge event when the bleed is opened (dashed lines) and closed (solid lines). The presence of bleed reduces the pressure rise significantly during the reverse flow period at all of the IPC stations. By comparing Figures 5.17 and 5.20, it is possible to verify that the results with bleed are much closer to the experiment in terms of over-pressure magnitude. This suggests that the bleed valves were opened during the reverse flow period of the surge event in the experimental test.

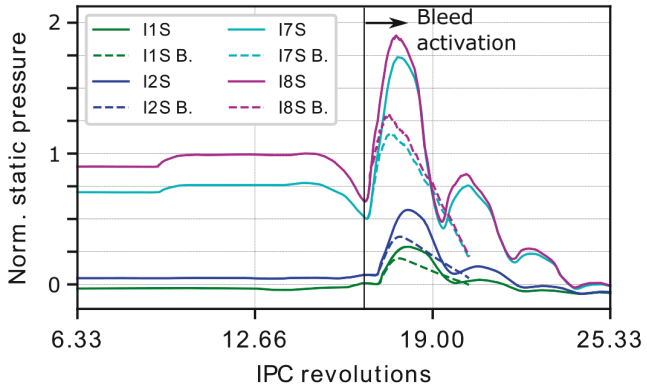


Figure 5.20: CFD time history of cross-sectional averaged static pressure with (dashed lines) and without (solid lines) bleed flow.

Figure 5.21 shows the recorded over-pressure (as a ratio between the maximum pressure increase and initial condition at each core station) and static pressure axial variation throughout the compression system. For the simulation without the bleed patch, it is visible in Figure 5.18b that the maximum recorded pressures follow the linear curve described by Mazzawy [1]. Figure 5.21a shows that when the bleed patch is activated, the

maximum over-pressures from H3R to plenum decrease to a nearly zero value. This is a consequence of the extraction of high pressure gas present downstream of the H3S station through the bleed patch during reverse flow. Figure 5.21a also shows that the maximum recorded over-pressures are much lower for the case where the bleed is activated.

The bleed patch is directly connected to the main gas path in the numerical model and, as a consequence, it is expected to have a stronger effect than what would be observed in the real geometry. The bleed system has manifolds located around the bleed off-takes which have a finite volume, as well as restrictive slots in the gas path wall to ensure the flow extraction is reasonably symmetric. For this reason, the author acknowledges that a bleed system geometry should be included in the model for realistic representation however, developing the software tools for such geometry is out of the scope of this work. Furthermore, from an engineering design perspective, the worst case scenario where the bleed valves remain closed should be considered when conducting surge load predictions.

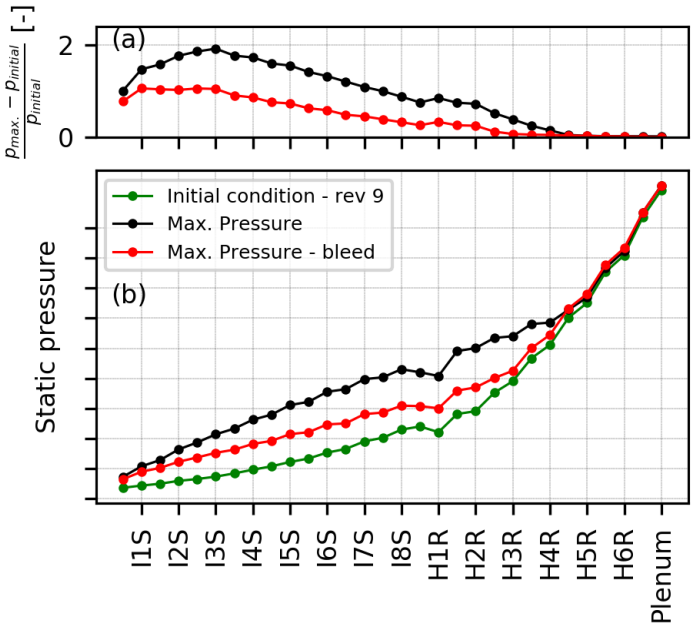


Figure 5.21: Over-pressure (a) and static pressure (b) axial variation across the compression system with and without the bleed patch.

Blow-down

Figures 5.16b and 5.17 show that, during revolutions 18 and 25, the static pressure decreases which indicates that the compression system is going through the blow-down phase of the surge cycle. A fluctuation on the pressure signal is observed during this period which is driven by the HPC secondary surges which will be studied in chapter 6. A discrepancy is encountered in the calculated HPC surge frequency between CFD and measured data, being approximately 55 Hz and 35 Hz, respectively.

The system overall blow-down period is under-predicted by the CFD. Figure 5.16b

shows that the static pressures at I1S and I8S in revolution 25.33 are nearly the same. In contrast, Figure 5.17 shows that for the experimental data, the pressure difference between these two stations is still large at revolution 25.33. This result can also be justified by the bleed system geometry which was not modelled here. The bleed system located in the core contains air in the manifolds located around the bleed off-takes which may contribute towards a larger surge period.

Despite the various discrepancies discussed above, the model is capable of capturing the main flow features and trends of a surge event in a three-shaft engine compression system.

5.6 Concluding remarks

During engine operation, the IPC and HPC operating conditions are controlled by the turbines however, for modelling purposes, a core compressor matching process needs to be employed in order to achieve a realistic pre surge condition. This chapter proposes a methodology for surge modelling of a three-shaft engine compression system in a computationally efficient manner by performing the fewest number of iterations as possible. The methodology consists in dividing the system compressors into subdomains and performing an iterative matching process to reach the target operating point in an engine deck. After, a perturbation is introduced in the flow to drive one of the compressors towards the stability line resulting in a full system surge.

To the best of the author's knowledge, this is the first time that the pre and post stall behaviour of a mid power surge event in a three-shaft engine is studied numerically and validated with experimental data. For the condition studied, the compressor stall appears first in the front stages of the IPC and expands axially towards the rear stages causing a pressure decrease in the front of the HPC. Consequently, the HPC surges and a steep rise in pressure is observed across all IPC stations.

The model presented in this work resulted in an over-prediction of the maximum over-pressures relative to the experimental results. A discussion is presented where these differences were attributed to experimental uncertainties and the assumption of a bleedless system during the surge event. Furthermore, it has been demonstrated numerically that the use of a compression system with bleed off-takes can significantly reduce the maximum over-pressures recorded during a surge event. The effects of bleeds and secondary air-system need to be considered by component designers when accounting for robustness to surge loads.

6 Aerodynamic loading considerations in high power surge

6.1 Problem description and overview

Compressor surge imposes a limit on aero-engine operability and can compromise integrity because of significant aerodynamic loads imparted on the engine components. The majority of publications related to surge structural loadings distinguishes two critical moments of structural solicitation during a surge cycle: Firstly, the initial few instants where a shock wave propagates upstream through the compression system [1, 34]; secondly, the reverse flow phase where previous studies [35–37] showed that aeroelastic phenomena can occur and lead to blade failure. This chapter aims to study the system behaviour of a compression system during surge and offers an explanation of the main physical phenomena which contributes to the maximum recorded over-pressure during a surge event.

The chapter focus on high power surge cases. Surges at high power condition will result in the highest loads on the engine components and therefore, they are of greater importance for safety. The numerical model presented in chapter 5 (see Figure 5.1) is used. However, this chapter considers larger tip clearances to facilitate the surge initiation at design condition. This geometry is representative of a deteriorated engine.

As shown in the previous chapter, surge simulations are performed in two steps. First, the steady state solution of a matched compression system is obtained. After, the surge is initiated by introduction of a disturbance in the flow field. In this chapter, an analysis of the effect of two types of surge initiation on the maximum loading recorded during surge is presented:

- Case A2 - The engine is operating at a high power condition close to design and the surge event is initiated via abrupt throttling of the core nozzle. This is a close approximation to the "fuel-spike" situation where a very short duration over-fuelling causes the HPC working line to transiently rise which can provoke a surge originating in the HPC.

- Case B - This case considers a high power operating condition similar to case A2. The surge initial disturbance is introduced by opening the inlet guide vane (IGV) and closing stator 1 (I1S) to mismatch the IPC. Instead of rising the compressors operating condition to the surge line as case A2, the objective is to move the IPC surge line towards a lower pressure ratio condition so that the surge is initiated.

To evaluate the effect of the tip clearances on the surge dynamics, case A1 (introduced in the previous chapter) is compared with case A2. The tip clearances of case A2 are larger than A1. The summary of all cases studied is presented in Table 6.1.

Table 6.1: Case studies for high power surge analysis.

Case	Initial Cond.	Tip clearances	Trigger	Surge onset location
A1	High power	Nominal	HPC throttle	HPC
A2	High power	Open	HPC throttle	HPC
B	High power	Open	VSVs turning	IPC

6.2 Cases A1 and A2 - HPC surge

6.2.1 Overall transient behaviour

In case A2, the compression system is operating at high power condition and surge is initiated via sudden throttling of core nozzle to mimic a "fuel-spike". Figures 6.1 and 6.2 show the surge transient overall performance of the HPC and IPC, respectively, in terms of static pressure ratio as a function of corrected inlet mass flow ($\dot{m}\sqrt{T_0}/P_0$), referenced as "$\bar{m}$". HPC shaft revolutions are used to indicate elapsed time from revolution zero, which are labelled on these figures to indicate how the operating condition of each compressor varies with time.

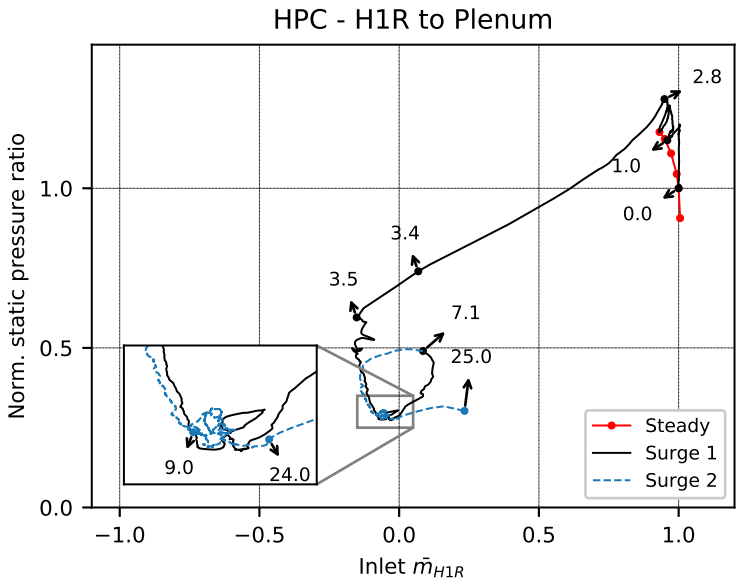


Figure 6.1: HPC characteristic and transient performance between revolution 0 and 25 - case A2.

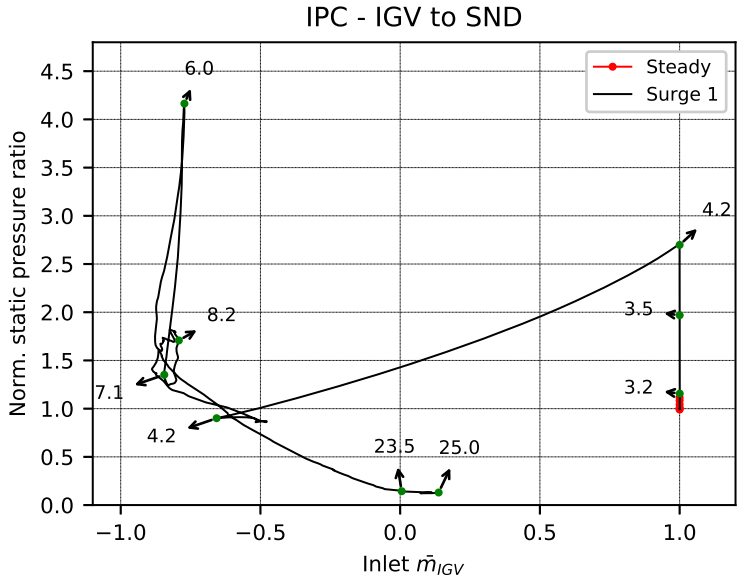


Figure 6.2: IPC characteristic and transient performance between revolution 0 and 25 - case A2.

Figure 6.1 shows that upon closure of the core nozzle, the operating condition of the HPC rises along the steady state characteristic. At revolution 2.8, the HPC stability boundary is reached, which results in a rapid reduction in the mass flow and pressure ratio. The HPC inlet flow is reversed by revolution 3.5. Beyond this point, the flow at the HPC inlet oscillates between reverse and forward flow until a temporary convergence is observed between revolution 9 and 24 where the flow through the compressor is nearly zero (zoomed box in Figure 6.1).

The corresponding behaviour of the IPC in Figure 6.2 shows that the IPC remains on its pre surge (steady) characteristic until revolution 3.2 at which point the pressure ratio rises rapidly, reaching over twice the pre surge level by revolution 4.2. Revolution 3.5 corresponds to the point at which the HPC inlet flow has already dropped below zero (see Figure 6.1). Around revolution 4.2, the IPC pressure ratio falls with the inlet mass flow reversing almost instantaneously. The flow through the IPC is reversed for nearly 20 shaft revolutions until the recovery starts by revolution 23.5.

Further insight into the initial phases of the surge can be gained from Figure 6.3, which shows the evolution of cross-sectional averaged[1] mass flow and static pressure as a function of HPC shaft revolutions at the inlet of several axial locations of the HPC and I7S. The sudden core nozzle closure produces a compression wave (CW) which propagates upstream through the HPC (indicated in Figure 6.3b as "CW_1"). This perturbation decelerates the flow and causes a temporary reduction in mass flow and an increase in static pressure on all stages.

After this initial CW_1, Figure 6.3 shows that the HPC mass flow and pressure initially

[1]Circumferentially and radially area averaged.

appear to stabilise across all stations over the period indicated as Δt_1. This period is followed by a second compression wave, labelled as "CW_2" in Figure 6.3b. This second compression wave propagates upstream and causes, albeit to a lesser extent, a further mass flow drop and pressure rise across all HPC stations. The second compression wave is generated by successive reflections of the first compression wave (CW_1) on the plenum inlet and outlet, i.e., a component of the first compression wave bounces back and forth inside the plenum. The period Δt_1 marked in Figure 6.3b is the travel time in a round trip between the plenum inlet and outlet.

This process is repeated a third time ("CW_3" in Figure 6.3b), which leads to a maximum plenum pressure reached at revolution 2.8. After, the HPC can no longer sustain the pressure ratio and hence, surges. The surge inception occurs over the period Δt_2 and it is discussed in the next section. The initiation of surge generates a much stronger compression wave in the HPC front stages, labelled "surge shock wave" in Figure 6.3b.

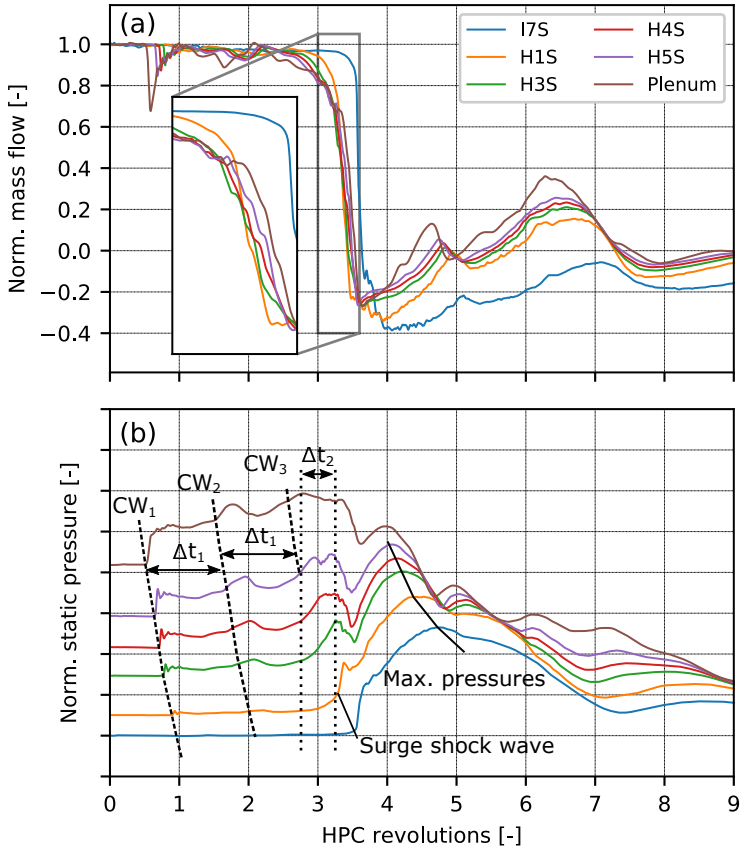


Figure 6.3: Time history of cross-sectional averaged mass flow (a) and static pressure (b) at several HPC stations and I7S between revolution 0 and 9 - case A2.

Figure 6.4 shows the time history of cross-sectional averaged mass flow and static pressure plotted against HPC shaft revolutions at the inlet of several axial locations of the IPC and H1S. Figure 6.4b shows that at approximately revolution 3.5, the shock wave arrives at SND causing a sharp rise in static pressure and decrease in mass flow. Since at this time instant the static pressure and mass flow at I1S remains unchanged, the instantaneous IPC pressure ratio inevitably rises to a level significantly beyond the steady-state level (see Figure 6.2). The upstream propagating shock wave causes an almost instantaneous flow reversal in all of the IPC stations as indicated in Figure 6.4a.

Figures 6.3 and 6.4 show that the maximum pressures occur after the surge shock wave passes. This indicates that the surge shock wave is not the root cause for the maximum aerodynamic loads (maximum over-pressures) at either the HPC or IPC stations. As shown in Figure 6.2, the IPC pressure ratio rises over twice the pre surge level by revolution 4.2 which is about 0.6 revolutions after the shock wave arrival at SND (Figure 6.4b). This phenomena will be discussed in a later section of this chapter.

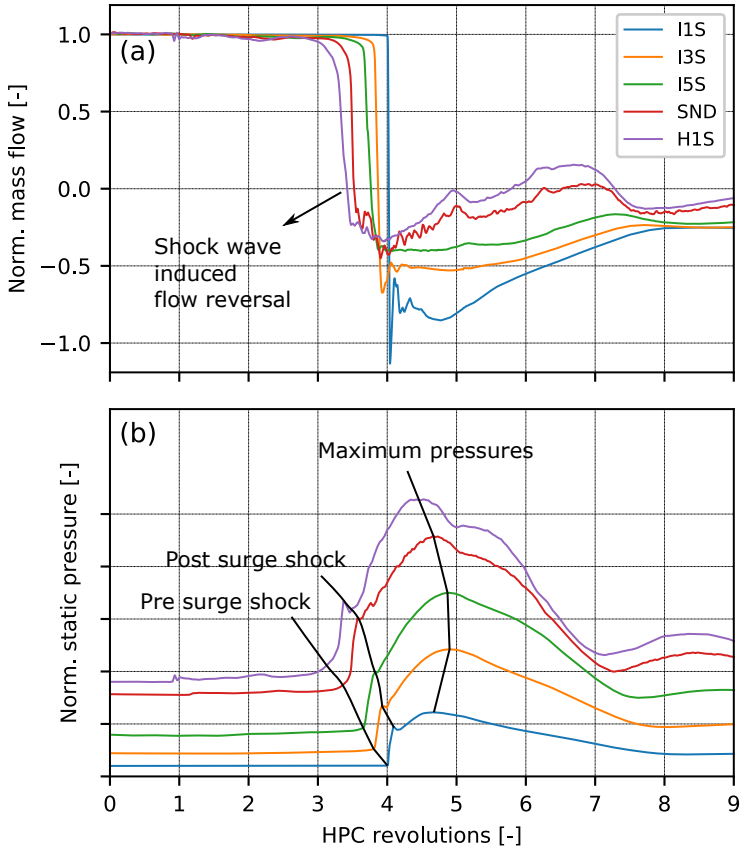


Figure 6.4: Time history of cross-sectional averaged mass flow (a) and static pressure (b) at several IPC stations and H1S between revolution 0 and 9 - case A2.

6.2.2 Surge initiation

Figure 6.3a showed that the initial mass flow decrease occurs at the inlet of plenum, H5S and H4S which indicates that surge was initiated in the rear stages of the compression system. Figure 6.5 presents the development of axial velocity contours in the rear stages of the HPC (H4S, H5S and H6S inlets) at several time instants over the period marked as Δt_2 in Figure 6.3b. Examination of the flow field indicates that the surge inception occurred in an axisymmetric fashion and therefore, only a slice of the annulus is presented here.

At around revolution 2.8, the tip of H6R blades stall and a low axial velocity region is formed at the casing region at H6S inlet. This correspond to the time instant when the static pressure at the plenum inlet starts to drop in Figure 6.3b. Figure 6.5 shows that stage 5 (revolution 3.0) and stage 4 (revolution 3.2) also stall in a time ordered manner and at revolution 3.2, half of the annulus is blocked. By revolution 3.44, the HPC has surged and the flow is fully reversed without going through a rotating stall phase.

Figure 6.3b shows that between revolution 3.0 and 3.3, the static pressure at H4S is approximately constant whilst it increases at H3S prior to the flow reversal. By definition, the passing of a CW through a station must inevitably rise the static pressure and thus, this behaviour proves that the surge induced CW is generated near H4S.

Figure 6.3a shows that the front stations of the HPC (H1S) are the first to show full flow reversal. By analysing the corresponding pressure signal, one can confirm that the flow reversal occurs around revolution 3.4 which corresponds to the surge CW passing through that station. This result shows that the surge CW originates as a consequence of the stall process in the rear stages of the HPC and propagates along the core towards the inlet causing a full flow reversal at the front stations first. Eventually, the flow is also reversed in the rear stages and the blow-down period is initiated.

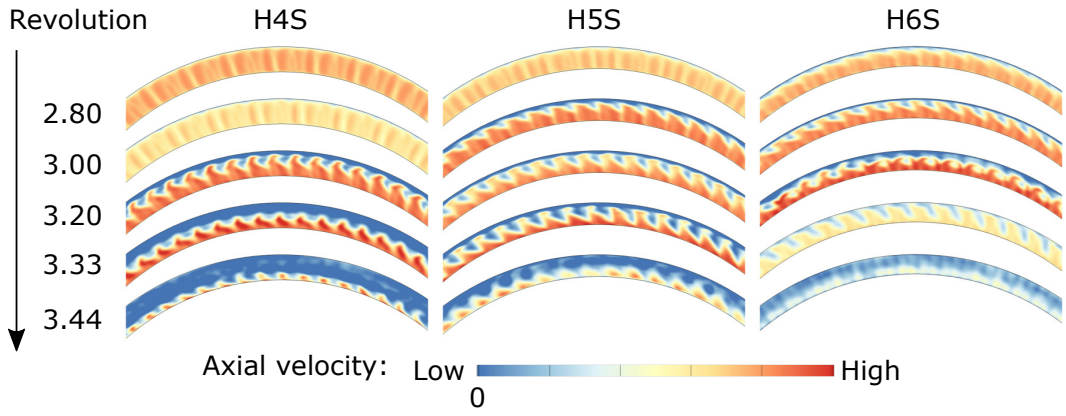


Figure 6.5: Axial velocity contours at the inlet of several HPC stations - case A2.

6.2.3 Surge induced compression wave

Figure 6.6 illustrates the core meridional view of circumferential averaged axial Mach number at different time instants for case A2. At revolution 3.34, the HPC stalls and a CW is generated. The passing of this compression wave at each of the core stations results in instantaneous flow reversal.

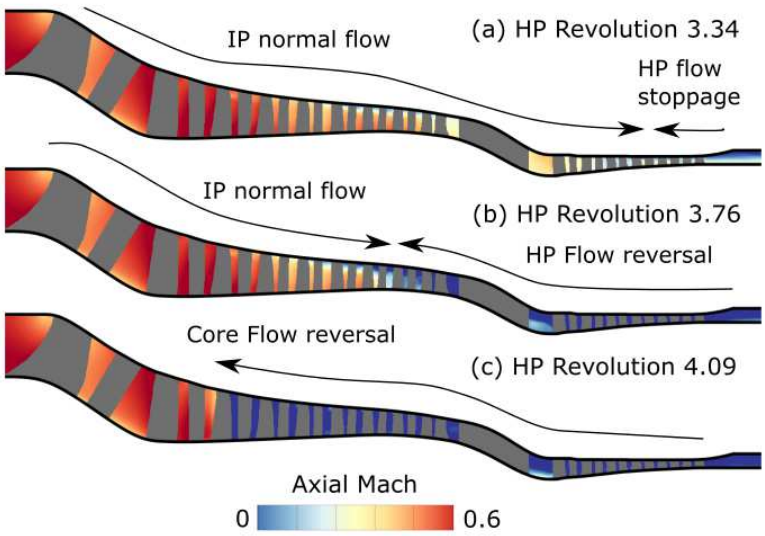


Figure 6.6: Circumferential averaged axial Mach number at revolutions 3.34, 3.76 and 4.09 - case A2.

Figures 6.3 and 6.4 show that the mass flow overshoot induced by the passing of the surge shock wave becomes larger as it travels towards the front of the compression system. This suggests that the surge shock wave behaviour changes as it propagates through the compressor. In this work, the shock wave strength is defined as the pressure ratio in each of the stations after and prior the wave passes through ($p_{post\ surge}/p_{pre\ surge}$). These points are sketched in Figure 6.4b as "Pre surge shock" and "Post surge shock". The solid line in 6.7a presents the strength of this shock wave at various axial stations calculated from the unsteady CFD results (labelled as "3D URANS"). Stations downstream of H1R were not included since they did not show a discontinuity in the pressure signal and thus, it was not evident that a shock wave was present. The shock wave strength increases as it propagates towards the core inlet as seen in Figure 6.7a.

High power surges are characterized by the presence of a well defined CW which ultimately coalesces into a shock wave as it propagates upstream. Widely used low fidelity models [1, 7, 34] for surge load predictions consider that a normal shock wave is instantaneously formed at the location of the surge inception and propagates through a bladeless duct. To validate the assumption of normal shock theory for this type of problems, it is

hypothesised that the pressure ratio across the shock wave can be modelled using:

$$\frac{p_{post}}{p_{pre}} = \frac{2\gamma Ma^2_{shock,\ rel.} - (\gamma - 1)}{\gamma + 1} \tag{6.1}$$

where γ is the real gas constant. To compute $Ma_{shock,\ rel.}$, it is necessary to obtain the absolute axial shock wave speed (Ma_{shock}) and pre surge flow axial Mach number (Ma_{pre}). Ma_{shock}, presented in Figure 6.7b, is computed considering the distance ds in Figure 6.8 and the time interval that the wave takes to travel this distance. The flow condition prior to the arrival of the shock wave is used to calculate Ma_{pre} which is shown in Figure 6.7b. Considering the shock frame of reference, $Ma_{shock,\ rel.}$ is obtained and the shock strength is computed with the CFD results in Figure 6.7a (labelled $Eq.1$). The 1D normal shock wave equation shows a similar trend to the 3D CFD results and thus, it can be considered a good approximation for modelling this type of problems.

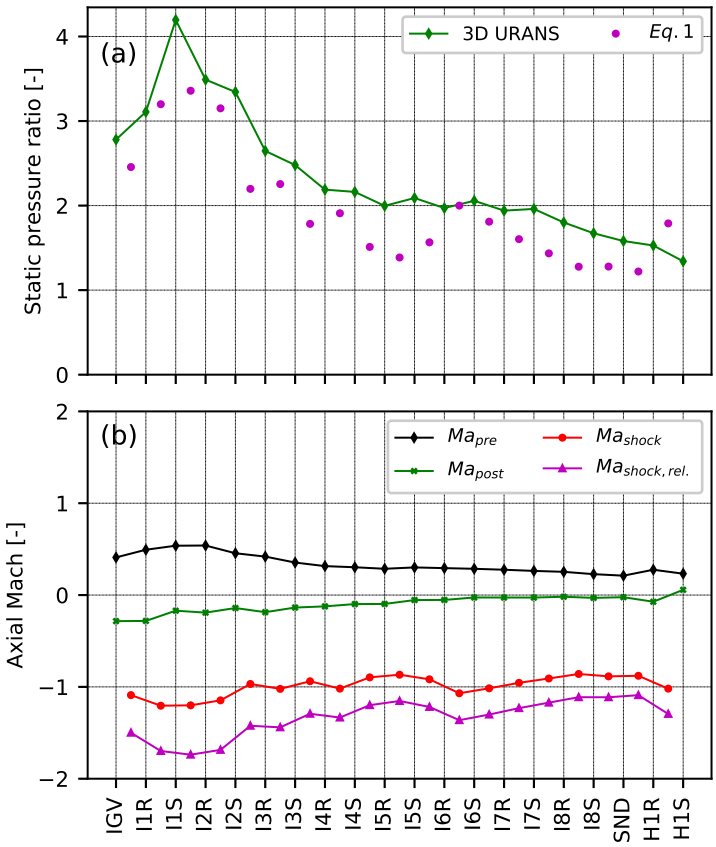


Figure 6.7: Shock wave strength (a) and axial Mach number (b) at the IPC stations and HPC front stage - case A2.

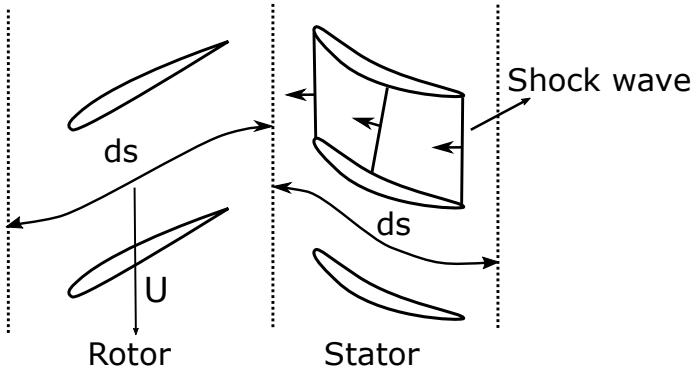


Figure 6.8: Normal shock wave modelling.

6.2.4 Effect of tip clearances on surge

This section studies the impact of tip clearances on surge dynamics. The case studied until this point (case A2) considered a tip clearance configuration representative of a deteriorated engine. For comparison, a surge simulation of case A1 (introduced in the previous chapter) is performed. Case A1 considers smaller tip clearances where the major differences were on IPC stage 5, 6 and 7 as shown in Table 6.2.

Table 6.2: Tip clearance sizes normalized by blade span [%].

Case	R5	R6	R7
A1	1.1	1.2	1.2
A2	1.2	1.8	1.6

Figures 6.9 and 6.10 show a comparison of the transient behaviour (static pressure ratio as function of corrected mass flow) between A1 and A2 for the HPC and IPC, respectively. The results show that the compressors behaviour is very similar however, the HPC operation crosses the stability limit at an higher pressure ratio in case A1.

To gain further insight into these phenomena, the steady-state performance of the HPC and IPC as well as the block performance of the IPC (split between front and rear stages) are shown in Figure 6.11. The initial conditions for cases A1 and A2 are indicated as "P1*" and "P1", respectively. Figures 6.11a and 6.11b show that the starting conditions are very similar for the two cases. However, the HPC stall point is reached at a smaller pressure ratio for case A2 relative to case A1 (see Figure 6.11a). This is caused by a different compressor matching between the IPC and HPC as the system is throttled to the stability limit. Figure 6.12 shows that as the mass flow in the HPC is reduced, the aerodynamic speed decreases at a higher rate for case A2 relative to A1 which explains why the HPC reaches higher pressure ratios in case A1 (see Figure 6.9).

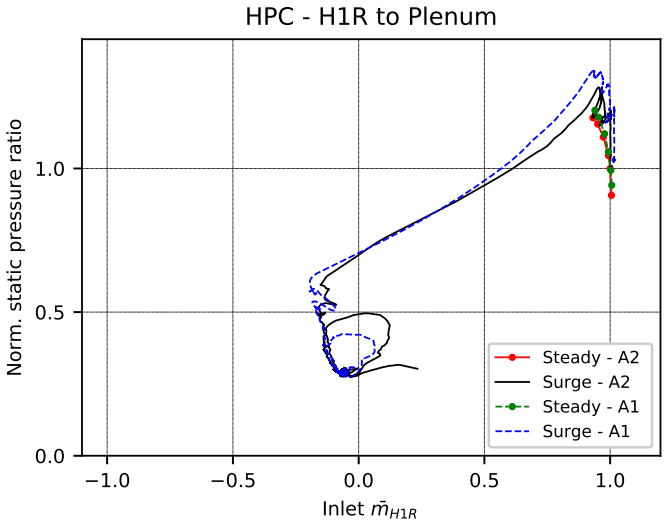


Figure 6.9: HPC characteristic and transient performance - cases A1 and A2.

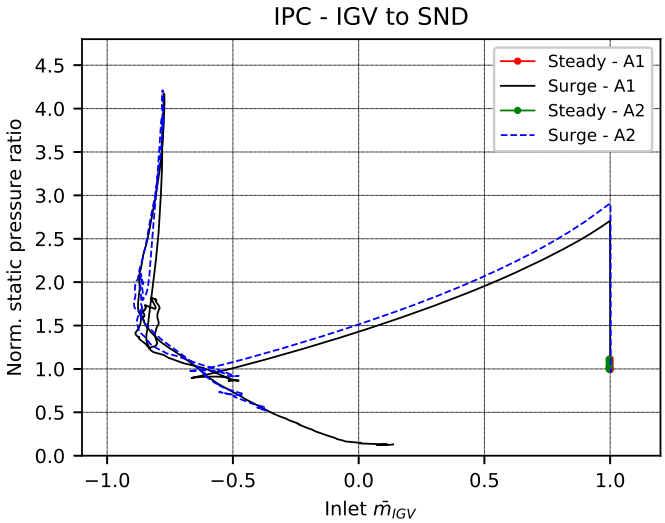


Figure 6.10: IPC characteristic and transient performance - cases A1 and A2.

Figure 6.11b shows that the IPC is operating at a very similar condition as the core nozzle is throttled however, the pressure ratio split between front and rear blocks differs significantly between cases A1 and A2. Figure 6.11d shows that for the same HPC inlet mass flow, the static pressure ratio across the IPC rear stages is lower for case A2 relative to case A1. This is caused by an increase in blockage and loss levels due to the larger clearances. It is also observed that the front stages compensate for the pressure loss in the rear stages as shown in Figure 6.11c for case A2.

In conclusion, the changes in the IPC tip clearances only affect the pre surge operating condition. This leads to a higher pressure ratio at surge inception when the tip clearances are tighter. The compressor transient behaviour during the surge event follows a similar trend independently of the tip clearance configuration.

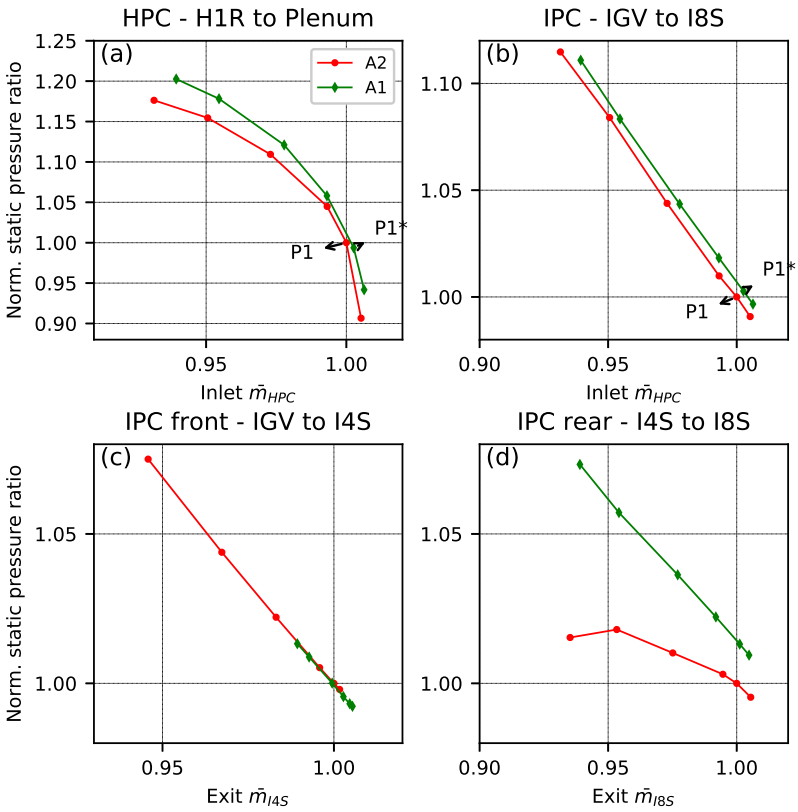


Figure 6.11: HPC (a) and IPC (b) performance. Front (c) and rear (d) IPC block performance. - cases A1 and A2.

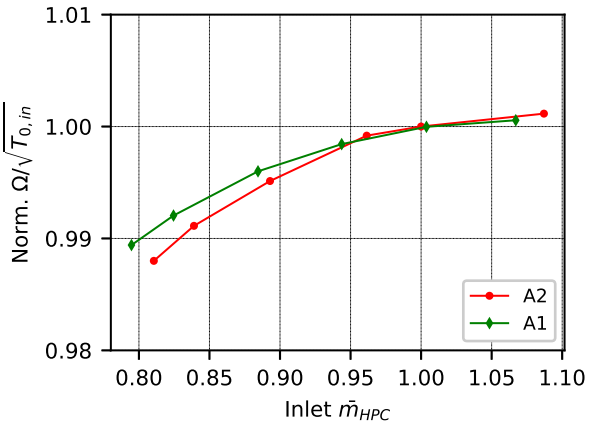


Figure 6.12: Effect of the IPC tip clearances configuration on the HPC aerodynamic speed - cases A1 and A2.

6.3 Case B - IPC surge

6.3.1 Overall transient behaviour

In case B, the compression system is operating at high power condition and surge is initiated via malschedule of the IPC VSVs. By opening the IGV and closing the I1S, the IPC front stage can be overloaded to the extent that it stalls and drives the compression system to surge. It is demonstrated that the change in VSVs setting does not cause an immediate stall of the IPC front stage however, due to the deliberate compressor mismatching, the IPC rear and mid stages stall which ultimately results in overloading of the IPC front stage. Figures 6.13 and 6.14 show the time history of the HPC and IPC operation, respectively, with selected operating points labelled with the elapsed number of HPC revolutions. The time instant at which the IGV and I1S were adjusted[2] is referred herein as revolution zero.

Figure 6.15 shows the cross-sectional averaged mass flow and static pressure against HPC shaft revolution at various axial stations of the IPC and H1S. From revolution 20, the static pressure decreases for stations downstream of I3S, which indicates that the front stages of the IPC stalled. This process corresponds to the mass flow decrease in Figure 6.14 between revolution 20-23. During this period, the HPC inlet pressure (indicated in Figure 6.15 by H1S) also drops. Since the plenum pressure stays constant until this point, the falling inlet pressure implies that the HPC pressure ratio must inevitably rise as can be seen in the transient operation in Figure 6.13. By revolution 23, the HPC is operating at a significantly higher pressure ratio than it can tolerate and promptly stalls, originating a shock wave which propagates upstream across the HPC front stages and IPC. The arrival of the HPC shock wave at H1S inlet is marked in Figure 6.15a.

After revolution 23, the HPC pressure ratio falls rapidly and its inlet mass flow becomes negative as shown in Figure 6.13. Thereafter, multiple cycles of HPC mass flow oscillations between reverse and forward flow are observed. During these cycles, Figures 6.14 and 6.15b show that the IPC remains in reverse flow and several pressures pulses are visible at revolutions 28.3, 31.5 and 35.

[2]The VSVs are turned via morphing of the mesh to simulate solid body rotation around their spindle axes.

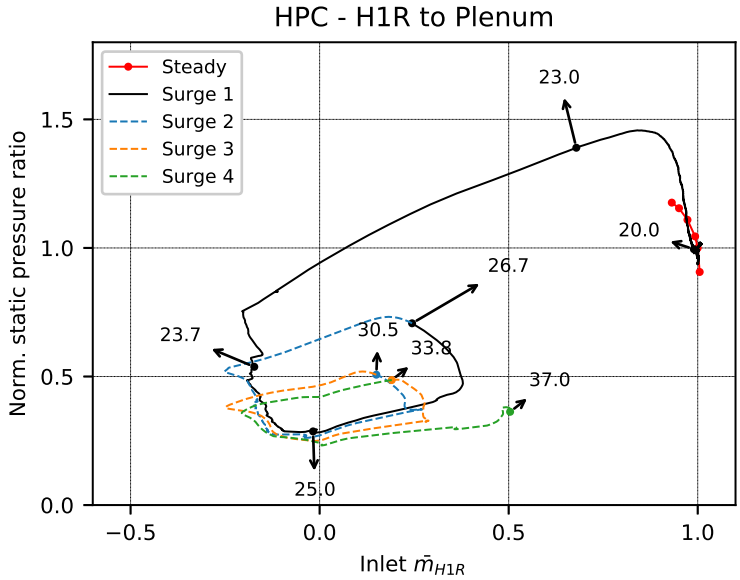


Figure 6.13: HPC characteristic and transient performance between revolution 0 and 37 - case B.

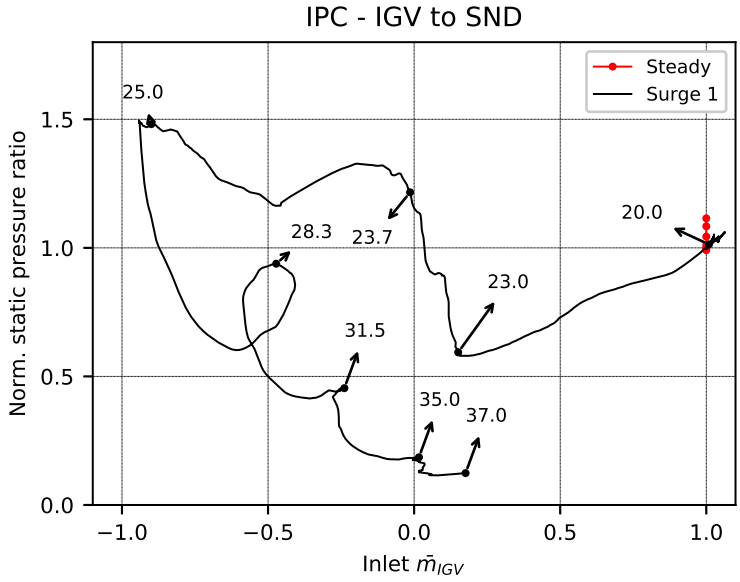


Figure 6.14: IPC characteristic and transient performance between revolution 0 and 37 - case B.

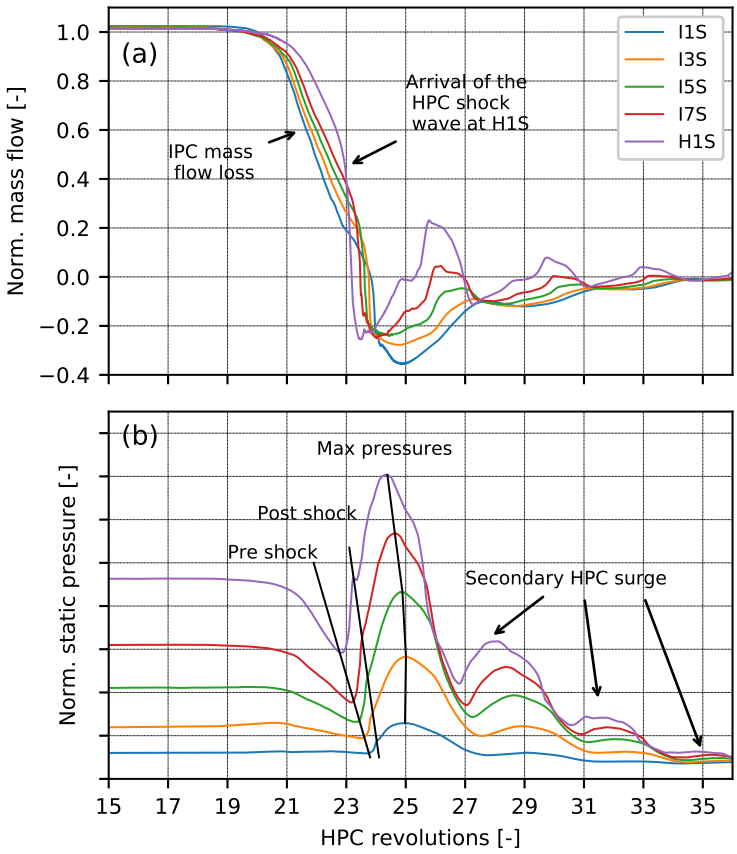


Figure 6.15: Time history of cross-sectional averaged mass flow (a) and static pressure (b) at several IPC stations and H1S between revolution 15 and 36 - case B.

6.3.2 Surge initiation

Figure 6.16 shows the IPC overall and block steady characteristics as well as the transient performance between revolutions 0 and 20.5. The points marked in these plots indicate the elapsed HPC revolutions. Figure 6.16a shows that the IPC overall operation moves to a higher mass flow and pressure ratio as a result of VSVs angles change. The IPC overall operation remains approximately constant between revolutions 2 and 18.5. After, the IPC mass flow and pressure ratio start dropping.

The IPC rear stages operation deviates from the steady characteristic and settles on a lower pressure ratio point between revolution 11 and 18.5 as shown in Figure 6.16d. Figure 6.16c shows that the mid block pressure ratio and mass flow decrease during this period. This suggests that stall occurs first in the rear and subsequently in the mid stages. From revolution 11, Figure 6.16b shows that the IPC front stages pressure ratio rises to compensate for the pressure ratio drop in the mid and rear stages. Consequently, the front stages stall between revolution 18.5 and 20.5.

Figure 6.17 shows the percentage of annulus area with negative mass flow at the inlet of several stations of the IPC during the surge event. The results show that from revolution 4.9, the reverse flow area at I7S inlet increases to around 2% and it stays approximately constant until revolution 20. The blockage region in the rear stages expands axially to the mid stages around revolution 10 as seen by the increase in annulus area with negative flow at I5S inlet. The blockage increase in the mid and rear stages loads the front stages until stall occurs, where the reverse flow area increases at a much higher rate as shown between revolution 20 and 22 at I1S inlet.

The events described above are illustrated in Figure 6.18 which shows the axial velocity across the annulus at I1S, I5S and I7S inlets. At revolution 4.9, I7S shows signs of stall at the casing region. Between revolution 11 and 18.5, the stalled region is also observed at I5S which indicates that it has grown axially. Ultimately, I1R stalls originating a single stall cell at revolution 20.5. Figure 6.15a shows that, from revolution 21 onwards, the mass flow progressively decreases in an ordered manner from I1S to H1S, which indicates that the front stage stall caused the IPC to surge.

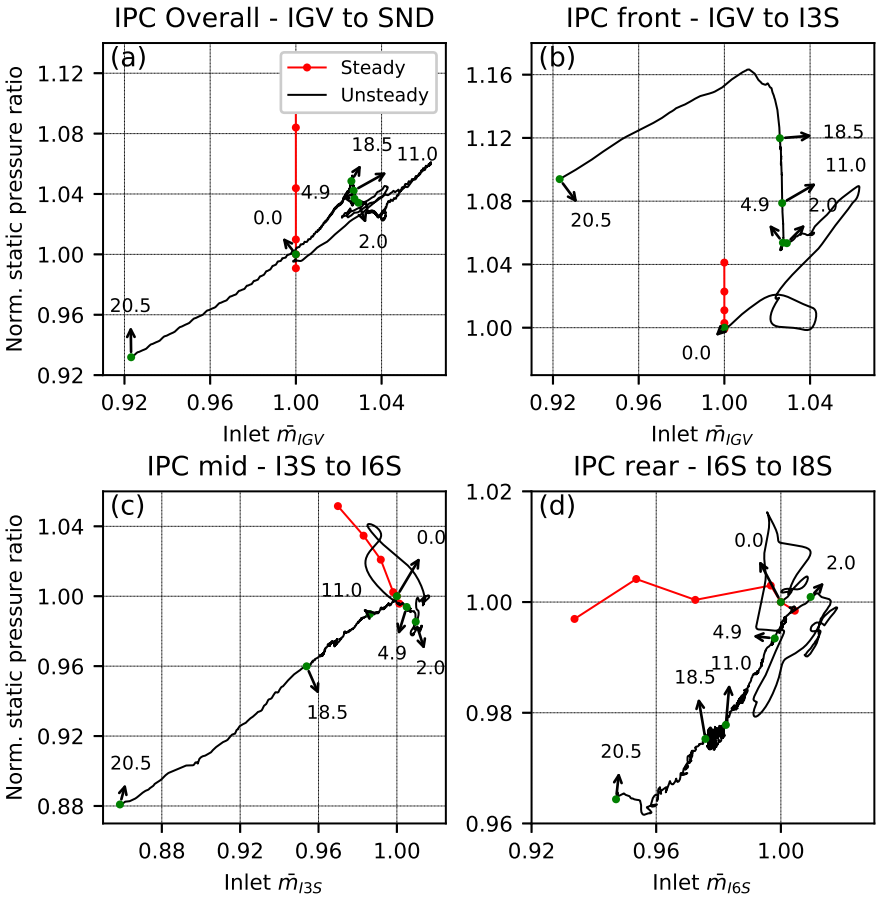


Figure 6.16: IPC overall and block performance between revolution 0 and 20.5 - case B.

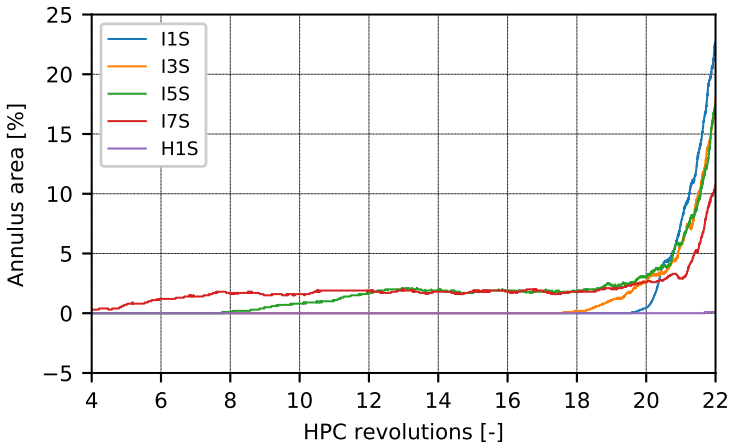


Figure 6.17: Annulus area with negative mass flow at the inlet of several IPC stations and H1S - case B.

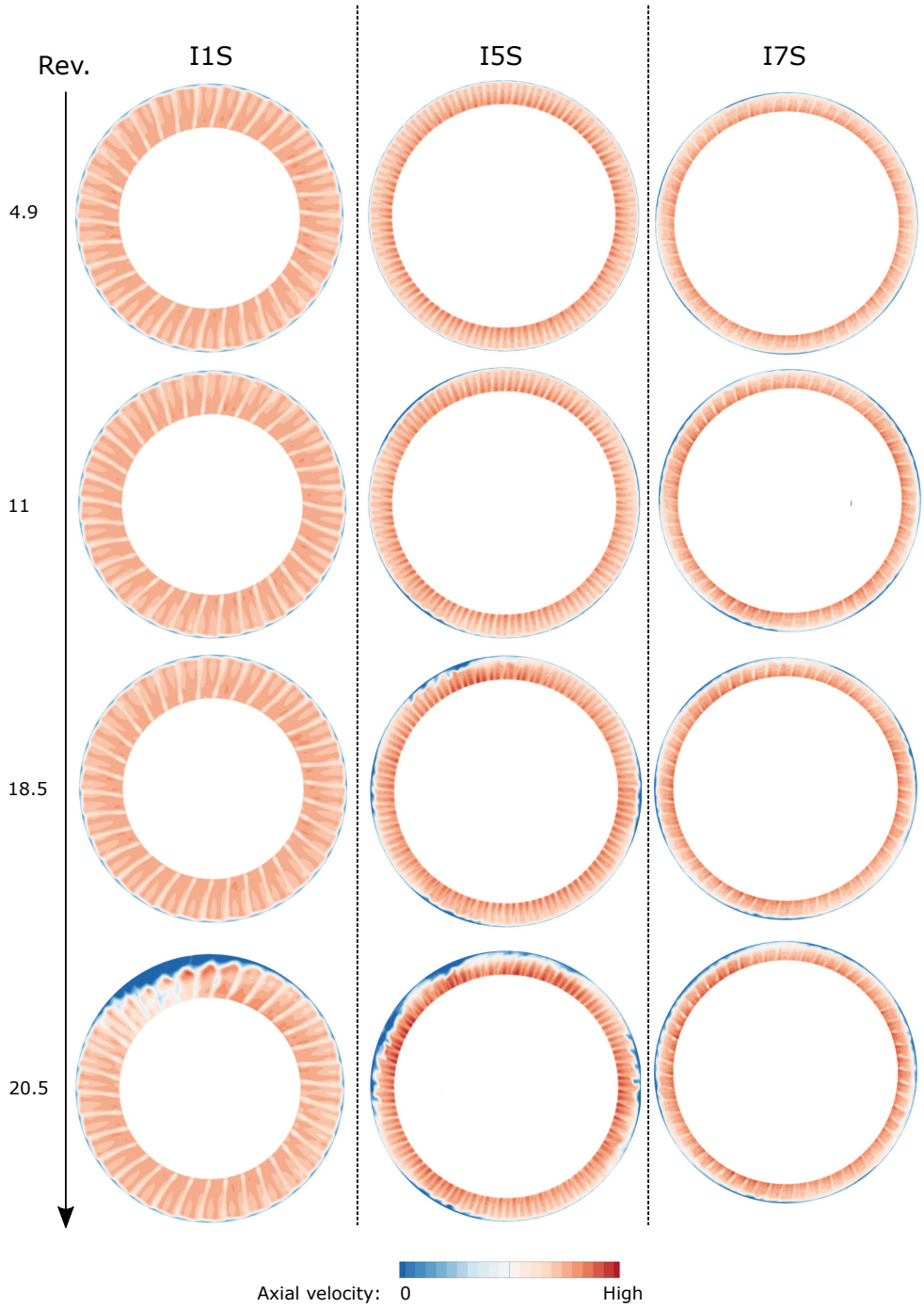


Figure 6.18: Axial velocity contours during the pre surge development at I1S, I5S and I7S inlets - case B.

To visualize the mechanism of surge onset across the whole system, the circumferential variation of axial Mach number at 50% span between HPC revolutions 16 and 27 at I1S, I7S, H1S, H6S inlets is shown in Figure 6.19. Around revolution 19, the I1S inlet shows a short scale disturbance that quickly expands circumferentially and axially between revolution 20 and 23 as observed in Figures 6.19a and Figure 6.19b. By revolution 23, the stalled region occupies about 70% of the annulus at I1S inlet and 50% at I7S inlet.

After the IPC stall, the HPC inlet pressure decreases rapidly and the H6R stalls around revolution 23. This originates a shock wave which propagates towards the front of the system promptly reversing the flow at the stations located upstream as seen in Figure 6.19. Similarly to the surge inception in case A2, the surge initiation in the HPC occurs in a nearly axisymmetric fashion (see Figures 6.19c and 6.19d). Figure 6.19 also shows that, as the shock wave propagates upstream, existing non-axisymmetric flow features vanish and a complete flow reversal is observed at all stations.

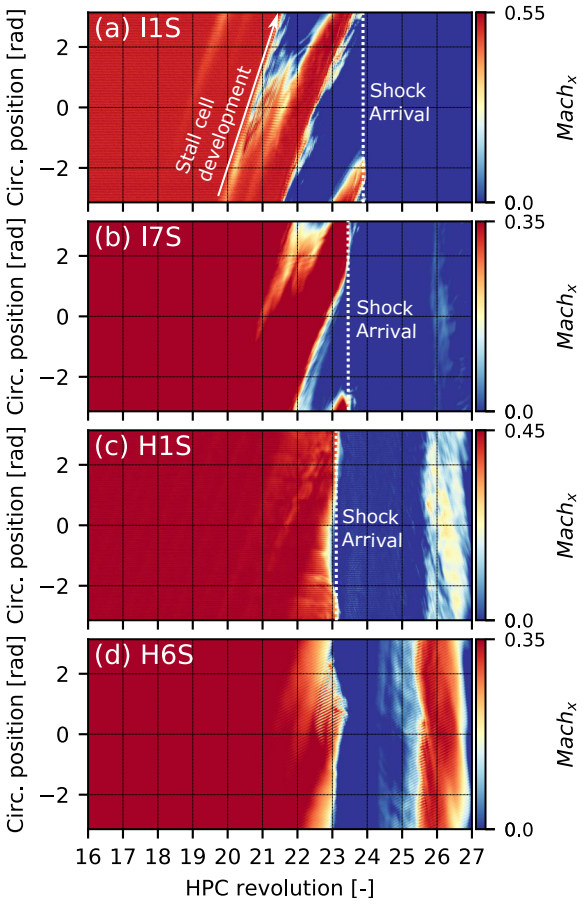


Figure 6.19: Axial Mach number at 50% span of I1S, I7S, H1S and H6S inlets during the surge onset - case B.

Figure 6.20 illustrates the core meridional view of circumferential averaged axial Mach number at three different time instants for case B. The IPC flow changes from a normal operation at revolution 9.71 towards a low Mach number operation at revolution 22.80.

At this revolution, a slight drop in axial Mach number is observed across the HPC but it remains unstalled. At revolution 23.58, the HPC has surged and a full core flow reversal is visible.

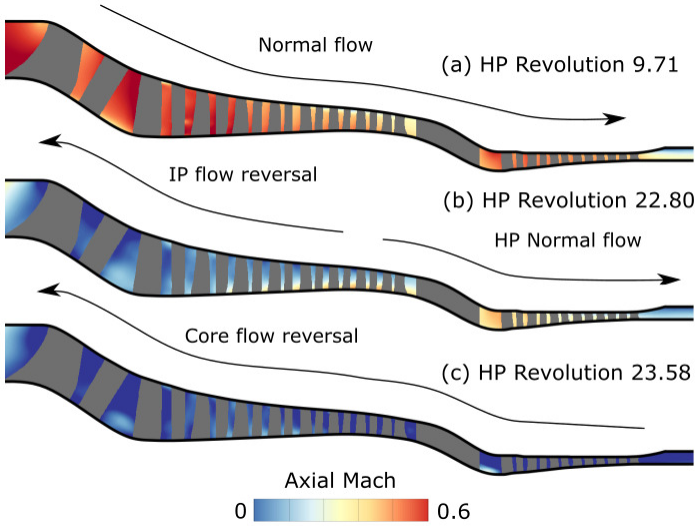


Figure 6.20: Circumferential averaged axial Mach number at revolutions 9.71, 22.80 and 23.58 - case B.

6.4 Comparison between cases A2 and B

6.4.1 Surge induced compression wave

For case A2, the HPC rear stages stall first inducing a CW which travels towards the front of the compression system. For case B, the surge occurs in two steps: rotating stall development in the IPC and subsequent HPC surge. Due to the time lag between the two events in case B, two distinct pressure waves are expected to travel towards the front of the compression system. Since the first CW originates in the IPC, it can only be observed at stations further upstream. Therefore, to distinguish the behaviour of the surge induced CW between the two cases, the fan outlet plane is analysed.

Figure 6.21 shows a comparison in terms of cross-sectional averaged static pressure at the fan outlet for cases A2 and B. For clarity, the case B pressure signal is shifted by 19.8 revolutions so that the time of the HPC shock wave arrival matches that of case A2. In case A2, a single pressure wave, identified as “HPC shock wave”, causes sharp rise in pressure around revolution 4.5. In case B, two pressure waves are identified as “IPC CW” and “HPC CW’ in Figure 6.21. The first wave causes a gradual static pressure increase at the fan outlet whilst the second promotes a steeper change in static pressure. These two pressure signals are respectively attributed to the IPC rotating stall and subsequent HPC surge shock wave showed in Figure 6.19 .

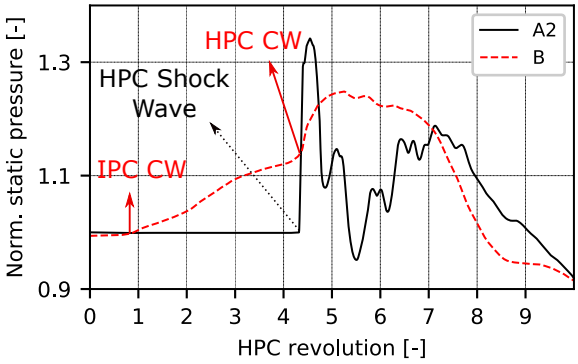


Figure 6.21: Time history of cross-sectional averaged static pressure at the fan outlet - cases A2 and B.

6.4.2 Aerodynamic loading

Figure 6.22 shows a comparison between the initial steady-state solution at revolution 0 and the pre shock wave pressures and maximum recorded pressures for each core station inlet in cases A2 and B (see Figures 6.4 and 6.15). The results show that the maximum recorded pressures in case A2 are significantly higher than the values observed in case B. This is a consequence of a higher exit pressure prior to surge in case A2 (caused by throttling) than in case B (surge line dropped towards the working line). This figure also shows that before surge, the compression system static pressure decreases below the initial condition in case B and increases substantially in case A2. This contributes to the lower levels of maximum pressure in case B. Since higher loads are recorded for case A2, the surge initiation via fuel-spike should be considered for a conservative evaluation in structural integrity testing.

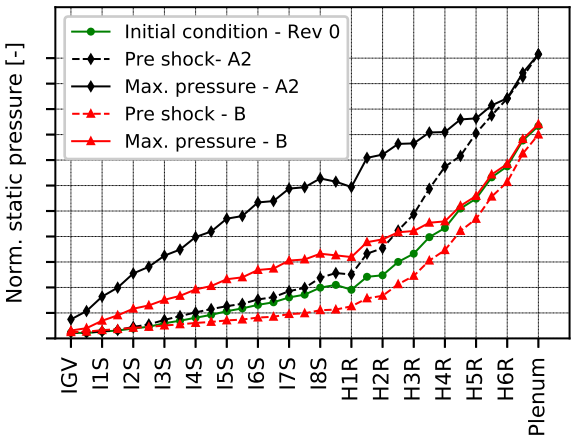


Figure 6.22: Static pressure in the core stations at initial condition, arrival of the CW ("Pre shock") and time instant of maximum pressure ("Max. pressure") - cases A2 and B.

6.5 Maximum over-pressures and plenum size effects

Literature on engine surge often associates the maximum over-pressure values observed during surge as a direct consequence of the surge shock wave [1, 34]. This differs from the observations in Figures 6.4 and 6.15 where the maximum pressures are recorded after the passing of the surge shock wave through each of the core stations. The time history of static pressure at H1S inlet for cases A2 and B is shown in Figure 6.23. It is seen that the resultant over-pressure can be attributed to two phases of pressure increase: a sharp increase driven by the passing of the surge shock wave (denoted by Δp_{shock}) followed by a period with more gradual growth (denoted by $\Delta p_{secondary}$). Case A2, which surged at higher exit pressure condition, experienced a higher pressure rise than case B in both these two phases. The main objective of this section is to identify the mechanism which drives this secondary pressure rise. Two main hypotheses are considered: this feature is driven by 1) the pre surge condition, i.e., the pressure in the plenum volume at the moment of the surge inception, and/or 2) the downstream geometry of the compression system.

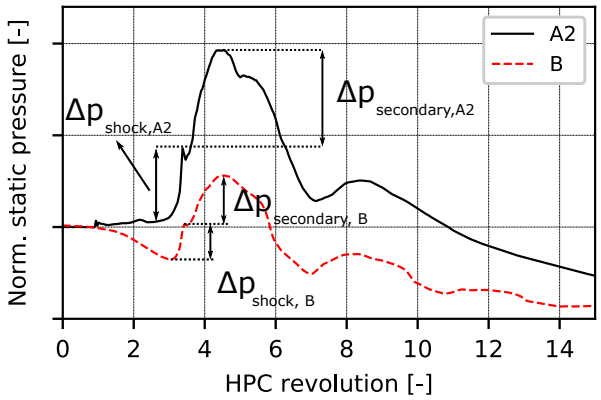


Figure 6.23: Time history of cross-sectional averaged static pressure at H1S inlet - cases A2 and B.

In order to study the effect of the downstream geometry on the surge induced over-pressure, additional plenum configurations for case A2 were investigated. The schematic of the three geometries used as well as the time history of H6S inlet pressure are shown in Figure 6.24. The static pressure is plotted in natural logarithmic scale to aid the identification of the blow-down rate. The results show that surge is initiated[3] (around revolution 6) at a similar compressor exit pressure level and it is independent of the plenum volume used. During blow-down, the static pressure at the HPC exit decreases exponentially (linear in log-scale) which indicates that the HPC blow-down follows a relationship of type:

$$p(t) = p_0 \cdot exp(-kt) \tag{6.2}$$

where p_0 is the plenum pre surge pressure, t is time and k is the blow-down rate. Moreover,

[3]The starting times for $V1$ and $V2$ signals were shifted to match the initial plenum pressure drop of $V3$.

the results show that the blow-down rate is a function of the plenum volume where larger volumes cause longer depressurisation.

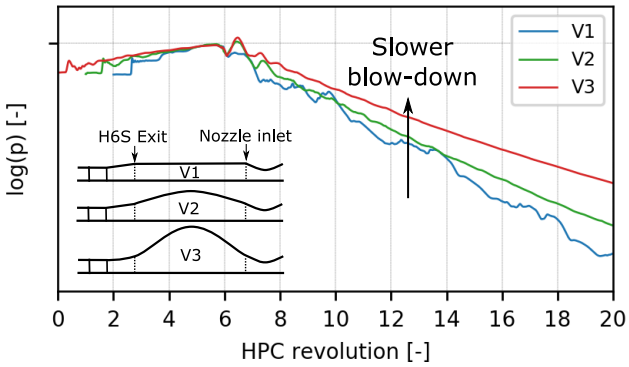


Figure 6.24: Time history of cross-sectional averaged static pressure at H6S inlet with different plenum volumes - case A2.

Figure 6.25 shows the time history of static pressure at H1S inlet. All three cases experienced very similar level of surge shock induced spike (denoted by Δp_{shock}) and secondary pressure rise (denoted by $\Delta p_{secondary}$), indicating that the plenum volume has negligible influence on the maximum over-pressure amplitude. However, it is observed that larger plenum volumes expose the compressor to high over-pressure levels for longer periods of time, which may bring aeroelastic challenges in real applications.

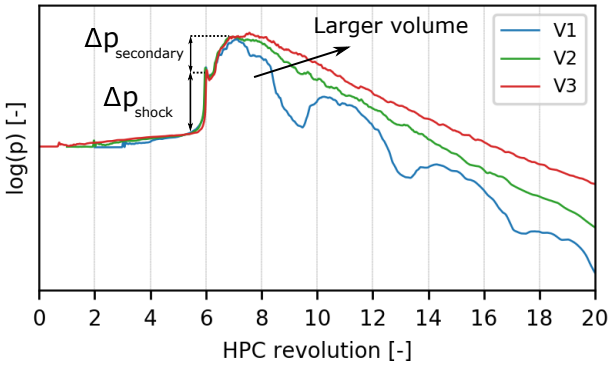


Figure 6.25: Time history of cross-sectional averaged static pressure (log-scale) at H1S inlet with different plenum volumes - case A2.

Figure 6.26 shows a comparison of mass flow and static pressure time histories for the smaller plenum volume ($V1$) and the larger plenum volume ($V3$). Static pressures at H1S and H6S inlets are shown with solid and dashed lines, respectively. It can be seen that the HPC with small volume ($V1$) experienced several "mini-surges" (oscillation of mass flow between positive and negative values) during the blow-down, which are not present for the case with large volume ($V3$). A closer examination of the static pressure time history for the smaller volume ($V1$) reveals that a transient condition with zero pressure gradient across the HPC (H1S to H6S) occurred at around revolution 7.2. This zero pressure

gradient condition is driven by the rapid reduction in pressure at the compressor exit whilst the HPC inlet experiences over-pressure induced by the surge. With this favourable condition, HPC recovery is temporarily achieved before the compressor falls back into reverse flow (as the compression system as a whole is still in blow-down). This process is repeated several times during the entire blow-down period, however the amplitude of the oscillation reduces as time progresses. The aforementioned oscillations are not present for the case with larger volume (V3) which is due to the absence of a zero pressure gradient condition as the plenum pressure decreases more gradually.

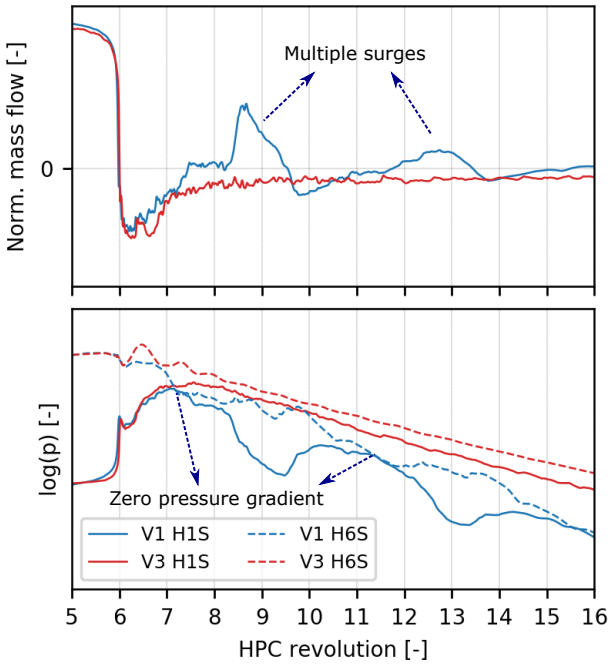


Figure 6.26: Time history of cross-sectional averaged mass flow (a) and static pressure (log-scale) (b) at H1S and H6S inlets with different plenum volumes - case A2.

The analysis above showed that the downstream plenum volume has negligible impact on the over-pressure experienced inside the compressor during surge. It is thus reasonable to infer that the maximum pressure value is largely determined by the compressor exit pressure before surge, where higher exit pressure results in higher over-pressure (shock induced spike and secondary rise). Figure 6.26 shows that, when the HPC recovery occurs in case $V1$, the pressure decreases rapidly at H1S inlet whereas in case $V3$, the inlet pressure decreases gradually with a constant blow-down rate. This indicates that the secondary pressure rise is affected by the flow direction inside the compressor. As the flow is reversed after the passing of the surge shock wave, high pressure from downstream is blown towards the front of the compressor. This back flow of high pressure gas is believed to be the cause for the secondary pressure rise. However, as the whole compression system is in blow-down (pressure is decreasing everywhere), a trade-off between the two effects takes place, giving rise to a local pressure maximum shortly into the blow-down process.

For the cases studied here, the maximum pressure is recorded approximately one revolution after the surge shock wave passes through.

6.6 Concluding remarks

The aerodynamic behaviour of a three-shaft engine compression system during two high power surge events was investigated in detail. The first event considered a surge initiation via a sudden throttling of the HPC to mimic a fuel-spike whilst the second considered a VSVs malschedulling of the IPC. This is the first time that a URANS simulation is successfully conducted to model a high power surge event of a fully assembled compression system.

The maximum pressures recorded in the core compressors were caused by a combined effect of the surge shock wave passing and high pressure gas blown towards the front of the engine during the plenum depressurization. This is a new finding since until this point, it was thought that the maximum pressures were solely caused by the shock wave passing.

It was demonstrated that for high pressure ratio compression systems, a surge shock wave develops almost instantaneously (without rotating stall development) in the HPC independently of the surge trigger. The surge shock wave travels in an approximately axisymmetric fashion and increases in strength as it propagates towards the front of the engine.

Furthermore, it was found that the maximum over-pressure obtained during the surge event is dictated by the compressor exit pressure at the moment of the surge inception, which is determined by the surge inception mechanism. A conservative approach to obtain the maximum loads during testing should consider the surge trigger via a fuel-spike.

Finally, several downstream geometries were tested for surge initiated via abrupt throttling of the HPC. It was found that the downstream geometry of the compression system has a negligible impact on the maximum over-pressure amplitude experienced during surge. The blow-down rate increases as the volume is decreased and under certain circumstances, this increase can result in multiple surges of the HPC with smaller amplitudes. It is observed that for lower blow-down rates, the compressor is exposed to higher over-pressure levels for a longer period, which indicates that larger volumes may bring aeroelastic challenges.

7 Evaluation of a single passage model for surge behaviour predictions

7.1 Problem description and overview

The capability of using 3D full annulus (FA) unsteady RANS computations to model the post stall behaviour in a three-shaft engine compression systems was demonstrated in the previous chapters. However, such models require substantial computational resources and hence, cannot be performed routinely. This chapter investigates the accuracy of a simplified and low cost method for surge modelling: 3D single passage (SP) unsteady RANS. This is achieved by comparing the FA and SP methods and identifying the periods of surge when the flow field can be approximated by an axisymmetric solution.

Surge is characterized by a large amplitude axial oscillation through the compression system. Past research on surge modelling using a SP method showed promising results [35, 41]. This method assumes that the surge unsteadiness is only in the axial direction and periodicity at each passage is maintained during the complete surge cycle. This suggests that surge is an axisymmetric phenomena. However, these results were not compared against FA results and thus, further investigations are required to evaluate the capability of the SP model.

To cover a wide range of pre and post stall compressor behaviours, three distinct cases are studied. The first and second are cases A2 and B introduced in chapter 6, which consider the numerical model of a three-shaft engine compression system. The third case, named case S, considers a single-shaft core compressor where the surge is initiated via a gradual reduction of the core nozzle area. For each case, two simulations are performed: one considering a FA model and another considering a SP model.

From the cases studied in the previous chapters, case A2 presents the maximum pressures which should be considered by component designers when accounting for robustness to surge loads and thus, it is of great relevance. Case B is presented to evaluate the effect of using a SP method when rotating stall develops prior to the surge onset in a engine compression system. The pressure ratio of case S at surge onset is much lower than cases A2 and B. Consequently, a shock wave does not form promoting the development of rotating stall for a longer period prior to surge. This results in a “mild surge” (in contrast to a “deep surge”) event where the flow is not fully reversed across all of the compressor stations. Case S also provides an opportunity to make a comparison of the aerodynamic loading between a compressor rig and engine compression system. Table 7.1 summarizes

the conditions which were tested.

Table 7.1: Case studies for evaluation of a SP model for surge predictions.

Case	Surge shock wave	Rotating stall	Surge onset location
A2	Yes	No	HPC rear
B	Yes	Yes	IPC front
S	No	Yes	IPC rear

7.2 Case A2

7.2.1 Overall transient operation

Case A2 considers the compression system initially operating at design condition and the surge is initiated via sudden throttling of the core nozzle area. This procedure aims to mimic a "fuel-spike" in engine environment. Figure 7.1 and 7.2 show the transient overall performance of the surge event for the HPC and IPC, respectively, in terms of pressure ratio as function of corrected inlet mass flow function ($\dot{m}\sqrt{T_0}/P_0$), referred to as "$\bar{m}$". The operating points identified on these plots show the elapsed number of HPC revolutions from revolution zero for the FA model. The FA and SP models results are shown with solid and dashed lines, respectively, for all figures in this chapter. The compression system surge cycle is divided into 3 main periods which will be discussed individually: surge initiation, blow-down and system recovery.

Figures 7.1 and 7.2 show that the predictions using the SP model follow a similar trend to the FA model during the surge initiation. During the blow-down phase, Figure 7.1 shows that the two models behave differently. Several oscillations of larger magnitude in mass flow and pressure ratio are recorded for the SP model relative to the FA model. For both models, these oscillations are caused by the secondary surges occurring in the HPC during the system blow-down as shown in Chapter 6.

The system recovery is initiated around revolution 23.5 when considering the FA model as can be seen by the HPC operation returning to its original characteristic in Figure 7.1. On the other hand, the SP model is unable to capture the system recovery and instead, the flow at the HPC converges to a near zero flow condition whilst mass flow oscillations at the IPC inlet are seen in Figure 7.2. The differences highlighted above are investigated in the following sections.

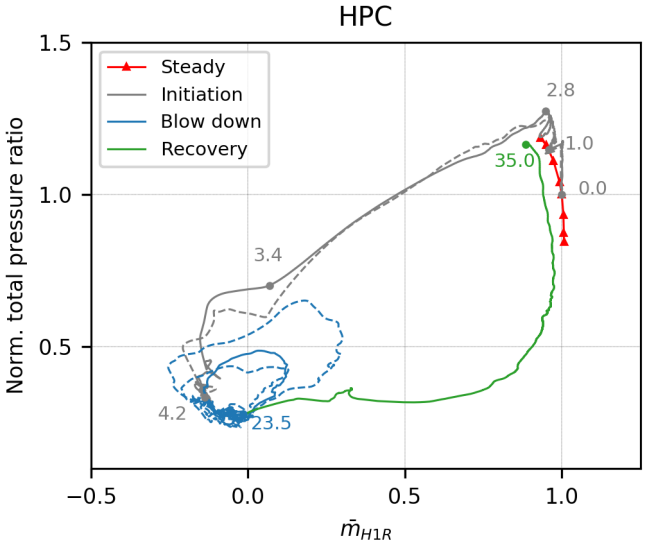


Figure 7.1: HPC characteristic and transient performance between revolution 0 and 35. FA model in solid lines and SP model in dashed lines - case A2.

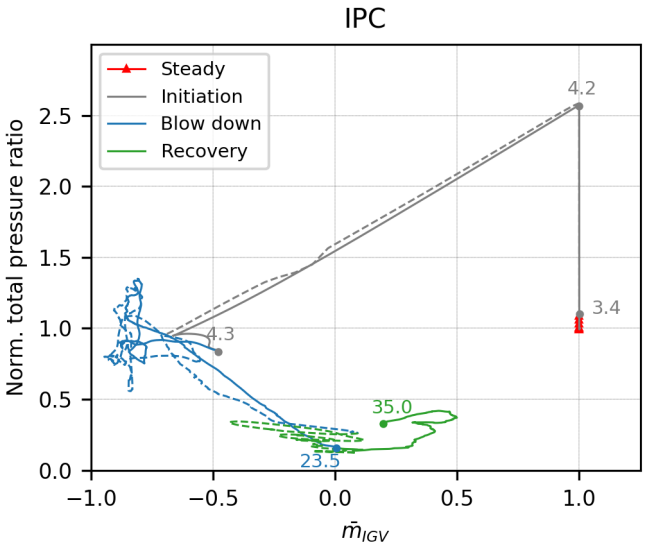


Figure 7.2: IPC characteristic and transient performance between revolution 0 and 35. FA model in solid lines and SP model in dashed lines - case A2.

7.2.2 Surge initiation

Further insight can be gained from Figure 7.3 which shows a comparison between the time evolution of cross-sectional averaged mass flow and static pressure at the inlet of several HPC stations for the FA and SP models, identified by solid and dashed lines, respectively. The abrupt closure of the core nozzle induces a compression wave (CW_1) which upon arrival at H6S inlet (around revolution 0.6) rises the static pressure and decreases mass flow. This wave is partially transmitted upstream of the HPC and partially reflected, travelling back and forth between the plenum outlet and inlet. Both models show a

similar variation in mass flow and static pressure until the arrival of the reflected wave indicated as CW_2. The reflected wave is stronger for the SP model relative to the FA model as can be seen by the larger increase in static pressure and larger drop in mass flow. As a consequence, the HPC rear stages show a premature surge onset for the SP model relative to the FA model as identified on Figure 7.3 by "SP Surge" and "FA Surge". Despite the time lag of approximately 0.7 revolutions between the surge onset of both models, the maximum pressure level reached at each of the HPC stations is approximately the same.

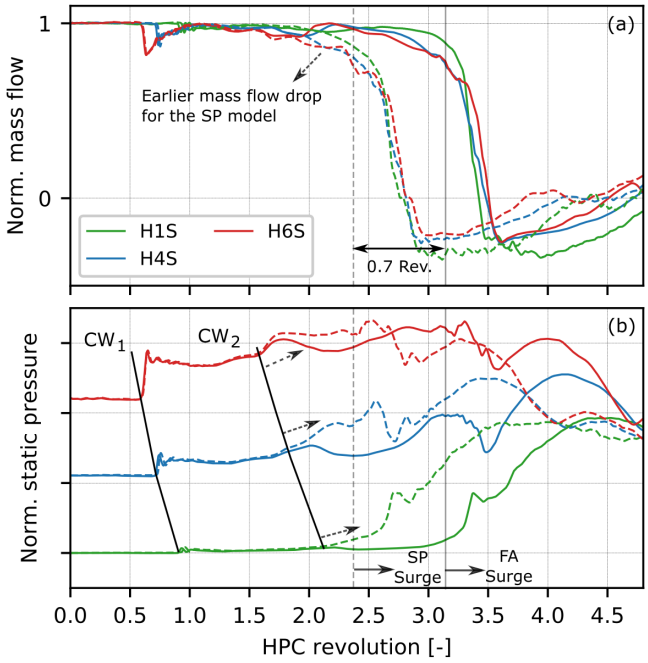


Figure 7.3: Time history of cross-sectional averaged mass flow (a) and static pressure (b) at H1S, H4S and H6S inlets - case A2.

The surge inception is studied to comprehend the differences between the two models. Figure 7.3a shows for both models that the mass flow drops first at H6S which suggests that stage 6 of the HPC stalls first. The time history of the FA model axial velocity at 95% span of H6S inlet and its corresponding modal content is presented in Figure 7.4. These plots were constructed based on interpolation of axial velocity numerical probes around the annulus. In this figure, the axial velocity modal content is normalized by the average velocity, $\bar{U}_x$, at each time step, i.e., mode 0 of the velocity spectrum (m=0).

Circumferential disturbances introduced by the potential field of H6S (m=144) and the first and second harmonic of H6R wake (m=66 and m=132) are captured by the FA approach. The decrease in axial velocity just before revolution 2 in Figure 7.4a shows that after the arrival of CW_2, H6R stalls and non-axisymmetric flow features appear (indicated in Figure 7.4b). These flow features emerge as broadband signals in multiple mode orders around m=66 (H6R blade count) and m=0.

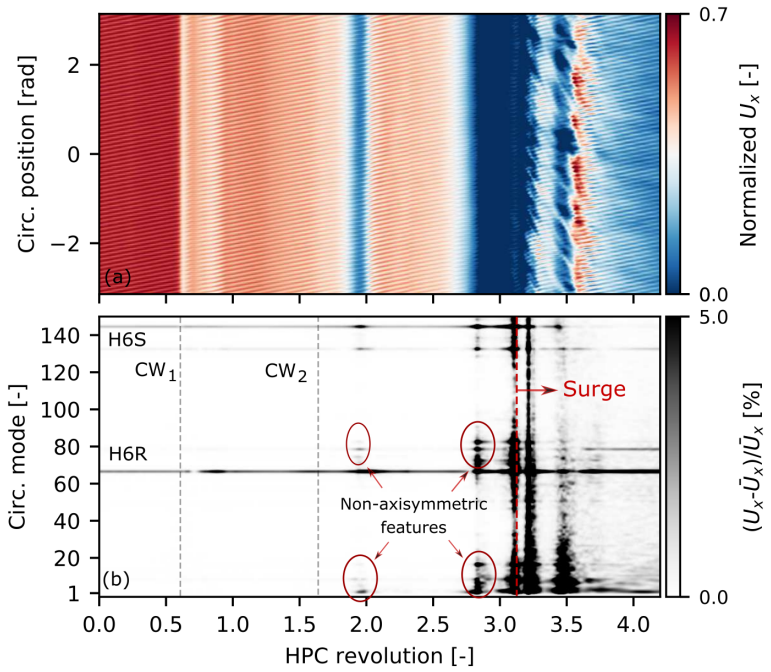


Figure 7.4: Time history of axial velocity (a) and corresponding modal content (b) at 95% span of H6S inlet - case A2.

The SP model considers a periodic boundary condition and thus, the solution modal content is limited to the harmonics of H6R and non-axisymmetric flow features are not captured. A comparison between the sum of the first three harmonics (m=66, m=132 and m=198) of axial velocity amplitude at H6R exit plane[1] for the FA and SP solutions at different time instants is presented in Figure 7.5. The axial velocity disturbance introduced by H6R has a similar magnitude for the FA and SP solutions until H6R stalls just before revolution 2. By revolution 2.08, the intensity of this disturbance for the SP model rises above 3 times the value registered in the FA model result. This phenomenon indicates that the stalled region at H6R has grown in an axisymmetric manner for the SP model. For the FA solution, the amplitude of H6R harmonics decrease after revolution 2 as the H6R recovers to its forward flow operation after a short period of low axial velocity (see Figure 7.4a).

The FA model has the ability to capture circumferential disturbances on other modes rather than the H6R harmonics (see Figure 7.4b), which is not the case for the SP model due to the enforced periodicity. Since the SP model stalls first, it is shown that the ability to model non-axisymmetric flow features plays an important role in delaying the stall inception even though the dominant modes are the H6R harmonics for both solutions.

The result above also shows that the stalling mechanism is not completely periodic, even when the dominant mode is the blade passing frequency (BPF). This indicates that the SP approach is not able to predict accurate solutions during the surge inception period even without the development of rotating stall.

[1]The H6R outlet mixing plane solution was expanded to 360^o for post-processing.

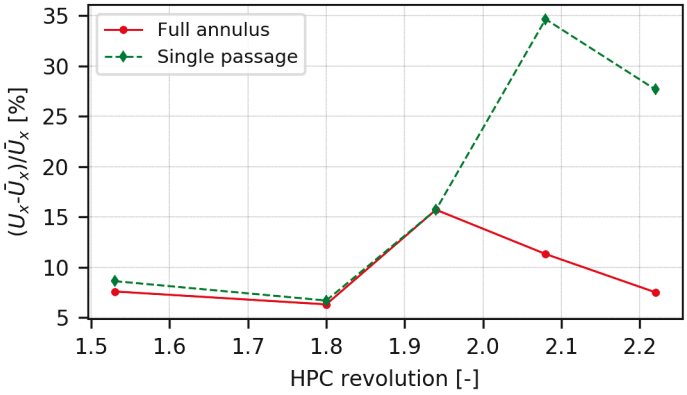


Figure 7.5: Time history of the H6R harmonics of axial velocity for the FA and SP solutions prior to surge - case A2.

7.2.3 Blow-down

The time evolution of normalized mass flow and static pressure (log-scale) at several stations of the compression system is shown in Figure 7.6. The starting time of the SP results was shifted to match the FA results. The SP results are referred in the new time scale. This is applied to all the plots that follow where the x-axis is "HPC revolution".

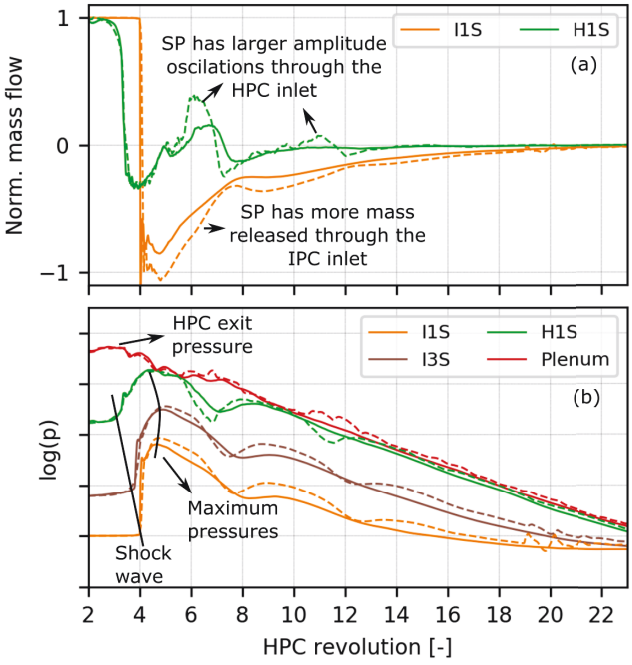


Figure 7.6: Time history of cross-sectional averaged mass flow (a) and static pressure (log-scale) (b) at the inlet of several IPC and HPC stations - case A2.

Figure 7.3 shows that the HPC surge is initiated around revolution 3. After, Figure 7.6b shows that a shock wave propagates upstream across the core stations. This shock wave causes a steep rise in static pressure and instantaneous flow reversal in the HPC and IPC

stations. The magnitude of these variations is similar for both the SP and FA models. This relates to the fact that both models predict a similar compressor exit pressure prior to inception of surge as shown in Figure 7.6b. This figure also shows that the blow-down rate is very similar between the two models.

The main differences between the predictions of the two models are observed between revolutions 5 and 12. During this period, the HPC initiates a temporary recovery as shown in Figure 7.6a. Since the overall system is still in blow-down, the HPC flow reverses again and an oscillation between positive and negative mass flow is observed at H1S. This process is repeated during the entire blow-down period, however the amplitude of the oscillation reduces as time is progressed.

The phenomena described above is more pronounced when using the SP model. Figure 7.6a shows that the SP result has mass flow oscillations of larger magnitude at the HPC inlet. These differences are a consequence of faster switching between reverse and forward flow across the HPC achieved with the SP model. This is shown in Figure 7.7 which presents a comparison between the time history of stalled region (defined by the annulus area percentage with reverse flow) at the I1S and H1S for the FA and SP models. For the FA model, the stalled region at H1S varies in a gradual fashion. In contrast, the SP model tries to completely recover to its forward flow condition for revolutions 6-7 and 10-12.

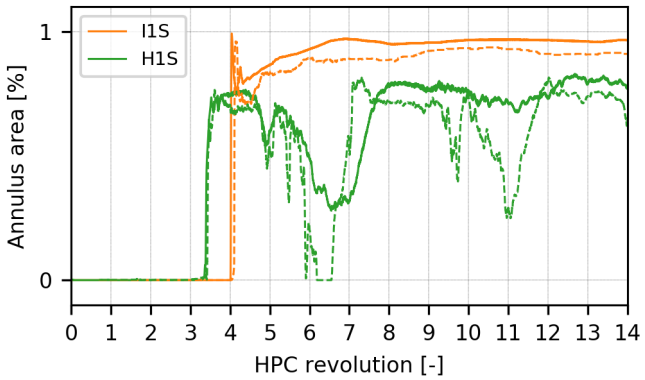


Figure 7.7: Time history of annulus area with negative mass flow at I1S and H1S inlets between revolutions 0 and 14 - case A2.

Figure 7.7 shows that, after the arrival of the surge shock wave at I1S inlet, the region of reverse flow occupies above 90% of the annulus and stays approximately constant during most of the blow-down period for the two models. Figure 7.8 presents the time evolution of normalized axial velocity at 50% span of I1S inlet and its corresponding modal content for the FA solution. The flow reverses after the arrival of the surge shock wave. During the reverse flow period, the flow field is approximately periodic where the predominant disturbances are driven by the potential field of I1R and wake of I1S as visible in Figure 7.8b.

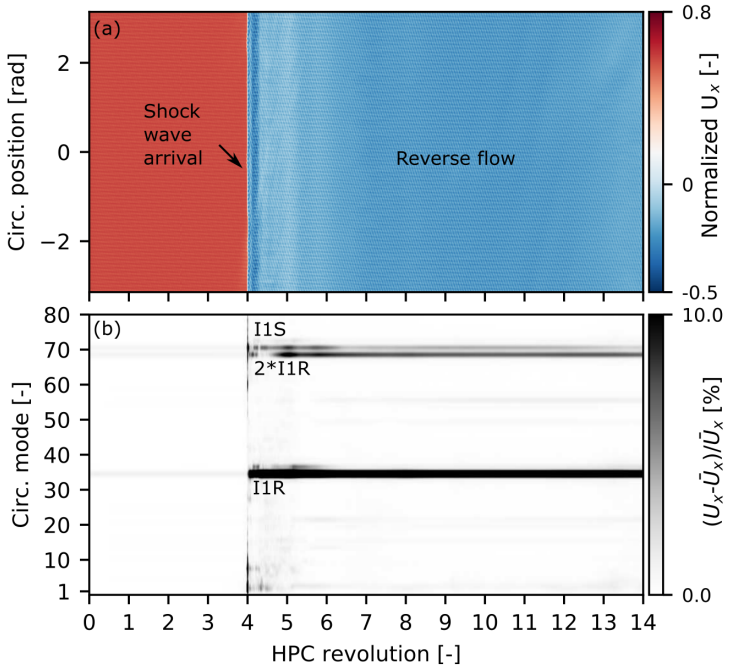


Figure 7.8: Time history of axial velocity (a) and corresponding modal content (b) at 50% span of I1S inlet between revolutions 0 and 14 - case A2.

An analogous plot to Figure 7.8 is shown for the inlet of H2S in Figure 7.9. As the HPC attempts to recover (around revolution 5), several short scale rotating cells are formed as seen by the presence of broadband type low order modes identified in Figure 7.9b. These short scale disturbances coalesce into a large scale cell which rotates at approximately 50% shaft speed as shown by amplification of mode 1 (m=1) identified in Figure 7.9b and positive axial velocity in Figure 7.9a. Thereafter, the HPC falls back into reverse flow operation because the compression system as a whole is still in blow-down. This process is illustrated in Figure 7.10 which shows the axial velocity contours at H2S inlet for revolutions 6, 6.7 and 7.5. The cells mentioned above are not common stall cells since the flow direction is positive inside the cell region. The same phenomena was observed during the recovery period in a test rig [43].

The results presented above show that when a compressor flow is fully reversed, the flow field can be approximated by an axisymmetric solution. When the recovery starts, low order modes dominate which implies that non-axisymmetric flow features are present that cannot be captured with the SP model. Nonetheless, despite the local differences that are shown in the predictions between the models, the overall system transient behaviour is well captured with the SP model until the beginning of the overall system recovery.

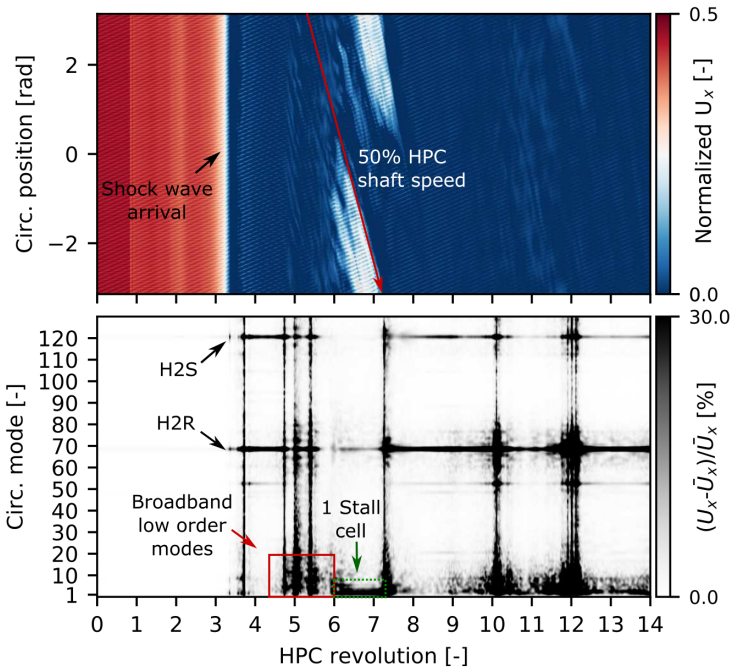


Figure 7.9: Time history of axial velocity (a) and corresponding modal content (b) at 50% span of H2S inlet between revolutions 0 and 14 - case A2.

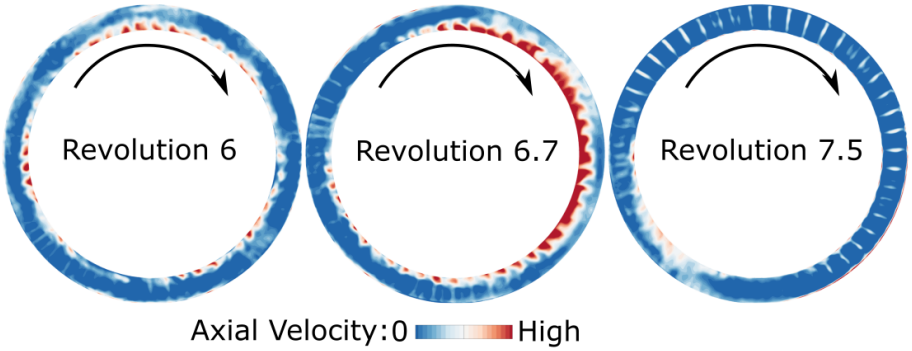


Figure 7.10: Axial velocity contours at H2S inlet during revolutions 6, 6.7 and 7.5.

7.2.4 System recovery

After revolution 23.5, the overall system recovery is initiated when considering the FA model as seen in Figure 7.1 and 7.2. In contrast, the SP model solution is unable to initiate the recovery. Mass flow and pressure ratio oscillations are observed at the IPC and an approximately zero flow equilibrium condition is reached at the HPC. This disparity between the models is examined in this section.

A comparison of the time evolution of mass flow and stalled region (defined by the percentage of annulus area with reverse flow) at I1S and H1S inlets between the two models is shown in Figure 7.11. Figure 7.11a shows that the SP model prediction of the IPC and HPC mass flow stabilizes around zero. In contrast, the FA solution mass flow

becomes positive from revolution 23.5. Figures 7.11b and 7.11c show that the stalled region size decreases in a gradual fashion for the FA solution as both of the compressors initiate recovery. This is not the case for the SP model, which shows a rapid transition between fully forward and reversed (1 and 0) flow conditions.

Further insight into the recovery process is gained from Figure 7.12 which shows time history of normalized axial velocity and corresponding modal content at 50% span of I1S inlet when considering the FA solution. It can be seen in 7.12a that after revolution 23, the flow transitions to a forward flow condition in a non-axisymmetric fashion. This flow is characterized by the formation of rotating cells with positive axial velocity. This phenomena can also be seen by the increase in amplitude of the low order modes identified in Figure 7.12b between revolutions 23.5 and 26. These cells grow rapidly between revolution 24 and 28 enforcing the reverse flow region to collapse into a single rotating stall cell which occupies about 70% of the annulus by revolution 30.

This result suggests that the presence of non-axisymmetric flow features facilitate the gradual recovery of the machine. Hence, the SP cannot model the transition from reverse to forward flow accurately.

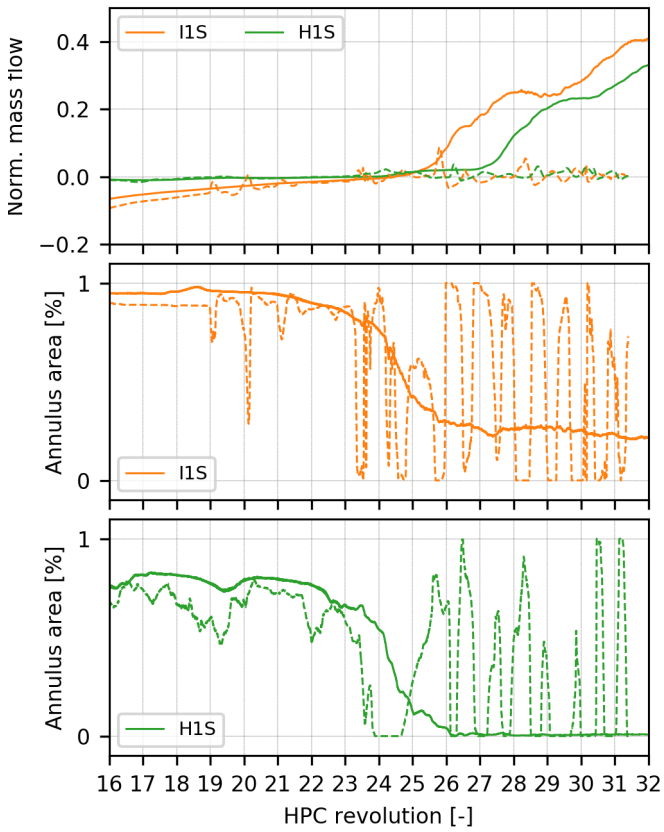


Figure 7.11: Time history of mass flow (a) and annulus area with negative mass flow at I1S (b) and H1S (b) inlets between revolutions 16 and 32 - case A2.

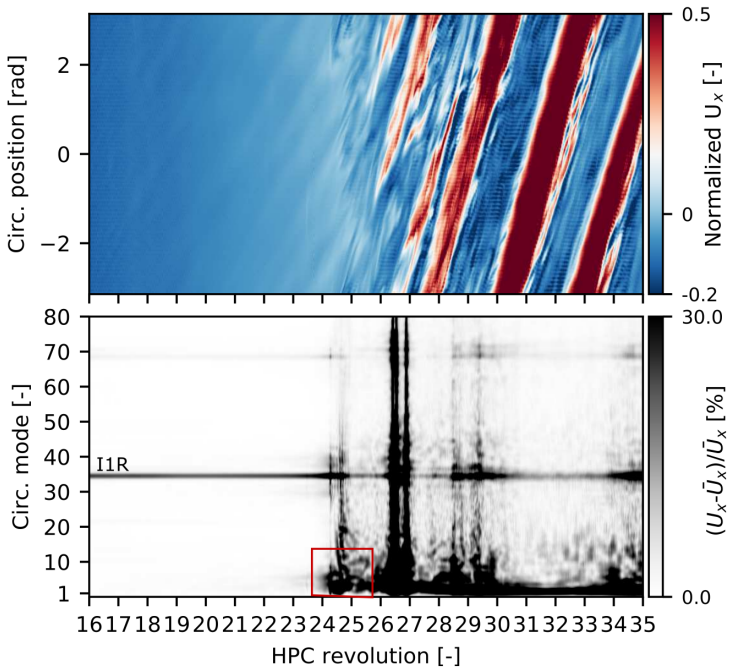


Figure 7.12: Time history of axial velocity (a) and corresponding modal content (b) at 50% span of I1S inlet between revolutions 16 and 35 - case A2.

7.3 Case B

7.3.1 Overall transient operation

Figure 7.4 shows that case A2 does not go through a phase of rotating stall before surge. From a modelling point of view, using a SP model for case A2 seems suitable because the main flow features are nearly axisymmetric until the beginning of the recovery. In case B, the compression system surge is initiated by a different process: malschedule of the IPC VSVs. By opening the IGV and closing the I1S, the IPC front stage is overloaded to an extent that it develops rotating stall prior to surge. This case is slightly more challenging to model using a SP model because of its inevitable non-axisymmetry. Evidently, the SP model is not capable of capturing the surge onset process accurately however, it is of interest to know if further insights can be gained in terms of system dynamics and aerodynamic loading.

Figures 7.13 and 7.14 show the time evolution of the HPC and IPC behaviour, respectively, for the FA (solid lines) and SP (dashed lines) models with selected points labelled as elapsed number of HPC revolutions for the FA solution. The time instant at which the IGV and I1S were adjusted is herein referred as revolution zero. Similarly to Figures 7.1 and 7.2, the cycle is divided into 3 main periods: initiation, blow-down and recovery.

Figures 7.13 and 7.14 show that the trigger and development of surge until revolution 25 is significantly different between the two models. In contrast, the SP model presents a good approximation to the FA result between revolution 25 and 35 which corresponds

to the blow-down period. These results indicate that this period is not affected by the surge initiation. The system behaviour during the blow-down and recovery shows a similar trend to case A2, i.e., the same conclusions can be obtained and thus, these periods are not studied further. The focus here is to investigate the discrepancies and similarities during the surge initiation. Firstly, the key aspects of this surge event are identified based on the FA model and secondly, the SP result is analysed and a comparison is made.

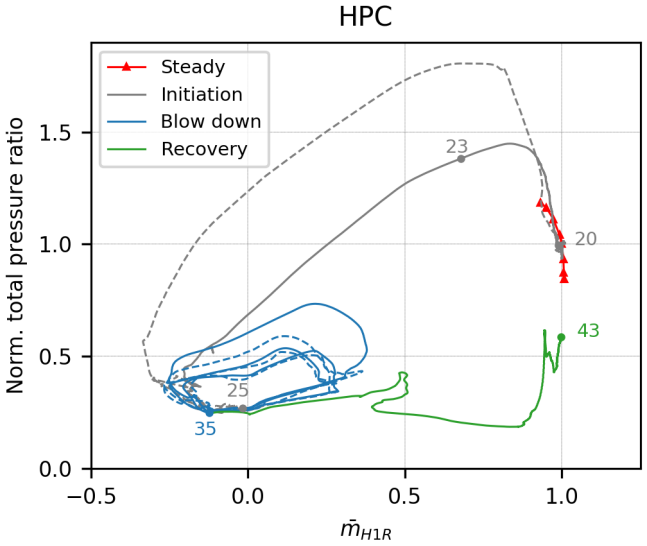


Figure 7.13: HPC characteristic and transient performance between revolution 0 and 43. FA model in solid lines and SP model in dashed lines - case B.

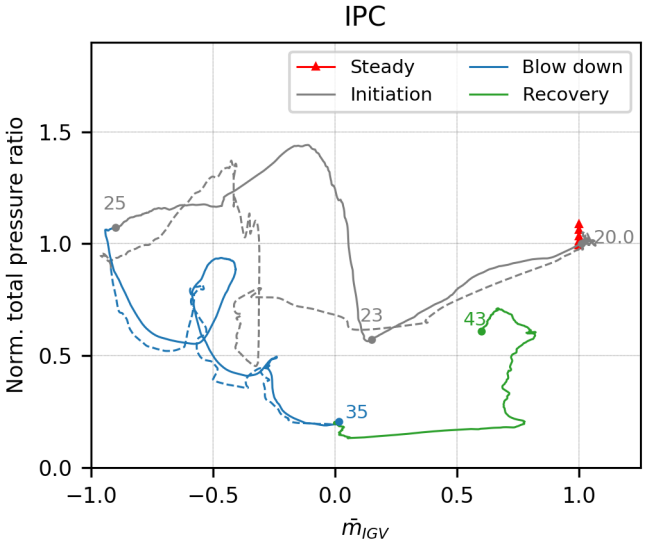


Figure 7.14: IPC characteristic and transient performance between revolution 0 and 43. FA model in solid lines and SP model in dashed lines - case B.

7.3.2 Surge initiation

Figure 7.15a shows the time evolution of mass flow on the front stages of the IPC (I1S) and HPC (H1S). Figure 7.15b shows the time evolution of static pressure at several core stations. These plots show the obtained results with the FA (solid lines) and SP (dashed lines) models. As demonstrated later, the surge inception time and location are different between the computations and therefore, the SP result horizontal axis is shifted by 16.1 revolutions to match the HPC surge initiation of the FA result for all the figures in this section.

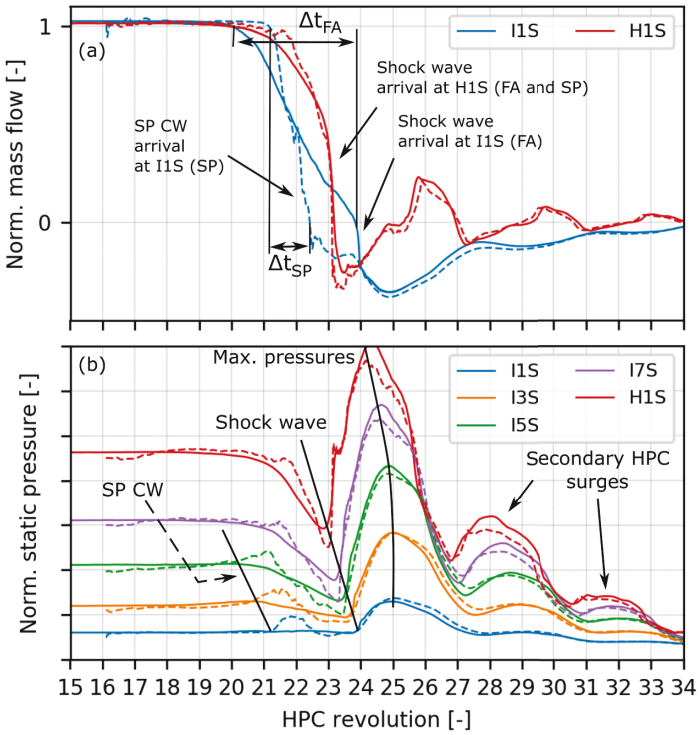


Figure 7.15: Time history of cross-sectional averaged mass flow (a) and static pressure (b) at the inlet of several IPC stations and H1S - case B.

FA model

The surge initiation for case B was analysed in chapter 6 however, for clarity it will be briefly described here with the support of the FA model results (solid lines) in Figure 7.15. Figure 7.15a shows that from revolution 20 onwards, the mass flow decreases at I1S which indicates that the IPC front stage has stalled. Consequently, the IPC loses the ability to pressurise and the static pressure decreases at all stations (except I1S) between revolutions 21 and 23 as seen in Figure 7.15b. The surge onset mechanism can be visualized by revisiting Figure 7.16, seen previously in chapter 6. This figure shows the circumferential variation of axial Mach number at 50% span for several core stations.

Around revolution 19, the inlet of I1S shows a short scale disturbance that quickly

expands circumferentially and axially between revolution 20 and 23. This rotating stall cell is observed in Figures 7.16a and 7.16b. As a result of the IPC stall, the HPC inlet pressure decreases. Since the HPC exit is held at a near constant value up to this point (the nozzle area is unchanged), the HPC pressure ratio inevitably rises crossing the stability limit around revolution 23 as shown in Figure 7.13. The HPC stalls rapidly and a shock wave propagates towards the core inlet promptly reversing the flow at the upstream stations as seen in Figure 7.16.

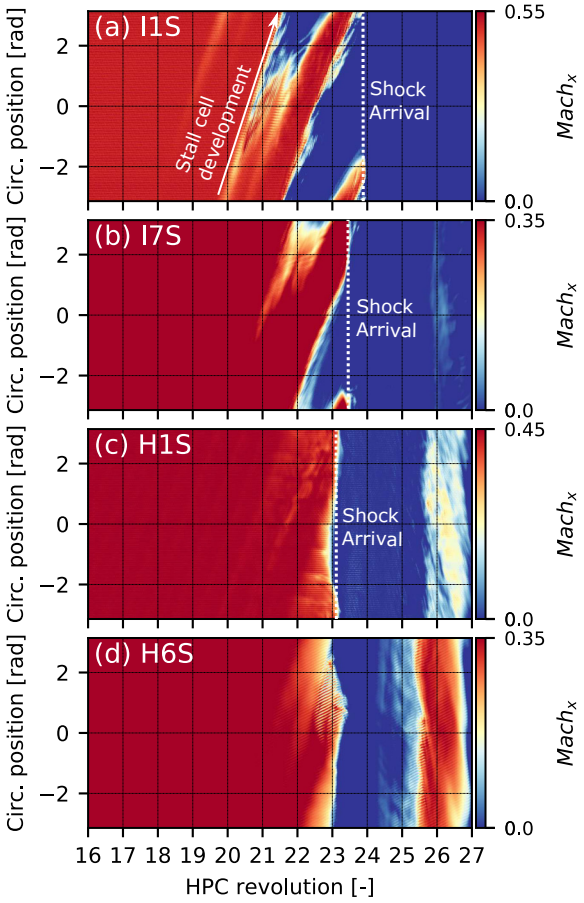


Figure 7.16: Time history of axial Mach number at 50% span of I1S, I7S, H1S and H6S inlets between revolutions 16 and 27 - case B.

The surge onset mechanism in Figures 7.16c and 7.16d show that rotating stall does not develop in the HPC. This is attributed to the short time scales involved in the surge inception which do not allow rotating stall to develop. Figures 7.16a and 7.16b also show that as the shock wave propagates upstream, non-axisymmetric flow features vanish, and a complete flow reversal is observed at all stations. This effect is also visible in Figure 7.15a which shows that the mass flow gradient changes after the arrival of the shock wave as indicated at I1S.

SP model

The main discrepancies found between the two models appear during the surge initiation period. Figure 7.15a shows that the flow reverses first at the IPC inlet when considering the SP model. For the FA model, the flow reverses first at the HPC inlet. This difference relates to the periods of surge inception identified in Figure 7.15a as Δt_{FA} and Δt_{SP} for the FA and SP models, respectively. The SP model registers a shorter period of surge inception than that of the FA model.

Figure 7.15b shows a static pressure increase at the stations upstream of I5S before the flow reverses at the I1S. This is linked to the stall onset of the SP solution. For the FA solution in chapter 6, it was demonstrated that a stable rotating stall pattern develops in the rear stages of the IPC before the surge onset is triggered by overloading stage 1. For the SP model, instead of developing a rotating stall pattern, a compression wave forms and propagates upstream of stage 6 as indicated by "SP CW" in Figure 7.15b. This wave is responsible for the premature flow reversal at the IPC and shorter surge initiation period (Δt_{SP}) as seen in Figure 7.15a. For the FA model, Figure 7.15a shows that the mass flow at I1S inlet decreases more gradually relative to the SP model. This relates to the development of rotating stall between revolutions 20 and 24 shown in Figure 7.16, which is not captured with the SP model.

Figure 7.17 shows a comparison of the time history of stalled region (defined by the annulus area percentage with reverse flow) at several core stations from HPC revolution 20 to 24 between the two models. For the FA model, Figure 7.17a shows that the stalled region increases through time in a gradual manner from the front to the back of the IPC until revolution 23. By revolution 24, the HPC has surged and the shock wave has passed through most of the core, which causes the flow to reverse in 55-80% of the annulus in all stations. For the SP model, Figure 7.17b shows that the stalled region rapidly expands upstream from I6S with the I3S registering about 35% of reversed flow area by revolution 22. By revolution 23, the "SP CW" has passed through all of the IPC stations. The stalled region occupies 30% of the annulus at I8S and increases linearly to nearly 100% at IGV.

Figure 7.15a shows that the flow reverses at H1S in a similar fashion for the two models. This suggests that the HPC surge is independent of the IPC flow condition, i.e., forward or reverse flow. For the SP model, Figure 7.15b shows that the HPC stalled region increases from H3S rearwards by revolution 23. Between SND and H2S, the forward flow condition is maintained because the surge shock wave (generated in the HPC) has not arrived yet. By revolution 24, the surge shock wave has passed through all the core stations and the annulus region with reverse flow is very similar for the two models.

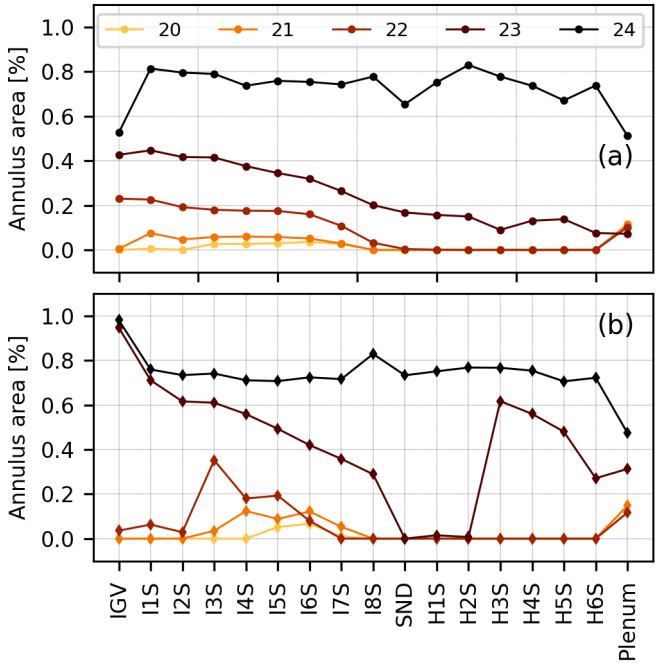


Figure 7.17: Annulus area with negative mass flow along the core for HPC revolutions 20, 21, 22, 23 and 24 when using the FA (a) and SP models (b) - case B.

7.4 Case S

7.4.1 Numerical model

The compression system studied above considered two core compressors running on different shafts with different speeds operating at a high power condition. These cases are characterized by an axisymmetric flow field from the moment of the shock wave passing through the core to the beginning of the recovery, i.e., the blow-down. As a result, the SP model presents a good approximation of the flow field behaviour during this period. In contrast, the surge inception and recovery initiation flow physics are not captured accurately since they are characterized by the formation of non-axisymmetric flow features. Because surge events are not always characterized by a full flow reversal and presence of a shock wave, the accuracy of the SP model is tested next in a surge event for which a shock wave is not formed. In case S, the surge occurs via a gradual growth of a rotating stall cell.

Case S considers the numerical domain shown in Figure 7.18. This domain is formed by the LPC and IPC of the compression system previously used with a plenum volume located downstream of the SND. The focus here is on the IPC. The purpose of including the LPC domain in this study is to ensure a stable and time varying boundary condition at the IPC inlet during the surge event. The plenum volume has a similar size to the one located downstream of the HPC in the previous cases. The pressure ratio of the compression system in case S is approximately 5 times smaller than the one in case A2. For comparison purposes, the B-parameters [32] for case A2 and S were calculated: a)

case A2 - 1.4; b) case S - 0.7. The numerical settings (grids and time step) used in this calculation are identical to the ones used in case A2 and B. The surge is initiated by smoothly throttling the core nozzle which effectively drives the IPC towards the surge line.

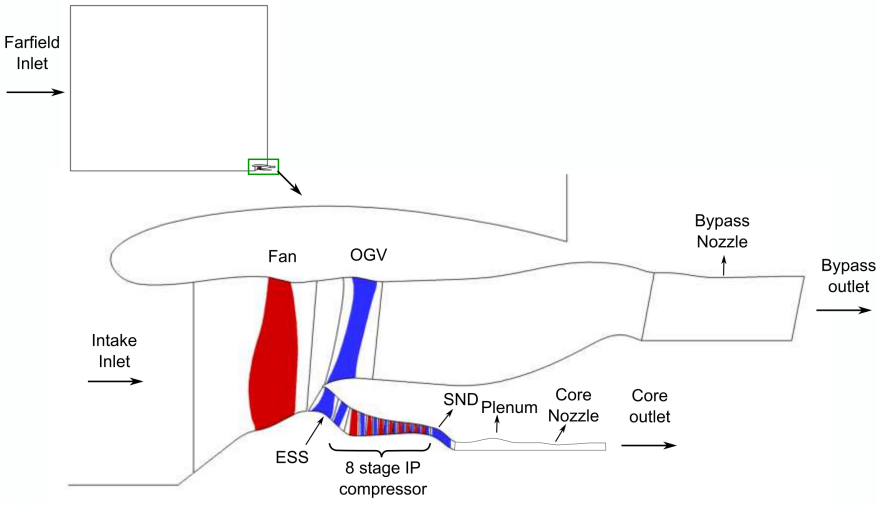


Figure 7.18: Meridian view of the numerical domain considered in case S.

7.4.2 Overall transient operation

Figure 7.19 presents the time history of mass flow and static pressure for the FA and SP models at the inlet of several IPC stations. Three surge cycles were simulated for each of the models.

Figure 7.19a and 7.19c show that for the FA model, the mass flow and static pressure decrease across all stations after the surge onset. Between revolutions 5 and 7, a compression wave propagates upstream (identified as "Stall CW" in Figure 7.19c). This behaviour is similar to what was observed in Figure 7.6 however, in this case the CW does not develop into a shock wave and a discontinuity in static pressure across the IPC stations is not observed. After revolution 15, the compressor has recovered completely into a positive flow condition and the second surge cycle is initiated. The same process is repeated on the following cycles.

Figure 7.19 shows that the IPC surge behaviour is different between the two models. The first disparity is found during the first surge cycle where the surge onset occurs around 2 revolutions earlier for the SP model. This difference can be explained by analysing Figure 7.20, which shows the time history of normalized axial velocity and corresponding modal content at 90% span for I6S inlet when using the FA model. This figure shows that the tip region stalls and a rotating stall pattern develops between revolution 2 and 7. The SP model is unable to capture rotating stall and thus, the IPC surges earlier as seen previously for case A2. Due to the earlier surge initiations, shorter surge periods are registered with the SP model relative to the FA model in surges 2 and 3 seen in Figure 7.19. The SP

results show that a compression wave forms and develops into a shock wave as indicated in Figure 7.19d by "SP shock wave". This is caused by the shorter surge initiation period associated with the rapid growth of a stalled region as seen previously in case B.

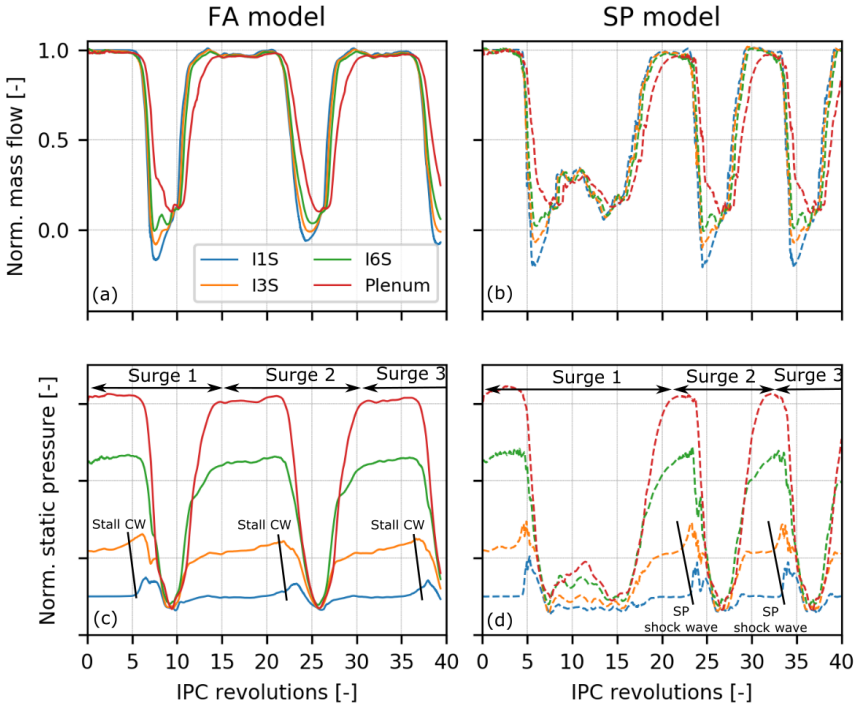


Figure 7.19: Time history of cross-sectional averaged mass flow ((a) and (b)) and static pressure ((c) and (d)) at the inlet of several IPC stations when using the FA and SP models, respectively - case S.

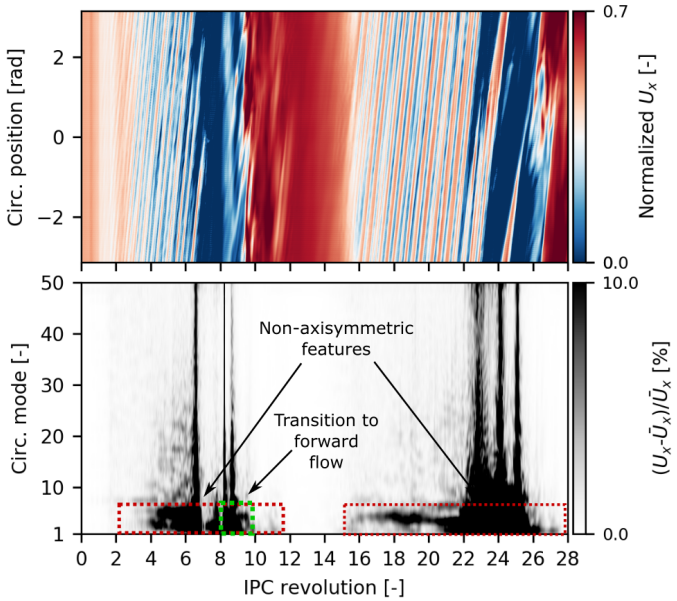


Figure 7.20: Time history of axial velocity (a) and corresponding modal content (b) at 90% span of I6S inlet between revolutions 0 and 28 - case S.

For case S, the flow only reverses completely at the stations located upstream of I6S (see Figure 7.19a). Figure 7.21 presents the normalized axial velocity contours at I1S and I6S inlets at different time instants during the FA model blow-down period in surge 2 (see Figure 7.19). The results show that as time progresses, a single large scale stall cell is present across the IPC stations and grows circumferentially between revolution 22 and 24. Between revolutions 24 and 25, the flow is fully reversed at I1S inlet whilst the stall cell size remains approximately constant at I6S inlet. By revolution 26, the flow recovers to its forward axisymmetric condition at I6S inlet and the non-axisymmetric recovery process is initiated at I1S inlet. The flow is never reversed fully at the rear stages of the IPC in this surge event and hence, a detailed study of the flow condition using a SP model is inaccurate. This was not the same as in case A2, where the IPC compressor reverse flow period is axisymmetric (see Figure 7.8).

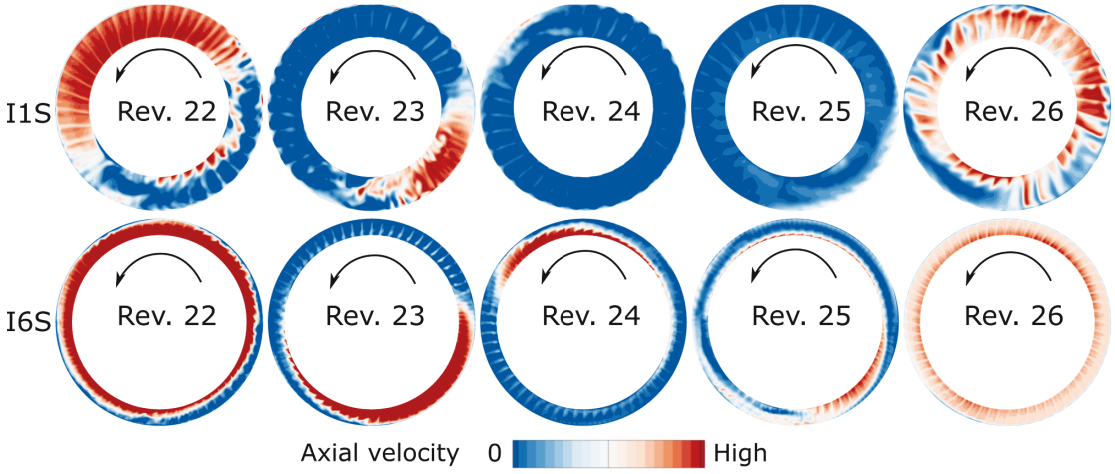


Figure 7.21: Axial velocity contours at I1S and I6S inlets during surge 2 - case S.

Another significant difference between the SP and FA model relates to the recovery of the IPC. It was previously demonstrated for case A2 that the transition between reverse and forward flow is characterized by non-axisymmetric flow features and thus, it was not expected for the SP model to recover. For the same reason, Zhao et. al. [43] also conducted CFD simulations of a high pressure compressor where the recovery was not achieved when using a SP model. For case S, the compressor goes through a surge of smaller magnitude (see revolution 10-15 in Figures 7.19b and 7.19d) before recovering from surge 1 whilst it recovers immediately for surges 2 and 3. These observations indicate that recovery can be achieved when using a SP model however, the FA results provide evidence that the flow field is not realistic.

7.5 Aerodynamic loading considerations

Figures 7.6 and 7.15 show that the maximum pressures in the three-shaft compression system surge are recorded just after the shock wave passing. The compressor behaviour during the shock wave propagation and blow-down period can be approximated by an axisymmetric solution and thus, it is hypothesised that the maximum aerodynamic loads can be estimated using a SP model.

Figure 7.22 shows a comparison of static pressure between the initial condition at revolution 0, prior to the arrival of the surge shock wave and maximum recorded pressures at each of the core stations for case A2. The solid and dashed lines are used for the FA and SP models, respectively. The estimated maximum pressures are similar for both models. Prior to the arrival of the shock wave, the SP solution presents higher values of static pressure in the HPC. This is a consequence of the differences between the models during the surge initiation period discussed before.

Figure 7.23 shows an analogous plot to Figure 7.22 for case B. The results show that the maximum pressures predicted with the two models are similar. The CW caused by the rapid stalling process when using the SP model does not have a significant impact on the maximum pressures recorded.

From cases A2 and B, it can be concluded that in a deep surge (the flow reverses fully across the compressors) the maximum over-pressure at each station is independent of the surge initiation mechanism. This is in agreement with the findings in chapters 5 and 6, where it has been shown that the maximum over-pressures are mainly dependent on the compression system exit pressure.

Figure 7.24 shows a similar comparison as the plots in Figures 7.22 and 7.23 for case S. For this case, the SP model over-predicts the values of maximum pressure recorded at the IPC stations. In surge events where the flow does not reverse fully throughout the compressor, the maximum over-pressures are driven solely by the compression wave formed during the stall inception process. As previously seen in Figure 7.19, the rapid surge onset when considering the SP model leads to the formation of a shock wave which is not the case for the FA model.

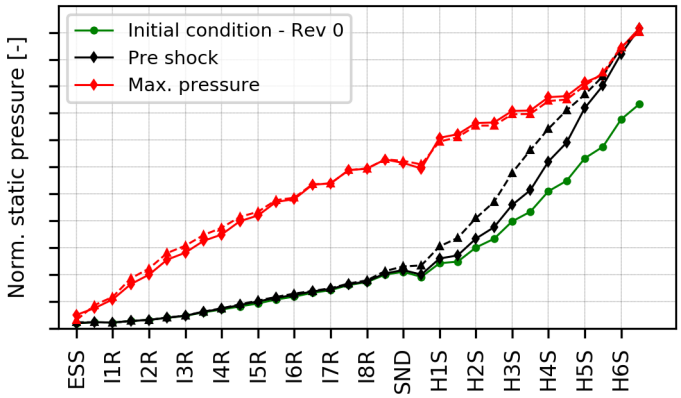


Figure 7.22: Static pressure in the core stations at initial condition, arrival of the CW ("Pre shock") and time instant of maximum pressure ("Max. pressure") for the SP and FA results - case A2.

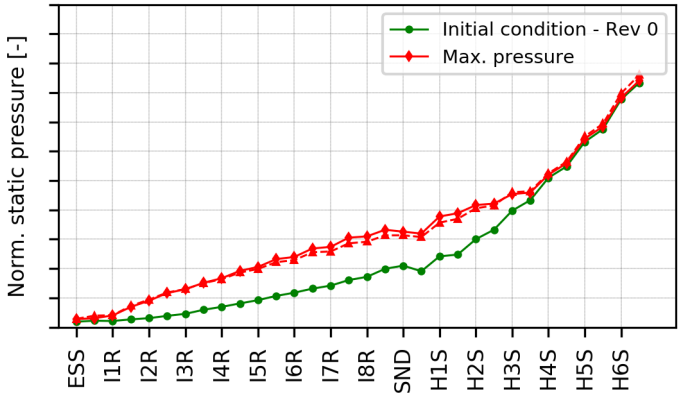


Figure 7.23: Static pressure in the core stations at initial condition, arrival of the CW ("Pre shock") and time instant of maximum pressure ("Max. pressure") for the SP and FA results - case B.

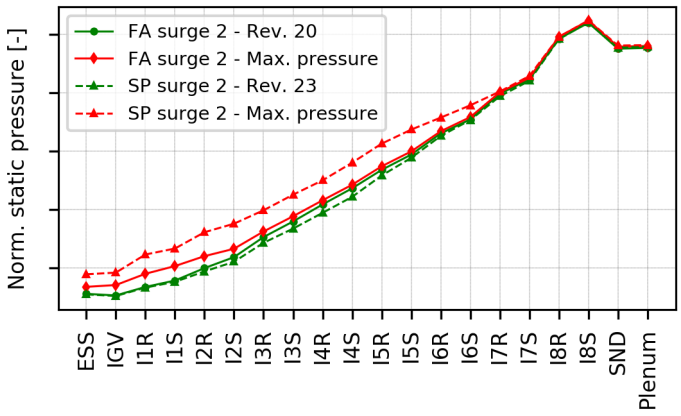


Figure 7.24: Static pressure in the IPC stations at initial condition, arrival of the CW ("Pre shock") and time instant of maximum pressure ("Max. pressure") in surge 2 for the SP and FA results - case S.

7.5.1 Comparison of aerodynamic loads between a rig and engine compression system

The cases studied in this chapter provide an opportunity to compare the aerodynamic loads experienced in a surge event on a rig and an engine compression system. Figure 7.25 shows a comparison of the maximum over-pressure registered between each of the surge events studied in this chapter when considering the FA model. The results show that the maximum over-pressures values are registered for case A2. For this case, the surge is initiated by throttling of the HPC of the engine compression system (IPC and HPC). As a consequence, the pressure ratio at the instant of surge onset is larger when compared with the other cases. Case B registers the second maximum over-pressures for a similar reason, i.e., the system pressure ratio is higher for the entire compression system than to case S (IPC only).

For case S, Figure 7.25 shows that the over-pressure is only noticeable for stations located upstream of I2S. For the remaining stations, the over-pressure is nearly zero. For this case, a surge shock wave is not formed and the flow does not reverse to the same extent during blow-down as seen with entire engine compression system. The results shown here suggest that surge rig testing is not representative of the compressor's response when assembled within an engine for surge load estimations.

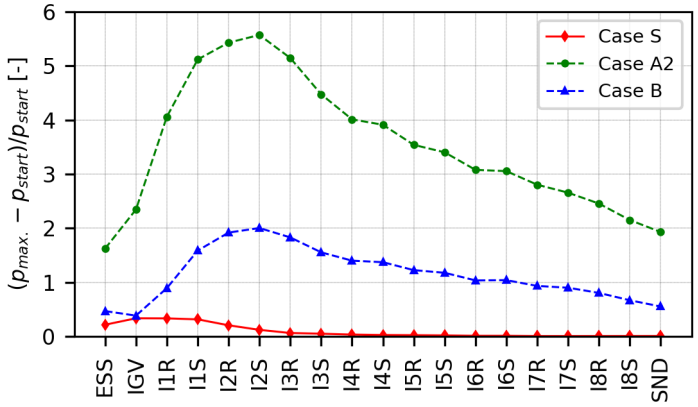


Figure 7.25: Over-pressure at the inlet of IPC axial stations for cases A2, B and S.

7.6 Concluding remarks

In this chapter, a comparison between full annulus (FA) and single passage (SP) URANS models for the prediction of two axial compression systems' surge behaviour was analysed. Firstly, the models were tested on a three-shaft engine compression system surge initiated by two distinct mechanisms - throttling of the HPC and malschedule of the IPC VSVs. Secondly, a surge event on a single-shaft core compressor rig (lower pressure ratio relative to engine) was investigated.

The SP model is an adequate alternative to the FA model to study the overall system dynamics in engine compression systems operating at high power condition from the moment of surge onset until the beginning of the overall system recovery. These surge events are characterized by a period of full flow reversal where the flow is nearly axisymmetric. For compressor rigs with lower pressure ratio, the blow-down period can be characterized by a rotating stall pattern and thus, the SP model provides unrealistic results.

It has been demonstrated that the SP model is unable to predict two key moments of the surge event accurately: the surge onset and the beginning of the recovery phase. These moments are characterized by non-axisymmetric flow features which play an important role in delaying the surge onset and ensuring a gradual flow field change from reverse to forward condition.

The SP model is not capable of predicting the surge inception accurately even if a full rotating stall does not develop prior to surge. In contrast to cases where rotating stall develops for the FA model, the use of a SP model can lead to the formation of shock waves which propagate upstream of the compression system. For surge events characterized by long periods of flow reversal, these shock waves have a negligible impact on the prediction of maximum over-pressures. For surge events where the flow reverses for a short amount of time or it does not fully reverse (mild surge), the maximum over-pressures are over-predicted.

Finally, it is observed that the maximum recorded pressures during surge are significantly larger for an engine compression system relative to a compressor rig. Therefore, surge rig testing may not be representative of the compressor's response when assembled within an engine for surge load estimations.

8 Conclusion and further work

Recent development towards lighter weight structures, shorter intakes, higher by-pass ratios and higher pressure ratios to minimize fuel consumption are driving further developments in gas turbine engine technologies. To cope with these design requirements, new engine core compression systems are being designed however, they are constrained by aerodynamic design decisions that are dependent on stall and surge. As a consequence, research on this subject is of greater importance to ensure modern compression systems reliability and operability. This thesis presented a detailed investigation focused on both the fundamental physical phenomena as well as the numerical strategies and requirements for modelling the flow behaviour during near and post stall conditions in modern high speed compression systems. This chapter draws the main conclusions and presents a series of recommendations for future work.

8.1 Summary of the findings

Objective 1

Develop and validate a numerical strategy for accurate prediction of near and post stall flows in modern high speed compression systems. Study the effect of turbulence modelling and grid refinements.

In Chapter 3, a comparison between the prediction capability of two turbulence models in a high speed multi-stage compressor was shown. Numerical and physical modelling uncertainties of the SA formulation were investigated. It was found that the MSA model gives a better prediction of the compressor stability line relative to the original SA model. The solutions obtained with the MSA model have higher levels of turbulence in localized separation regions and, as a consequence, numerical solutions are obtained closer to the stability limit.

Tip leakage flow modelling using the SA formulation results in an under-prediction of eddy viscosity in the near casing region. Ultimately, these results in premature flow separation and early compressor stall. This issue is more relevant for multi-stage arrangements. In single-stage compressors, the premature flow separation does not affect the flow behaviour of the blade rows located downstream and therefore, it might not compromise the stall margin prediction to the same extent. In order to improve the prediction of the stability boundary, an alternative formulation is proposed where the destruction term in the SA formulation is neglected in cells which consider the casing as the closest surface.

The effect of the tip gap size on the compressor performance was demonstrated. It was shown that both experiments and CFD are very sensitive to small changes in tip clearance sizes. This result shows the importance of accurate measurement of tip clearance during experimental campaigns which should be shared with CFD engineers for improvement of RANS models. Furthermore, it was also shown that CFD predictions are worse for larger tip clearances.

Finally, the "best" available CFD model was defined in order to be used in the following chapters for near and post stall modelling applications. A comparison is made for different aerodynamic speeds of the compressor to demonstrate the limitations of this RANS model in capturing the stability boundary. The CFD results showed a higher correct mass flow condition for the same levels of pressure ratio and an under-prediction of the stall margin when compared to measured data.

Objective 2

Study the near stall behaviour of a modern high speed compression system at high and low power conditions and determine the main flow features.

Chapter 4 presents a study on unsteady effects in a modern multi-stage compressor at two operating conditions: low and high speed. The results obtained using a steady single passage and unsteady full annulus models were presented and compared with experimental data. The results provide evidence that URANS CFD methods are capable of capturing the relevant flow features which characterize the flow behaviour in multi-stage compressors at both low and high speed conditions of operation.

It was demonstrated that in multi-stage compressors, unsteady full annulus models are required when one of the compressor stages is locally stalled and operates on the positive slope of the characteristic. The flow field is characterized by a rotating stall pattern with a high number of short-scale stall cells embedded in one of the compressor stages. For the low speed case, 16-18 stall cells rotate in the I2S blade-row at around 11% shaft speed. For the high speed case, 33-35 stall cells rotate in the I4R blade-row at approximately 70%-80% shaft speed.

Unsteady effects and the development of non-axisymmetric flow features in multi-stage compressors are strongly correlated with the formation of rotating stall in one of the compressor's stages. For low speeds, rotating stall is seen on the front stages over a wider operating range. For high speeds, the presence of non-axisymmetric flow features is limited to the rear stage and operating conditions near the stability boundary. Consequently, the differences between the steady single passage and unsteady full annulus models are more evident at lower speeds than higher speeds.

Objective 3

Development and validation of an efficient numerical methodology for surge modelling in a three-shaft engine compression system.

During engine operation, the IPC and HPC operating conditions are controlled by the turbines however, for modelling purposes, a core compressor matching process needs to be employed in order to achieve a realistic pre surge condition. Chapter 5 proposes a methodology for surge modelling of a three-shaft engine compression system in a computationally efficient manner by performing the fewest number of iterations as possible. The methodology consists in dividing the system compressors into subdomains and performing an iterative matching process to reach the target operating point in an engine deck. After, a perturbation is introduced in the flow to drive one of the compressors towards the stability line resulting in a full system surge.

To the best of the author's knowledge, this is the first time that the pre and post stall behaviour of a mid power surge event in a three-shaft engine is studied numerically and validated with experimental data. For the condition studied, the compressor stall appears first in the front stages of the IPC and expands axially towards the rear stages causing a pressure decrease in the front of the HPC. Consequently, the HPC surges and a steep rise in pressure is observed across all IPC stations.

The model presented in this work resulted in an over-prediction of the maximum over-pressures relative to the experimental results. A discussion is presented where these differences were attributed to experimental uncertainties and the assumption of a bleedless system during the surge event. Furthermore, it has been demonstrated numerically that the use of a compression system with bleed off-takes can significantly reduce the maximum over-pressures recorded during a surge event. The effects of bleeds and secondary air-system need to be considered by component designers when accounting for robustness to surge loads.

Objective 4

Determination of the three-shaft compression system post stall response to two types of aerodynamic disturbances: compression system fuel spike and IPC variable stator vanes (VSV) malschedule.

The aerodynamic behaviour of a three-shaft engine compression system during two high power surge events was investigated in chapter 6. The first event considered a surge initiation via a sudden throttling of the HPC to mimic a fuel-spike whilst the second considered a VSVs malschedulling of the IPC. This is the first time that a URANS simulation is successfully conducted to model a high power surge event of a fully assembled compression system.

The maximum pressures recorded in the core compressors were caused by a combined effect of the surge shock wave passing and high pressure gas blown towards the front of the engine during the plenum depressurization. This is a new finding since until this point, it

was thought that the maximum pressures were solely caused by the shock wave passing.

It was demonstrated that for high pressure ratio compression systems, a surge shock wave develops almost instantaneously (without rotating stall development) in the HPC independently of the surge trigger. The surge shock wave travels in an approximately axisymmetric fashion and increases in strength as it propagates towards the front of the engine.

Furthermore, it was found that the maximum over-pressure obtained during the surge event is dictated by the compressor exit pressure at the moment of the surge inception, which is determined by the surge inception mechanism. A conservative approach to obtain the maximum loads during testing should consider the surge trigger via a fuel-spike.

Finally, several downstream geometries were tested for surge initiated via abrupt throttling of the HPC. It was found that the downstream geometry of the compression system has a negligible impact on the maximum over-pressure amplitude experienced during surge. The blow-down rate increases as the volume is decreased and under certain circumstances, this increase can result in multiple surges of the HPC with smaller amplitudes. It is observed that for lower blow-down rates, the compressor is exposed to higher over-pressure levels for a longer period, which indicates that larger volumes may bring aeroelastic challenges.

Objective 5

Propose, test and demonstrate the advantages and disadvantages of a computationally cheaper model for the prediction of surge behaviour in modern compression systems.

In chapter 7, a comparison between full annulus (FA) and single passage (SP) URANS models for the prediction of two axial compression systems' surge behaviour was analysed. Firstly, the models were tested on a three-shaft engine compression system surge initiated by two distinct mechanisms - throttling of the HPC and malschedule of the IPC VSVs. Secondly, a surge event on a single-shaft core compressor rig (lower pressure ratio relative to engine) was investigated.

The SP model is an adequate alternative to the FA model to study the overall system dynamics in engine compression systems operating at high power condition from the moment of surge onset until the beginning of the overall system recovery. These surge events are characterized by a period of full flow reversal where the flow is nearly axisymmetric. For compressor rigs with lower pressure ratio, the blow-down period can be characterized by a rotating stall pattern and thus, the SP model provides unrealistic results.

It has been demonstrated that the SP model is unable to predict two key moments of the surge event accurately: the surge onset and the beginning of the recovery phase. These moments are characterized by non-axisymmetric flow features which play an important role in delaying the surge onset and ensuring a gradual flow field change from reverse to forward condition.

The SP model is not capable of predicting the surge inception accurately even if a full rotating stall does not develop prior to surge. In contrast to cases where rotating stall develops for the FA model, the use of a SP model can lead to the formation of shock waves which propagate upstream of the compression system. For surge events characterized by long periods of flow reversal, these shock waves have a negligible impact on the prediction of maximum over-pressures. For surge events where the flow reverses for a short amount of time or it does not fully reverse (mild surge), the maximum over-pressures are over-predicted.

Finally, it is observed that the maximum recorded pressures during surge are significantly larger for an engine compression system relative to a compressor rig. Therefore, surge rig testing may not be representative of the compressor's response when assembled within an engine for surge load estimations.

8.2 Suggestions for future research

This thesis explored successfully the current modelling capability for the prediction of the flow behaviour in axial compression systems at near and post stall conditions. The tools developed and tested provide a foundation for future research in stall and surge. Furthermore, the data generated from the computations can be used as a reference for development of low fidelity models for surge and rotating stall predictions.

The model selected in chapter 3 for prediction of multi-stage compressor's performance showed a good agreement with experimental results across the entire range of the compressor map. However, the CFD results showed a constant overflow all speeds, which indicates that there is a recurrent off-set relative to measured data. This has been attributed to the presence of geometric features but this hypothesis needs to be verified. For this purpose, it is required to improve the meshing software tools currently available.

Chapter 3 showed that the stability margin is under-predicted as a result of an under-prediction of eddy viscosity in the tip leakage flow. Furthermore, the CFD model ability to predict compressor's performance is worst as the rotor tip clearances increase. This suggests that turbulence modelling improvements are needed for prediction of the flow in the near casing region. Other turbulence models or other variants of the SA model can be studied to improved the compressor flow behaviour near stall operation. Alternatively, high fidelity models such as direct numerical simulation, large eddy simulation or detached eddy simulation can be used but validation is required.

The unsteady CFD results presented in chapter 4 showed a credible agreement with the measured data for aerodynamic predictions prior to stall. This modelling technique could be enhanced to investigate other aspects of this problem such as vibration which is typically associated with off-design operation close to the stability boundary. Further research can be performed on the flow features such as rotating stall cells propagation speed, number of cells and aeroelastic response. At the time of this investigation, the experimental evidence available was not enough to support further analysis.

The cases analysed in chapters 5 and 6 represent the highest fidelity simulations to date in a three-shaft engine during surge. To the best of the author's knowledge, this is also the first time worldwide that this type of calculation was successfully carried out. It should be noted that the numerical solutions at different time steps were saved providing the opportunity of revising distinct moments of the surge cycle at a much lower computational cost. For example, the calculations can be resumed at the beginning of the reverse flow period to study a rotor aeroelastic response. Similarly, it is possible to impose an aerodynamic perturbation or geometric changes (opening bleed valves, turning the VSV's, etc.) to evaluate the change on the surge dynamics.

The numerical domain used in chapters 5, 6 and 7 considered the presence of the low pressure system in order to provide an accurate boundary condition for the core compressors. Consequently, data has been generated in this domain during the different types of surge events which provides an opportunity to investigate the impact of surge on the aerodynamic loading of the fan and intake. For example, low-fidelity correlations such as the ones given by Mazzawy [1] and Marshall [7] for the prediction of surge loads across the compression system could be fine tuned.

Bibliography

[1] R. S. Mazzawy, "Surge-induced structural loads in gas turbines," *Journal of Engineering for Gas Turbines and Power*, vol. 102, pp. 162–168, jan 1980.

[2] I. J. Day, "Stall, Surge, and 75 Years of Research," *Journal of Turbomachinery*, vol. 138, no. 1, p. 011001, 2015.

[3] J. Whurr and J. Hart, "A Rolls-Royce Perspective on Concepts and Technologies for Future Green Propulsion Systems," in *Encyclopedia of Aerospace Engineering*, pp. 1–9, Chichester, UK: John Wiley Sons, Ltd, dec 2015.

[4] I. J. Day and N. A. Cumpsty, "Measurement and interpretation of flow within rotating stall cells in axial compressors.," *J Mech Eng Sci*, vol. 20, pp. 101–114, apr 1978.

[5] J. P. Longley, "A review of nonsteady flow models for compressor stability," apr 1994.

[6] T. R. Camp and J. Day, "A study of spike and modal stall phenomena in a low-speed axial compressor," in *Proceedings of the ASME Turbo Expo*, vol. 1, p. V001T03A109, ASME, jun 1997.

[7] F. L. Marshall, "Prediction of inlet duct overpressures resulting from engine surge," *Journal of Aircraft*, vol. 10, pp. 274–278, may 1973.

[8] M. Righi, V. Pachidis, L. Könözsy, and L. Pawsey, "Three-dimensional through-flow modelling of axial flow compressor rotating stall and surge," *Aerospace Science and Technology*, 2018.

[9] N. A. Cumpsty, "Compressor aerodynamics," *Longman Scientific Technical*, 1989.

[10] S. Dixon and C. Hall, *Fluid Mechanics and Thermodynamics of Turbomachinery*. No. May 2009, 2010.

[11] C. C. Koch and L. H. Smith, "Loss sources and magnitudes in axial-flow compressors," *Journal of Engineering for Gas Turbines and Power*, 1976.

[12] J. D. Denton, "Loss mechanisms in turbomachines," *Journal of Turbomachinery*, 1993.

[13] S. Lieblein, "Aerodynamic Design of Axial-flow Compressors. VI - Experimental Flow in Two-Dimensional Cascades," tech. rep., 1955.

[14] W. D. McNally and P. M. Sockol, "Review-computational methods for internal flows with emphasis on turbomachinery," *Journal of Fluids Engineering, Transactions of the ASME*, 1985.

[15] H. W. Emmons, C. E. Pearson, and H. P. Grant, "Compressor Surge and Stall Propagation," *ASME Transactions*, 1955.

[16] N. M. McDougall, N. A. Cumpsty, and T. P. Hynes, "Stall inception in axial compressors," in *Proceedings of the ASME Turbo Expo*, 1989.

[17] V. H. Garnier, A. H. Epstein, and E. M. Greitzer, "Rotating waves as a stall inception indication in axial compressors," *Journal of Turbomachinery*, 1991.

[18] J. Dodds, *Rotating stall in variable geometry compressors.* PhD thesis, Imperial College London, 2016.

[19] I. J. Day, "Stall inception in axial flow compressors," *Journal of Turbomachinery*, 1993.

[20] D. A. Hoying, C. S. Tan, H. D. Vo, and E. M. Greitzer, "Role of blade passage flow structures in axial compressor rotating stall inception," *Journal of Turbomachinery*, 1999.

[21] M. Inoue, M. Kuroumaru, T. Tanino, and M. Furukawa, "Propagation of multiple short-length-scale stall cells in an axial compressor rotor," *Journal of Turbomachinery*, 2000.

[22] C. Brandstetter, M. Jüngst, and H. P. Schiffer, "Measurements of radial vortices, spill forward, and vortex breakdown in a transonic compressor," *Journal of Turbomachinery*, vol. 140, may 2018.

[23] G. Pullan, A. M. Young, I. J. Day, E. M. Greitzer, and Z. S. Spakovszky, "Origins and structure of spike-type rotating stall," *Journal of Turbomachinery*, vol. 137, may 2015.

[24] H. Vo, C. S. Tan, and E. M. Greitzer, "Criteria for spike initiated rotating stall," *Journal of Turbomachinery*, vol. 130, jan 2008.

[25] A. Deppe, H. Saathoff, and U. Stark, "Spike-type stall inception in axial-flow compressors," in *ETC 2005 - 6th Conference on Turbomachinery: Fluid Dynamics and Thermodynamics*, 2005.

[26] M. A. Bennington, J. D. Cameron, S. C. Morris, C. Legaul, S. T. Barrows, J. P. Chen, G. S. McNulty, and A. R. Wadia, "Investigation of tip-flow based stall criteria using rotor casing visualization," in *Proceedings of the ASME Turbo Expo*, 2008.

[27] R. E. Peacock, "A review of turbomachinery tip gap effects. Part 2: Rotating machinery," *International Journal of Heat and Fluid Flow*, 1983.

[28] N. M. McDougall, "A comparison between the design point and near-stall performance of an axial compressor," *Journal of Turbomachinery*, 1990.

[29] J. A. Storer and N. A. Cumpsty, "Tip leakage flow in axial compressors," *Journal of Turbomachinery*, 1991.

[30] J. Dodds and M. Vahdati, "Rotating stall observations in a high speed compressor-part II: Numerical study," *Journal of Turbomachinery*, vol. 137, may 2015.

[31] E. M. Greitzer, "Surge and Rotating Stall in Axial Flow Compressors—Part I: Theoretical Compression System Model," *Journal of Engineering for Power*, vol. 98, p. 190, apr 1976.

[32] E. M. Greitzer, "Surge and Rotating Stall in Axial Flow Compressors—Part II: Experimental Results and Comparison With Theory," *Journal of Engineering for Power*, vol. 98, p. 199, apr 1976.

[33] I. J. Day, "Axial compressor performance during surge," *Journal of Propulsion and Power*, vol. 10, no. 3, pp. 329–336, 1994.

[34] P. X. Huang and R. S. Mazzawy, "Shock tube simulation of the transient surge phase inside an axial compressor," in *Proceedings of the ASME Turbo Expo*, vol. 2A-2018, American Society of Mechanical Engineers, jun 2018.

[35] M. Vahdati, G. Simpson, and M. Imregun, "Unsteady flow and aeroelasticity behaviour of aero-engine core compressors during rotating stall and surge," in *Proceedings of the ASME Turbo Expo*, vol. 130, pp. 153–163, 2008.

[36] H. Schoenenborn, V. Chenaux, and P. Ott, "Aeroelasticity at reversed flow conditions - Part 1: Numerical and experimental investigations of a compressor cascade with controlled vibration," in *Proceedings of the ASME Turbo Expo*, vol. 6, pp. 1171–1181, American Society of Mechanical Engineers Digital Collection, may 2011.

[37] H. Schoenenborn and T. Breuer, "Aeroelasticity at reversed flow conditions-part II: Application to compressor surge," *Journal of Turbomachinery*, vol. 134, pp. 61031–1–61031–8, nov 2012.

[38] L. C. Young and W. D. Beaulieu, "Review of hammershock pressures in aircraft inlets," *Journal of Aircraft*, vol. 12, pp. 210–216, may 1975.

[39] R. N. Gamache and E. M. Greitzer, "Reverse flow in multistage axial compressors," *Journal of Propulsion and Power*, vol. 6, pp. 461–473, may 1990.

[40] P. Waniczek, H. Schoenenborn, and P. Jeschke, "Experimental and analytical surge cycle analysis of a high pressure aero engine compressor," in *Proceedings of the ASME Turbo Expo*, vol. 8, pp. 2731–2741, American Society of Mechanical Engineers Digital Collection, jul 2012.

[41] T. Giersch, *Numerical Models for the Vibration Response of High Pressure Compressor Rotors with Validation for Forced Response and Surge*. PhD thesis, 2018.

[42] F. Crevel, N. Gourdain, and X. Ottavy, "Numerical simulation of aerodynamic instabilities in a multistage high-speed high-pressure compressor on its test rig-part II: Deep surge," *Journal of Turbomachinery*, vol. 136, oct 2014.

[43] F. Zhao, J. Dodds, and M. Vahdati, "Flow physics during surge and recovery of a multi-stage high-speed compressor," in *Proceedings of ASME Turbo Expo 2020: Turbomachinery Technical Conference and Exposition*, (London), 2020.

[44] J. P. Longley and T. P. Hynes, "Stability of flow through multistage axial compressors," *Journal of Turbomachinery*, vol. 112, pp. 126–132, jan 1990.

[45] I. J. Day and C. Freeman, "The unstable behavior of low and high-speed compressors," *Journal of Turbomachinery*, vol. 116, no. 2, pp. 194–201, 1994.

[46] N. Courtiade and X. Ottavy, "Experimental study of surge precursors in a high-speed multistage compressor," *Journal of Turbomachinery*, 2013.

[47] F. Crevel, N. Gourdain, and S. Moreau, "Numerical simulation of aerodynamic instabilities in a multistage high-speed high-pressure compressor on its test-rig-part I: Rotating stall," 2014.

[48] F. Zhao, J. Dodds, and M. Vahdati, "Poststall behavior of a multistage high speed compressor at off-design conditions," *Journal of Turbomachinery*, vol. 140, p. 121002, oct 2018.

[49] P. R. Spalart and S. R. Allmaras, "One-equation turbulence model for aerodynamic flows," in *30th Aerospace Sciences Meeting and Exhibit*, no. 1, pp. 1–21, 1992.

[50] K. B. Lee, M. Wilson, and M. Vahdati, "Validation of a numerical model for predicting stalled flows in a low-speed fan-Part I: Modification of Spalart-Allmaras turbulence model," *Journal of Turbomachinery*, vol. 140, may 2018.

[51] J. Moreno, J. Dodds, S. C. Stapelfeldt, and M. Vahdati, "Deficiencies in the SA Turbulence model for the prediction of the stability boundary in highly loaded compressors," *Journal of Turbomachinery*, pp. 1–35, jul 2020.

[52] A. I. Sayma, M. Vahdati, L. Sbardella, and M. Imregun, "Modeling of three-dimensional viscous compressible turbomachinery flows using unstructured hybrid grids," *AIAA Journal*, vol. 38, pp. 945–954, jun 2000.

[53] A. Jameson, W. Schmidt, and E. Turkel, "Numerical solution of the Euler equations by finite volume methods using Runge Kutta time stepping schemes," American Institute of Aeronautics and Astronautics (AIAA), jun 1981.

[54] R. C. Swanson and E. Turkel, "On central-difference and upwind schemes," *Journal of Computational Physics*, vol. 101, pp. 292–306, aug 1991.

[55] M. Choi, N. H. Smith, and M. Vahdati, "Validation of Numerical Simulation for Rotating Stall in a Transonic Fan," *Journal of Turbomachinery*, vol. 135, nov 2012.

[56] F. Menter, "Improved two-equation k-omega turbulence models for aerodynamic flows," *NASA Technical Memorandum*, no. 103978, pp. 1 – 31, 1992.

[57] D. C. Wilcox, "Formulation of the k-ω turbulence model revisited," in *AIAA Journal*, vol. 46, pp. 2823–2838, nov 2008.

[58] Y. Liu, L. Lu, L. Fang, and F. Gao, "Modification of Spalart-Allmaras model with consideration of turbulence energy backscatter using velocity helicity," *Physics Letters, Section A: General, Atomic and Solid State Physics*, vol. 375, pp. 2377–2381, jun 2011.

[59] L. Ma, L. Lu, J. Fang, and Q. Wang, "A study on turbulence transportation and modification of Spalart-Allmaras model for shock-wave/turbulent boundary layer interaction flow," *Chinese Journal of Aeronautics*, vol. 27, pp. 200–209, apr 2014.

[60] K. B. Lee, J. Dodds, M. Wilson, and M. Vahdati, "Validation of a numerical model for predicting stalled flows in a low-speed fan-part II: Unsteady analysis," *Journal of Turbomachinery*, vol. 140, may 2018.

[61] S. Kim, G. Pullan, C. A. Hall, R. P. Grewe, M. J. Wilson, and E. Gunn, "Stall Inception in Low-Pressure Ratio Fans," *Journal of Turbomachinery*, vol. 141, jul 2019.

[62] S. Stapelfeldt and M. Vahdati, "Improving the Flutter Margin of an Unstable Fan Blade," *Journal of Turbomachinery*, vol. 141, jul 2019.

[63] F. Wang, M. Carnevale, L. di Mare, and S. Gallimore, "Simulation of multistage compressor at off-design conditions," *Journal of Turbomachinery*, vol. 140, feb 2018.

[64] P. R. Spalart, "Direct simulation of a turbulent boundary layer up to Rθ= 1410," *Journal of Fluid Mechanics*, vol. 187, pp. 61–98, 1988.

[65] M. V. Zagarola and A. J. Smits, "Scaling of the mean velocity profile for turbulent pipe flow," *Physical Review Letters*, vol. 78, no. 2, pp. 239–242, 1997.

[66] M. Cevik, H. D. Vo, and H. Yu, "Casing treatment for desensitization of compressor performance and stability to tip clearance," *Journal of Turbomachinery*, vol. 138, dec 2016.

[67] X. Nan, F. Lin, S. Wang, L. Liu, N. Ma, and J. Chen, "The analysis of axial momentum of the rotor tip flows for axial compressors with circumferential grooves,"

in *Proceedings of the ASME Turbo Expo*, vol. 2A, American Society of Mechanical Engineers (ASME), sep 2014.

[68] X. Nan, F. Lin, T. Himeno, and T. Watanabe, "The behavior of the casing boundary layer with the presence of tip leakage vortex," in *Proceedings of the ASME Turbo Expo*, vol. 2A-2018, American Society of Mechanical Engineers (ASME), aug 2018.

[69] D. E. Van Zante, A. J. Strazisar, J. R. Wood, M. D. Hathaway, and T. H. Okiishi, "Recommendations for achieving accurate numerical simulation of tip clearance flows in transonic compressor rotors," in *Journal of Turbomachinery*, vol. 122, pp. 733–742, American Society of Mechanical Engineers Digital Collection, oct 2000.

[70] G. T. Chen, E. M. Greitzer, C. S. Tan, and F. E. Marble, "Similarity analysis of compressor tip clearance flow structure," *Journal of Turbomachinery*, vol. 113, pp. 260–269, apr 1991.

[71] X. He, F. Zhao, and M. Vahdati, "Uncertainty Quantification of Spalart-Allmaras Turbulence Model Coefficients for Compressor Tip Flow Features," *Journal of fluids engineering*, apr 2020.

[72] L. He, "Method of simulating unsteady turbomachinery flows with multiple perturbations," *AIAA Journal*, 1992.

[73] S. C. Stapelfeldt and L. Di Mare, "Reduced passage method for multirow forced response computations," *AIAA Journal*, 2015.

[74] F. Montomoli, E. Naylor, H. P. Hodson, and L. Lapworth, "Unsteady effects in axial compressors: A multistage simulation," *Journal of Propulsion and Power*, vol. 29, no. 5, pp. 1001–1008, 2013.

[75] N. Gourdain, X. Ottavy, and A. Vouillarmet, "Experimental and numerical investigation of unsteady flows in a high speed three stages compressor," in *8th European Conference on Turbomachinery: Fluid Dynamics and Thermodynamics, ETC 2009 - Conference Proceedings*, pp. 247–266, 2009.

[76] W. Zhang, S. Stapelfeldt, and M. Vahdati, "Influence of the inlet distortion on fan stall margin at different rotational speeds," *Aerospace Science and Technology*, 2020.

[77] L. Sbardella, A. I. Sayma, and M. Imregun, "Semi-structured meshes for axial turbomachinery blades," *International Journal for Numerical Methods in Fluids*, vol. 32, pp. 569–584, mar 2000.

[78] M. Vahdati, A. I. Sayma, C. Freeman, and M. Imregun, "On the use of atmospheric boundary conditions for axial-flow compressor stall simulations," *Journal of Turbomachinery*, 2005.

E-theses letter: request to reproduce an extract from a third party's published work

9th March 2021

Dear Rolls-Royce plc,

I am completing my PhD thesis at Imperial College entitled 'Investigation of near and post stall behaviour of axial compression systems'.

I seek your permission to reprint, in my thesis an extract from (put in the list of papers here):

1. Moreno, J, Dodds, J, Vahdati, M, & Stapelfeldt, S. "Deficiencies in Turbulence Modelling for the Prediction of the Stability Boundary in Highly Loaded Compressors." *Proceedings of the ASME Turbo Expo 2019: Turbomachinery Technical Conference and Exposition*. *Volume 2A: Turbomachinery*. Phoenix, Arizona, USA. June 17–21, 2019. V02AT39A025. ASME. https://doi.org/10.1115/GT2019-91227
2. Moreno, J., Dodds, J., Stapelfeldt, S., and Vahdati, M. (December 2, 2020). "Deficiencies in the Spalart–Allmaras Turbulence Model for the Prediction of the Stability Boundary in Highly Loaded Compressors." ASME. *J. Turbomach*. December 2020; 142(12): 121012. https://doi.org/10.1115/1.4047784
3. Moreno, J, Dodds, J, Sheaf, C, Zhao, F, & Vahdati, M. "Aerodynamic Loading Considerations of Three-Shaft Engine Compression System During Surge." *Proceedings of the ASME Turbo Expo 2020: Turbomachinery Technical Conference and Exposition*. *Volume 2A: Turbomachinery*. Virtual, Online. September 21–25, 2020. V02AT32A011. ASME. https://doi.org/10.1115/GT2020-14305
4. Moreno, J, Dodds, J, Sheaf, C, Zhao, F, & Vahdati, M. "Aerodynamic Loading Considerations of Three-Shaft Engine Compression System During Surge." ASME. *J. Turbomach.* [Accepted and waiting for the doi]

I would like to include the extract in my thesis which will be added to the Imperial College library, including ethesis (link to spiral) and made available to the public under a creative common license.

If you are happy to grant me all the permissions requested, please return a signed copy of this letter. If you wish to grant only some of the permissions requested, please list these and then sign.

Yours sincerely,

Jose Pedro Nunes Teixeira Vaz Moreno

Permission granted for the use requested above:

I confirm that I am the copyright holder of the extract above and hereby give permission to include it in your thesis which will be made available, via the internet, for non-commercial purposes under the terms of the user licence.

Signed: Digitally signed by Bolger, John
Date: 2021.03.10 08:45:01 Z

Organisation: Rolls-Royce Plc